Study of on-body antennas and channel properties for short-range communications in the context of Wireless Body Area Sensor Networks (WBASN)

Rizwan Masood

UNIVERSITE
BRETAGNE
LOIRE

THÈSE / Télécom Bretagne
sous le sceau de l'Université Bretagne Loire

pour obtenir le grade de Docteur de Télécom Bretagne
En accréditation conjointe avec l'Ecole Doctorale Sicma
Mention : Sciences et Technologies de l'Information et de la Communication

présentée par
Rizwan Masood
préparée dans le département Micro-ondes
Laboratoire Labsticc

Study of on-body antennas and channel properties for short-range communications in the context of Wireless Body Area Sensor Networks (WBASN)

Thèse soutenue le 29 mars 2016
Devant le jury composé de :

Olivier Sentieys
Professeur, ENSSAT – Lannion / président

Christophe Delaveaud
Ingénieur R&D (HDR), CEA-LETI - Grenoble / rapporteur

Rodolphe Vauzelle
Professeur, XLIM-SIC, Université de Poitiers / rapporteur

Ronan Sauleau
Professeur, IETR – Université de Rennes 1 / examinateur

Patrice Pajusco
Directeur d'études, Télécom Bretagne / examinateur

Christian Person
Professeur, Télécom Bretagne / Directeur de thèse

Yann Toutain
Directeur R&D, Satimo Bretagne – Microwave Vision Group, Brest / Invité

N° d'ordre : 2016telb0396

Sous le sceau de l'Université Bretagne Loire

Télécom Bretagne

En accréditation conjointe avec l'Ecole Doctorale Sicma

Study of on-body antennas and channel properties for short-range communications in the context of Wireless Body Area Sensor Networks (WBASN)

Thèse de Doctorat

Mention : Sciences et Technologies de l'Information et de la Communication (STIC)

Présentée par **Rizwan Masood**

Département : Micro-ondes

Laboratoire : Lab-STICC Pôle : Micro-ondes et matériaux (MOM)

Directeur de thèse : Christian Person

Soutenance le 29 mars 2016

Jury :

Christophe Delavaud	Ingénieur R&D - HDR, CEA-Leti, Grenoble (Rapporteur)
Rodolphe Vauzelle	Professeur XLIM-SIC, Université de Poitiers (Rapporteur)
Christian Person	Professeur, Télécom Bretagne, Brest (Directeur de thèse)
Ronan Sauleau	Professeur, IETR - Université de Rennes 1(Co-encadrant de thèse)
Olivier Sentieys	Professeur, ENSSAT, Lannion (Examinateur)
Patrice Pajusco	Directeur d'études, Télécom Bretagne, Brest (Examinateur)
Yann Toutain	Directeur R&D, Satimo – Microwave Vision Group, Brest (Invitée)

------ To my mother and father

"There are only two ways to live your life. One is as though nothing is a miracle. The other is as though everything is a miracle."

——Albert Einstein

Look up at the stars and not down at your feet. Try to make sense of what you see, and wonder about what makes the universe exist. Be curious.

—— Stephen Hawking

Acknowledgements

This dissertation is the outcome of my PhD thesis which was initiated in Brest, France during January, 2013. Firstly, I would like to express my sincere thanks and gratitude to Prof. Christian Person for giving me the wonderful opportunity to work under his patronage on a very rich and enchanting research area. His supreme research spirit and aptitude really polished my intuitive and critical approach towards science. Apart from his valuable guidance and support, he has been very kind, welcoming and friendly to me as a human being. It was also a wonderful experience for me to work in Lab-STICC laboratory surrounded by gifted minds and smart scientists.

I would also like to express my sincere thanks to Prof. Ronan Sauleau, the supervisor of my thesis for his valuable guidance and directions throughout the course of thesis. More particularly, his guidelines for a number of technical reports accomplished during this thesis have been remarkable. His superb technical writing immersed with precision and flair also polished my writing skills. I would also like to express my special thanks to Cominlabs and Brittany region of France to sponsor the BoWI project and hence, this thesis.

I would like to acknowledge Pascal Coant, Raymond Jezequel, and Jean-Marc Autret from the Microwaves department for their technical support during various measurements realized in this thesis. I am also very grateful to Prof. Patrice Pajusco for his insightful suggestions and valuable guidelines.

A special mention goes to all my great friends and brilliant colleagues especially Abdelrahman Ijjeh, Axelle Pillain, Georges Mikhail, Gloria Makhoul, John Eric Ortiz Guzman, Lyes Rahmouni, and Maksims Abalenkovs to name only a few for the wonderful time and cherishing moments that we spent together.

Above all, I would like to express my profound thanks and gratefulness to my parents, brothers, sisters and all other family members for their special love, affection and cares for me regardless of the physical distances.

Abstract

This thesis finds its place in the framework of BoWI project. BoWI stands for Body-World Interaction and is a novel and innovative inspiration of Wireless Body Area Networks (WBANs). The major scientific contributions of this thesis are focused around two main topics for WBAN applications: (*i*) Radio channel characterization and (*ii*) antenna design with stable performance in proximity to human body while offering tunable features e.g., radiation pattern and polarization.

For the first project, smart sensors were used incorporating ultra-miniaturized chip antennas under pattern diversity configuration which were developed by one of the project partners. These sensors were used to investigate the off-body radio channel considering various parameters such as delay spread and channel capacity using real-time multipath channel measurements. Significant improvement in channel capacity has been reported exploiting the 2×2 MIMO configurations compared to SISO systems especially at high SNRs. Small-scale channel fading has also been investigated for both off- and on-body channels using real-time measurement data. A robust fitting algorithm has been developed for this purpose, based on Maximum Likelihood Estimation and Kolmogorov-Smirnov test as goodness of fit. Optimum first-order fading models have been reported for both off- and on-body channels using the proposed fitting algorithm on real-time measurement data. For numerical channel studies, a robust channel simulator was also developed using an electrically small chip antenna on realistic 3D body morphologies with tunable gestures. The simulator includes various enhancements such as local mesh refinement and reduction techniques, hence offering the power to simulate arbitrary WBASN scenarios under limited simulation resources. The scope of the channel simulator has also been demonstrated for sample body postures showing its interest for posture classification in interactive gesture recognition concept as used in BoWI project.

For the second sub-project, various simulation studies were first undertaken to consider the critical impact of human body on antenna performance. Antenna topologies with stable on-body performance and appropriate radiation patterns were designed for both on-and off-body applications e.g., Inverted-F antenna and short-circuited ring path antenna. Based on the characteristic mode theory of patch antennas, a compact dual-mode dual-pattern polarization diversity antenna has been designed. The antenna offers appropriate radiation characteristics for both on- and off-body applications at single frequency, meanwhile offering a negligible cross-coupling between the two modes and a stable on-body performance. It provides two different forms of diversities (radiation and polarization) in a single package, hence circumventing the use of antenna arrays since space and form factor are crucial for wearable applications. The antenna is also a suitable candidate for diversity and MIMO applications while providing reasonable diversity gain (close to 10 dB). Finally, the performance of radiation pattern and polarization diversities simultaneously has been demonstrated for body-centric applications. Significant improvements in link budget have been reported which are corroborated by both full-wave simulations and real-time measurements.

Table of Contents

List of Figures

List of Tables

Chapter 0. Résumé en français

0.1. Introduction

Les réseaux de capteurs corporels sans fils (Wireless Body Area Sensor Networks "WBASNs" en anglais) sont l'une des principales technologies émergeantes pour résoudre plusieurs défis de la vie quotidienne. Ils fournissent une large gamme d'applications intéressantes et innovantes dans plusieurs domaines: soins de santé, sports, divertissement, surveillance et contrôle environnemental. Cette thèse s'inscrit dans le cadre du projet BoWI «Body-World Interaction» qui signifie l'interaction entre le monde et le corps et qui présente une nouvelle inspiration de WBASNs. Le projet BoWI a été financé par le Labex CominLabs par l'ANR dans le cadre du programme «Investissements d'avenir» et par la Région Bretagne. Les principales contributions scientifiques de cette thèse se concentrent autour de deux thèmes clés pour les applications WBASNs, à savoir la caractérisation du canal radio et la conception des antennes, qui sont étroitement liés.

Pour la première partie, de nombreuses campagnes expérimentales ont été menées sur des sujets humains dans des environnements riches en trajets multiples en utilisant des antennes puce ultra-miniaturisées (seulement quelques *mm* d'empreinte) montées sous la configuration de la diversité de rayonnement. De nombreux paramètres du canal radio ont été étudiés dans ce contexte, par exemple, la capacité du canal, l'étalement du temps de propagation et l'évanouissement, en fonction de leur importance du point de vue propagation. Un simulateur de canal numérique a été également mis au point. Il est capable de simuler des scénarios de WBASNs arbitraires en utilisant des morphologies corporelles réalistes et accordables. L'application du simulateur a également été démontrée pour le concept interactif de reconnaissance des gestes tel que proposé par le projet BoWI.

Pour la deuxième partie, une antenne multi-mode a été conçue fournissant la diversité du rayonnement, et de la polarisation à une seule fréquence pour optimiser l'efficacité de liaison pour les communications on-body. Cette conception évite l'utilisation de réseaux d'antennes pour ces applications puisque les différents diagrammes de rayonnement et la polarisation sont nécessaires pour chaque cas. La convenance de la diversité de rayonnement et de la polarisation pour des applications BAN a également été démontrée grâce à des améliorations significatives dans le budget de liaison.

0.2. Caractérisation des canaux radio pour WBASNs en utilisant des antennes puce ultra-miniaturisées

Le projet BoWI emploie principalement les normes existantes WPAN et WBAN des standards d'IEEE 802.15.6, 802.15.4 respectivement. Afin de soutenir la recherche préliminaire entre les différents partenaires du projet, une plate-forme innovante et portable a été développée par les partenaires du projet BoWI, nommé Zyggie (Fig. 0.1 (a)). Le capteur Zyggie comprend une plaque de substrat multicouche ayant deux

antennes puce LTCC (monopôles) de dimensions de 7 × 2 × 1,20 mm^3 fonctionnant dans la bande ISM 2.4 GHz (soit une longueur physique de $\lambda_0/18$ seulement à 2,40 GHz). Les antennes puce sont montées orthogonalement pour supporter la diversité du rayonnement comme le montrent les diagrammes de rayonnement mesurés en 3D et illustrés sur la Fig. 0.1 (b), (c).

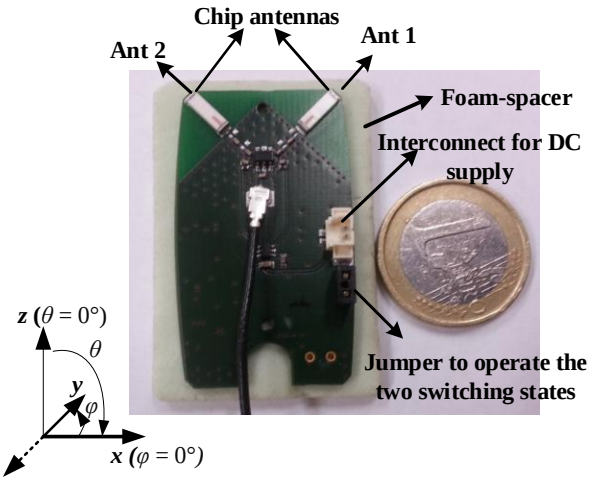

(a)

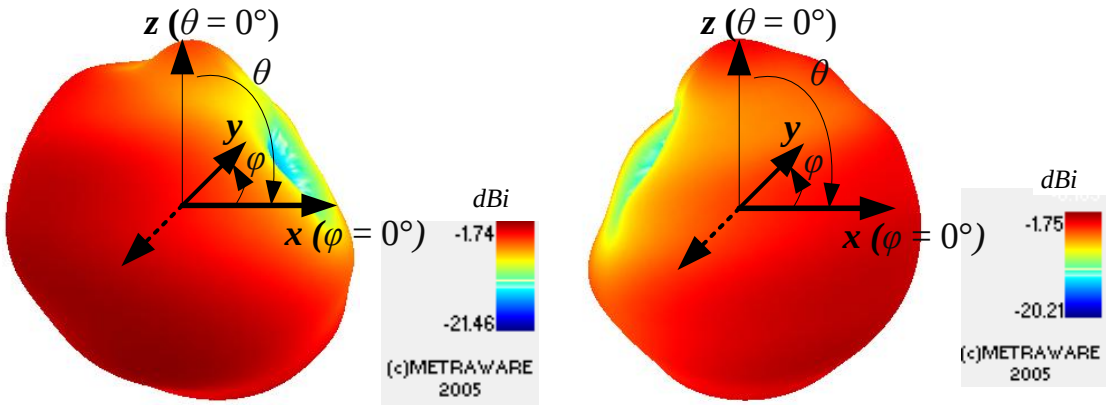

(b) (c)

Figure 0.1. Le capteur Zyggie utilisé pour des études de canal et de propagation, (b, c) les diagrammes de rayonnement 3D mesurés pour (b) Ant 1 et (c) Ant 2 à 2,40 GHz illustrant la diversité du rayonnement.

La performance de la diversité du canal off-BAN a également été étudiée en utilisant des mesures de canal en temps réel, en exploitant la diversité des antennes puce miniaturisées de capteurs Zyggie (Fig. 0,1 (a)). Les mesures ont été effectuées sur une personne avec un IMC de 23,4 dans un environnement indoor dans la configuration off-body, comme l'indique la Fig. 0.2 (a). La capacité ergodique C (bits/s/Hz) du canal a été calculée pour un canal MIMO 2×2 obtenu en utilisant les gains mesurés h_{ij} (i, j) ε $\{1, 2\}^2$ des sous-canaux de transfert complexes. Les résultats sont montrés sur la Fig. 0.2 (b) pour les deux configurations LoS et NLoS, et comparés par rapport à ceux de canaux idéaux 1×1 (SISO) et 2x2 (MIMO) i.i.d Rayleigh. Comme on peut le remarquer, le régime de la diversité proposée peut offrir une capacité améliorée par rapport à un système SISO, surtout pour un RSB élevés avec une augmentation moyenne de la capacité de 2 bps/Hz (=min. (M, N)) par 3 dB de hausse du RSB.

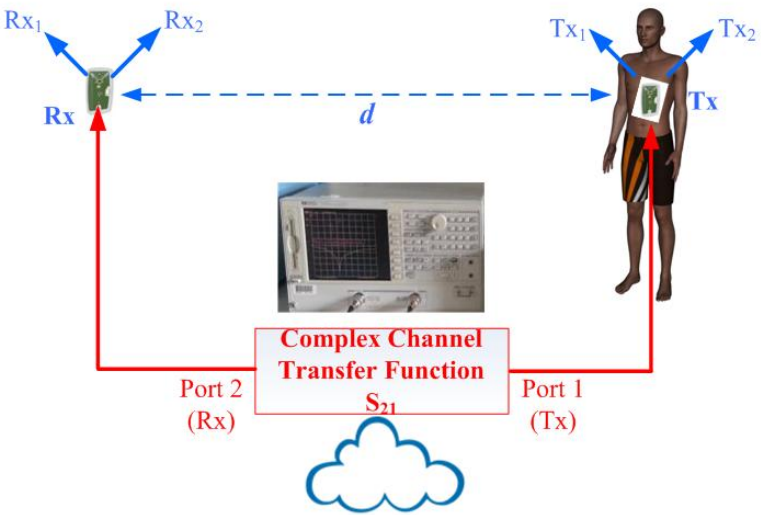

(a)

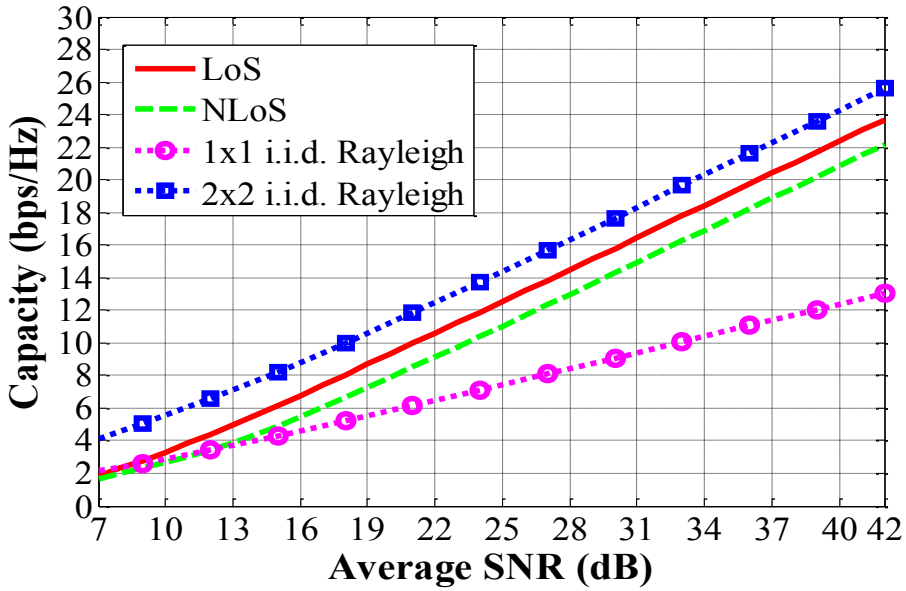

(b)

Figure 0.2. (a) Configuration de mesure du canal de diversité off-body. Une orientation de + 45 ° a été considérée pour les antennes Tx_2 et Rx_2 et -45 ° pour Tx_1 et Rx_1 (b) La capacité moyenne mesurée par rapport au RSB.

Afin de relever les défis de fiabilité de la liaison, du transfert de données, ainsi que d'autres services, la connaissance du modèle de canal s'avère très importante pour la modélisation au niveau du système. Par conséquent, nous avons proposé et mis en œuvre un algorithme robuste basé sur le test Kolmogorov-Smirnov (K-S) d'hypothèse pour détecter le modèle de distribution du meilleur ajustement des données empiriques de canal radio. Dans ce contexte, sept distributions standards ont été utilisées comme points de repère qui sont couramment utilisés pour décrire statistiquement l'évanouissement du canal, à savoir Normal (N), Lognormal (LG), Rayleigh (R), Weibull (W), Gamma (G), Exponentiel (E) et Nakagami-m (NG). Le schéma de principe de l'algorithme proposé est représenté sur la Fig. 0.3.

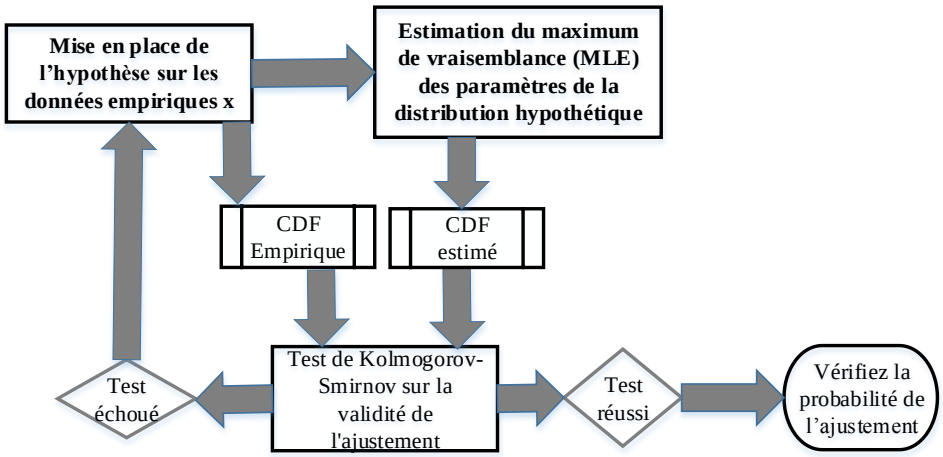

Figure 0.3. L'algorithme d'ajustement proposé pour l'étude statistique des canaux empiriques.

L'algorithme d'ajustement a également été appliqué pour déterminer le meilleur modèle à petite échelle de premier ordre pour l'évanouissement des canaux off-body en utilisant des capteurs Zyggie (Fig. 0.4). Les données mesurées ont été utilisées pour l'étude statistique en utilisant l'algorithme d'ajustement proposé. Les modèles correspondants détectés par l'algorithme pour tous les scénarios mesurés sont listés dans le tableau 0.1. Sur la base des résultats statistiques, une distribution normale a été recommandée pour les canaux off-body sous les scenarios LoS et une distribution de Weibull pour les scénarios QNLoS.

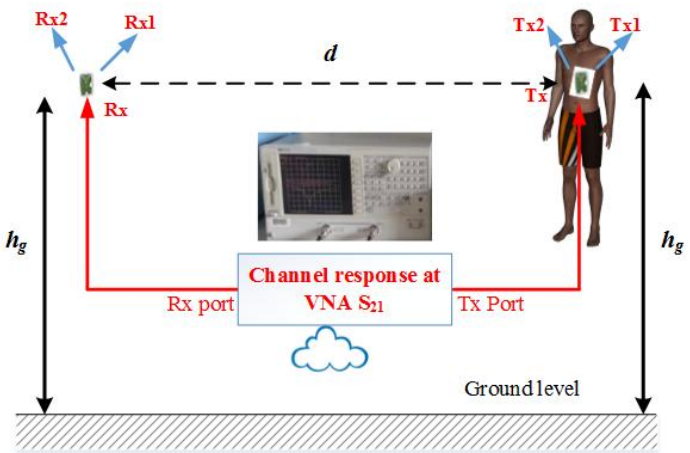

Figure 0.4. Configuration de mesure de canal off-body (LoS).

Liaison	*d* (cm)	Scenarios	Modèles recommandés
Tx_1Rx_1	50	LoS	Normal (μ = 0.6356, σ = 0.1226)
		QNLoS	Weibull (η = 0.3564, β = 2.0059)
Tx_1Rx_1	100	LoS	Normal (μ = 0.6430, σ = 0.0857)
		QNLoS	Weibull (η = 0.3542, β = 2.0265)
Tx_2Rx_2	100	LoS	Normal (μ = 0.6277, σ = 0.1105)
		QNLoS	Weibull (η = 0.3467, β = 2.1415)

Tableau 0.1. Les résultats statistiques du canal en utilisant l'algorithme d'ajustement proposé pour différents scénarios de mesure de canal off-body à 2,40 GHz pour le sujet humain.

La caractérisation statistique pour des canaux on-body statiques et dynamiques et à bande étroites a été également étudiée en utilisant l'algorithme d'ajustement proposé sur les mesures de canal on-body en temps réel. Trois canaux on-body ont été mesurés à savoir le chest-wrist, le chest-hip et chest-thigh (Fig. 0.5). Pour chacun des canaux de mesure, deux autres scénarios sont envisagés, à savoir le scenario quasi-statique et dynamique. Les données mesurées ont été utilisées comme entrée de l'algorithme pour déterminer le meilleur modèle de l'évanouissement à petite échelle. Les résultats correspondants pour tous les scénarios mesurés sont listés dans le tableau 0.2. Sur la base de ces résultats, une distribution de Weibull a été recommandée pour le canal chest-wrist et chest-thigh. Pour le canal chest-hip quasi-statique, une distribution normale a été observée pour premier ordre d'évanouissement dû à la propagation LoS dominante qui change à Nakagami-*m* pour le scénario dynamique à cause de l'ombrage causé par le mouvement du corps.

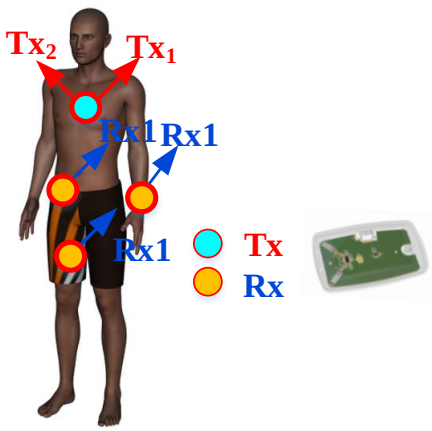

Figure 0.5. Emplacement des nœuds de capteurs Tx/Rx pour des mesures de canal on-body sur un sujet humain.

Canal	Scenario	Modèle recommandé	Les paramètres estimés des modèles	
Tx_1: Chest, Rx_1: Wrist	Quasi-statique	Weibull	η = 0.4443	β = 2.3312
	Dynamique	Weibull	η = 0.3247	β = 1.7278
Tx_2: Chest, Rx_1: Hip	Quasi-statique	Normal	μ = 0.5035	σ = 0.1443
	Dynamique	Nakagami	m = 2.1766	ω = 0.1888
Tx_2: Chest, Rx_1: Thigh	Quasi-statique	Weibull	η = 0.4094	β = 2.2560
	Dynamique	Weibull	η = 0.4286	β = 2.3301

Tableau 0.2. Les résultats des statistiques de canal pour divers scénarios de mesures de canal on-body.

0.3. La conception des antennes et l'interaction avec le corps humain aux fréquences ISM

Le corps humain est un milieu à pertes avec des paramètres très élevés aux fréquences micro-ondes et peut fortement influencer la performance de l'antenne fonctionnant à proximité. Afin d'étudier l'impact du corps humain, une antenne monopôle imprimée avec un plan de masse partiel a été conçue pour la bande passante ISM 2,4 GHz (2,40 à 2,4835 GHz) et placée sur un modèle de tissu à perte. On a observé que les paramètres de l'antenne sont très dégradés à proximité du corps, par exemple, la fréquence est décalée en raison de variations de l'impédance d'entrée et le gain dans les plans E et H diminue simultanément avec le rendement de rayonnement en raison des pertes provoquées par le tissu. En outre, l'espacement entre l'antenne et le corps a été observé comme étant un facteur très important pour contrôler la performance de l'antenne sur le corps. L'effet maximal au niveau du coefficient de réflexion, du gain ainsi que de l'efficacité de l'antenne a été observé pour un espacement minimum. Cependant, l'impact des tissus du corps devient de moins en moins sévère quand l'espacement augmente jusqu'à ce que nous approchons des performances dans l'espace libre. Ceci est dû à la réduction de l'interaction de champ proche de l'antenne avec le tissu corporel, lorsque l'espacement augmente.

Pour des applications on-body, un rayonnement omnidirectionnel dirigé parallèle à la surface du corps avec une polarisation verticale est nécessaire. Une antenne monopole est connue pour être un candidat approprié pour telles applications. Cependant, elle a une hauteur assez importante ($\lambda_0/4$ où λ_0 = 12,5 *cm* @ 2,40 GHz) et n'est pas une solution réalisable pour des applications on-body en raison de problèmes de portabilité. Par conséquent, une antenne Inverted-F (IFA) a été conçue pour une résonance dans la bande passante ISM 2.4 GHz, tout en conservant un profil plus bas que son homologue antenne monopôle (hauteur de $\lambda_0/12$ seulement à 2,4 GHz) et en réalisant avec succès les exigences optimales des deux diagrammes de rayonnement et de polarisation pour des

applications on-body. La performance de l'antenne a également été validée à proximité du corps humain, et a été rapportée comme étant très stable et comparable à celle dans l'espace libre, grâce à un plan de masse complet.

Une antenne patch anneau court-circuitée (Fig. 0,6) a également été prise en compte dans le but de concevoir une antenne unique utilisable pour des communications on- et off-body à une seule fréquence (2,45 GHz). Les deux premiers modes TM_{01} et TM_{11} de cette antenne ont été étudiés en détail. Le mode TM_{01} offre un diagramme de rayonnement omnidirectionnel azimutal avec une polarisation verticale (appropriée pour des liaisons on-body) tandis que le mode TM_{11} offre un maximum de rayonnement dans la direction bordée (approprié pour des liens off-body). Deux prototypes différents de l'antenne ont été conçus pour atteindre la diversité de rayonnement requise pour des applications on- et off-body à 2,45 GHz comme le montrent les figures Fig. 0,7 et Fig. 0,8 respectivement. Ce concept de différents modes excités à la même fréquence est utilisé en outre pour la conception d'une seule antenne de diversité de rayonnement à 2,45 GHz.

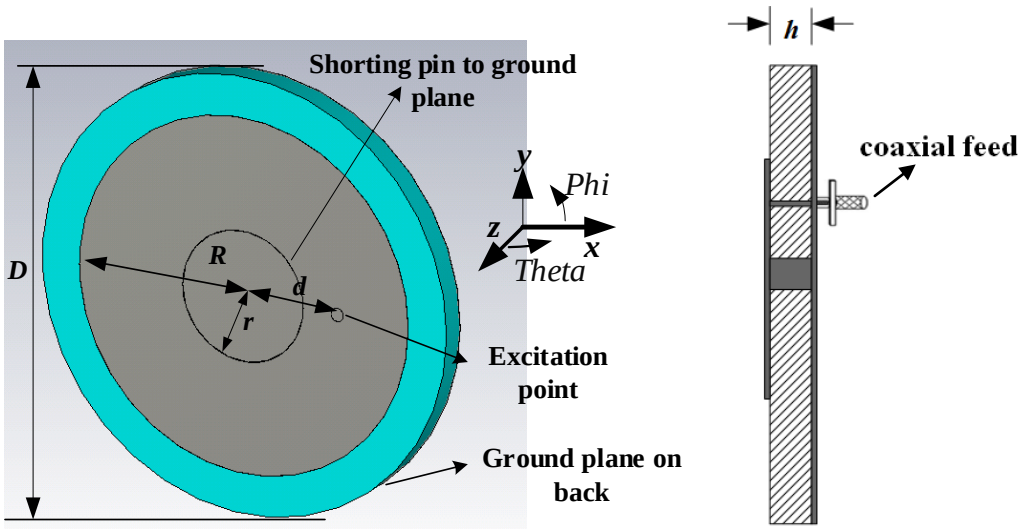

Figure 0.6. (a) Configuration de l'antenne patch anneau court-circuité (b) Vue de côté.

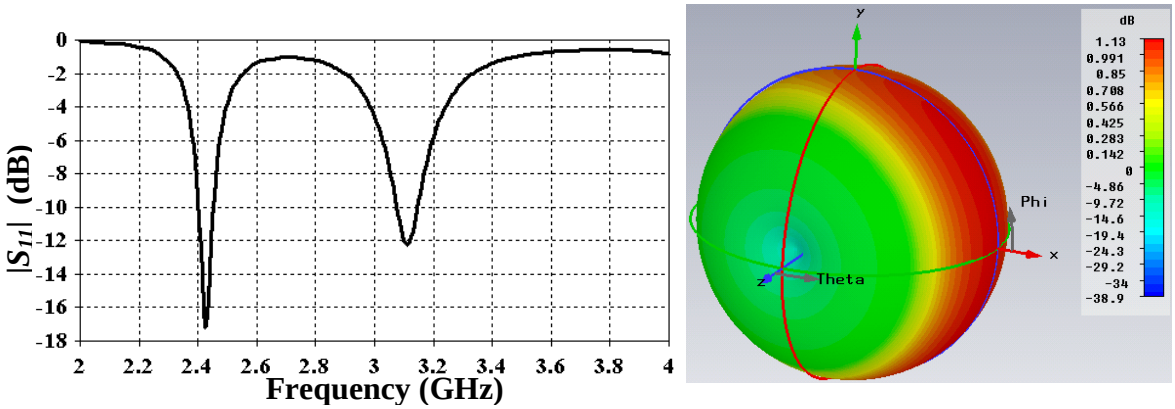

(a) (b)

Figure 0.7. (a) Coefficient de réflexion simulé de l'antenne montrant la première résonance (TM_{01}) à 2,45 GHz. Les dimensions optimisées en *mm*: R = 21.8, r = 8, d = 12,45, D = 53,6 en Fig. 0.6. (b) Le diagramme de rayonnement en 3D de l'antenne à 2.45 GHz (système de coordonnées représenté sur la Fig. 0,6).

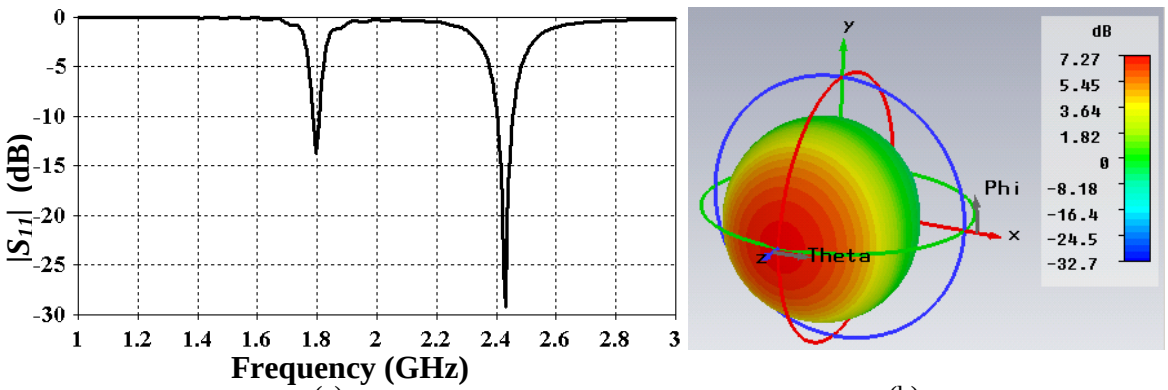

(a) (b)

Figure 0.8. (a) Coefficient de réflexion simulé de l'antenne montrant la première résonance à 2,45 GHz. Les dimensions optimisées en *mm*: R = 26, r = 7.5, d = 11.45, D = 62 en Fig. 0.6. (b) Le diagramme de rayonnement en 3D de l'antenne à 2.45 GHz (système de coordonnées représenté sur la Fig. 0,6).

0.4. Conception d'une antenne puce miniaturisée et simulateur de canal numérique

Le projet BoWI est basé sur un réseau de capteurs corporel sans fil à différents endroits sur le corps en utilisant un ensemble de postures (appelées alphabets) pour interagir avec le monde numérique. Par conséquent, un simulateur de canal numérique robuste a été développé dans ce contexte avec le pouvoir de simuler des scénarios de WBASNs arbitraires dans différentes postures.

Dans la première étape, une antenne puce à méandre (MCA) électriquement petite a été conçue avec des dimensions globales de quelques *mm* seulement (Fig. 0,9), afin de pouvoir l'utiliser en conjonction avec le simulateur de canal. L'antenne résonne dans la bande passante d'ISM 2,4 GHz (2,40 à 2,4835 GHz) avec un coefficient de réflexion $|S_{11}|$ <-10 dB comme le montre la Fig. 0,10.

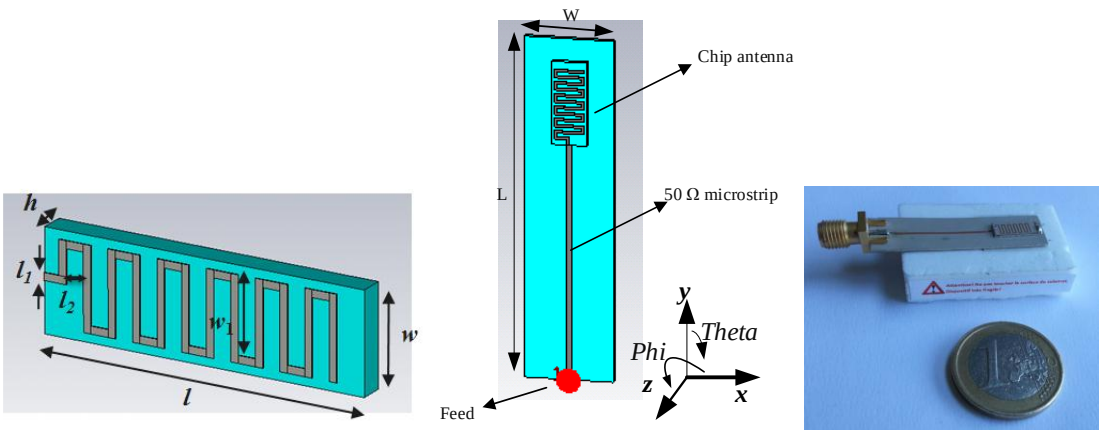

(a) (b) (c)

Figure 0.9 (a) La configuration du MCA avec des dimensions (*mm*): l = 9.5, w = 4, h = 0.635, l_1= 0.3, l_2= 0.4, w_1= 3 (b) MCA avec un microruban 50Ω adapté à l'antenne, dimensions (*mm*): L = 39, W = 10 (c) Photo du prototype fabriqué de l'antenne.

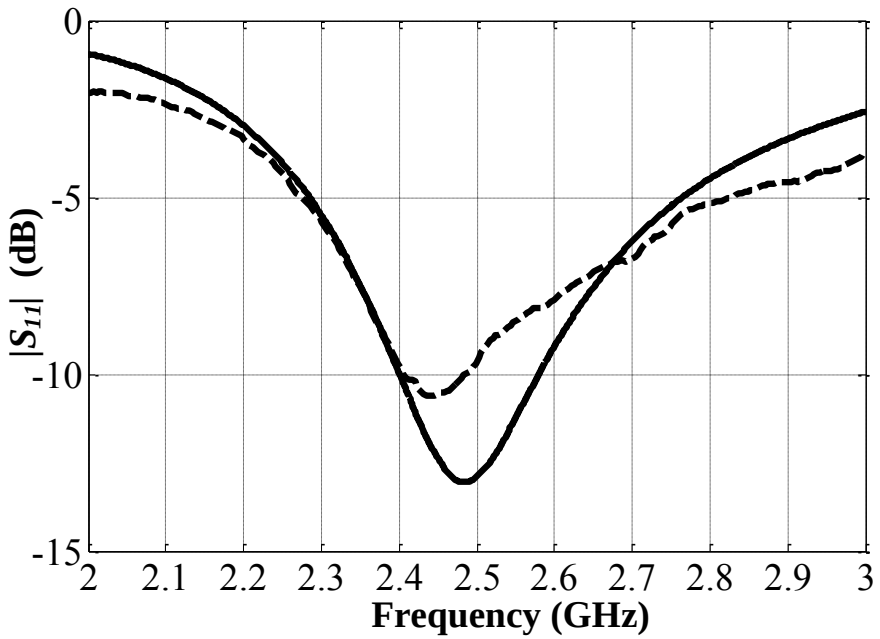

Figure 0.10. Coefficient de réflexion de l'antenne puce dans l'espace libre. Simulation (——) et de mesure (– – –).

Un simulateur de canal robuste a été développé en tenant compte des morphologies du corps réalistes et accordables, sur CST Microwave Studio en utilisant l'antenne puce conçue. Le simulateur a été réalisé après l'exécution des plusieurs améliorations de simulation intelligentes afin de diminuer l'énorme taille du problème qui devrait être réalisée avec des ressources limitées. Le simulateur a été testé avec succès pour diverses postures du corps. Les résultats de simulation pour l'une des postures du corps sont présentés sur la Fig. 0,11. L'application du simulateur de canal a également été démontrée pour la classification des postures en fonction des modèles basés sur l'estimation des distances.

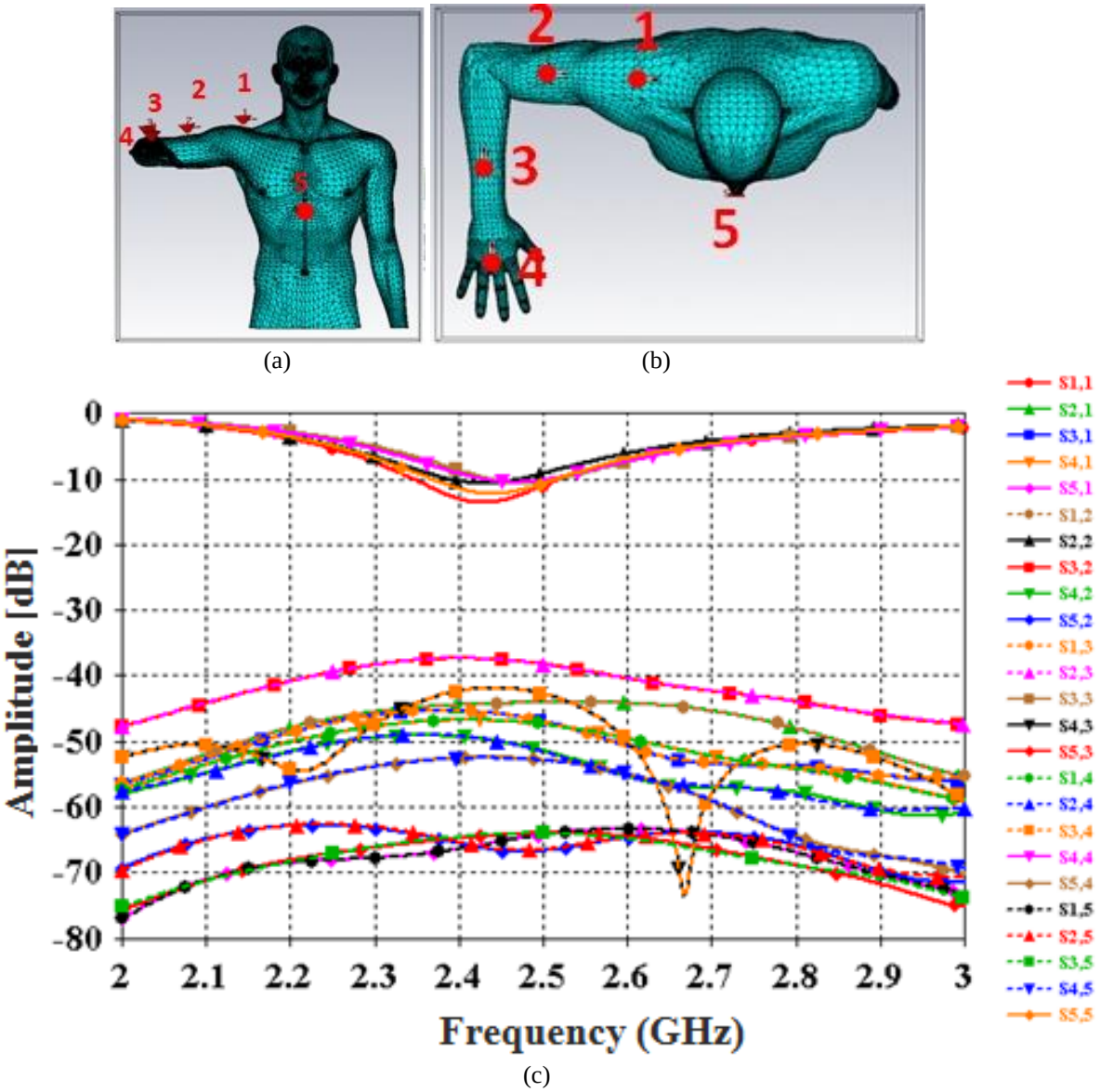

(a) (b)

(c)

Figure 0,11. (a), (b) L'alphabet de posture avec les placements des nœuds / antennes (c) Les paramètres S simulées.

0.5. Antenne à diversité de rayonnement et de polarisation

Pour des communications on-body, un diagramme de rayonnement omnidirectionnel azimutal est nécessaire avec une polarisation verticale. D'autre part, pour des communications off-body, le rayonnement de l'antenne doit être dirigé à l'opposé du corps (direction broadside). Cela implique que des antennes distinctes sont nécessaires pour les opérations on- et off-body pour une performance optimale BAN du point de vue rayonnement et polarisation. Cependant, l'espace et le facteur de forme sont des paramètres crucials pour BANs. Par conséquent, une seule antenne bi-mode (Fig. 0.12, Fig. 0.13) a été proposée pour fournir simultanément les deux types de diversités de rayonnement et de polarisation à 2,45 GHz.

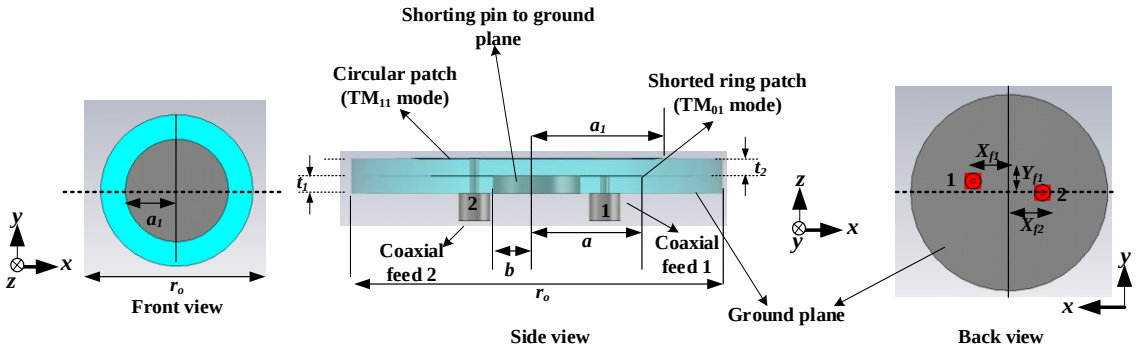

(a) (b) (c)

Figure 0,12. Disposition de l'antenne de la diversité bi-mode (substrat RT5880, ε_r = 2.2, t_1 = t_2 = 3.175 *mm*) (a) Vue de face (b) Vue latérale (c) Vue arrière. Dimensions optimisées (en *mm*): a = 19.35, b = 8, a_1 = 23, r_o = 68, X_{f1} = 12.5, Y_{f1} = 4, X_{f2} = 11.4.

(a) (b) (c)

Figure 0.13. Photographie du prototype fabriqué (a) Vue d'ensemble Top (b) Vue de dessus de la couche prise en sandwich (c) Vue d'ensemble de la base.

L'antenne offre des diversités de diagramme de rayonnement et de polarisation appropriées pour les applications on- et off-body avec une performance stable sur le corps et un couplage intermodal négligeable comme le montrent les paramètres S représentés sur la Fig. 0,14. Il est clair que l'ensemble des paramètres S mesurés pour les deux modes à 2,45 GHz sont inférieurs à -10 dB avec un coefficient de couplage $|S_{21}|$ de -18 dB à 2,45 GHz.

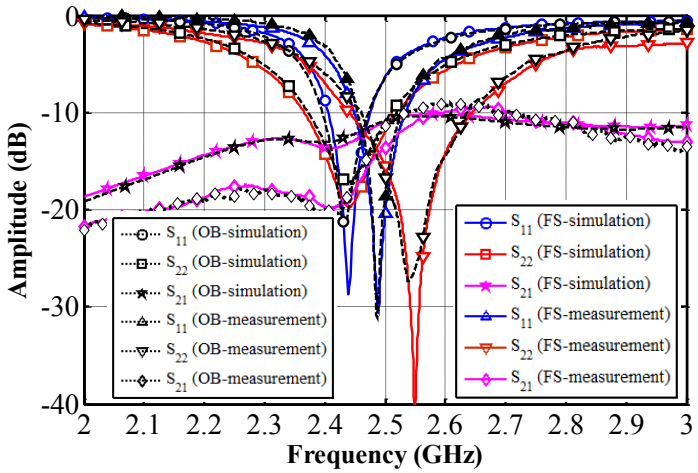

Figure 0. 14. Les paramètres S simulées et mesurées de l'antenne dans l'espace libre (FS) et sur le corps humain (OB).

Les diagrammes de rayonnement 3D des deux modes de résonance (TM_{01} et TM_{11}) à 2,45 GHz, sont également illustrés sur la Fig. 0,15. On peut remarquer que l'antenne génère avec succès la diversité de rayonnement jugée appropriée pour des opérations on- et off-body. Le gain de l'antenne atteint 1.11 dBi pour le mode fondamental TM_{01} avec un rendement total de 92% à 2,45 GHz. Le gain du mode TM_{11} est 7.12 dBi avec un rendement total de 93% à 2,45 GHz.

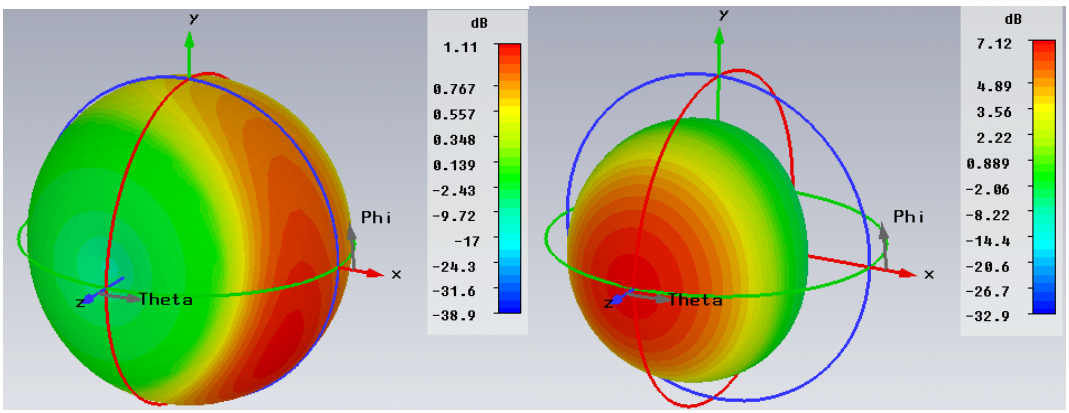

(a) (b)

Figure 0.15. Les diagrammes de rayonnement en 3D de l'antenne de diversité à 2,45 GHz pour (a) le port 1 (mode TM_{01}) et (b) le port 2 (mode TM_{11}) (système de coordonnées représenté sur la Fig. 0.12)

En outre pour des applications de diversité, le coefficient de corrélation d'enveloppes (ECC) de l'antenne a été calculé et il présente des valeurs proches de zéro avec un gain de diversité de l'ordre de 10 dB à 2,45 GHz (Fig. 0.16). Cela justifie également la convenance de l'antenne proposée pour les systèmes de diversité et MIMO.

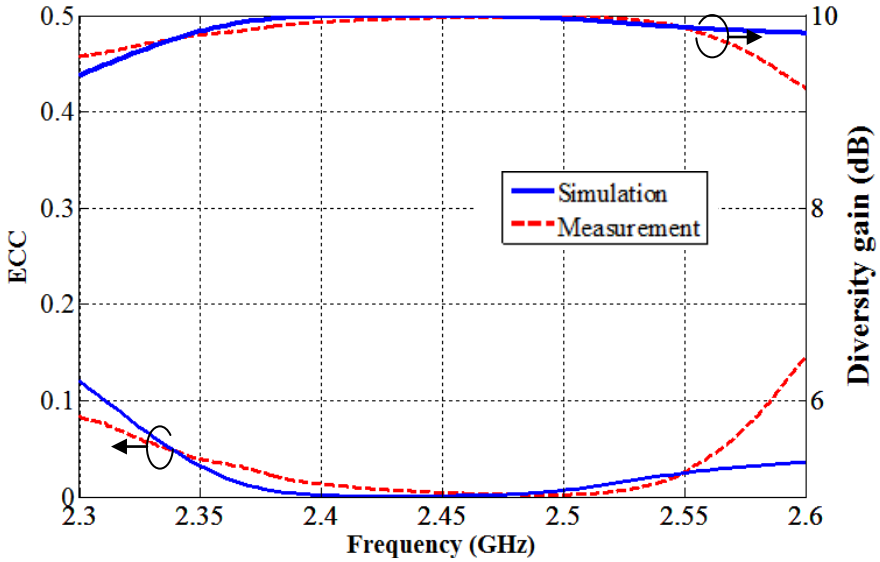

Figue. 0.16. ECC et le gain de diversité de l'antenne.

Une fois que la diversité de rayonnement et de polarisation a été obtenue avec l'antenne proposée, son intérêt pour des applications on-body à 2,45 GHz a été étudié. Une amélioration significative dans le budget de liaison a été rapportée pour des simulations pleines ondes ainsi que pour des mesures réalistes (jusqu'à 15 dB et 9 dB respectivement).

0.6. Conclusions

L'utilité des antennes puce ultra-miniaturisées a été démontrée en combinaison avec la diversité pour les WBASNs de l'avenir de faible puissance et miniaturisés, et ce grâce aux débits de données améliorés par rapport aux systèmes SISO. Un algorithme robuste a été développé pour le montage statistique des données de canal en temps réel et des modèles d'évanouissement ont été proposés pour les communications on- et off-body.

Deux antennes patch bi-mode différentes ont été conçus avec des caractéristiques de rayonnement appropriées pour des applications on- et off-body à l'ISM 2,45 GHz. Les antennes ont montré des performances aussi stables à proximité du corps que dans l'espace libre, tout en offrant la diversité de rayonnement pour des applications on- et off-body. Une antenne puce électriquement petite a été conçue couvrant toute la bande passante d'ISM 2.4 GHz et offrant des performances stables sur le corps. Un simulateur de canal numérique robuste a été développé en utilisant les antennes puce miniatures et des morphologies corporelles réalistes ayant la capacité de simuler les scénarios de BAN arbitraires avec des paramètres personnalisés (par exemple, la posture du corps, le type d'antenne / localisation, etc.). La portée du simulateur du canal a également été démontrée pour la détection de la posture.

La conception d'une antenne bi-mode à diversité a été présentée dans la bande ISM 2,4 GHz avec des diagrammes de rayonnement et de polarisation appropriés pour les communications on- et off-body. L'antenne pourrait être considéré comme étant candidat utile pour la diversité et les systèmes MIMO, grâce à sa corrélation croisée négligeable et un gain de diversité aux alentours de 10 dB. Enfin, l'apport de la diversité de

rayonnement et de polarisation a été démontré avec un gain remarquable rapporté dans le budget de liaison pour des applications portables.

Chapter 1. Context and state-of-the-art

Contents

1.1. General Introduction, Wireless Body Area Sensor Networks

Body-centric communication takes its place within the sphere of personal area networks (PANs) and body area networks (BANs) [1]. A Body Area Sensor Network (BASN) is a special-purpose, short-range sensor network (SN) that operates in the body area i.e., in the near vicinity of human body, hence providing a network of either wired or wireless sensors or devices. In the former case, the various communicating nodes comprising the network are connected by wires, hence comprising a wired BASN whereas for the latter case, the sensors or devices must have a wireless connectivity, henceforth giving rise to Wireless Body Area Sensor Networks (WBASNs). The exchange of data between the various wireless nodes comprising a WBASN is achieved wirelessly using antennas and radio signals employing various existing standards e.g., Bluetooth, Zigbee, Bluetooth Smart or Low Energy (LE), LTE, Ultra-wideband (UWB), mm-waves etc.

The wireless sensors incorporating a WBASN can further record human vital signs or other physiological data for a number of applications such as healthcare services, assistance for disabled or handicapped, user authentication and entertainment etc. These sensors can further provide the recorded data to a central node called the body area aggregator or coordinator which serves as a central coordinating device performing a multitude of functions such as sensing, data fusion for various cooperating nodes distributed across the body along with the processing or conditioning of the data etc [2]. The aggregator also behaves as a user interface and a gateway between WBASN to next higher-level infrastructures or stakeholders e.g., existing systems and networks in hospitals and retirement communities [2].

A WBASN can be either wearable (non-invasive) or implantable (invasive) where the former includes all the devices located outside the perimeter of human body whereas the latter must include at least one in-body or implanted device. The WBASN concept and its integration with other higher-level environments is illustrated in Fig. 1.1 [2]. The different WBASNs should also be capable of exchanging information with each other (e.g., broadcast, listen etc.) as well as with external networks such as local area network (LAN) and internet etc. The hierarchy of the networks is shown in Fig. 1.2 where power consumption and data rate increase with each processing level [2].

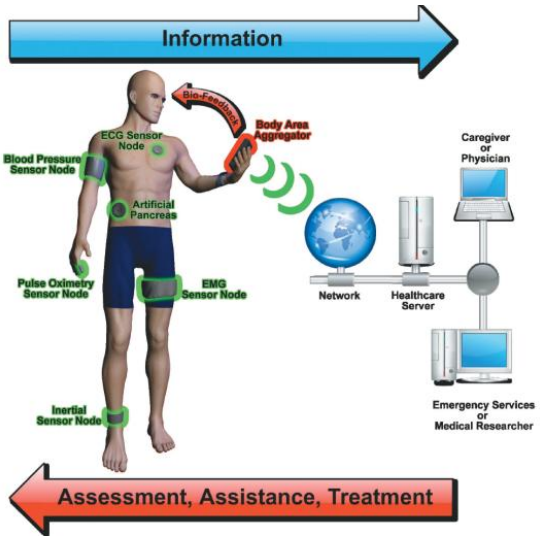

Figure 1.1. WBASN concept, environment and its integration with higher-level infrastructures [2].

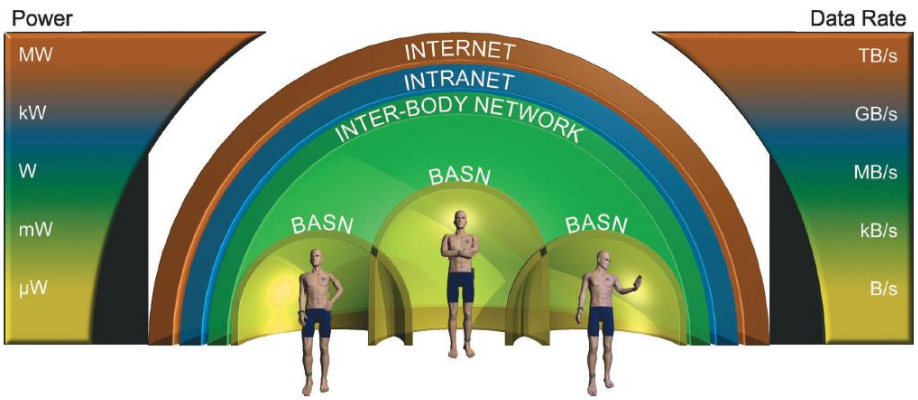

Figure 1.2. Hierarchy of networks and resources [2].

Challenges

Antennas and radio propagation are vital parts of wireless nodes comprising a WBASN. Since WBASN operates in close vicinity of the human body, this means that both the transmitter and receiver are also in immediate environment of the body area. This implies that the human body effects on the transmitting and receiving antennas are crucial unlike the conventional WSNs. Moreover, as a transmission medium, the human body offers completely different channel characteristics compared to the typical wireless media. Human body is considered as a hostile environment for radio due to its abnormally high tissue parameters (e.g. permittivity and conductivity) at microwave frequencies. The existing technology under discussion still suffers from many challenges and unstable antenna behavior in proximity to body due to various contributing factors such as high tissue parameters, body movement and highly dynamic body-centric radio channel in a real-time environment.

Moreover, the human body also introduces a safety issue which has higher priority compared to other wireless communication standards due to the close proximity of WBASN nodes [3]. Therefore, systems and devices comprising WBASN must also comply with the specific absorption rate (SAR) standards for human safety evaluation in

their operating frequency bands. Moreover, due to the more focus on personalized data, more stringent requirements are needed in terms of quality of service (QoS) to keep a reliable communication link e.g., extremely low power consumption for long term use, and a high data rate for real time transmission [3]. Also for social acceptance, WBASNs must have fewer and smaller nodes relative to conventional WSNs and also the nodes must be noninvasive [3].

Applications and usage scenarios

A special task group of IEEE 802.15 was set up in December 2007 for wireless personal area networks (WPANs) and is referred as the task group 6 i.e., IEEE802.15.TG6 [4]. The TG6 is dedicated to WBASNs (though not limited to humans only) for defining standards for various applications [3]. BASNs have number of exciting applications or usages and are one of the key enabling technologies to cope with various challenges to enhance the overall quality of everyday life using their breakneck computing power along with the artificial intelligence. BASNs provide a wide range of innovative applications including medical support, remote patient monitoring, physical rehabilitation, entertainment and consumer electronics with enhanced features e.g., physical activity based mp3 players and gesture controlled video gaming.

There are different categorizations for application and usage models of body area communications. Some of the most promising applications proposed by Astrin and Kohno [5] are listed in Table 1.1 [2].

TABLE 1.1 USAGE MODELS AND SCENARIOS FOR BODY-CENTRIC COMMUNICATIONS [2], [5]

Medical and healthcare applications	**Assistance to people with disabilities**	**Consumer electronics and user identification**
Medical check-up	Blind person	Wireless headphone
Medical diagnosis and treatment	Speech disability	Audio/video streaming share
Physical rehabilitation	Artificial hands and legs	User identification
Physiological monitoring	Accident prevention for elderly people	Automatic payment

Moreover for elderly population which is constantly increasing in the modern era, WBASN can remarkably facilitate the quality of life. e.g., According to the Population Reference Bureau [6], the 65- and above population will comprise almost 20% of the overall population of the developed countries by the next 20 years. BASNs can significantly improve the quality of life of elderly people by active collaboration among communities such as physicians, nurses, psychologists, and sociologists while collecting valuable information from physiological sensors [2]. Remote monitoring of patients and elderly people with wearable and implantable BASNs can increase early detection of emergency conditions along with reducing the dependency of elderly people on caregivers to live an independent quality life and can also provide a wide range of healthcare services for people with various physical and cognitive disorders [7].

Moreover, research is being undertaken in WABSN applications in sophisticated areas such as deep brain stimulation, drug delivery, heart regulation, and prosthetic actuation to help protect potentially life-threatening environments such as soldiers, first responders, and deep-sea and space explorers [2].

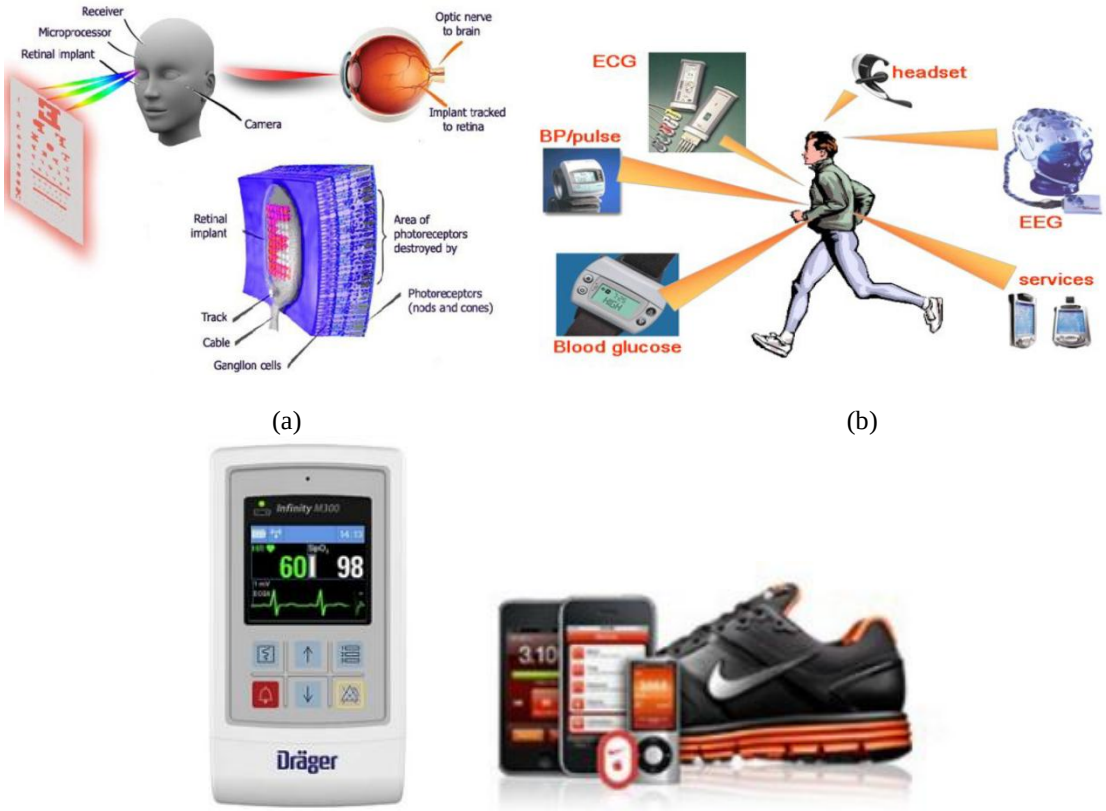

(a) (b)

(c) (d)

Figure 1.3. (a) An implantable WBASN (artificial retina) which can help blind people to improve their vision [7]. (b) European initiative MobiHealth system to create a generic platform for home healthcare to monitor patients outside the hospital environment [8] (c) Infinity M300 Dräger system which can measure ECG, hearth rate,O_2 (30 mW power consumption) [9] (d) Nike + iPod SportKit which can measure calories and speed [10] and provide enhanced music options with mp3 integration.

1.2. Introduction to BoWI project

This PhD thesis finds its place in the BoWI project which stands for Body-World Interaction [11] and is focused on the society challenge called Digital Environment for the Citizen as well as the social challenge of ICT for personalized medicine. BoWI is sponsored by Labex CominLabs, France under French National Research Agency program "Investing for the Future" and Brittany region of France. BoWI is an inspiration of wearable WBASN which means that there are no implants in the BoWI network and the communication between the participating nodes is mainly achieved through wireless infrastructure only (IEEE 802.15.4- ZigBee™).

The principle goal of the BoWI project is the design of pioneer interfaces for an accurate gesture and body movement estimation using miniature, low-power, autonomous and wearable wireless sensor nodes. These sensors are powered by inertial measurement units (IMUs) to extract the information of velocity, orientation, and position using devices such as accelerometers, magnetometers, gyroscopes and antennas and further using this information for 3D reconstruction of the human actor wearing the BoWI network. This interactive concept opens new vistas to develop number of new features and usages for a plethora of exciting and innovative applications while interacting with the body language with smart environments such as home, media, information systems, entertainment and health systems (Fig. 1.4). This will also influence all existing motion capture technologies which are not only composed of several cumbersome devices but are also limited by their high cost constraint and operating environments (e.g., Xsens Moven [12]).

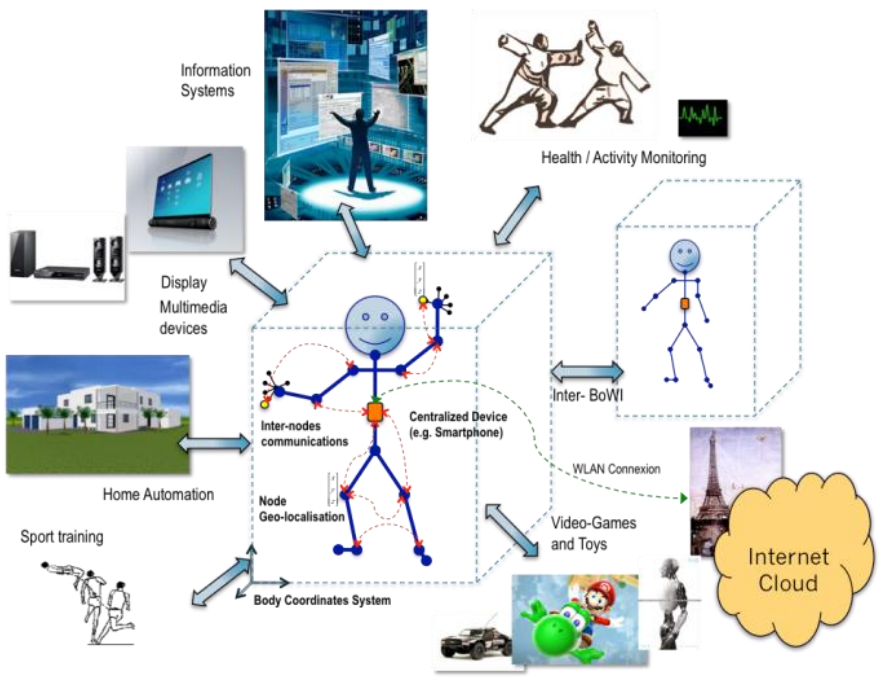

Figure. 1.4. BoWI concept and possible interactions [11].

BoWI was undertaken by a multidisciplinary research consortium with a tight research alliance between different research laboratories located in France [11]. This PhD dissertation focuses on the antennas and radio propagation part of the BoWI project which is a vital component of BoWI wireless nodes operating in close proximity to human body. Moreover, human body is considered as a hostile environment for BoWI as long as the radio part is concerned due to the abnormally high tissue parameters (e.g. permittivity and conductivity) at microwave frequencies. The objective is therefore to achieve optimum radio performance for BoWI by investigating first the various radio channels in proximity to human body (e.g., on-body, off-body) and then propose miniaturized antenna solutions with stable and robust performance in proximity to body.

1.3. Radio and propagation for WBASNs

This section discusses the state-of-the-art for various existing channel models for WBASN applications. The first prototype platform of BoWI project is based on IEEE 802.15.4 ZigBee™ infrastructure as will be discussed in the coming chapters, therefore the core work in this thesis is focused on unlicensed industrial, scientific and medical (ISM) band i.e., 2.40-2.4835 GHz. Moreover, there is also a future perspective of BoWI to utilize Ultra-wide band (UWB) i.e., 3.1-10.6 GHz in the next generation BoWI sensors due to the improved distance estimation accuracy of UWB. Therefore, state-of-the-art for UWB is also mentioned here.

Unfortunately, there is no generic channel model for WBASNs in contrast to wireless sensor networks. This is because of a number of limitations of WBASNs, some of which are as follows:

1. The most important consideration is the proximity of human body, being in the near-field of antennas comprising the wireless sensor nodes. This is because of high permittivity and conductivity of human body which causes significant losses and negatively impacts the antenna near-field distributions and hence, the radiation patterns and efficiency.
2. The propagation channels are time-varying because of the continuous body movements in contrast to typical WSNs which are subjected to stationary environments most of the time.
3. The channel is subject-specific and hence, can vary based on the body morphology e.g., gender, age, weight, height etc.
4. Body-centric channel is also sensitive to sensor placement and may need special requirements to minimize and detect placement error or calibration parameters.
5. The positioning of wireless nodes (or antennas) on the body such as their spacing or body proximity has significant impact on the channel. Antennas may be in line-of-sight (LoS) or non-line-of sight (NLoS) so can be shadowed or unshadowed by the body based on the subject body posture.
6. Surrounding environment would also influence the channel. Indoor and outdoor environments would offer different multipath profiles because of the surrounding objects and body motion will also introduce Doppler effect.

7. The channel models include individual antenna effects when proposed from measurements made with particular antennas (or sensors). This means that a specific channel model may not be applied with reliable accuracy for other antenna types (which are not used during its modeling). A more accurate way is to withdraw antenna characteristics from the channel model, a phenomenon named as antenna de-embedding. Once antennas are de-embedded, a channel may be valid with considerable accuracy for other types of antennas as well.

A number of channel models for WBASNs have been proposed in the literature based on different scenarios and constraints e.g., [1], [3]- [4], and [13]- [34]. Both the static and dynamic channel models have been proposed so far. Static scenarios are those where there is no significant motion of the BAN subject, however, slight involuntary movements may occur e.g., breathing movements caused by the chest whereas dynamic scenarios include significant or forced body movements e.g., walking, running or routine activities or chores etc. The static channel models are mostly characterized by path loss whereas for dynamic channel models, number of other parameters also need special attention e.g., shadowing, power delay profile, Doppler spectrum etc.

The Task Group TG6 of IEEE802.15.6 [4] is primarily concerned with modeling of wireless channels for WBASNs for medical and non-medical devices that can be placed inside body (implants) or on surface of human body. It has received number of contributions from different authors concerning different scenarios. A summary of various models can be found in [13].

Classification of WBASN channels

Since BoWI is a wearable WBASN in contrast to implantable WBASN, it is assumed for classification of scenarios that all the operating devices are located outside of the body parameter and are fully non-invasive. The IEEE 802.15 Task Group 6 (TG6) [4] founded in 2007 is responsible for setting the communication standards for WBASNs. The communications for wearable WBASNs can be classified into following four scenarios based on recommendations of Channel model subcommittee report [35].

1. On-body, Line-of-sight (LoS) named as Sc1
2. On-body, Non-line-of-sight (NLoS) named as Sc2
3. Off-body, LoS named as Sc3
4. Off-body, NLoS named as Sc4

The models for an on-body node communicating to another on-body node is named as CM3 whereas the model for an on-body communicating node to an off-body device is named as CM4 [35]. Furthermore, these scenarios may include a LoS or NLoS (Fig. 1.5). For scenario CM4 (i.e., Ss3 and Sc4), the communication takes place between an on-body node to some external device which can be a base station or an access point (AP) (e.g., smartphone, wireless router etc.) or some wireless node on some other human body. In the latter case, the communication is called body-to-body communication. An overview of all these scenarios is shown in Fig. 1.5.

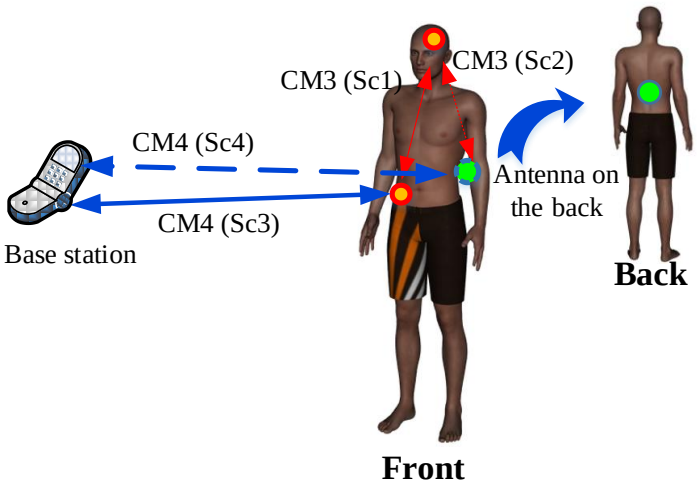

Figure 1.5. Possible communication scenarios in a typical WBAN.

1.3.1. On-body channel models

Recommendations for channel models for scenario CM3 (i.e., Sc1 (LoS) and Sc2 (NLoS)-Fig. 1.5) for ISM band and UWB were presented in [14] which was a summary of contributions submitted to the IEEE P802.15 Working Group 6 dedicated for WPANs. Path loss models for the ISM band and UWB were presented in this report whereas a power delay profile model was also presented for UWB case. The placement of sensor nodes for the measurements is shown in Fig. 1.6 along with the distance between the two body-worn antennas (Tx-Rx) [14]. These antenna positions on body were chosen so as to cover most of the applications as listed in 15.6 Application Matrices [16].

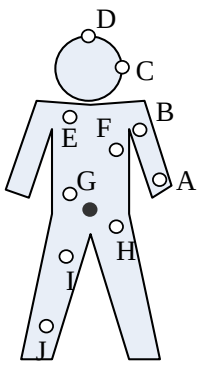

Position index	Position	Distance *d* [mm]	
		ISM band (2.4 GHz)	UWB
A-1	Left hand	408	410
A-2	Left hand	386	390
B	Left upper arm	414	424
C	Left ear	562	570
D	Head	734	742
E	Shoulder	392	402
F	Chest	248	258
G	Right rib	170	176
H	Left waist	174	180
I	Thigh	402	400
J	Ankle	998	984

(a) (b)

Figure 1.6. (a) Measurement positions on the human body for channel model proposals (b) Distances between the two body-worn antennas (Tx-Rx). [14]

Channel transfer function (CTF) was characterized by measurement of S-parameters using a vector network analyzer (VNA) on a male subject having a weight of 64 kg weight and a height of 173 cm (typical values for healthy Japanese males). The

measurements were taken in both hospital room and anechoic chamber. The following path-loss model was proposed from the measurements (applicable for both ISM band and UWB) [14]

$$L_{\text{path}}(d) = a \cdot \log_{10} d + b + N \qquad (1.1)$$

where L_{path} is the path loss in dB, d is the Tx-Rx distance in mm, N is the normally distributed random variable (Gaussian) with standard deviation σ_N, and a, b are the parameters derived by least square fitting to the measured average path loss, ${l_{\text{path}}}^{p}{}_{j}(d)$, which is given by

$${l_{\text{path}}}^{p}{}_{j}(d) = -10 \cdot \log_{10}\left\{\frac{1}{N_{\text{F}}}\sum_{m=1}^{N_F} {PL}^{p}{}_{j}\left(f(m)\right)\right\} \text{ [dB]} \qquad (1.2)$$

where f_m is the frequency corresponding to the m^{th} sample point at the measurement. The parameters for the path loss model (1.1), which were derived from the measured data, are also listed in Table 1.2 [14].

Parameters	2.4 GHz	UWB
a	7.84	19.8
b	34.1	5.97
σ_N	3.98	4.17

(a)

Parameters	2.4 GHz	UWB
a	30.0	44.9
b	-18.3	-54.5
σ_N	7.02	3.22

(b)

Table 1.2. Parameters of path loss models for 2.4GHz and UWB for (a) hospital room and (b) anechoic chamber. [14]

A dynamic channel model for the ISM band was proposed in [15] using full-wave commercial simulator CST Microwave Studio (MWS) [36]. Realistic motion scenarios such as walking and running were emulated in the simulation using animation software Poser [37]. The possibility of Multiple-Input Multiple-Output (MIMO) configuration for on-body channel was studied in this work using correlation among the contributing channels and signal to noise ratio (SNR) for the antenna placement on a homogeneous body model as shown in Fig. 1.7. Two typical human day-to-day activities were studied in this work i.e., walk and run. In order to investigate the channel behavior during each of them, 30 time frames were generated for each, with 1/30s duration each. The correlation statistics of quasi-line-of-sight (QLoS) class for three scenarios (stand, walk and run) are also shown in the Fig. 1.7 when the Tx is on the belt (WA_F). The correlation was observed to be much lower when the body is moving than when it is standing [15]. It was hence, concluded that body movement decorrelates the signals [15]. For the dynamic scenarios, the mean correlation was found to be below 0.7 for all pairs (except for HE_B & HE_L and HE_B & HE_R), which is required for MIMO configuration. Therefore, the presented work [15] suggests the suitability of MIMO considerations for on-body applications.

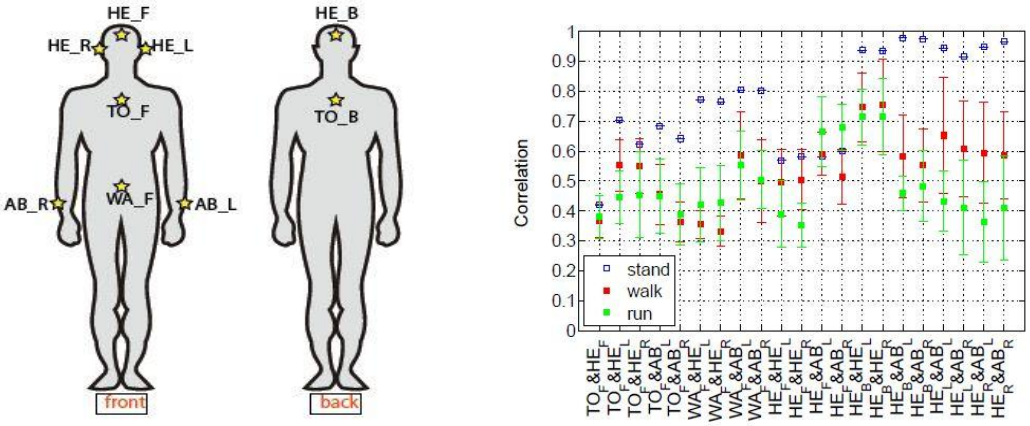

(a) (b)

Figure 1.7. (a) Placement of antennas on body (b) Correlation for pairs of antennas for QLoS class (Tx on WA_F). [15]

A measurement-based channel model for UWB multilink WBAN was proposed in [17]. In this model, 12 nodes were placed on the body to create the WBAN as shown in Fig. 1.8. Two scenarios were considered for measurement; person standing still (static model) and walking around (dynamic). For each case, further two polarizations were measured; one with antenna positions vertically-mounted with body surface and other with antenna positions normal to the body. The power versus distance plot for the measurements is shown in Fig. 1.8 [17].

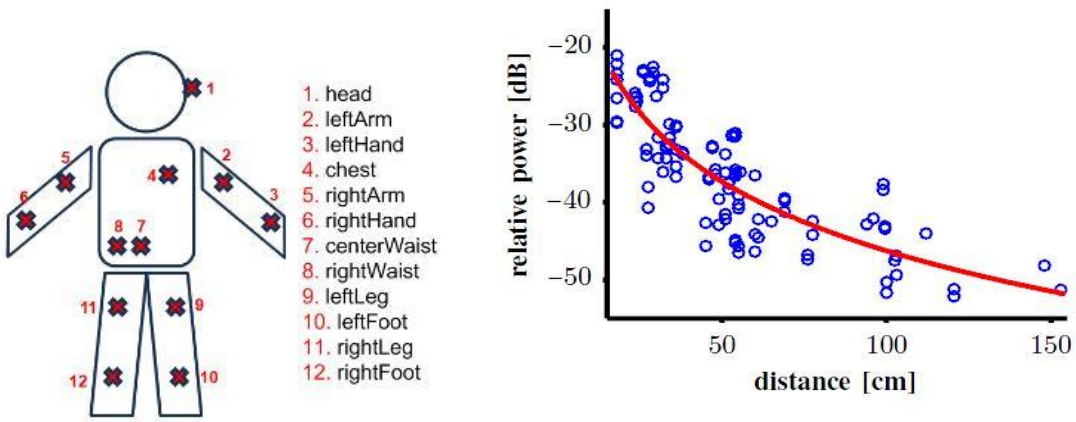

(a) (b)

Figure 1.8. (a) Placement of sensor nodes on the body and (b) Power versus distance for the case of normal polarization [17].

Link fading was modeled by a log-normal distribution in this model. The power level was modeled as a function of distance by (1.3) [17]

$$\mathrm{P}_{ij}^{\mathrm{dB}} = P_o^{\mathrm{dB}} - 10\mathrm{n}\log\left(\frac{d}{d_0}\right) \tag{1.3}$$

where d_{ij} is the distance between the Tx node j and the Rx node i, n is the path-loss exponent and P_0^{dB} is the reference received power at distance d_0. The autocorrelation function of link ij, R_{ij} was modeled by (1.4) [17]

$$R_{ij} = \alpha_{ij} e^{-\beta_{ij} t} + (1 - \alpha_{ij}) e^{-\gamma_{ij} t} . (\cos(2 f_{ij} t)) \quad (1.4)$$

which includes both the decay and periodic nature of the autocorrelation (due to motion). It was also proposed in [17] that link capacity might improve if used multiple hops to go from a Tx to Rx. For this, the authors studied a case with all nodes of their WBAN communicating with the base station node located on center hip (node 7) in Fig. 1.8. For nodes further away from the base station, the authors studied the effect of relaying to improve the transmission. The results are shown in the Fig. 1.9 for one-, two- and three-hop capacities for vertically polarized antennas and when the subject is moving around. The authors concluded that multiple hops can improve reliability in case of some links. i.e., it may be preferable sometimes to have several short distance hops rather than a direct link. e.g., in the case of head, use of two relay nodes causes some improvement in the capacity.

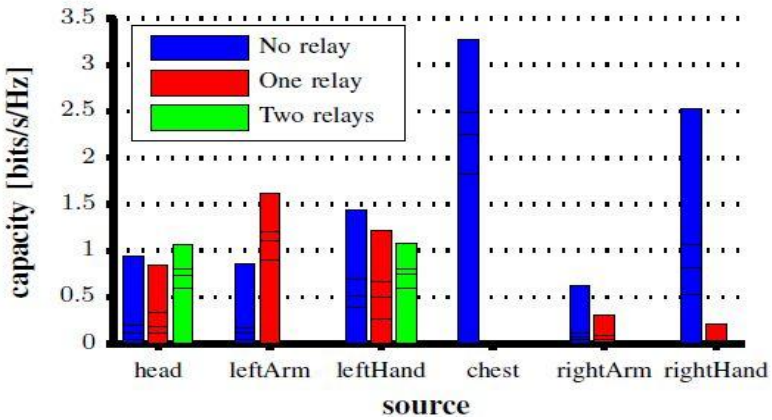

Figure 1.9. One-, two- and three-hop capacities [17].

In order to meet the challenges of link reliability, data transfer, and other services, knowledge of reliable channel distribution for fading is also crucial for system-level modeling. This requires accurate modeling of the BAN propagation channel in order to understand the essential characteristics of the propagation in real-time multipath environment. Various models exist for channel fading for on-body communications. e.g., a model for the received signal strength versus angle around the body was proposed in [38] using the Finite-difference time-domain (FDTD) method for narrowband on-body channels. A more complete narrowband on-body statistical model was introduced in [39] by considering also the influence of the surrounding environment. Statistical characterization of dynamic narrowband on-body channels was presented in [40] and it was shown that Weibull, Gamma and lognormal distributions generally provide good fitting for received signal amplitude (Fig. 1.10).

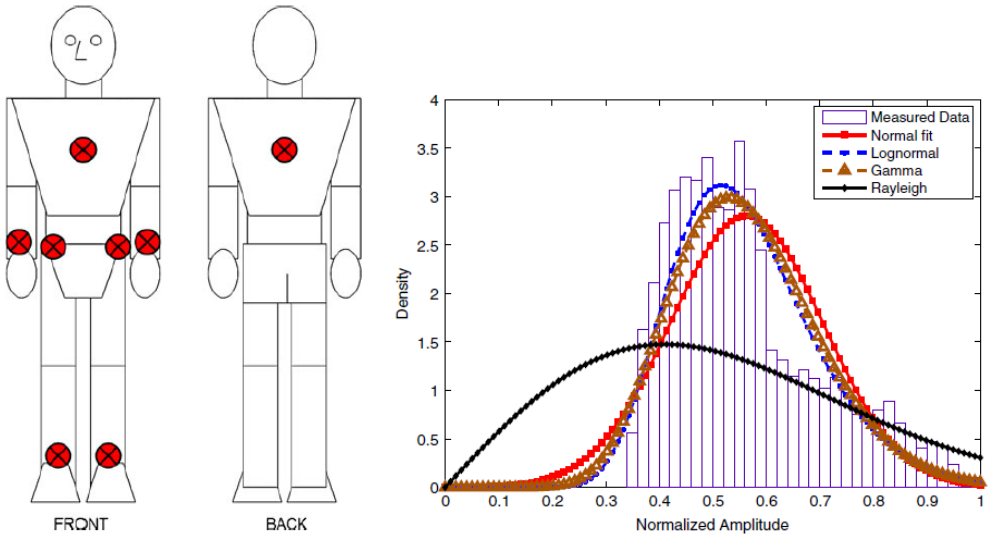

(a) (b)

Figure 1.10. Antenna positions for channel fading measurements proposed in [40]. (b) Probability density function (PDF) for back to chest channel in running scenario at 2.36 GHz (10 MHz bandwidth) showing lognormal distribution as the best fit [40].

The stability of dynamic narrowband on-body area channel was characterized in [41] based on real-time measurements. Small scale narrowband fading for on-body channels was presented in [42] in an open office area and a Nakagami-*m* model was recommended for channel fading. Small-scale statistics for narrowband on-body channels for various mixed everyday activities were presented in [43] using a range of transceiver locations on-body and it was proposed that Gamma and Weibull distributions provide excellent fits for the agglomerated data for various on-body links. Moreover, it has also been reported that Lognormal, Weibull, and Gamma models are most often the best fits for first-order small-scale fading for body-centric channels out of the commonly attempted distributions for fitting [43].

Moreover, antenna diversity has also been considered for on-body applications to cope with fading and to provide enhanced benefits such as improvement in channel capacity and diversity gain, resulting in less transmit power without increasing the signal bandwidth. Results for on-body measurements with antenna diversity were reported in [44] for an indoor environment at 2.45 GHz using monopole antennas. The reported diversity gain showed that diversity can offer noticeable improvement for on-body radio channels. Measurement results for receive diversity were reported in [45] for UWB on-body applications highlighting the significance of diversity techniques for NLoS on-body propagation scenarios. On-body diversity performance was also investigated in [46] for anechoic chamber and multipath indoor environments, considering random body movements. Significant diversity gain values were reported for NLoS and dynamic channels i.e., channels involving large body movements [46].

Radio channel capacity for a 2x2 MIMO system using on-body measurements at 2.45 GHz was reported in [47]. Measurements were taken for three on-body channels namely belt-wrist, belt-chest, and belt-head in an indoor environment. Chanel capacity was

computed assuming zero CSI (Channel State Information) and an improvement in channel capacity was reported with antenna diversity compared to Rayleigh fading channels (Fig. 1.11).

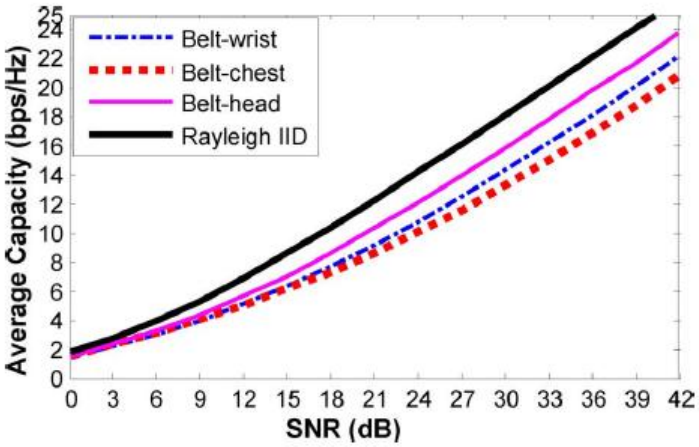

Figure. 1.11. Average capacity versus SNR for on-body MIMO channel measurements. [47]

Channel capacity for on-body MIMO channels at single tone of 2.45 GHz was presented in [48] for two on-body channels i.e.., belt-head and belt-chest. The channel capacity was computed from the measured data using both classic uniform power and the waterfilling schemes and it was shown that that at low SNR range, the waterfilling scheme outperforms the equal power allocation scheme from the perspective of channel capacity [48].

1.3.2. Off-body channel models

The channel model CM4 applicable for off-body scenarios (i.e., Sc3 (LoS) and Sc4 (NLoS) in Fig. 1.5) at ISM 2.4 GHz was proposed in [19] which was a summary of contributions submitted to the IEEE P802.15 Working Group 6 dedicated for WPANs. Measurements were performed for a receiving antenna placed at various distances away from the human body while the transmitter was placed on a human subject either on chest or right wrist. The details of measurement set-up, derivation and data analysis can be found in [19]. A lognormal distribution was recommended as the best-fit for the subject walking or standing with the transmitter on the chest or wrist whereas Normal distribution was recommended as the best-fit only for those scenarios when the subject is standing still. Moreover, Nakagami-*m*, Gamma and Weibull distributions were found to be the best fits for approximately equivalent number of scenarios [19].

The channel model CM4 (Scenarios Sc3 and Sc4) for off-body UWB (3.1-10.6 GHz) communications was proposed in [20]. Channel measurements were done in an office environment. The Tx antenna was fixed near to wall, while the Rx antenna positions (placed on body) were changed. Details on set-up, derivation and data analysis can be found in [20]. The following generic channel model was proposed for both LoS and NLoS scenarios [20]

$$h(t) = \sum_{m=0}^{\infty} \alpha_m \delta(t - \tau_m) \tag{1.5}$$

$$\overline{|\alpha_m|^2} = \Omega_0 e^{-\tau_m / \Gamma - k[1-\delta(m)]} \tag{1.6}$$

$$\angle \alpha_m \propto \text{Uniform}[0, 2\pi) \tag{1.7}$$

where $h(t)$ is complex impulse response, m is number of the path ray, τ_m is the sampling rate, a_m is the ray amplitude, Ω_0 is the path loss. and k is related to the K-factor [20].

In order to accomplish reliable communication between an on-body gateway and external access point, knowledge about the distribution of the channel fading is also crucial. Various references exist for off-body channel fading statistics e.g., [49]-[52] Statistical analysis for off-body channel was reported in [53] for UWB in two different environments (anechoic chamber and indoor), and it was proposed that the path loss is best modeled by a Normal distribution. Statistical model for UWB off-body channel was also presented in [54] for 3.5-6.5 GHz frequency band in a corridor and office environment and it was suggested that the small scale channel variations of the received signal strength follow a Normal distribution. Experimental characterization of UWB off-body channel was also investigated for indoor environment in [55] and a Lognormal distribution was proposed as the best-fit for modeling the path loss.

A characterization of the dynamic narrowband off-body area channel was presented in [56] based on time-domain channel measurements at 820 MHz and 2.36 GHz for two cases when the subject is standing still and walking. It was proposed using Akaike-Information Criterion (AIC) [57] that the Lognormal distribution provides a good fitting model for most of the investigated scenarios (Fig. 1.12).

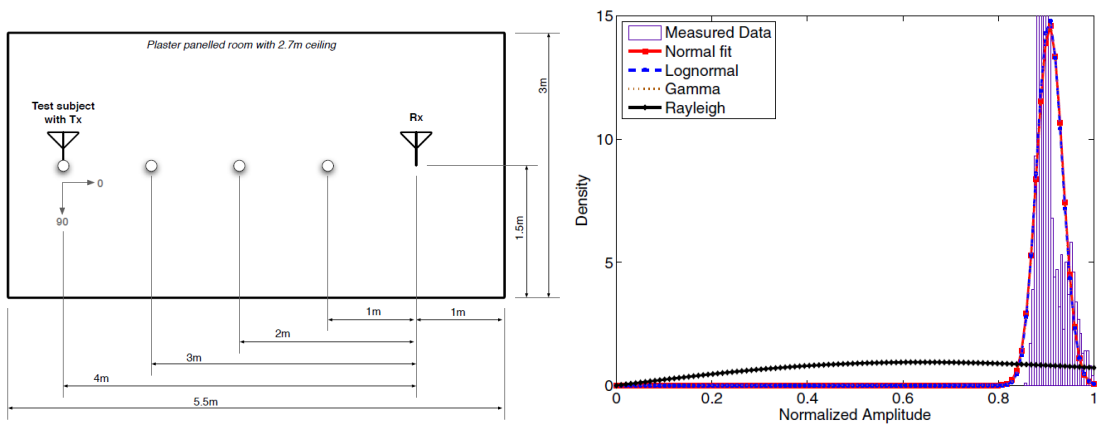

(a) (b)

Figure 1.12. Experimental set up for off-body channel fitting studies in [56]. (b) PDF of Tx on right wrist to off-body Rx (distance = 4 m) at 180° orientation with subject standing still at 2360 MHz suggesting Lognormal distribution as the best-fit. [56]

Moreover, antenna diversity has also been considered for off-body applications for remarkable advantages of MIMO such as improved channel capacity and diversity gain, resulting in low transmit power which is highly desired for today's autonomous WBASN applications. Measurement results for receive diversity were reported in [58] for on/off-body applications using tapered slot antennas where it was shown that 50% improvement in diversity gain was achieved for off-body case than on-body counterpart making UWB off-body channel better candidate for diversity consideration. A statistical power delay profile model for the evaluation and design of UWB off-body communication systems was reported in [59] using omnidirectional antennas (Skycross®).

A theoretical model for off-body MIMO channel measurements was presented in [60] for an indoor environment. Measurements were conducted for 2.45 GHz NLoS channels between a mobile user equipped with wearable textile patch antennas (walking at a speed of about 1 m/s) and a fixed base station at a fairly constant distance of 17 m. The Tx antenna centres were separated by 10 λ (122 cm) and 1.5 λ (18 cm) in two subsequent measurement series and were mounted such that they exhibit slanted cross (/dual) - polarizations (+45°/−45°). The channel capacity was computed from the measured data assuming no CSI at the transmitter. Scenario and results are shown in Fig. 1.13. Significant improvement in channel capacity were reported by MIMO considerations.

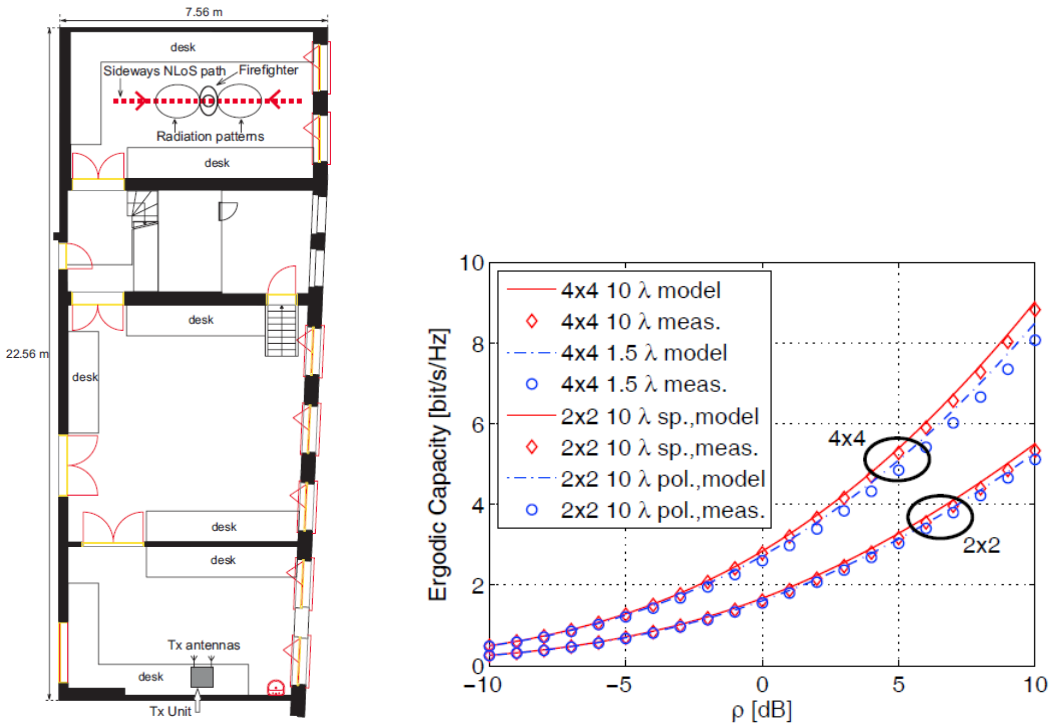

(a) (b)

Fig. 1.13. (a) Measurement environment (floor-plan), indicating Tx-Rx positioning. (b) Ergodic capacity characteristics for proposed model and measurements for different MIMO orders, transmit antenna spacings (1.5 λ, 10 λ) and diversity types (spatial, polarization). ρ is the average SNR. [60]

1.4. Electromagnetic characterization and modeling of human body

1.4.1. Electromagnetic characteristics of body tissues

Human body is characterized by high values of electrical parameters such as permittivity and conductivity; reason being high values of water and salt content in the body tissues. Many references exist for various tissue parameters at microwave frequencies e.g., [61]-[65]. A Model proposed by Cole-Cole [66] can be used to find the permittivity of different types of tissues at various frequencies.

$$\varepsilon(\omega) = \varepsilon_{\infty} + \sum_{m=1}^{4} \frac{\Delta\varepsilon_m}{1 + (j\omega\tau_m)^{(1-\alpha_m)}} + \frac{\sigma_j}{j\omega\varepsilon_0} \tag{1.8}$$

where ε_∞ is the material permittivity at optical frequencies (THz), ε_0 is the permittivity of free space, σ_j is the ionic conductivity and ε_m, α_m, τ_m are material parameters for the dispersion medium (tissue).

Various parameters for range of body tissue types needed to find ε at any frequency were reported in [67]. Table 1.3 [1] shows the electromagnetic properties of different human tissues at ISM band, 2.45 GHz using (1.8) and values of various parameters from [67].

Tissue name	Conductivity [S/m]	Relative Permittivity	Loss Tangent	Penetration Depth [m]
Aorta	1.467	42.47	0.24837	0.023761
Bladder	0.69816	17.975	0.27927	0.032545
Blood	2.5878	58.181	0.31981	0.015842
Bone, Cancellous	0.82286	18.491	0.31996	0.028087
Bone, Cortical	0.40411	11.352	0.25597	0.044616
Brain, Gray Matter	1.843	48.83	0.27137	0.02031
Breast Fat	0.14067	5.137	0.1969	0.085942
Cartilage	1.7949	38.663	0.3338	0.018638
Cerebro Spinal Fluid	3.5041	66.168	0.38078	0.012537
Cornea	2.3325	51.533	0.32544	0.016548
Eye Sclera	2.0702	52.558	0.28321	0.018773
Fat	0.10672	5.2749	0.14547	0.11455
Gall Bladder Bile	2.8447	68.305	0.29945	0.015592
Heart	2.2968	54.711	0.30185	0.017286
Kidney	2.4694	52.63	0.33736	0.015811
Liver	1.7198	42.952	0.2879	0.020434
Lung, Inflated	0.81828	20.444	0.28779	0.02963
Muscle	1.773	52.668	0.24205	0.021886
Skin, Dry	1.4876	37.952	0.28184	0.022198
Skin, Wet	23.984	20.369	0.84665	0.0010736
Small Intestine	3.2132	54.324	0.42529	0.012438
Stomach	2.2546	62.078	0.26114	0.018707
Testis	2.2084	57.472	0.27628	0.018394
Tongue	1.8396	52.558	0.25167	0.021083

Table 1.3. Electromagnetic Properties of different human tissues at 2.45 GHz. [1]

1.4.2. Phantoms for modeling human body

Once the electrical characteristics of human body are known, the body can be modeled by physical or emulated structures called phantoms. Phantoms can emulate electrical characteristics of human body for simulation or measurement purposes at desired frequencies. This is also necessary in scenarios where in-vivo measurements cannot be taken. This makes phantoms ideal for medical research in areas such as X-ray, magnetic resonance imaging (MRI), and hyperthermia applications. Moreover, specific absorption rate (SAR) studies can also be conducted using phantoms which are not feasible with living subjects due to radiation dose safety concerns. Various safety standards specify the acceptable levels of radiation in terms of SAR such as those provided by the International Commission on Non-Ionizing Radiation Protection (ICNIRP) [68] and the Institute of Electrical and Electronics Engineers (IEEE) [69].

Phantoms can be classified into the following types.

a. Physical phantoms
b. Numerical Phantoms

1.4.2.1. Physical Phantoms

Physical phantoms are made from solid, liquid, or gel and are intended to make measurements in controlled laboratory environments. They can be classified on the basis of the tissue types they represent e.g., they can represent low-water content tissue, such as

bones and fats, having low permittivity and low loss. They can also represent high-water content tissues such as brain, skin and muscles, which have higher permittivity and loss. Based on their final state of matter, they can be classified as solid (dry), semisolid (gel) and liquid phantoms.

a. Liquid Phantoms

Liquid phantoms are composed of a container filled with liquid having same electrical characteristics as the tissue in the human body, for the defined frequency range. The liquid is enclosed in a thin shell, usually made of fiberglass material with low relative permittivity and conductivity [1]. Most recipes for the liquid contain sugar, diacetin or di-ethylene glycol butyl ether (DGBE) in different proportions to control permittivity of the solution, while salt (NaCl) is used to adjust conductivity [70] of the solution. Such phantoms do not represent human body accurately, since their internal structure is replaced with a homogeneous medium. Moreover, they do not allow measurement of SAR close to the surface of the body. However, these phantoms have the advantage of being easiest to fabricate. They are useful for experimental study of on- and off-body scenarios where the antennas are located outside the body perimeter and there is negligible field distribution inside the body due to the high medium attenuation e.g., at microwave frequencies. Such phantoms are not suitable for experimental study of in-body scenarios i.e., for implants. Liquid phantoms proposed by Ogawa et al. [71] and [72] are shown in Fig. 1.14.

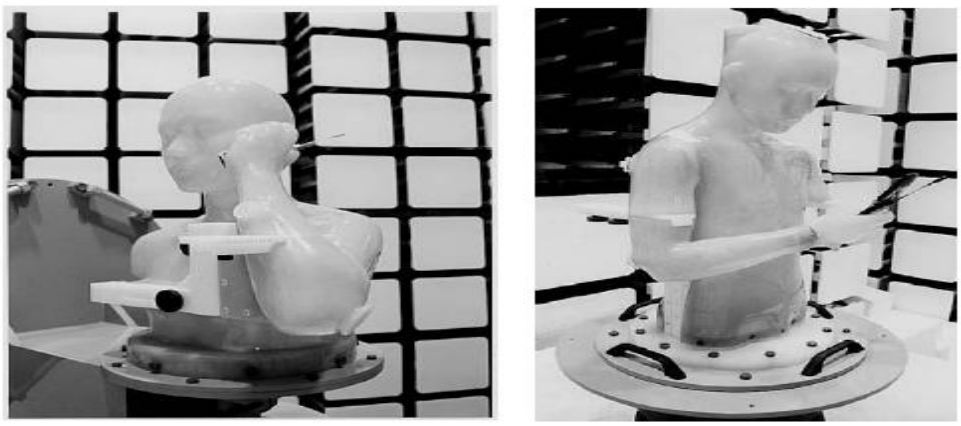

(a) (b)

Figure 1.14. Liquid phantoms proposed by Dr. K. Ogawa [71] and [72] in (a) talk position and (b) viewer position. Source [1]

b. Semisolid Phantoms

In these phantoms, self-shaping coagulants are used to replace the outer shell of liquid phantoms. One of the popular gel phantom was developed by Guy [70], which is composed of water, sodium chloride, TX-150 (polyamide resin), and polyethylene powder. Ito et al. [73] have developed the self-shaping phantom based on Guy's recipe adding sodium dehydroacetate and agar, used as preservative and coagulant to Guy's recipe. These types of phantoms are suitable only for simulating high-water content

tissues such as muscle and brain but can adjust the electrical characteristic over a wide frequency range [1]. The disadvantage of such phantoms is that the materials degrade over time, due to the loss of water and growth of fungi. An agar-based semisolid phantom [73]- [75] is shown in Fig. 1.15.

Figure 1.15. Realistic human torso phantom called TYX-151. Source [1]

c. Solid (Dry) Phantoms

A solid phantom is made of materials that are capable of preserving their shape for long periods of time. Most recipes for solid phantoms are composed of mixtures such as ceramic and graphite powder [76], silicone rubber mixed with carbon fiber [77] and conductive plastic containing carbon black [78]. These phantoms are suited for measuring SAR on the surface of human body which is done by the method of thermography [79]. They are also best suited for the study of the propagation around, as well as inside the body, since they accurately represent the inhomogeneous structure of the human body. These phantoms have excellent mechanical and dielectric properties that do not degrade over long time, but they need special and expensive equipment to fabricate them along with special procedures in production (such as very high temperature and pressure). A dry phantom simulating human head is shown in Fig. 1.16.

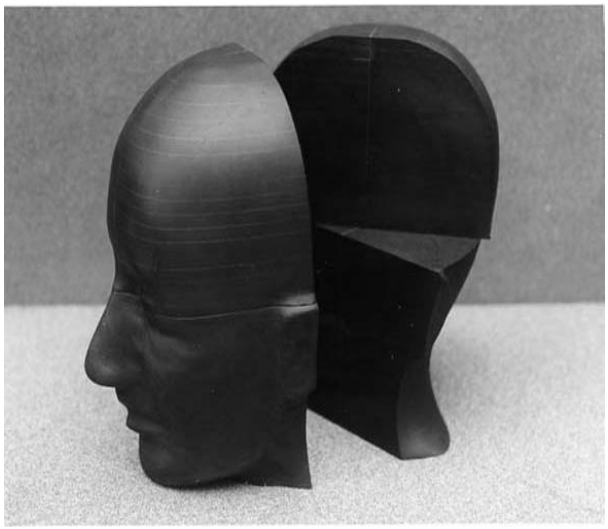

Figure 1.16. Human-head dry phantom. Source [1]

1.4.2.2. Numerical Phantoms

Numerical phantoms comprise of embedded numerical codes to investigate the effect of different parameters such as Scattering (S-) parameters and SAR in human body. Numerical phantoms are used for theoretical analysis and computational simulations using methods such as Finite-difference time-domain (FDTD) and method of moments (MoM). They can further be classified as numerical phantoms and voxel phantoms based on the level of their detail and complexity.

a. Theoretical Phantoms

Theoretical phantoms are structurally simple homogenous phantoms mainly used for EM dosimetry. Spherical models such as those proposed in [80]- [81] are used for EM dosimetry inside the human head. Cylindrical phantoms proposed in [82]- [83] are used for whole-body models. These models are useful for studying channel propagation around the body or in scenarios where electromagnetic field distributions inside the body are not so critical. They are hence, not accurate for the study of SAR in scenarios where radiation dose is critical for human health. The homogenous head and full-body models from full-wave simulator CST MWS [36] are shown in Fig. 1.17. Mostly such structures are enough for most high frequency applications and yield results much faster than voxel models.

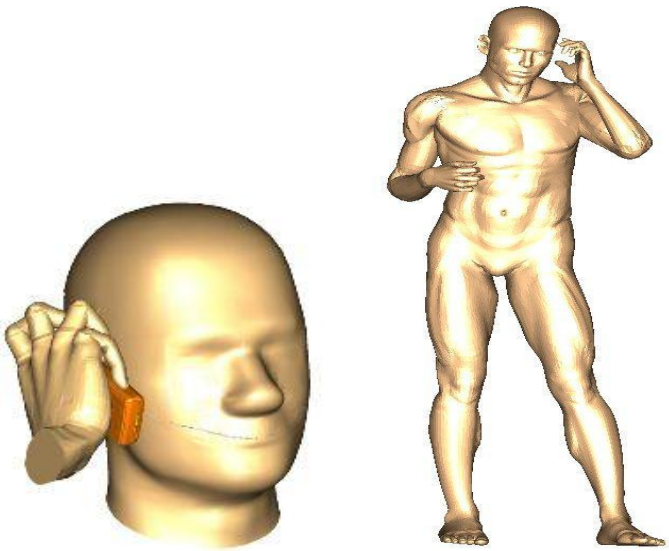

(a) (b)

Figure 1.17. Human head with cell-phone and full body models in CST MWS [36].

b. Voxel Phantoms

Voxel models are more complex and realistic and widely used in sophisticated medical imaging technologies, such as MRI and X-ray computed tomography (CT). Numbers of precision voxel models have been proposed in literature e.g., [84], [85] Some of them are shown in Fig. 1.18 and 1.19. One of the well-known human voxel model widely used for advanced BAN simulation studies is VIP-man [87] which is based on the data taken by Visible Human Project (VHP).

(a) (b)

Figure 1.18. Highly accurate voxel models comprising around 143 million 1.2 mm cubic voxels. (a) FAX06 (b) MAX 06. [88]

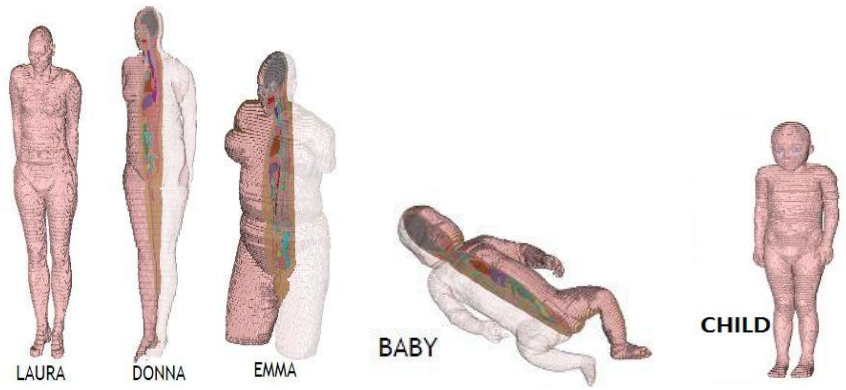

Figure 1.19. CST MWS Voxel family [36].

1.5. Antennas for WBASN applications

Antenna design for WBASNs is a crucial task. An antenna with stable parameters in proximity to body is required. Most crucial parameters to investigate in proximity to body are impedance matching, radiation efficiency, radiation pattern, polarization, and SAR. Radiation efficiency of an antenna is much degraded when placed close to the body because of high permittivity and conductivity offered by the tissue. Normally, high radiation efficiency and low SAR are desirable properties of an antenna designed for WBASN applications. Moreover, a polarization which is normal to the body surface is preferred for on-body communication. Finally, an antenna designed for use around the human body must be tuned in proximity to body so that the antenna can offer stable performance in a real-time working environment even on the lossy body. This can be studied using tissue phantoms in full wave simulation tools as CST MWS.

More robust requirements for WBASNs include meeting challenges of wide bandwidth and radiation pattern stability in proximity to body. Antennas with ground plane normally have stable performance in proximity to body since ground plane masks the radiation incidence towards the body, hence reducing the near-field interactions. However, antennas with full ground plane mostly suffer from narrow bandwidth compared to those having partial or incomplete ground planes. Whereas, antennas lacking a complete ground plane suffer prominently in proximity to body because they pose direct radiation interaction with lossy human body. The performance parameters of such antennas with partial ground planes can be stabilized in proximity to body using special material enhancements such as Polymeric Ferrite Sheets (PFS) and structures as electromagnetic bandgap (EBG). Such materials mask the incidence of radiation towards the body, however the efficiency of antenna drops by using such techniques. In the following sections, some of the antennas for WBASN applications from the contemporary literature are presented along with their performance parameters mainly for ISM 2.4 GHz band or IEEE ultra wideband (UWB).

1.5.1. Antennas for ISM band and UWB

A cavity slot antenna for 2.45 GHz on-body communications was proposed in [89]. The presented antenna has a relatively high efficiency of more than 50% even in the vicinity of human body. The layout of the antenna along with its tuned dimension is shown in Fig. 1.20. This antenna is capable of producing a vertically polarized wave along the surface of the body, which is well supported as a surface wave.

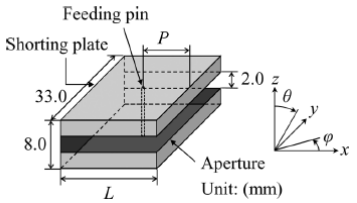

(a)

	In free space	With PEC plate	With phantom
Antenna length (mm)	25	27	28.5

(b)

Figure 1.20. (a) Cavity slot antenna for on-body communications and (b) its tuned dimensions [89].

In order to reduce the antenna effective size, such antennas have also been proposed where the casing radiates most of the power whereas the actual antenna acts as a resonator to set the resonant frequency. One of such antennas has been proposed in [90] and shown in Fig. 1.21. This antenna is integrated into a wrist watch as part of the WBASN. It comprises a PIFA antenna designed for Bluetooth transceiver that is integrated in wristwatch casing [90].

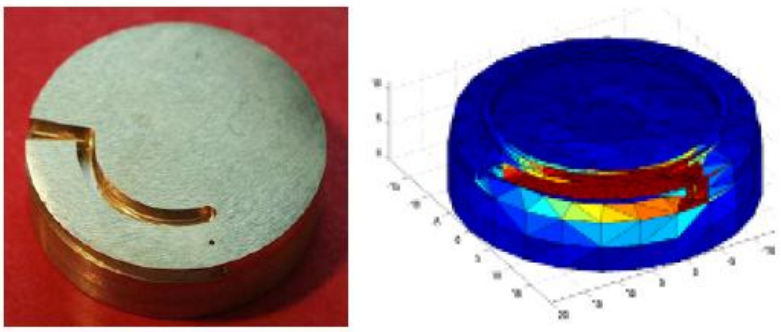

(a) (b)

Figure. 1.21. (a) Bluetooth antenna and (b) its surface current distribution [90].

A narrow-band band top-loaded monopole was also proposed in [90] with a miniature size of 40x40x5 mm^3 for ISM 2.4 GHz. This antenna has an impedance bandwidth of 2.36-2.5 GHZ (@ S_{11}<-10dB) on human body-model and exhibits omni-directional behavior in the azimuth plane (Fig. 1.22).

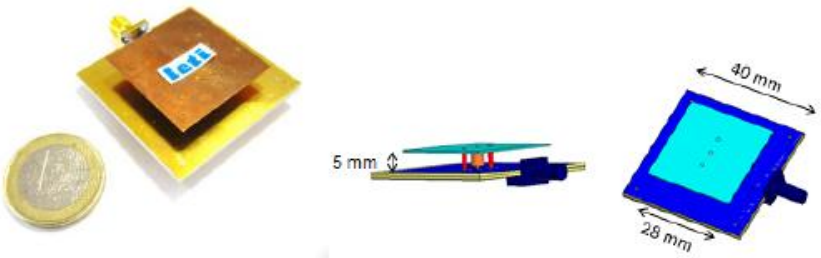

Figure 1.22. Narrowband top loaded monopole antenna. [90]

A wristwatch-type UWB antenna was proposed in [91] which can operate within the 7.25-10.25 GHz range and shows satisfactory on-body performance. The layout is shown in Figure 1.23.

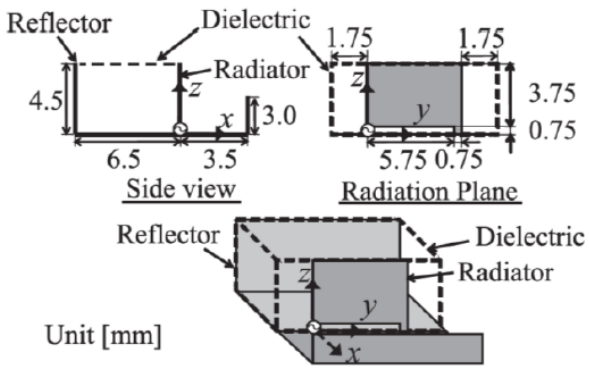

Figure 1.23. A compact UWB on-body antenna [91].

An UWB antenna suitable for on-body communications in the 3.1-10.6 GHz range has been proposed in [92] and shown in Figure 1.24. This antenna is also capable of producing a vertically polarized wave along the surface of the body.

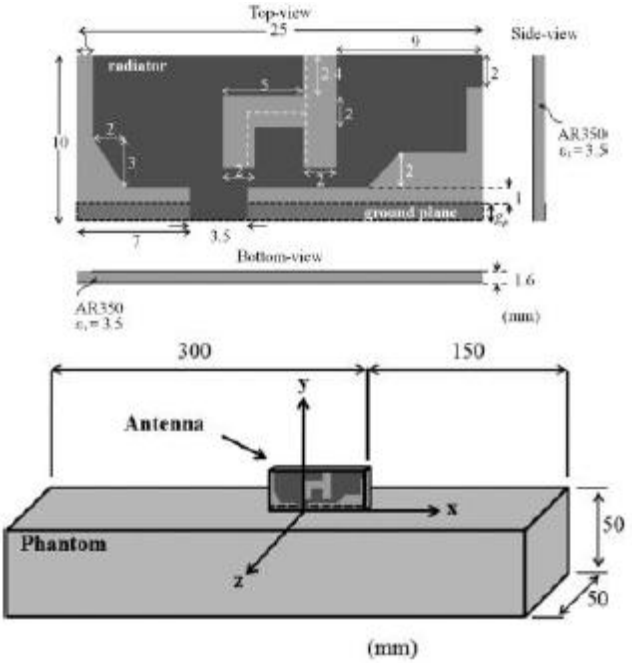

Figure 1.24. A compact UWB on-body antenna [92].

A wideband planar monopole with integrated balun was proposed in [90] using elliptical shape of the dipole arms in the ground plane and folding up the dipole arms for miniaturization. The antenna exhibits good radiation efficiency in the band 1.5-5 GHz. A prototype has been realized on FR4 substrate and shown in Figure 1.25.

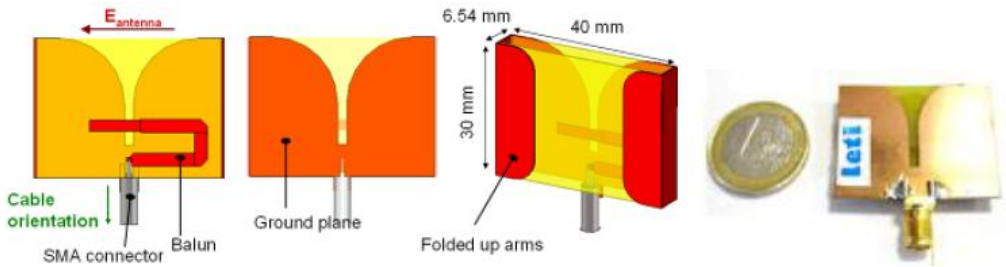

Figure 1.25. Wideband planar monopole with integrated balun [90].

A zeroth-order resonant (ZOR) antenna on a flexible substrate has been proposed in [93]. It has a zero phase constant (β = 0) which implies that the resonant condition is independent of the physical dimensions. Hence, the antenna performance is independent of substrate deformation [93]. The antenna is fabricated on Rogers RO3003® substrate (ε_r = 3.0, t = 0.5mm) and maintains its bandwidth in the ISM band even by bending up to 70 mm. (Fig. 1.26)

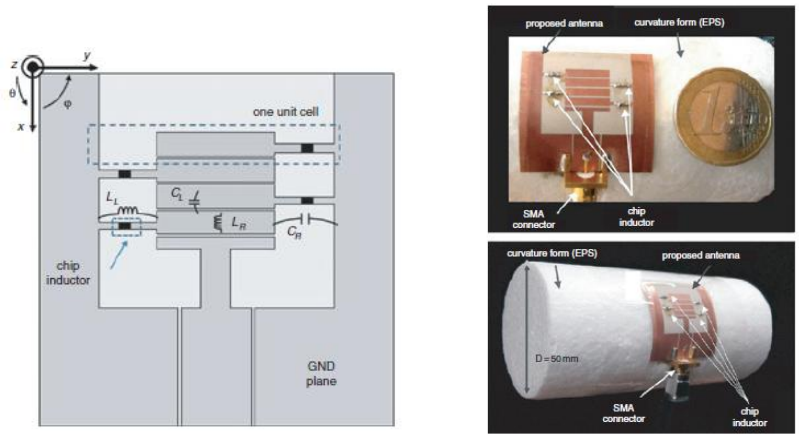

(a) (b)

Figure 1.26. Flexible ZOR antenna (a) layout (b) fabricated prototype (top) and prototype bending on cylindrical Styrofoam with D = 50 mm (bottom). [93]

1.5.2. Antennas with material enhancements

The performance parameters of antennas for WBASN application can be improved in proximity to body using special materials such as Polymeric Ferrite Sheets (PFS) and structures as electromagnetic bandgap (EBG). Such materials mask the incidence of radiation towards the body, however the efficiency of antenna drops by using such techniques.

Planar antennas were proposed in [94] employing thin PFS on the backside of antenna to reduce the body impact on the default antenna behavior. Ferrite forms an opaque media for microwave at the ISM frequencies and hence, it could be used for the isolation of antenna from surroundings more particularly, for the case of antennas without a complete ground plane. Three different low profile antennas were proposed i.e., PIFA (Planar Inverted-F Antenna), IIFA (Integrated Inverted-F Antenna) and CWPA (Coplanar Wire Patch Antenna) which were all realized on FR4 substrate (Fig. 1.27).

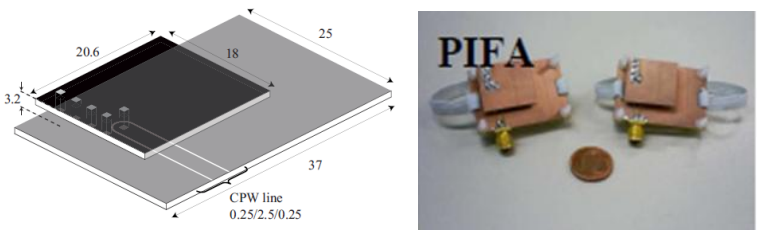

(a)

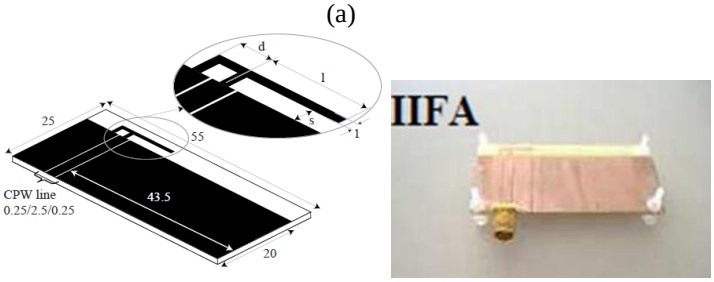

(b)

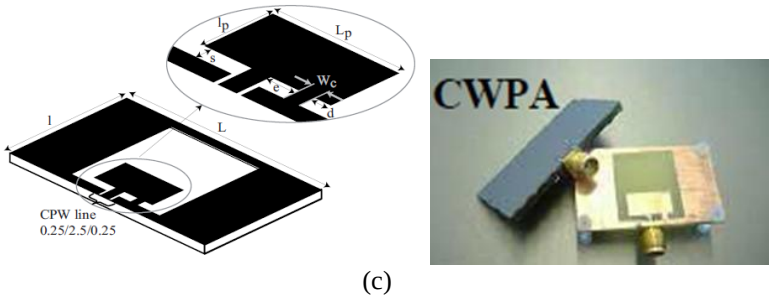

(c)

Figure 1.27. (a) PIFA (Planar Inverted-F Antenna), (b) IIFA (Integrated Inverted-F Antenna) and (c) CWPA (Coplanar Wire Patch Antenna) along with the fabricated prototypes realized on FR4 substrate [94].

Another dual-band coplanar patch antenna integrated with an EBG substrate has been proposed in [95]. The antenna structure is made from common clothing fabrics and operates at the 2.45 and 5 GHz wireless bands. The band gap array consists of 3x3 elements but reduces radiation into the body by more than 10 dB, hence causing improvement in the antenna gain by 3 dB. The conducting components are manufactured from a woven conducting fabric "Zelt" to a layer of thin felt material of 1.1 mm thickness using a very thin layer of adhesive (Fig. 1.28) [95].

Figure 1.28. Dual-band wearable textile antenna on an EBG substrate [95].

1.5.3. Wearable/Textile Antennas

A dual-band triangular patch antenna with a modified ground plane was proposed in [96]. The antenna operates at two frequency bands with a percentage bandwidth greater than 20% at 2.45 and 5 GHz network bands. The ground is modified by cutting a large rectangular slot in it which allows tuning the impedance matching for the two resonant bands. The conducting components are manufactured from woven conducting fabric 'Zelt' with a conductivity of 10^6 S/m and the substrate was thin felt material 1.1 mm thick and having ε_r= 1.38 and $tan\delta$ =0.02. This antenna was studied in the context of a wearable system that would be placed over a small EBG surface to reduce back radiation into the body [96]. (Fig. 1.29)

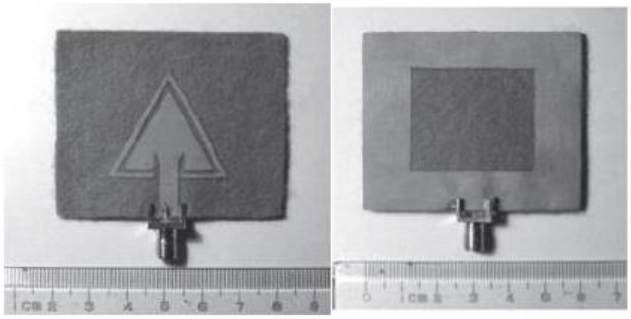

Figure 1.29. Dual-band triangular patch antenna with modified ground plane [96].

Osman et al. [97]-[99] presented different UWB antennas on jeans (ε_r=1.7, t= 1mm, $tan\delta$=0.025) for the UWB (3.1-10.6 GHz). (Fig. 1.30)

Figure 1.30. Microstrip-fed textile UWB antenna [97].

Antennas have also been proposed for wearable objects or accessories which can be worn on the body. A wearable button antenna for WLAN applications was presented in [100]. This antenna is made up of a button shaped cylindrical structure and a central metal disc connected to the metal ground plane. The resemblance of antenna with standard metal button offers great deal of camouflage and rigidness [100]. The antenna is designed for 2.4 GHz and 5 GHz bands and offers omnidirectional pattern for wearable devices located across the body. (Fig. 1.31)

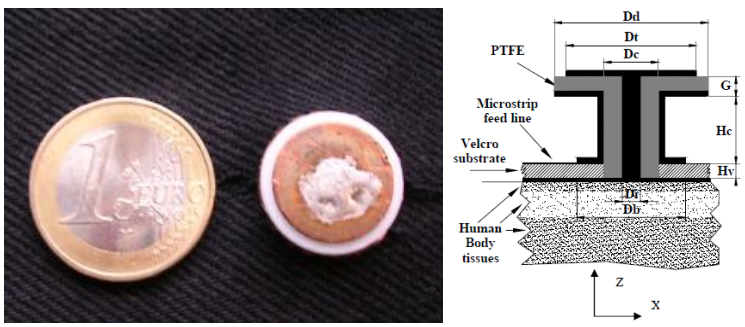

(a) (b)

Figure 1.31. (a) Wearable button antenna and (b) antenna on body model [100].

1.5.4. Adaptive or pattern-reconfigurable antennas

Pattern reconfigurability is also an important requirement in specific WBASN applications. Such antennas have also been proposed in literature which can offer pattern variability or tuning. A compact pattern-switching patch antenna was proposed in [101] for 2.45 GHz body-centric applications offering radiation modes for both on- and off-body links. The patterns of the antenna are switched using shorting pins which actually switch the operating modes of antenna. (Fig. 1.32)

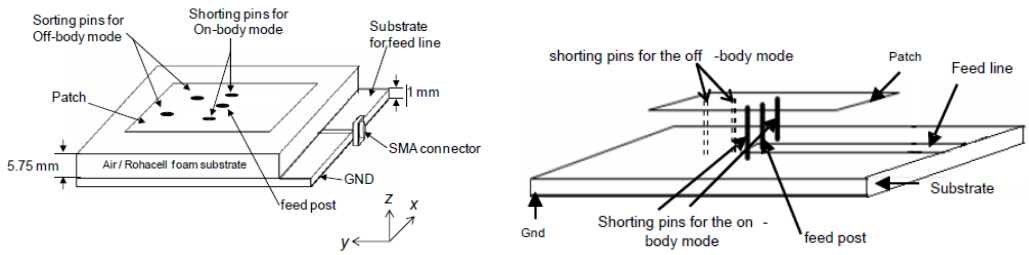

(a) (b)

Figure 1.32. (a) Geometrical layout of pattern-switching antenna (b) Cross-sectional view [101].

A novel dual-band patch antenna was proposed in [102] for 950MHz and 2.45GHz ISM band on-body applications. The proposed antenna consists of two short circuited ring patch elements integrated on the FR4 substrate. Both of the ring elements operate in the fundamental TM_{01} mode of a shorting-pin loaded ring patch and provide monopole-like radiation properties at both of the operating frequency bands for on-body applications (Fig. 1.33).

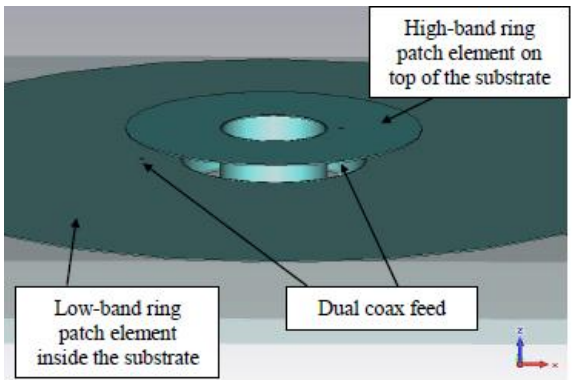

Figure 1.33. 3D layout of short-circuited ring patch antenna [102].

Reconfigurable beam steering has also been proposed in [103] using a microstrip patch antenna with a U-slot. The proposed antenna was manufactured on a fabric substrate and is capable to steer the bore-sight beam at the operation frequency of 6.0 GHz using two artificial switches. By configuring the switches, the antenna can give three beam directions (S0, S1, and S2) as shown in Fig. 1.34. The maximum beam directions are steerable in the H–plane (θ = 0°, 30°, and 331°respectively).

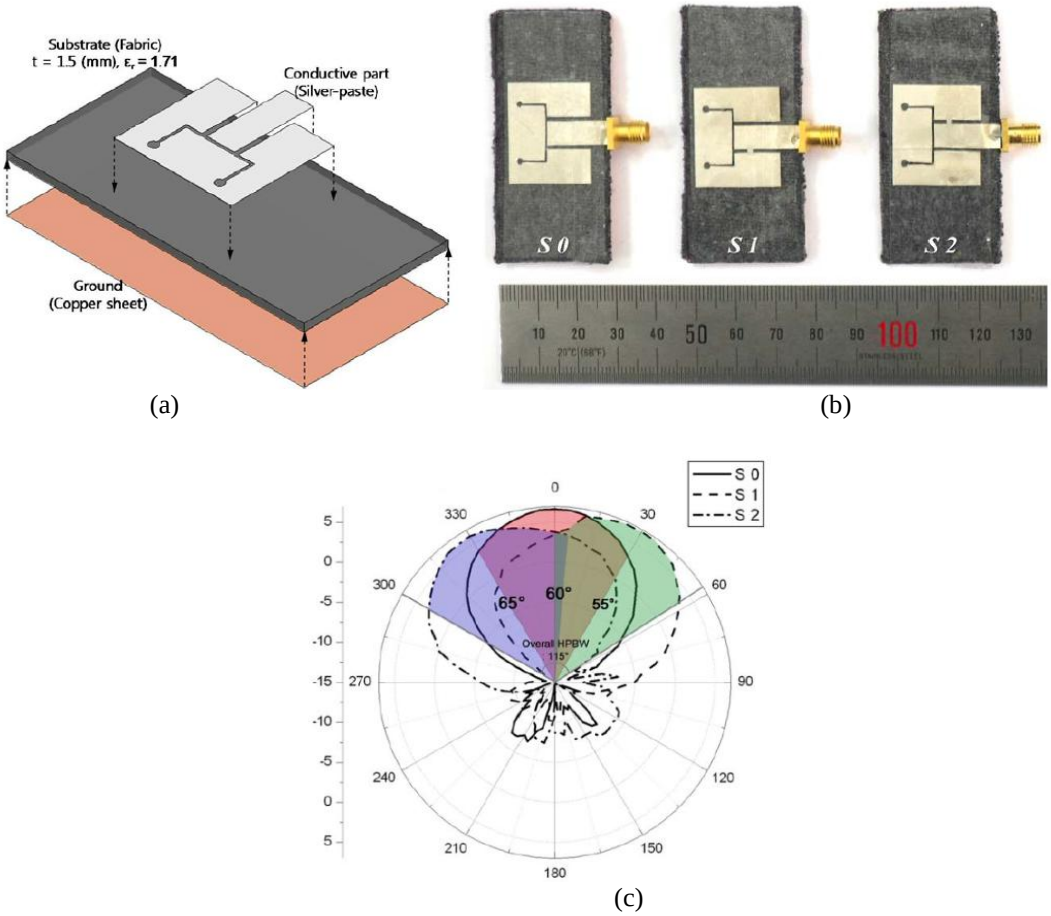

Figure 1.34. (a) Layout (b) photograph of fabricated prototypes and (c) radiation patterns reconfigurability. [103]

Another novel pattern reconfigurable Dipole-Yagi antenna operating at 2.5 GHz was proposed in [104] consisting of passive directors and reflectors surrounding the driven element (dipole). The beam switching can be achieved by using PIN diodes between the arms of directors and reflectors and switching them on and off for driving antenna bore-sight (Fig. 1.35). However, in this work, pattern reconfigurability was achieved using copper tape replacing PIN diodes as RF switches.

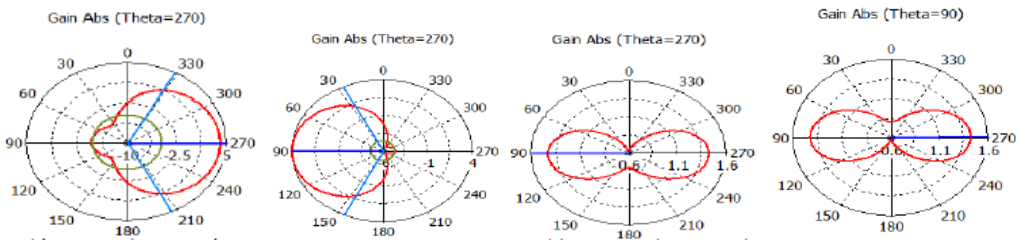

(c)

Figure 1.35. Pattern reconfigurable dipole-Yagi antenna (a) Layout (b) manufactured prototype on FR-4 substrate (c) radiation patterns when different switches are in ON state (left to right: 1st SW, 2nd SW, 3rd SW, 4th SW) [104].

A pattern reconfigurable antenna for BANs was proposed in [105] using a shorted rectangular patch antenna (Fig. 1.36). The antenna comprises two layers. A rectangular patch with ground plane and another T-junction microstrip line feed to excite patch at two symmetrical points with phase shift to excite both omni-azimuthal and directional modes at 2.45 GHz.

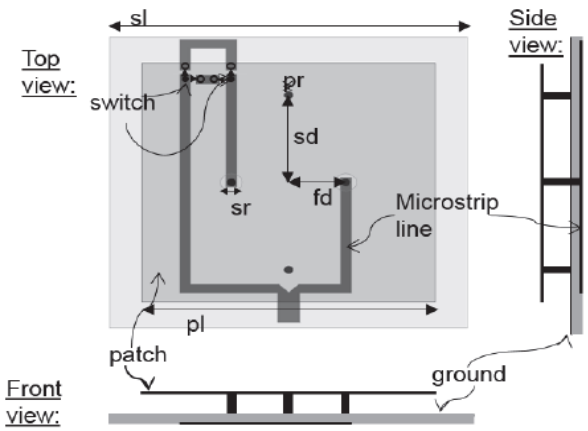

Figure 1.36. Layout of pattern reconfigurable antenna for on- and off-body modes [105]

A microstrip-fed ground modified antenna with pattern selectivity at 2.4 GHz was presented in [106]which can offer either omnidirectional mode or two directional modes which can be shifted by 180° using switches (Fig. 1.37). There are three switching states namely, when both switches are ON or when one of them is ON and the other is OFF. This results in different forms of radiation patterns as shown in Fig. 1.37. However, the on-body performance of this antenna is missing in the paper which may suffer since there are slots in the ground plane.

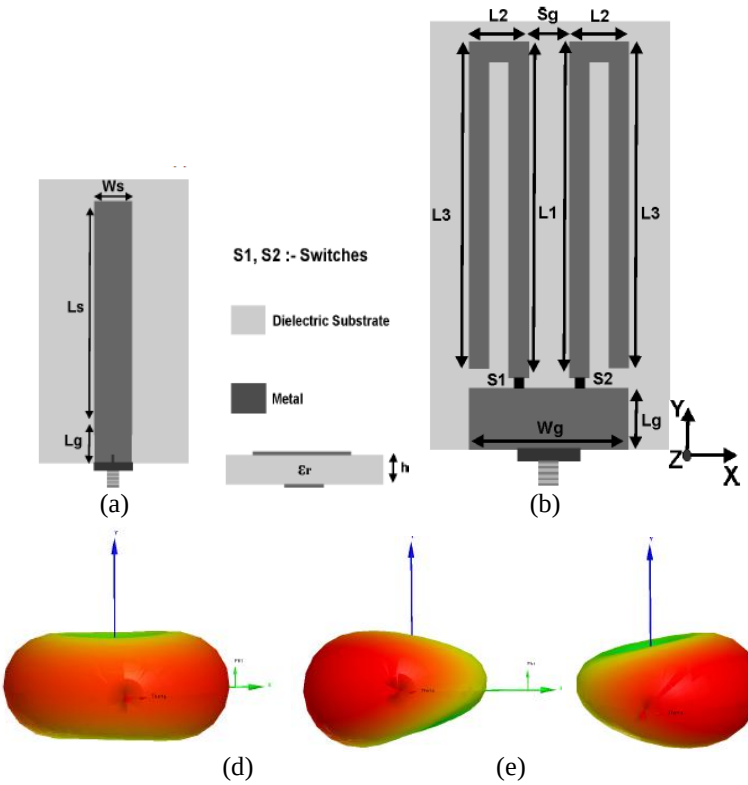

Figure 1.37. Layout of microstrip-fed ground modified antenna (a) Top view (b) Bottom view (c), (d), (e), Radiation patterns for three different states of the switches (S1 and S2) (c) S1=ON, S2=ON, (d) S1=ON, S2=OFF, (e) S1=OFF, S2=ON [106].

1.6. Conclusions

As evident, the WBASN technology still suffers from many challenges and unstable antenna behavior in proximity to body due to various contributing factors such as high tissue parameters, body movement and highly dynamic body-centric radio channel in a real-time environment. The objective of this thesis is therefore, to analyze the various radio channels first in proximity to human body (e.g., on-body, off-body) and then propose miniaturized antenna solutions with stable and robust performance in proximity to body.

Also, most of the work reported in the literature up till so far mainly used physically large-sized antennas (with reference to the operating wavelength λ_0) whereas there is a currently growing scope of low power and miniaturized sensors for medical and other smart applications of WBASNs. Since, antenna size is an important contributing factor to control the overall size of sensors comprising transmitters/receivers, there is a fundamental need to explore also the application of miniaturized antennas (e.g., chip antennas) for WBASN considerations. Moreover, with reference to the counterpart WSNs, the antenna diversity configurations are also needed to be explored further for WBASN applications due to the bottleneck requirements of high data rate, link reliability and low-power consumption of medical and other smart devices employing such networks. Finally, there is also an intrinsic need to develop simulators to simulate any WBASN scenario (e.g., body posture, sensor/antenna location etc.) under limited simulation resources to avoid costly redundant measurements and save time along with financial resources.

1.7. Thesis Structure

This PhD dissertation finds its place in the BoWI project [11] which comprised of a versatile consortium working on various sub-projects towards the common goal of final demonstrator. This dissertation forms part of sub-project on antennas and wireless channel models for WBASN applications at ISM 2.4 GHz frequencies in the framework of BoWI project.

The existing WBASN technology still suffers from many challenges and unstable antenna behavior in proximity to body at microwave frequencies. This thesis outlines the major challenges faced by the current technology along with new solutions and improved proposals. The thesis work is organized as follows.

Chapter 2 will introduce sensors used in the BoWI project incorporating miniaturized chip antennas under pattern diversity configuration. Implementing chip antennas on an arbitrary substrate will be discussed. Further, channel measurements will be presented exploiting chip antenna diversity in a multipath indoor environment in the context of short-range off-body communications. Various channel parameters such as power delay profile, delay spread and radio channel capacity for a 2x2 MIMO configuration will be investigated compared to the ideal capacity in case of Rayleigh fading channels. A robust algorithm will also be presented developed using Maximum Likelihood Estimation and

Kolmogorov-Smirnov test for selection of the best-fit channel fading model. Furthermore, small-scale first-order fading will be investigated using the proposed fitting algorithm for off-body and on-body radio channels using extensive real-time measurements conducted in a multipath indoor environment.

Chapter 3 will describe the antenna-body interactions and on-body propagation studies conducted using CST MWS [36]. The significance of various parameters such as the impact of human tissue properties, and the need of a certain minimum antenna-body intervening space for reliable radio performance will be elaborated. The design of a dual mode short-circuited ring patch antenna (SRPA) will also be presented here demonstrating the application of its first two resonant modes for both on-body and off-body applications. The on-body performance evaluation of the antenna will also be presented.

Chapter 4 will present the design and implementation of a miniaturized meander chip antenna along with its characterization in both free space and on human body. Furthermore, the development of a WBASN channel simulator in CST MWS [36] will be presented using 3D body model ghosts imported from commercial CAD-based tool (POSER [37]). The channel simulator was developed to provide interesting findings from radio perspective for the specific posture alphabets as used by the BoWI consortium and can be very useful for future WBASN simulation studies. The simulator offers the power to simulate any arbitrary WBASN scenario with desired body position/posture or antenna configurations etc. The development of simulator was faced by a number of rigorous scientific challenges which will also be highlighted here.

Chapter 5 will present the exploration of pattern diversity using standard radiation and polarization scenarios for optimal BAN performance e.g., omni-azimuthal radiation with orthogonal polarization to body (known to be suitable for on-body scenarios) and broadside radiation with polarization parallel to the body (known to be suitable for off-body scenarios). The study will be concluded with simulation results on the basis of which, design and experimental characterization of a pattern diversity antenna will be undertaken.

Finally, thesis conclusions and future perspective will be highlighted.

References

[1] P. S. Hall and Y. Hao, Antennas and Propagation for Body-Centric Wireless Communications, Norwood, MA, USA: Artech House, Inc, 2006.

[2] M.A. Hanson, H.C. Powell, A.T. Barth, K. Ringgenberg, B. H. Calhoun, J. H. Aylor, J. Lach, " Body Area Sensor Networks: Challenges and Opportunities," *Computer,* vol. 42, no. 1, pp. 58-65, Jan. 2009.

[3] J. Wang and Q. Wang, Body Area Communications: Channel Modeling, Communication Systems and EMC, Singapore: John Wiley & Sons, 2012.

[4] "http://www.ieee802.org/15/pub/TG6.html," [Online].

[5] A.W. Astrin, H.-B. Li, and R. Kohno, "Standardization for body area networks.," *IEICE Transactions,* Vols. E92-B, no. 2, 2009.

[6] K. Kinsella, D.R. Phillips, "Global aging: The challenge of success," *Pop. Bull.* , vol. 60, pp. 1-42., 2005.

[7] A. Darwish and A. E. Hassanien, "Wearable and Implantable Wireless Sensor Network Solutions for Healthcare Monitoring," *Sensors,* vol. 11, pp. 5561-5595, 2011.

[8] P. Khan, M.A. Hussain,K.S. Kwak, "Medical applications of wireless body area networks.," *JDCTA* , vol. 3, no. 3, pp. 185-193, 2009.

[9] "Drägerwerk 2010, Drägerwerk Infinity ® M300, http://www.draeger.com/," [Online].

[10] "www.nikeplus.nike.com," [Online].

[11] "http://www.bowi.cominlabs.ueb.eu/," [Online].

[12] "https://www.xsens.com/," [Online].

[13] K. Y. Yazdandoost and K. Sayrafian-Pour, ", Channel model for Body Area Network (BAN)," *IEEE P802.15-08-0780-09-0006,* April, 2009.

[14] T. Aoyagi, J-I. Takada, K. Takizawa, N. Katayama, T. Kobayashi, K. Y. Yazdandoost, H-B. Li and R. Kohno, "Channel Models for WBANs – NICT," *IEEE P802.15-08-0416-03-0006,* Sep. 2008.

[15] C. Oliveira, L. M. Correia, "Signal Correlation and Power Imbalance in Dynamic On-Body Communications," in *COST IC1004 TD(12)*, UK, Sep. 2012.

[16] D. Lewis, "802.15.6 Call for Applications - Response Summary," *IEEE 802.15-08-0407-02.*

[17] Stéphane Van Roy, François Quitin, LingFeng Liu, Claude Oestges, François Horlin, Jean-Michel Dricot and Philippe De Doncke, "Dynamic channel modeling and validation for multisensor body area networks," *IEEE Transactions on Antennas and Propagation,* vol. 61, no. 4, 2012.

[18] Guido Dolmans and Andrew Fort, "Channel models WBAN-Holst centre/IMEC-NL," in *IEEE 802.15-08-0418-01-0006*, July 2008.

[19] Dino Miniutti, Leif Hanlen, David Smith, Andrew Zhang, Daniel Lewis, David

Rodda, Ben Gilbert, "Narrowband on body to off body channel characterization for BAN," in *IEEE 802.15-08-0559-00-0006*, August 2008.

[20] Hirokazu Sawada, Takahiro Aoyagi, Jun-ichi Takada, Kamya Yekeh Yazdandoost, Ryuji Kohno, "Channel model between body surface and wireless access point for UWB band," in *IEEE 802.15-08-0576-00-0006*, August 2008.

[21] Nechayev, Y. I., et al., "On-Body Path Gain Variations with Changing Body Posture and Antenna Position," in *IEEE AP-S Int. Symp.*, Washington, D.C., July 2005.

[22] Kamarudin, M. R., N. I. Nechayev, and P. S. Hall, "Antennas for On-Body Communications," in *IEEE Int. Workshop on Antenna Technology, Small Antennas, Novel Metamaterials*, Singapore, March 2005.

[23] Nechayev, Y. I., et al., "Radio Channel Characterisation and Antennas for On-Body Communications," in *Loughborough Antenna and Propagation Conference*, Loughborough, U.K., April 2005.

[24] Nechayev, Y., et al., "Path Loss Measurements of On-Body Communication Channels," in *Int. Symp. Antennas and Propagation*, Sendai, Japan, August 2004.

[25] Nechayev, Y. I., et al., "Narrowband and Wideband Radio Channel Characterisation and Antennas for On-Body Communications," in *Workshop on Body Sensor Networks*, Imperial College, April 2005.

[26] Hall, P. S., M. Ricci, and T. M. Hee, "Measurement of On-Body Propagation Channels," in *IEEE Antennas and Propagation Int. Symp.*, June 2002.

[27] Hall, P. S., et al., "Characterisation of On-Body Communication Channels," in *UNSC/URSI National Science Meeting*, June 2004.

[28] Nechayev, Y. I., et al., "Antennas and Propagation for On-Body Communication Systems," in *11th Int. Symp. Antenna Technology and Applied Electromagnetics—ANTEM*, Saint Malo, France, June, 2005.

[29] G. Roqueta, A. Fort, C. Craeye, C. Oestges, "Analytical propagation models for body area networks," in *IET Seminar on Antennas and Propagation for Body-Centric Wireless Communications*, 2007.

[30] S.L. Cotton, W.G. Scanlon, G.A. Conway, "Autocorrelation of signal fading in wireless body area networks," in *2nd IET Seminar on Antennas and Propagation for Body-Centric Wireless Communications*, 2009.

[31] S. Van Roy, C. Oestges, F. Horlin, P. De Doncker, "Ultra-wideband spatial channel characterization for body area networks," in *2nd European Conference on Antennas and Propagation (EuCAP)*, 2007.

[32] N. Thepvilojanapong, S. Motegi, A. Idoue, H. Horiuchi, "Adaptive channel and time allocation for body area networks," *IET Communications, ,* vol. 5, no. 12, pp. 1637 - 1649, 2011.

[33] W. Thompson, K. Walker, R. Cepeda, M.A. Beach, J. McGeehan, "Ultra wideband body area network channel measurement and analysis using textile antennas," in *2nd IET Seminar on Antennas and Propagation for Body-Centric Wireless Communications*, 2009.

[34] M. Gallo, P.S. Hall, M. Bozzett, "Simulation and measurement of body dynamics

for on-body channel characterisation," in *IET Seminar on Antennas and Propagation for Body-Centric Wireless Communications*, 2007.

[35] K. Y. Yazdandoost, et al., "Channel Model for Body Area Network (BAN)," in *IEEE 802.15-08-0033-04*, Sep. 2008.

[36] "https://www.cst.com/," [Online].

[37] "http://my.smithmicro.com/poser-3d-animation-software.html," [Online].

[38] J. Ryckaert, P. De Doncker, R. Meys, A. de Le Hoye, and S. Donnay, "Channel model for wireless communication around human body," *Electron. Lett.*, vol. 40, no. 9, p. 543–544, Apr. 2004.

[39] A. Fort, C. Desset, P. Wambacq, and L. V. Biesen, "Indoor body-area channel model for narrowband communications," *IET Microw. Antennas Propag.*, vol. 1, no. 6, p. 1197–1203, 2007.

[40] D. Smith, L. Hanlen, J. Zhang, D. Miniutti, D. Rodda, and B. Gilbert, "First- and second-order statistical characterizations of the dynamic body area propagation channel of various bandwidths," *Annals of Telecommunications*, vol. 66, no. 3-4, pp. 187-203, 2011.

[41] J. Zhang, D.B. Smith, L.W. Hanlen, D. Miniutti, D. Rodda, and B. Gilbert, "Stability of narrowband dynamic body area channel," *IEEE Antennas and Wireless Propagation Letters*, vol. 8, pp. 53-56, 2009.

[42] W. G. Scanlon and S. L. Cotton, "Understanding on-body fading channel at 2.45 GHz using measurements based on user state and environment," in *Loughborough Antennas and Propagation Conference* , Loughborough, UK, Mar. 2008.

[43] D. B. Smith, D. Miniutti, T.A. Lamahewa, and L.W. Hanlen, "Propagation models for body-area networks: a survey and new outlook," *IEEE Antennas and Propagation Magazine*, vol. 55, no. 5, pp. 97-117, Oct. 2013.

[44] I Khan, L Yu, Y I. Nechayev, and P S. Hall, "Space and pattern diversity for on-body communication channels in an indoor environment at 2.45 GHz," in *2nd European Conference on Antennas and Propagation (EuCAP)*, Edinburgh, UK , Nov 2007.

[45] Q. H. Abbasi, M. M. Khan, S. Liaqat, M. Kamran, A. Alomainy, and Y. Hao, "Experimental investigation of ultra wideband diversity techniques for on-body radio communications," *Progress In Electromagnetics Research C*, vol. 34, pp. 165-181, 2013.

[46] I. Khan, P.S. Hall, A. A. Serra, A. R. Guraliuc, and P. Nepa, "Diversity performance analysis for on-body communication channels at 2.45 GHz," IEEE Transactions on Antennas and Propagation," vol. 57, no. 4, pp. 956-963, April 2009.

[47] I. Khan and P S. Hall, "Experimental evaluation of MIMO capacity and correlation for narrowband body-centric wireless channels," *IEEE Transactions on Antennas and Propagation*, vol. 58, no. 1, pp. 195-202, Jan. 2010..

[48] K. Ghanem, P. Hall, "Capacity Evaluation of On-body Channels Using MIMO Antennas," in *IEEE International Conference on Wireless and Mobile Computing, Networking and Communications*, Oct. 2009.

[49] P. Van Torre, L. Vallozzi, L. Jacobs, H. Rogier,M. Moeneclaey, J. Verhaevert, "Characterization of Measured Indoor Off-Body MIMO Channels with Correlated Fading, Correlated Shadowing and Constant Path Loss," *IEEE Transactions on Wireless Communications,*, vol. 11, no. 2, pp. 712-721, Feb. 2012.

[50] P. Van Torre, P. Vanveerdeghem, H. Rogier,, "Correlated shadowing and fading characterization of MIMO off-body channels by means of multiple autonomous on-body nodes," in *8th European Conference on Antennas and Propagation (EuCAP)*, 2014.

[51] S. L. Cotton, "Characteristics of shadowed fading in off-body communications channels at 2.45 GHz," in *General Assembly and Scientific Symposium (URSI GASS), XXXIth URSI*, Aug. 2014.

[52] Mackowiak, M.; Correia, L.M., "Statistical path loss model for dynamic off-body channels," in *IEEE 25th Annual International Symposium on Personal, Indoor, and Mobile Radio Communication (PIMRC)*, Sept. 2014.

[53] Q.H. Abbasi, M. M. Khan, S. Liaqat, A. Alomainy, and Y. Hao, "Ultra wideband off-body radio channel characterization for different environments," in *7th International Conference on Electrical & Computer Engineering (ICECE)*, Dec. 2012.

[54] A. A. Goulianos, T. W. C. Brown, B. G. Evans, and S. Stavrou, "Wideband power modeling and time dispersion analysis for UWB indoor off-body communications," *IEEE Trans. Antennas and Propag.*, vol. 57, no. 7, p. 2162–2171, Jul.2009.

[55] M. M. Khan, Q. H. Abbasi, A. Alomainy, and Y. Hao, "Radio propagation channel characterisation using ultra wideband wireless tags for body-centric wireless networks in indoor environment," in *International Workshop on Antenna Technology (iWAT)*, Hong Kong, Mar. 2011.

[56] D. Smith, L. Hanlen, J. Zhang, D. Miniutti, D. Rodda, and B. Gilbert, "Characterization of the dynamic narrowband on-body to off-body area channel," in *IEEE Int. Conf. on Communications*, Jun. 2009.

[57] H. Akaike, "A new look at the statistical model identification," *IEEE Trans. Automatic Control*, vol. 19, no. 6, pp. 716-723, 1974.

[58] Q.H. Abbasi, A. Alomainy, and Y. Hao, "Ultra wideband antenna diversity techniques for on/off-body radio channel characterisation," in *IEEE International Workshop on Antenna Technology (iWAT)*, March 2012.

[59] A. Goulianos, T. Brown, and S. Stavrou, "Power delay profile modelling of the ultra wideband off-body propagation channel," *IET Microwaves, Antennas & Propagation*, vol. 4, no. 1, pp. 62-71, January 2010.

[60] P. V. Torre, L. Vallozzi, L. Jacobs, H. Rogier, M. Moeneclaey, J. Verhaevert, "Characterization of Measured Indoor Off-Body MIMO Channels with Correlated Fading, Correlated Shadowing and Constant Path Loss," *IEEE Transactions on Wireless Communications*, vol. 11, no. 2, pp. 712-721, Feb. 2012.

[61] Geddes, L. A., and L. E. Barker, "The Specific Resistance of Biological Material—A Compendium of Data for the Biomedical Engineer and Physiologist," *Medical and Biological Engineering*, vol. 5, p. 271–293, 1967.

[62] Stuchly, M. A., and S. S. Stuchly, "Dielectric Properties of Biological Substances—Tabulated," *J. of Microwave Power,* vol. 15, no. 1, p. 19–26, 1980.

[63] Foster, K. R., and H. P. Schwan, "Dielectric Properties of Tissues and Biological Materials: A Critical Review," *Critical Reviews in Biomedical Engineering,* vol. 17, no. 1, p. 25–104, 1989.

[64] Gabriel, C., T. Y. A. Chan, and E. H. Grant, "Admittance Models for Open-Ended Coaxial Probes and Their Place in Dielectric Spectroscopy," *Physics in Medicine and Biology,* vol. 39, no. 12, p. 2183–2200, 1994.

[65] Duck, F. A., Physical Properties of Tissue: A Comprehensive Reference Book, HBJ New York: Academic Press, 1990.

[66] Gabriel, C., "Compilation of the Dielectric Properties of Body Tissues at RF and Microwave Frequencies," in *Brooks Air Force Technical Report, AL/OE-TR-1996-0037*, 1996.

[67] "An Internet Resource for the Calculation of the Dielectric Properties of Body Tissues," *Institute for Applied Physics, Italian National Research Council, http://niremf.ifac.cnr.it/tissprop/.*

[68] ICNIRP, "Guidelines for Limiting Exposure to Time-Varying Electric, Magnetic, and Electromagnetic Fields (Up to 300 GHz)," *Health Physics,* vol. 74, no. 4, p. 494–522, 1998.

[69] IEEE, "IEEE Recommended Practice for Determining the Peak Spatial-Average Specific Absorption Rate (SAR) in the Human Head from Wireless Communications Devices: Measurement Techniques," *IEEE Std. 1528-2003,* 2003.

[70] Guy, A. W., "Analyses of Electromagnetic Fields Induced in Biological Tissues by Thermographic Studies on Equivalent Phantom Models," *IEEE Trans. on Microwave Theory and Techniques,* vol. 19, no. 2, p. 205–214, 1968.

[71] Ogawa, K., et al., "A High-Precision Real Human Phantom for EM Evaluation of Handheld Terminals in a Talk Situation," in *Proc. Int. IEEE Antennas and Propagation Symp.,* July 2001.

[72] Ogawa, K., H. Iwai, and J. Hatakenaka, "A High-Precision Real Human Phantom for EM Evaluation of Handheld Terminal Antennas in a Talk Situation," *Trans. on IEICE.*, Vols. J85-B, no. 5, p. 676–686 (in Japanese), 2002.

[73] Ito, K., et al., "Development and Characteristics of a Biological Tissue-Equivalent Phantom for Microwaves," *Electron. Commun. Jpn. Pt. I-Commun.,* vol. 84, no. 4, p. 67–77, 2001.

[74] Okano, Y., et al., "The SAR Evaluation Method by a Combination of Thermographic Experiments and Biological Tissue-Equivalent Phantoms," *IEEE Trans. on Microwave Theory and Techniques,* vol. 48, no. 11, p. 2094–2103, 2000.

[75] Ishido, R., et al., "A Study on the Solid Phantoms for 3–6 GHz and Evaluation of SAR Distributions Based on the Thermographic Method," *Proc. 2004 Int. Symp. Electromagnetic Compatibility, EMC'04,* vol. 3, no. B3-2, pp. 577–580, Sendai, Japan, June 2004.

[76] Tamura, H., et al., "A Dry Phantom Material Composed of Ceramic and Graphite Powder," *IEEE Trans. on Electromagnetic Compatibility,* vol. 39, no. 2, p. 132–

137, May 1997.

[77] Nikawa, Y., M. Chino, and K. Kikuchi, "Soft and Dry Phantom Modeling Material Using Silicone Rubber with Carbon Fiber," *IEEE Trans. on Microwave Theory and Techniques,* vol. 44, no. 10, Part 2, p. 1949–1952, 1996.

[78] Chang, J. T., et al., "A Conductive Plastic for Simulating Biological Tissue at Microwave Frequencies," *IEEE Trans. on Electromagnetic Compatibility,* vol. 42, no. 1, pp. 76-81, 2000.

[79] Kobayashi, T., et al., "Dry Phantom Composed of Ceramics and Its Application to SAR Estimation," *IEEE Trans. on Microwave Theory and Techniques,* vol. 41, no. 1, p. 136–140, Jan. 1993.

[80] Kritikos, H. N., and H. P. Schwan, "Hot Spot Generated in Condition Spheres by Electromagnetic Waves and Biological Implications," *IEEE Trans. on Biomed. Eng.*, vol. 19, no. 1, pp. 53-58, 1972.

[81] Shapiro, A. R., R. F. Lutomirski, and H. T. Yura, "Induced Fields and Heating Within a Cranial Structure Irradiated by an Electromagnetic Plane Wave," *IEEE Trans. on Microwave Theory and Techniques,* vol. 19, no. 2, p. 187–196, 1971.

[82] Massoudi, H., et al., "Electromagnetic Absorption in Multilayered Cylindrical Models of Man," *IEEE Trans. on Microwave Theory and Techniques,* vol. 27, no. 10, p. 825–830, 1979.

[83] Nishizawa, S., and O. Hashimoto, "Effective Shielding Analysis for Three Layered Human Model," *IEEE Trans. on Microwave Theory and Techniques,* vol. 47, no. 3, p. pp. 277–283, 1999.

[84] Dimbylow, P. J., "The Development of Realistic Voxel Phantoms for Electromagnetic Field Dosimetry," in *Proc. Int. Workshop on Voxel Phantom Development*, Chilton, United Kingdom, July, 1995.

[85] Mason, P. A., et al., "Effects of Frequency, Permittivity, and Voxel Size on Predicted Specific Absorption Rate Values in Biological Tissue During Electromagnetic-Field Exposure," *IEEE Trans. on Microwave Theory and Techniques,* vol. 48, no. 11, 2000.

[86] Xu, X. G., T. C. Chao, and A. Bozkurt, "VIP-Man: An Image-Based Whole-Body Adult Male Model Constructed from Color Photographs of the Visible Human Project for Multiparticle Monte Carlo Calculations," *Health Phys.*, vol. 78, p. 476–486, 2000.

[87] Xu, X. G., T. C. Chao, and A. Bozkurt, "VIP-Man: An Image-Based Whole-Body Adult Male Model Constructed from Color Photographs of the Visible Human Project for Multiparticle Monte Carlo Calculations," *Health Phys.*, vol. 78, p. 476–486, 2000.

[88] R. Kramer, H. J. Khoury, J. W. Vieira, V. J. M Lima, "MAX06 and FAX06 : update of two adult human phantoms for radiation protection dosimetry," *Physics in medicine & biology,* vol. 51, no. 14, pp. 3331-3346, 2006.

[89] N. Haga, K. Saito, M. Takahashi, and K. Ito, "Characteristics of Cavity Slot Antenna for Body-Area Networks," *IEEE Transactions on Antennas and Propagation,* vol. 57, no. 4, p. 837–843, Apr. 2009.

[90] "Smart miniature low-power wireless microsystem for Body Area Networks," in *WiserBAN FP7-ICT-2009-5*.

[91] Y. Uno, K. Saito, M. Takahashi, and K. Ito, "Ultra wideband antenna wearing arm," *IEICE TRANSACTIONS on Communications,* Vols. J94-B, no. 9, p. 1114–1121, Sept. 2011.

[92] N. Chahat, M. Zhadobov, R. Sauleau, and K. Ito, "A Compact UWB Antenna for On-Body Applications," *IEEE Transactions on Antennas and Propagation,* vol. 59, no. 4, p. 1123–1131, Apr. 2011.

[93] T. J. Jung, J. H. Kwon, and S. Lim, "Flexible zeroth-order resonant antenna independent of substrate deformation," *Electronics Letters,* vol. 46, no. 11, p. 740–742, May 2010.

[94] T. Alves, R. Augustine, M. Grzeskowiak, B. Poussot, D. Delcroix, S. Protat, J.-M. Laheurte and P. Queffelec, "BAN antenna design using ferrite polymer composite," in *IEEE Proc. 3rd European Conf. On Antennas and Propag. (EuCAP),* , Mar. 2009.

[95] S. Zhu and R. Langley, "Dual-Band Wearable Textile Antenna on an EBG Substrate," *IEEE Transactions on Antennas and Propagation,* vol. 57, no. 4, p. 926–935, Apr. 2009.

[96] L. Liu, S. Zhu, and R. Langley, "Dual-band triangular patch antenna with modified ground plane," *Electronics Letters,* vol. 43, no. 3, pp. 140-141, Feb. 2007.

[97] M. A. R. Osman, M. K. A. Rahim, M. Azfar, N. A. Samsuri, F. Zubir, and K. Kamardin, "Design, implementation and performance of ultra-wideband textile antenna," *Progress In Electromagnetics Research B,* vol. 27, p. 307–325, 2011.

[98] M. A. R. Osman, M. K. A. Rahim, M. F. Ali, and N. A. Samsuri, "Compact Fully Textile UWB Antenna for Monitoring Applications," in *2011 Asia-Pacific Microwave Conference (APMC 2011),* Melbourne, Australia, Dec. 2011 .

[99] M. A. R. Osman, M. K. A. Rahim, N. A. Samsuri, M. K. Elbasheer, and M. E. Ali, "Textile UWB Antenna Bending and Wet Performances," *International Journal of Antennas and Propagation,* 2012.

[100] B. Sanz-Izquierdo, F. Huang, J.C. Batchelor, M. Sobhy, "Compact Antenna for WLAN on body applications," *36th European Microwave Conference,* Sept. 2006.

[101] R. Anupam, R. Chandran, G. A. Conway and W. G. Scanlon, "Pattern switching compact patch antenna for on-body and off-body communications at 2.45 GHz," in *3rd European Conference on Antennas and Propagation,* Berlin, Germany, March 2009 .

[102] Andrey S. Andrenko, Ichirou Ida, and Tatsuya Kikuzuki, "Dual-Band Patch Antenna with Monopole-Like Radiation Patterns for BAN Communications," in *7th European conference on Antennas and Propagation (EUCAP),* 2013.

[103] S.-J. Ha and C. W. Jung, "Reconfigurable beam steering using a microstrip patch antenna with a U-slot for wearable fabric applications," *IEEE Antennas and Wireless Propagation Letters,* vol. 10, p. 1228–1231, 2011.

[104] Ahyat, E.N., Rahman, T.A., Kamarudin, M.R., "A Novel Pattern Reconfigurable Dipole Yagi Antenna for Wireless Body Area Network (WBAN) Applications," in

International symposium on Antennas and Propagation (ISAP), Jeju, Korea, October 2011.

[105] S. Dumanli, "On-body antenna with reconfigurable radiation pattern," in *RF and Wireless Technologies for Biomedical and Healthcare Applications (IMWS-Bio)*, London (UK), Dec. 2014 .

[106] S. Raman, B. Graham, S.M. Crossan, N. Timmons, J. Morrison, V.A. Shameena, M. Pezholil, "Microstrip fed ground modified compact antenna with reconfigurable radiation pattern for BANs," in *Loughborough Antennas and Propagation Conference*, Loughborough, 2012.

Chapter 2. Radio channel characterization for WBASNs using ultra-miniaturized chip antennas

Contents

2.1. Introduction

WBASNs are promising and emerging 4G networks for short range communications, with widespread applications due to the currently growing scope of low power and miniaturized systems for medical devices and other smart systems. Also extremely low power consumption and reduced Specific Absorption Rate (SAR) are highly desired for long term battery use, along with reduced interference levels from nearby BANs or other systems operating in overlapping frequency bands. The hardware miniaturization and low-power consumption requirements of recent developments in WBASNs lead us to the consideration of ultra-miniaturized antennas for such systems, since antenna size is an important contributing factor to control the overall transceiver size. This is more particularly true in the lower GHz frequency range due to relatively large wavelengths (e.g., λ_0= 125 mm @ 2.40 GHz).

With these considerations, BoWI project [1] employed specific radio front ends with ultra-miniaturized chip antennas (having physical length of few *mm* only). The first BoWI prototype platform is based on IEEE 802.15.4 ZigBee^{TM} architecture and operates in the unlicensed industrial, scientific and medical (ISM) band i.e., 2.40-2.4835 GHz as will be discussed in the coming sections.

At ISM frequencies, radio propagation mainly involves two components. First, the on-body propagation component, which principally involves the propagation through the body surface by creeping waves [2]. This is due to the close proximity of the body which offers direct interaction with the near-field of antennas, hence supporting body surface as a transmission medium. Second, the multipath propagation which is due to the reflection or scattering from the surrounding environment of BAN-user such as floor or ground, furniture, metallic objects, buildings or immediate vehicle environment when the BAN user is on-board etc. Moreover, propagation from inside the body medium or across the body is negligible at ISM 2.4 GHz or higher frequencies due to the very high attenuation of human tissues at microwave frequencies e.g., the attenuation constant α = 3.89 dB/cm @ 2.40 GHz for muscle tissue (ε_r = 52, σ = 1.7 Sm^{-1}) [3].

The multipath fading in case of body-centric communications is much more serious than mobile communications due to the fact that the transmitter and receiver antennas are located in immediate environment of the human body which changes position continuously, hence moving the antennas seriously. This will result in significant fading due to reflections, and shadowing by movement of body parts etc. In order to overcome fading from multipath environment and to improve the output signal to noise ratio (SNR) without increasing the transmit power or signal bandwidth, antenna diversity can be a powerful tool [4]. The use of antenna diversity can offer significant improvements in perspective of SNR and channel capacity along with providing reasonable amount of diversity gain. This can result in less transmit power, which is the key requirement of current smart and low power WBASNs. This area for on-body communications has received comparatively less attention than mobile channels due to the constraints such as short-range and transceiver cost. Therefore, pattern diversity using ultra-miniaturized

chip antennas is also investigated in this thesis along with consideration of important radio parameters such as delay spread, channel capacity and fading using measurements in realistic multipath environments.

This chapter is organized as follows. In Section 2.2, the Zyggie prototype sensor [1] is introduced which was the first prototype platform developed by the BoWI project partners to support the preliminary research campaigns between various research groups. In Section 2.3, commercial chip antenna (Johanson® [5]) is characterized stand-alone on an arbitrary substrate along with its radiation pattern measurement. In Section 2.4 off-body channel measurements are presented exploiting the pattern diversity configuration using ultra-miniaturized chip antennas in real-time multipath indoor laboratory environment. The resulting radio channels are analyzed along with computation of interesting channel parameters such as power delay profile, RMS delay spread and radio channel capacity. In Section 2.5, a robust algorithm for distribution fitting of empirical radio channel data is presented for statistical study of body-centric channel fading. The application of the algorithm for off- and on-body channels is then presented using real-time measurements conducted in multipath indoor laboratory environment. Finally, conclusions are drawn in Section 2.6.

2.2. Zyggie prototype sensors and chip antennas

BoWI project mainly employs existing WPAN and WBAN standards as IEEE 802.15.6, 802.15.4 respectively. In order to support the preliminary research between different project partners, smart innovative platform was developed by one of the project partners which is named as Zyggie whose first version was released in Sept. 2013 [1]. Zyggie is an innovative WBASN platform which is based on IEEE 802.15.4 ZigBee™ architecture with associated hardware and software. A snapshot of prototype Zyggie sensor is shown in Fig. 2.1. Number of such Zyggie sensors can be worn non-invasively by a human subject on various body parts. Zyggie is supported by inertial measurement units (IMUs) (accelerometer, gyrometer, compass, and barometer), an ATmega256RFR2 embedded processor and a low-power radio module with miniaturized chip antennas to communicate the sensed data (e.g., velocity, orientation, and position) using wireless protocols to a coordinator element which can be further connected to a computer or a smartphone [1]. The sensor data and radio power are finally processed by Zyggie's distributed software to compute the position of each node which is further used for 3D reconstruction of the human actor wearing the BoWI network, making possible the human gesture and movement identification.

(a) (b)

Figure 2.1. (a) Zyggie hardware platform showing associated electronics (b) Zyggie sensor strapped on human wrist. [1]

For radio frequency (RF) measurements and propagation studies, the default Zyggie sensor was modified to incorporate only the components crucial for RF (i.e., removal of the micro-controller and other on-board electronics). The modified Zyggie sensor shown in Fig. 2.2 comprises a multi-layer substrate board having two miniaturized LTCC chip antennas (monopoles) with miniaturized dimensions of $7 \times 2 \times 1.20$ mm^3 from Johanson Tech® [5] tuned in the ISM 2.4 GHz band (i.e., physical length of $\lambda_0/18$ only @ 2.40 GHz). The sensor comprises an RF switch to select between the two antennas by mechanical opening or shortening of a jumper on-board. This switch can be powered by a 3.0 Volts DC power supply. Moreover, the sensor also offers a miniature UFL connector for access to front-end, therefore we also used short length UFL-SMA cables (length~10cm, characteristic impedance = 50 Ω) with the Zyggie sensor for portability to standard SMA instrument interfaces. There is no ground plane under the antennas on sensors, therefore foam-pad spacer ($\varepsilon_r = 1$) was added under the sensors to create 6 *mm* antenna-body spacing for BAN application to avoid the detuning of antennas due to the high permittivity influence of the body.

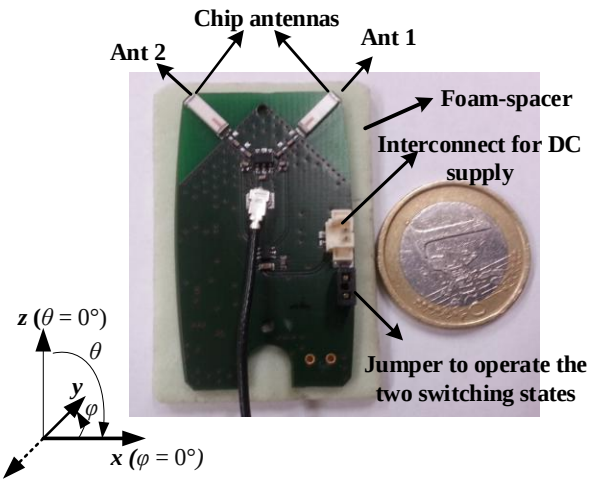

Figure 2.2. Modified Zyggie sensor for channel and propagation studies showing miniaturized chip antennas under pattern diversity configuration.

The chip antennas are mounted orthogonally to support radiation pattern diversity as evident from the 3D radiation patterns which were measured in SATIMO Stargate® (SG 24) system [6] and illustrated in Fig. 2.3. Each antenna compensates for radiation null of the other in the elevation plane (φ = 0°) providing an overall omnidirectional radiation in the elevation plane. This is more clear from the measured 2D patterns in the *xz*-plane plotted in Fig. 2.4 (a) which shows an overall 360° coverage in the elevation plane (φ = 0°).

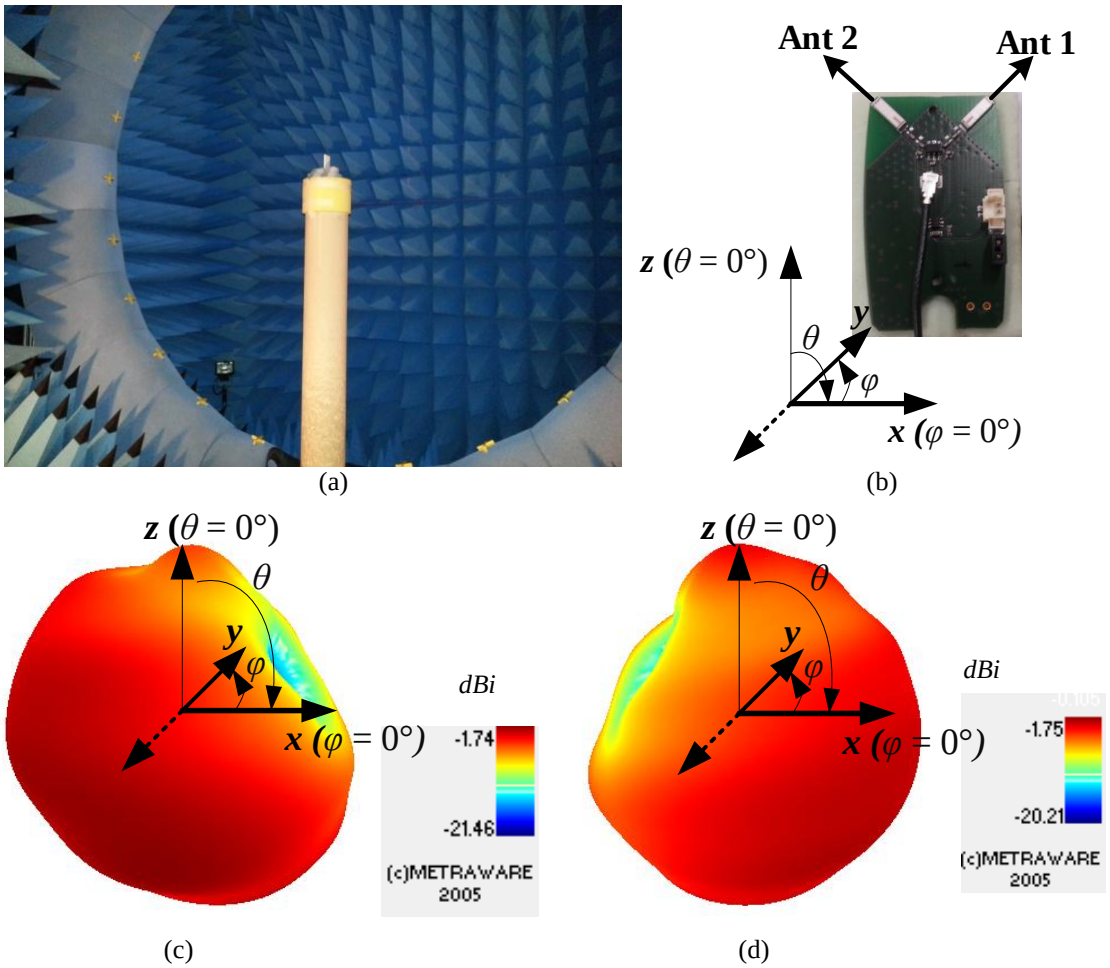

Figure 2.3. (a) Antenna measurement setup in SATIMO Stargate® (SG 24) system [6] (b) Measurement coordinate system (c, d) Measured 3D radiation pattern for (c) Ant 1 and (d) Ant 2 at 2.40 GHz illustrating radiation pattern diversity.

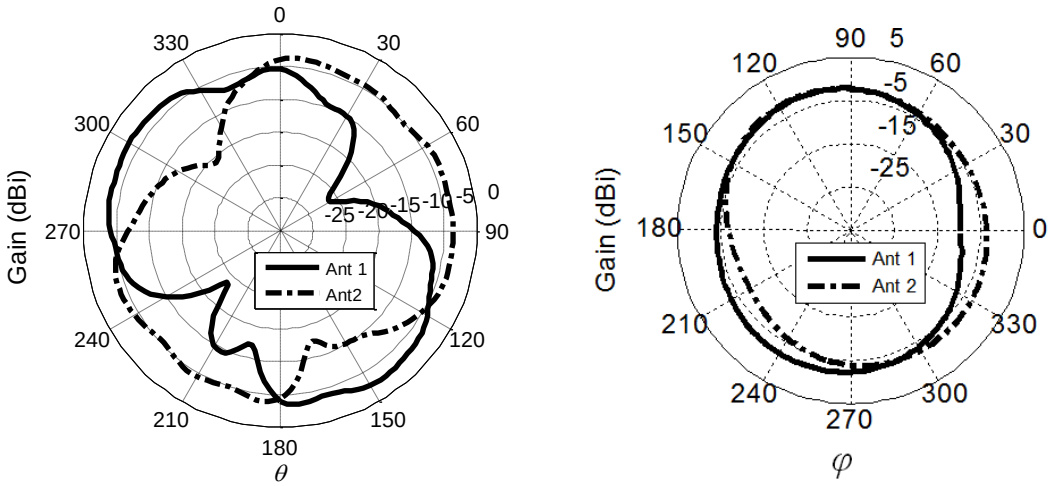

Figure 2.4. Measured radiation pattern in (a) *xz*-plane and (b) *xy*-plane at 2.40 GHz in free space (coordinate system shown in Fig. 2.3 (b)).

The radiation pattern of the chip antennas of the sensor were also measured on a liquid phantom characterizing approximately the FCC recommendations for human tissue properties at 2.4 GHz (ε_r = 51.95, σ = 1.89 S/m). Measurements were conducted in the same SATIMO Stargate® (SG 24) system [6] as used for free space measurements. The measurement configuration along with the radiation patterns is shown in Fig. 2.5. An antenna-body spacing of 6 *mm* was used using foam spacer which results in nearly same on-body performance as that of free space in terms of impedance matching. As evident from Fig. 2.5, the body tissue significantly attenuates the radiation in the back direction which is indeed due to the high tissue parameters at ISM frequencies e.g., the attenuation constant α = 4.32 dB/cm @ 2.40 GHz for equivalent phantom tissue parameters (i.e., ε_r = 51.95, σ = 1.89 S/m) [3].

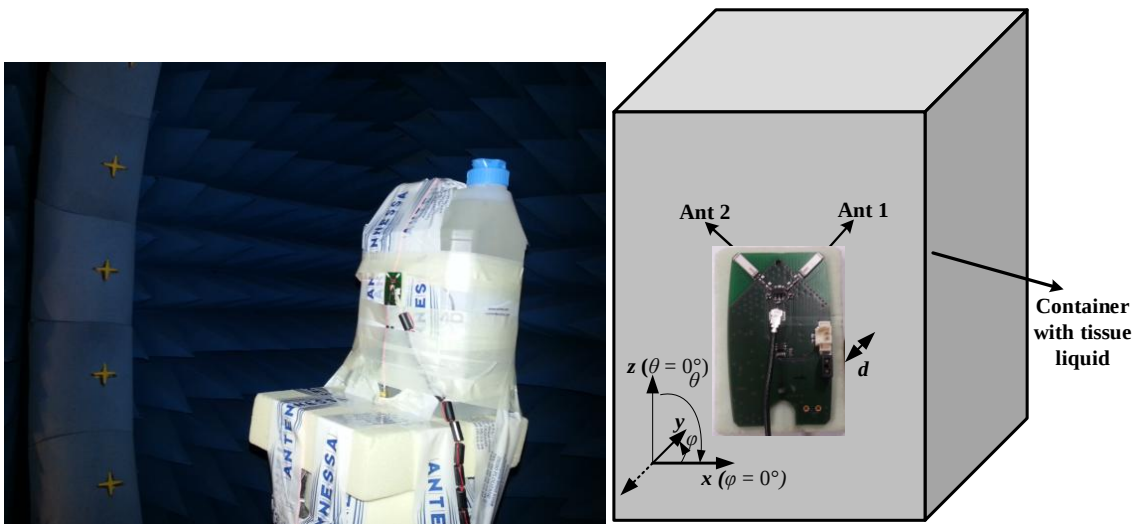

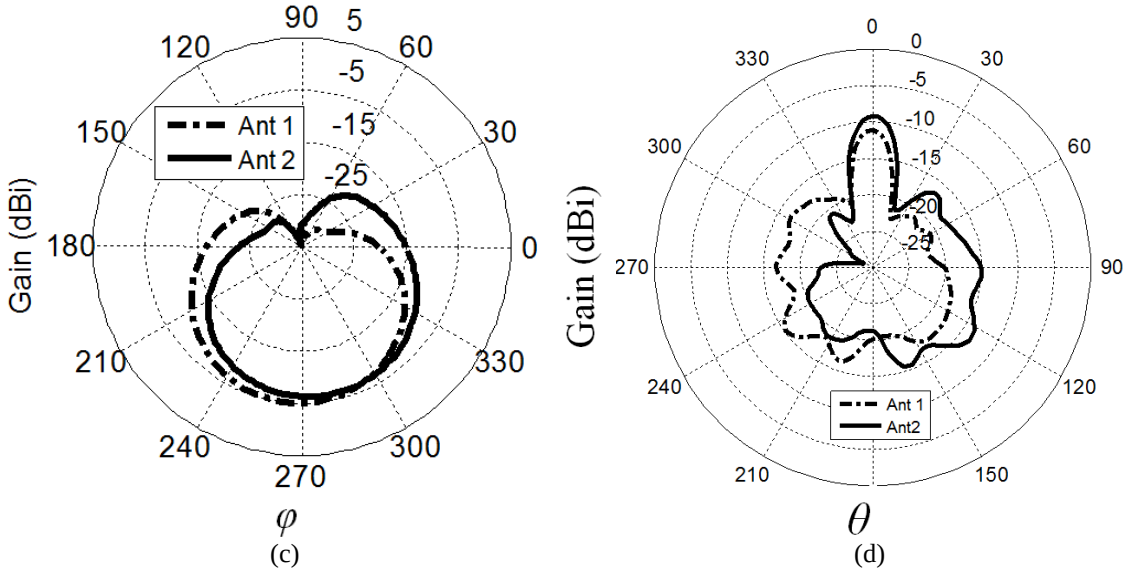

Figure 2.5. (a) Antenna measurement setup in SATIMO Stargate® (SG 24) system [6] showing Zyggie sensor on a liquid tissue container (b) Placement of Zyggie sensor on liquid tissue phantom with measurement coordinate system (c, d) Measured radiation pattern in (c) *xy*-plane and (d) *xz*-plane at 2.40 GHz with antenna-phantom spacing *d* of 6 *mm* (measured from the liquid container surface).

2.3. Characterization of chip antennas on an arbitrary substrate

The Zyggie prototype board comprises two chip antennas with pattern diversity whereas the antenna front-end was not accessible due to RF switch, capacitances and other on-board electronics which indeed introduce losses. Therefore, the idea was to implement single chip antenna in ISM 2.4 GHz on a low-cost substrate to characterize its behavior stand-alone such as its reflection coefficient, radiation patterns etc.

Prototype measurement

Initially, the same chip antenna of Zyggie sensor as explained in Section 2.2 (Fig. 2.2) was used for implementation on a substrate. The laminate AD-450 (ε_r = 4.5 and h = 0.508 mm) was chosen for the initial prototype, as a low-loss alternative of low-cost FR-4 substrates. A 50-Ω microstrip line was used to match the chip antenna with 50-Ω standard SMA interface. The objective was to find the impact of ground plane and also the substrate board for approximate resonance inside ISM 2.4 GHz. The layout of the adopted design is shown in Fig. 2.6 (a). A shift in the response of the antenna is obvious due to the fact that $\varepsilon_{r,eff}$ of the chip antenna changes due to the introduction of underlying substrate, hence changing the antenna resonant frequency (f_r). This was also observed during the preliminary prototype measurements. Therefore, in order to avoid fabrication time and cost, and estimate appropriate dimensions for resonance inside ISM 2.4 GHz band, an equivalent printed monopole antenna was designed in CST MWS [7] for simulation studies (i.e., replacing the chip antenna in Fig. 2.6 (a) by a planar monopole), while it was known from the manufacturer's datasheet [5] that the chip antenna also belongs to the monopole family. For simulation, similar substrate dimensions were used

as the first measured prototype and further, a number of parametric studies were undertaken to study the impact of critical dimensions on antenna resonant frequency f_r. Mainly two dimensions were found to be crucial apart from the length of antenna i.e., the width of ground plane w_g and length of the monopole beyond the antenna end s due to the near-field interaction of the antenna with the substrate.

Based on the simulation studies conducted in CST WMS [7], finally a new prototype board for the chip antenna was fabricated using the same substrate AD-450 (ε_r = 4.5 and h = 0.508 mm) with the appropriate dimensions w_g and s as shown in Fig. 2.6. Consequently, a resonance at ISM 2.4 GHz frequency is successfully achieved with $|S_{11}|$ <-10 dB at 2.4 GHz as shown in Fig. 2.6 (c). The worst impedance matching for ISM band stays at -8 dB at 2.48 GHz which is still an acceptable value for matching with SWR of 2.32. (e.g., matching with a return loss less than -6 dB (or SWR<3.0) has been reported as acceptable for portable UWB antennas [8]- [9]).

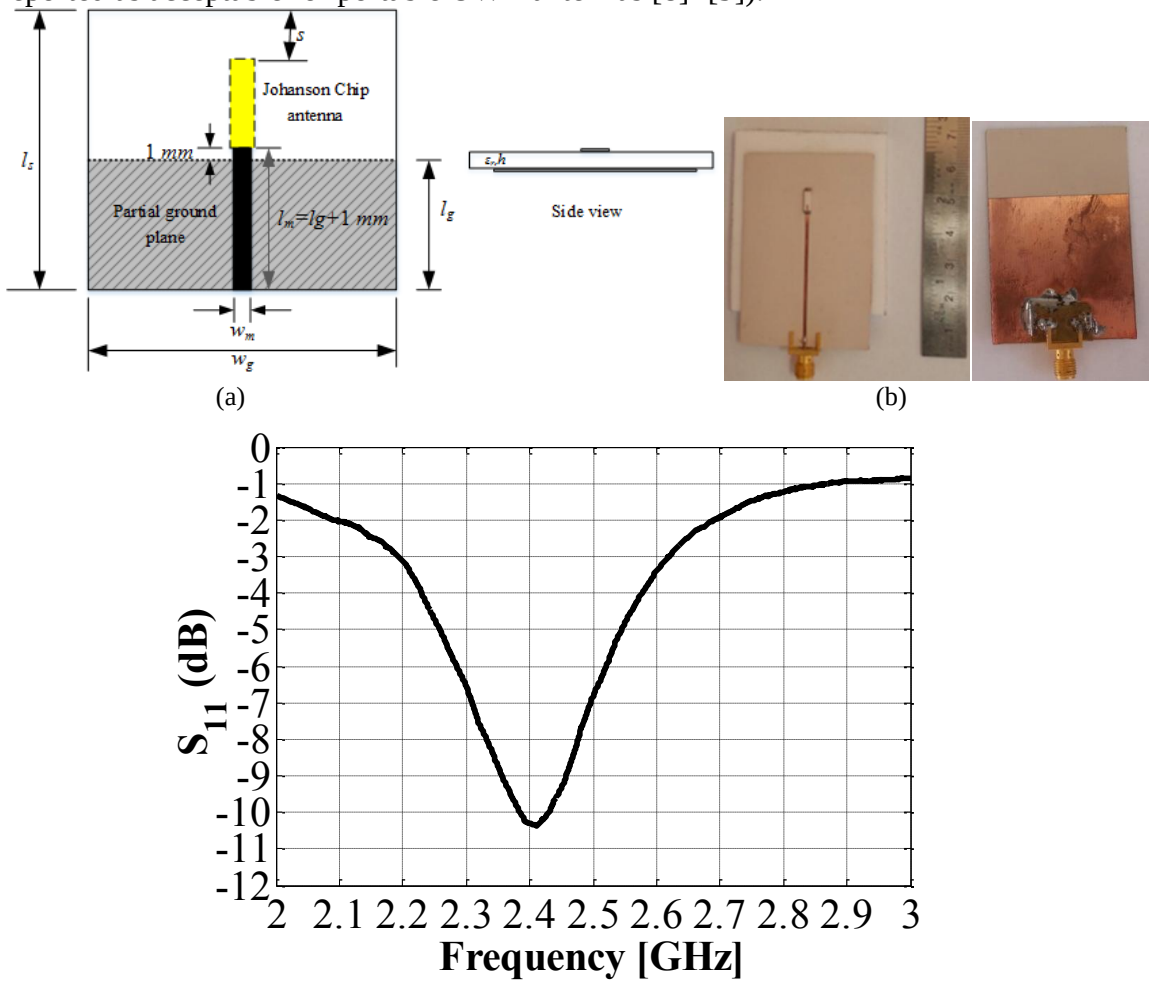

Figure 2.6. (a) Layout of the substrate board with chip antenna showing critical dimensions for matching (b) Photograph of the final fabricated prototype showing the chip antenna matched to a microstrip line feed (top and bottom views) (b) Measured reflection coefficient of the final fabricated prototype on AD-450 substrate with dimensions w_g = 40 mm, l_s = 59.5 mm, s = 10.5 mm, l_g = 40 mm, l_m = 41 mm, w_m = 0.95 mm (50 Ω).

The radiation patterns of the chip antenna on AD-450 substrate were also measured in SATIMO Stargate® (SG 24) system [6] illustrated in Fig. 2.7 along with the corresponding 2D radiation patterns. As evident, the chip antenna radiation patterns resemble in form to that of a monopolar antenna with a measured gain of 0.74 dBi at 2.40 GHz.

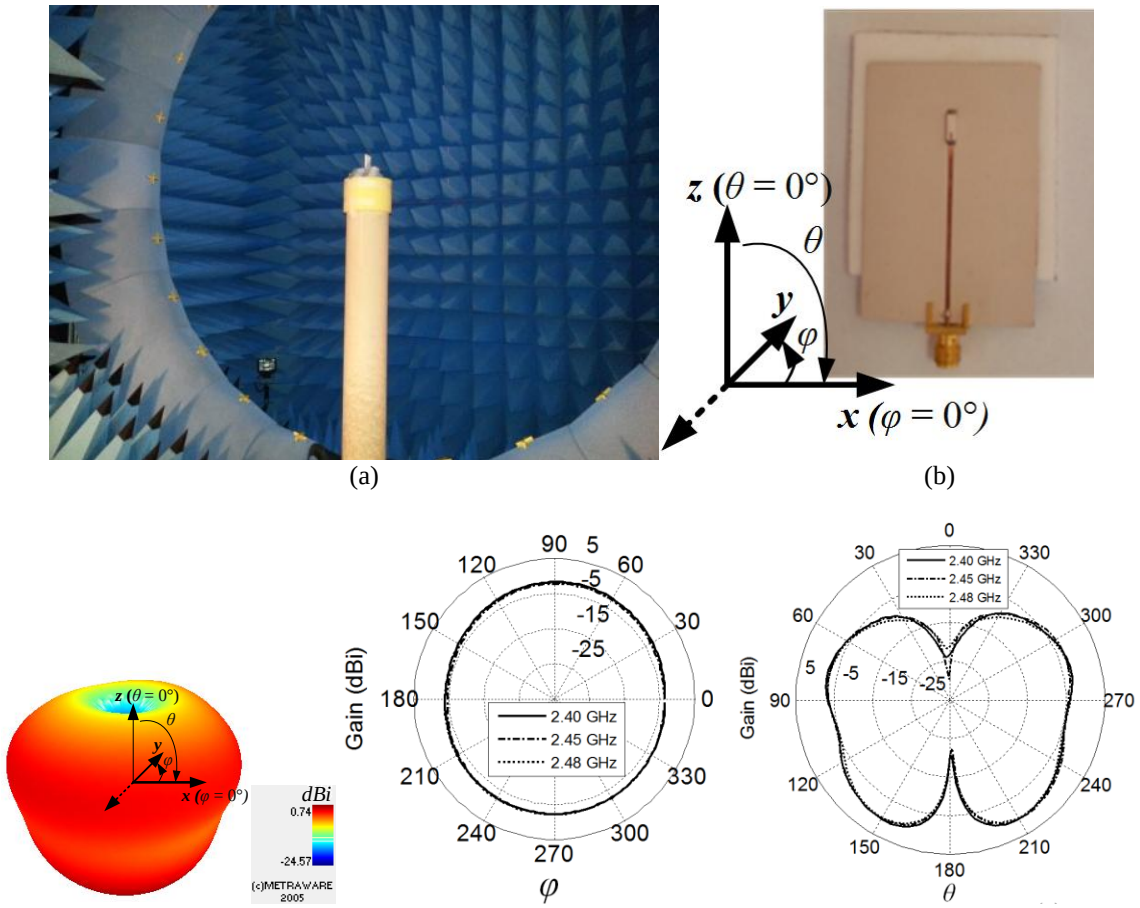

Figure 2.7. (a) Antenna measurement setup in SATIMO Stargate® (SG 24) system [6] (b) Measurement coordinate system (c) Measured 3D radiation pattern at 2.40 GHz (d, e) Measured radiation pattern in (d) *xy*-plane and (e) *xz*-plane for the fabricated prototype.

The return loss and radiation pattern of the chip antenna was also measured by placing the antenna board on a liquid phantom characterizing approximately the FCC recommendations for human tissue properties at 2.4 GHz (ε_r = 51.95, σ = 1.89 S/m). Pattern measurements were conducted in the same SATIMO Stargate® (SG 24) system [6] as used for free space measurements in Fig. 2.7. The measured return loss and radiation patterns are shown in Fig. 2.8. A similar antenna-body spacing of 6 *mm* was used as for the case of Zyggie sensor. This spacing causes slight frequency shift (≈65 MHz) towards lower frequency end resulting in an $|S_{11}|$ of -8.5 dB at 2.4 GHz. This is a normal phenomenon for body-centric applications due to high conductivity of the body. e.g., $|S_{11}|$ of -7 dB was reported in [10] for on-body channel measurements at 2.45 GHz for antenna-body spacing of 7–10 *mm* (including the clothing). The matching can be

improved further with spacing. e.g., antenna-body spacing of 30 *mm* was used in body-centric channel measurements in [11] to maintain the 10-dB matching on body ($|S_{11}|$ < -10 dB) within ISM 2.4 GHz bandwidth. However, such large spacings are also not very realistic considerations for body-centric applications. Also as evident from Fig. 2.8, the body tissue significantly attenuates the radiation in the back direction which is indeed due to the high values of tissue parameters mainly the conductivity σ at ISM frequencies e.g., the attenuation constant α = 4.32 dB/cm @ 2.40 GHz for equivalent phantom tissue parameters (i.e., ε_r = 51.95, σ = 1.89 S/m) [3].

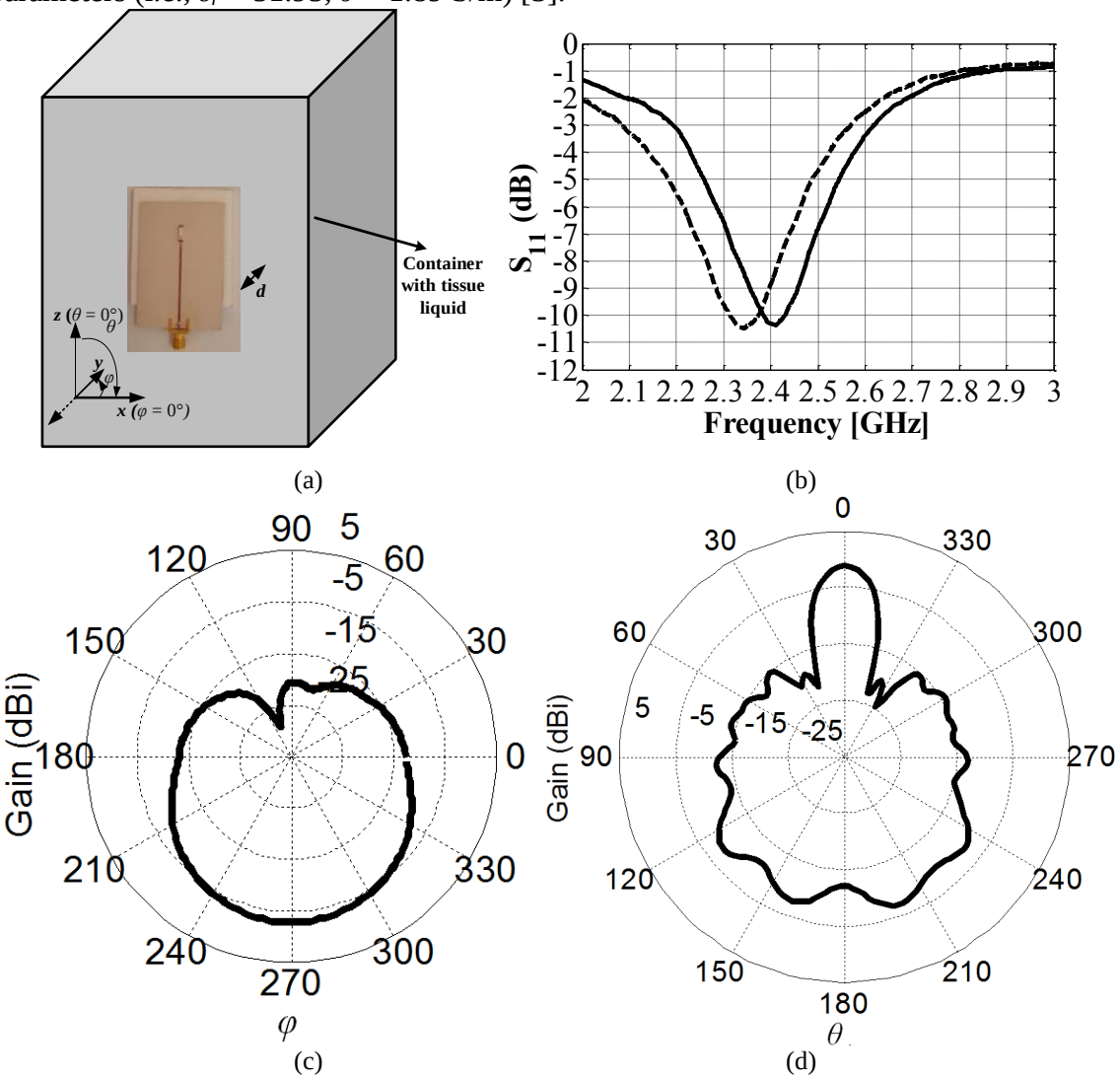

Figure 2.8. (a) Placement of chip antenna on liquid tissue phantom (b) Measured reflection coefficient of the antenna in free space (——) and on liquid tissue (– – –) (c, d) Measured radiation pattern in (c) *xy*-plane and (d) *xz*-plane at 2.40 GHz on liquid tissue.

2.4. Off-body diversity channel measurements

2.4.1. Introduction

Radio channel is an important metric to characterize WBASN performance. WBASN channel undergoes fading as a typical wireless channel. However, the radio channel in this case is prone to more severe effects because of proximity to human body which has high permittivity and conductivity. To cope with such fading, diversity can be a powerful tool [4]. The principle behind diversity is to exploit more than one independent and uncorrelated radio channels in a multipath radio environment. Diversity can be achieved in numerous ways (time or frequency domain) and by using multiple antennas known as antenna diversity. Antenna diversity can be achieved by using multiple antennas either at transmitter (Multiple-input, single-output (MISO)), receiver (Single-input, multiple output (SIMO)) or both transmitter and receiver (Multiple-input, multiple-output (MIMO)). It can be further classified as space diversity, pattern (angle) diversity and polarization diversity.

The use of antenna diversity increases the number of exploitable signal paths and hence, can offer improvement in perspective of signal-to-noise ratio (SNR), channel capacity etc. without increasing the signal bandwidth. Apart from that, antenna diversity can provide reasonable amount of diversity gain resulting in less transmit power, which is the key requirement of current smart and low power WBASNs. The signals from the various diversity branches can finally be combined to achieve improved SNR using various diversity combining techniques such as Selection Combining (SC), Switched Combining (SwC), Equal Gain Combining (EGC), and Maximal Ratio Combining (MRC) [4].

Measurement results for on-body antenna diversity were reported in [12] for an indoor environment at 2.45 GHz using monopole antennas. The reported diversity gain showed that diversity can offer improvement for on-body radio channels. On-body diversity performance was also investigated in [13] using monopoles and inverted-F antennas. Diversity reception techniques were reported in [14] for off-body channels using multiple-antenna wearable system at 868 MHz. A statistical power delay profile model for the evaluation and design of UWB off-body communication systems was reported in [15] using Skycross® omnidirectional antennas. Measurement results for diversity were also reported in [16] for on/off-body applications using tapered slot antennas and it was shown that 50% improvement in diversity gain was achieved for off-body case than on-body counterpart making UWB off-body channel better candidate for diversity consideration.

However, most of the measurement campaigns reported in the above citations used physically large-sized antennas (with reference to the operating wavelength λ_0), whereas there is a currently growing scope of low power and miniaturized sensors for medical and other smart applications of WBASNs. Antenna size is an important factor to control size of sensors especially in the lower GHz frequency range (e.g., λ_0= 125 *mm* @ 2.40 GHz). Therefore, in this section, off-body channel measurements are presented using the

miniaturized chip antennas of Zyggie sensors (as described in Section 2.2) which are mounted under pattern diversity configuration. The chip antennas have dimensions of 7×2×1.20 mm^3 which correspond to a physical length of $\lambda_0/18$ only (@ 2.40 GHz). Measurements were taken in a cluttered indoor laboratory environment containing various equipment such as tables, chairs, computers etc. thus providing a realistic multipath environment. Both line-of-sight (LoS) and non-line-of-sight (NLoS) scenarios were investigated. The subject considered for measurements was a healthy male with a height of 178 *cm* and a weight of 163 pounds.

2.4.2. Measurement set up

Measurements were taken using two identical multi-layer Zyggie sensors each having two miniaturized LTCC chip antennas (monopoles) radiating in ISM 2.4 GHz band. The sensor board and pattern diversity configuration has been shown in Fig. 2.2. Each antenna compensates for radiation null of the other in the elevation plane (φ = 0°), hence providing an overall pattern diversity by null-zone elimination (e.g., Fig. 2.3 (c), (d), Fig. 2.4 (a)).

One sensor board was deployed on body (chest) of a human subject as a transmitter (Tx) and the other one on a free space phantom (ε_r = 1) for alignment and orientation purpose as a receiver (Rx) at a distance *d* from Tx as shown in Fig. 2.9. The distance was also varied from 0.5-2 meter to study the variability of channel results. The receiver in free space was used to model the fixed access point in a BAN context which can be for example, a workstation or BAN coordinator in free space. The antennas were switched for measurement using the built-in RF switch on Zyggie sensor powered by 3.0 Volts DC power supply. Moreover, antenna-body spacing of 6 *mm* was always maintained whenever the sensor was used on the human body (Tx) using foam-pad spacer (ε_r = 1) to avoid detuning of antennas due to high permittivity influence of the body. Low loss cables (max. $|\hat{S}_{21}|$ < 2 dB for 2-3 GHz) having length of 3.0 meter and characteristic impedance of 50 Ω were used between the front-end of sensors and an Agilent VNA for measurements.

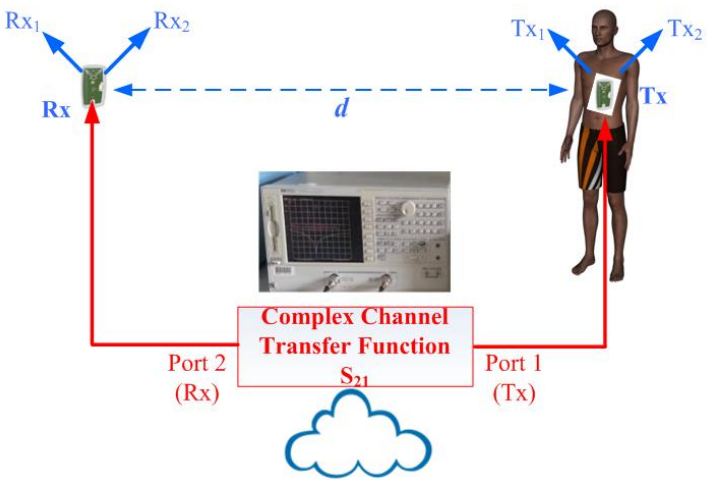

Figure 2.9. Measurement setup. +45° orientation was considered for antennas Tx_2 and Rx_2 and -45° orientation for Tx_1 and Rx_1.

In order to eliminate cable response from channel measurements, a full 2-port calibration was performed including the coaxial cables i.e., the calibration plane was considered at the interfaces of long coaxial cables instead of the direct interfaces of VNA to eliminate the cable response from measured channel transmission coefficients. The calibration of the instrument was also verified connecting the two ports of VNA directly through the two long coaxial cables used for measurements. A maximum calibration error of 0.05 dB only was observed in the frequency band 2-3 GHz. Static measurement scenarios were considered with standing human subject for each snapshot corresponding to sample distances. The measurements were repeatable for fixed posture and same distance d as long as the body was fully static during each measurement sweep (apart from involuntary breathing movements caused by the human chest).

The VNA was tuned in channel transfer function mode from 2-3 GHz to record the complex channel transfer function. A VNA transmit power of 0 dBm was used throughout the measurements which complies with the maximum permissible transmitted power limit for WBASN applications [17]. A total number of 1601 points were recorded for each frequency sweep from 2-3 GHz to have enough points for averaging for both LoS and NLoS scenarios corresponding to various distances d. Each measured response S_{ij}, $(i, j) \in \{1, 2\}^2$ contains the complex channel coefficients in the form of real and imaginary parts. The resultant data was stored for off-line post-processing with MATLAB® using a GPIB™ interface.

2.4.3. Power delay profile and delay spread

For extracting time domain statistics from complex channel transfer function (CTF), a MIMO channel was first constructed using the four measured sub-channel transmission coefficients i.e., S_{ij}, $(i, j) \in \{1, 2\}^2$ and the impulse response of MIMO channel was then computed by taking Inverse Fast Fourier Transform (IFFT) of CTF using MATLAB®. The power delay profile (PDP) P_h $(0, \tau)$ which indicates the strength of multipath components versus delay (time) was then found by taking the spatial average of the baseband impulse response [18] of all the four sub-channels i.e., Tx_iRx_j, $(i, j) \in \{1, 2\}^2$ for all frequency points (1601) between 2-3 GHz and shown in Fig. 2.10. Hence each sample point in Fig. 2.10 corresponds to the average PDP of the four sub-channels Tx_iRx_j, $(i, j) \in \{1, 2\}^2$ for fixed distance d.

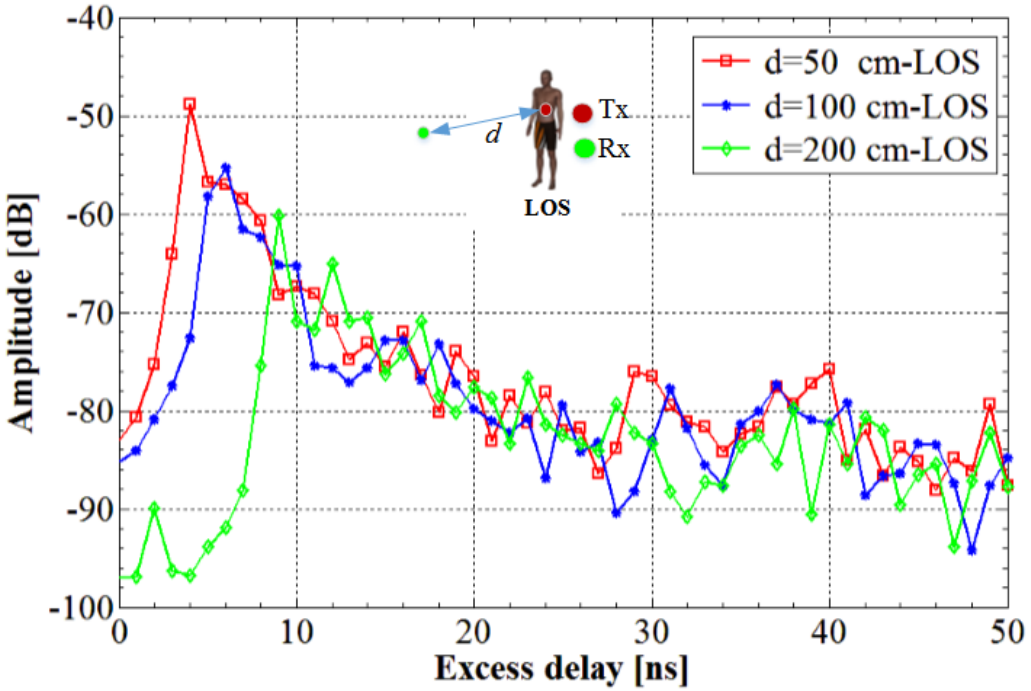

(a)

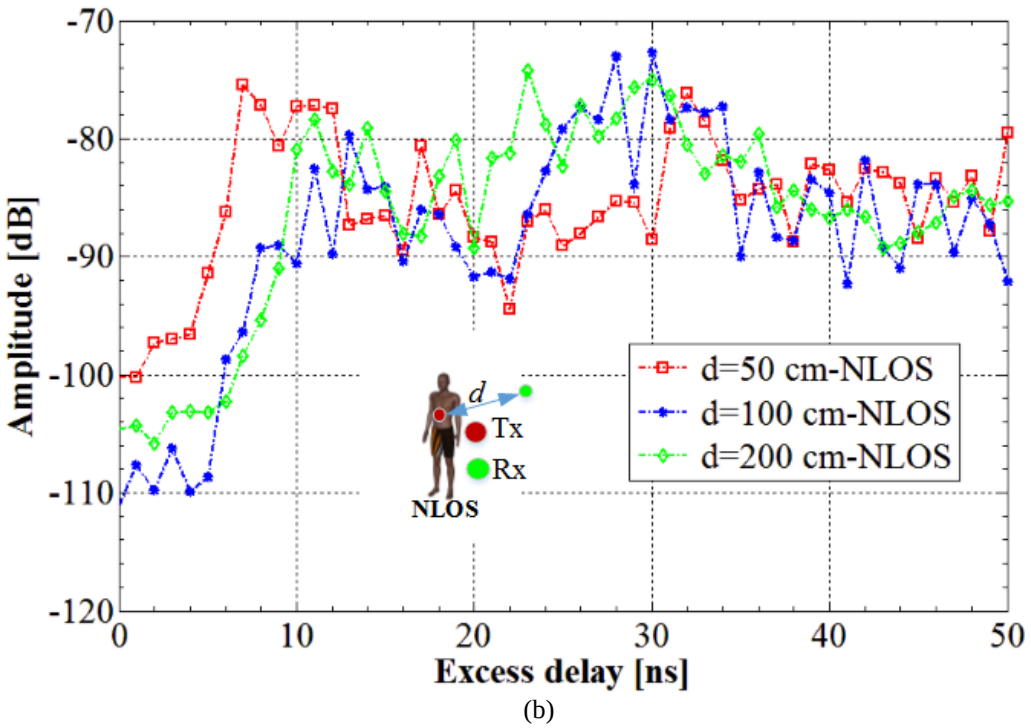

(b)

Figure 2.10. Average PDP of the channel computed from CTF for (a) LoS and (b) NLoS. Rx lies on free space phantom in all scenarios and Tx on-body.

The PDP shows the arrival of the direct signal component followed by the multipath components for each distance for LoS (Fig. 2.10 (a)). Moreover, for LoS scenarios it can be seen that there is the direct ray followed by the multipath rays (after delay) where the arrival of direct paths can be verified by distance formula i.e., $\Delta\tau \times c \approx \mathrm{d}$ considering the speed of electromagnetic radiation c in free space i.e., 2.998×10^8 *m/s*. Also, the amplitude of the direct component falls with increasing distance. For NLoS scenarios, Tx-Rx link was masked fully by the body as shown in the inset of Fig. 2.10 (b), hence resulting in very weak direct path (<-75 dB max.) due to the high attenuation of human tissue at microwave frequencies e.g., the attenuation constant α = 4.32 dB/cm @ 2.40 GHz for equivalent muscle tissue parameters (i.e., ε_r = 51.95, σ = 1.89 S/m) [3]. This implies that in NLoS scenarios, there is mainly the multipath propagation between Tx-Rx nodes.

The averaged PDP was then used to compute RMS delay spread (τ_{rms}) which gives the delay of multipath components, weighted proportional to their energy and hence, indicates the multipath richness of the channel. τ_{rms} was calculated from PDP as given by 2.1 [19].

$$\tau_{rms} = \sqrt{\frac{\int_{-\infty}^{\infty} (\tau - \tau_m)^2 P_h(0,\tau)\,\mathrm{d}\tau}{\int_{-\infty}^{\infty} P_h(0,\tau)\,\mathrm{d}\tau}} \tag{2.1}$$

$$\tau_m = \sqrt{\frac{\int_{-\infty}^{\infty} \tau P_h(0,\tau)\,\mathrm{d}\tau}{\int_{-\infty}^{\infty} P_h(0,\tau)\,\mathrm{d}\tau}} \tag{2.2}$$

where $P_h(0, \tau)$ corresponds to the PDP. The τ_{rms} obtained by the averaged PDP is listed in Table 2.1. The computed τ_{rms} lies within the typical range of delay spread for wireless indoor channels for both LoS and NLoS [18].

TABLE 2.1. RMS DELAY SPREAD

Scenario	τ_{rms} **(ns)**		
	d = 50 cm	***d = 100 cm***	***d = 200 cm***
LoS	7.7	13.6	21
NLoS	45.3	41	39.6

2.4.4. Radio channel capacity

The ergodic MIMO channel capacity C (bits/sec/Hz) was also computed constructing a 2x2 MIMO channel matrix H using the measured complex sub-channel transfer gains h_{ij}, $(i, j) \in \{1, 2\}^2$ [20]. It was assumed that the Channel State Information (CSI) is not

available at the Tx (i.e., channel is completely unknown at Tx) and that the transmitted power is uniformly distributed among the *M* (=2) transmitting antennas.

In the absence of CSI at the Tx, the channel capacity *C* (bits/sec/Hz) can be expressed by (2.3) assuming transmitted power to be uniformly distributed among the M transmitting antennas [20] i.e.,

$$C(\xi) = \log_2 \left[\det \left(I_N + \frac{\xi}{M} \mathbf{H}\mathbf{H}^* \right) \right] \tag{2.3}$$

where ξ is the average SNR per receive antenna, I_N is the $N \times N$ identity matrix, H is the normalized channel matrix and H^* is its complex conjugate transpose (Hermitian). The H matrix is comprised of measured complex sub-channel transfer gains h_{ij}, $(i, j) \in \{1, 2\}^2$ where i is the Tx index and j is the Rx index [20] i.e.,

$$H = \begin{bmatrix} h_{11} & h_{12} \\ h_{21} & h_{22} \end{bmatrix} \tag{2.4}$$

The MIMO channel matrix *H* was normalized using the Frobenius norm in order to remove the influence of power variations resulting from the path loss on the capacity computation [20]. Thereafter, only the randomness of the multipath channel on capacity is of interest. Such a normalization technique works for a 2x2 MIMO system [20]. In an ideal channel model, the MIMO sub-channels are assumed to be independent and identically distributed (i.i.d) with Rayleigh distribution of the envelopes and perfectly uncorrelated [20]. Therefore, The resulting MIMO channel capacity for the measured configuration was compared to that of the ideal channel model with i.i.d Rayleigh and perfectly uncorrelated sub-channels.

The ergodic equal power capacity for the measured channel matrix H computed by (2.3) using MATLAB® for both LoS and NLoS configurations is shown in Fig. 2.11 compared to that of 1x1 (SISO) and 2x2 (MIMO) i.i.d Rayleigh channels. The ergodic capacity for measured data was found by taking the average of resultant capacity matrix for each of the samples in the ISM frequency band (2.40-2.48 GHz). The i.i.d Rayleigh channel data was generated by MATLAB® using zero-mean, unit-variance complex Gaussian random variables.

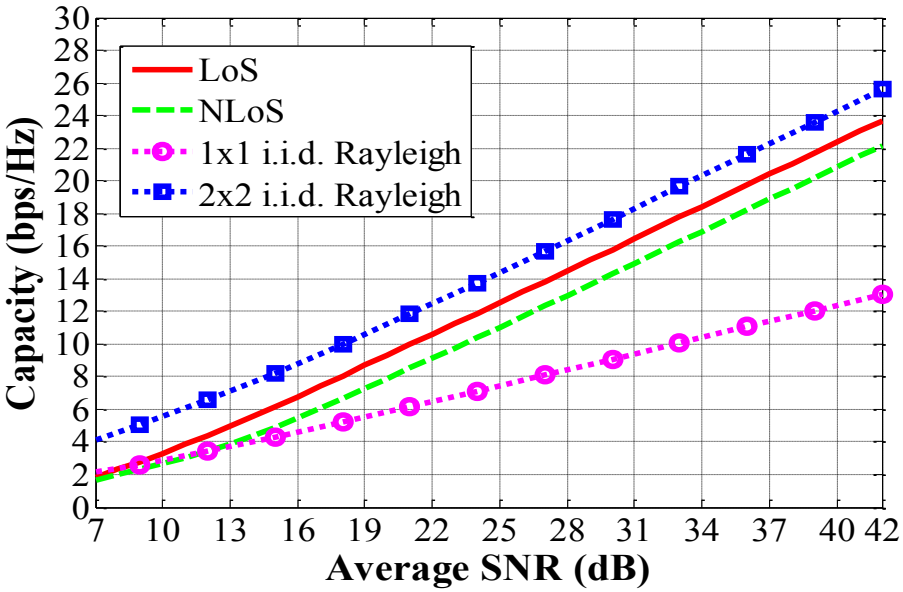

Figure 2.11. Average capacity versus SNR for measurement.

As depicted in Fig. 2.11, the proposed diversity scheme can offer improved capacity compared to SISO scheme for both LoS and NLoS configurations, especially at higher SNRs. It is known that in high SNR regime, the increase in capacity per 3 dB rise in SNR for an independent MIMO system is *min* (*M*, *N*) bps/Hz [21] where $M = N = 2$ for our case. It is also evident from Fig. 2.11 that the average capacity increase per 3 dB rise in SNR for our system is close to 2 bps/Hz (= min. (*M*, *N*)). Moreover, the capacity for NLoS scenario is also not too low comparable to that of LoS due to the fact that NLoS has lower correlation than LoS [20].

2.4.5. Conclusion

In Section 2.4, off-body channel measurements are presented exploiting chip antenna diversity in multipath indoor environment. Time domain statistics were discussed in the form of PDP resulting in typical values of τ_{rms} as for wireless indoor channel for both LoS and NLoS configurations. τ_{rms} is an important metric to limit data-rate to avoid inter-symbol interference (ISI) for multipath channels. The transmit symbol duration should be kept large enough compared to the reported τ_{rms} (typically a factor of 10 suffices), to have zero ISI without the use of an equalizer. Ergodic channel capacity was also computed from measured data assuming zero CSI at the transmitter. Results were compared with ideal i.i.d. Rayleigh SISO and 2x2 MIMO channels and it was observed that the proposed miniaturized chip antenna configuration can offer improved capacity compared to the SISO systems especially at higher SNRs. The results also prove the suitability of miniaturized chip antennas for today's smart and low power WBASNs.

2.5. Distribution fitting for WBASN channel fading

2.5.1. Introduction

In order to meet the challenges of link reliability, data transfer, and other services, reliable knowledge of channel model is crucial for system-level modeling. This requires accurate knowledge of the BAN propagation channel in order to understand the essential characteristics of the propagation in real-time multipath environments. Various models exist for on-body communications. e.g., A model for the received signal strength versus angle around the body was proposed in [22] using the finite-difference time-domain (FDTD) method for narrowband on-body channels. A more complete narrowband on-body statistical model was introduced in [23] by considering also the influence of the surrounding environment. Statistical analysis for off-body channel was reported in [24] for UWB off-body communication in two different environments (anechoic chamber and indoor), and it was proposed that the path loss is best modeled by a Normal distribution. Statistical model for UWB off-body channel was studied in [25] for 3.5-6.5 GHz frequency band in a corridor and office environment. It was suggested that the small scale channel variations of the received signal strength follow a Normal distribution. Experimental characterization of UWB off-body channels was investigated for indoor environment in [26], and a Lognormal distribution was proposed as the best fit for modeling the path loss.

A characterization of the dynamic narrowband off-body area channel was proposed in [27] based on time-domain channel measurements at 820 MHz and 2.36 GHz for two cases when the subject is standing and walking. It was proposed using Akaike-Information Criterion (AIC) [28] that the Lognormal distribution provides a good fitting model for most of the investigated scenarios. Moreover AIC [28] was also used in [29]-[30] to determine the optimum BAN channel model. Bayesian Information Criterion (BIC) (equivalent to the MDL (Minimum Description Length) criterion) [31] was used in [32] for the best model selection. However, for WBASNs with multi-link measurements, both AIC and BIC approaches (and thus also MDL) suffer from the limitation that they only provide a relative ordering of the attempted models [17] without an actual insight into the inherent distribution of the empirical model i.e., such methods can be used as a relative measure only by selection of the model with the optimum (lowest) AIC/BIC/MDL scores which correspond to minimum loss of information. Moreover, such methods could also lead to erroneous or misleading results in case of exceptional scenarios where for example, the empirical data under test does not follow indeed any of the attempted distributions uniquely or moreover, is not of a pure distribution type but is a mixed one instead. In these cases, use of these criteria as AIC, BIC, and MDL can be dubious, hence leading to misleading channel models having still ended up to some model with optimum (minimum) AIC/BIC/MDL scores.

Moreover, the previous studies discussed above do not refer to a systematic approach for the selection of the best-fit channel model in real-time scenarios where the distribution of the empirical data can fit very close to more than one standard distributions, making the selection of the best-fit a very cautious task. To meet these

challenges, we proposed and implemented a robust algorithm in MATLAB^{TM} to find the best-fit distribution model along with the estimated parameters for empirical radio channel data. The proposed algorithm can even detect the exceptional cases where the traditional relative score based criteria fail (e.g., AIC, BIC, MDL). The algorithm is well validated by using standard empirical data in MATLAB^{TM} and is found to be in excellent agreement with analytical data.

2.5.2. Proposed Fitting Algorithm

The main objective of the proposed algorithm is to determine the best-fit distribution model for empirical radio channel data along with the estimated parameters of the best-fit model. The fitting is attempted against seven standard distributions (termed as competent distributions here) commonly used to statistically describe fading i.e., Normal (*N*), Lognormal (*LG*), Rayleigh (*R*), Weibull (*W*), Gamma (*G*), Exponential (*E*) and Nakagami-*m* (*NG*) (which can also approximate Rician distribution [27]). The proposed algorithm is principally based on method of Maximum Likelihood Estimation (MLE) to find the optimum fitting of each attempted distribution type against standard empirical data and further using the Kolmogorov-Smirnov (K-S) test of statistics to detect the best-fit. In simple words, the mechanism of the algorithm is principally based on the merit of finding how close we can get to the empirical distribution using standard cumulative distribution functions (CDFs) and further the best-fit selection relies on choosing the CDF fitting closest to the empirical one using the K-S test. Since K-S test is sensitive to both location and shape of the empirical CDF, the algorithm correctly detects even the exceptional cases of mixed or non-unique empirical distribution types where the traditional approaches of relative score measures such as AIC, BIC and MDL fail. This is possible indeed by utilizing the significance level α (or confidence level (1-α)) in K-S testing and indicating a failure for all the competent distributions in case where none of the competent distributions lies close enough to the empirical CDF against assumed confidence level (95%). The block diagram of the proposed algorithm is represented in Fig. 2.12.

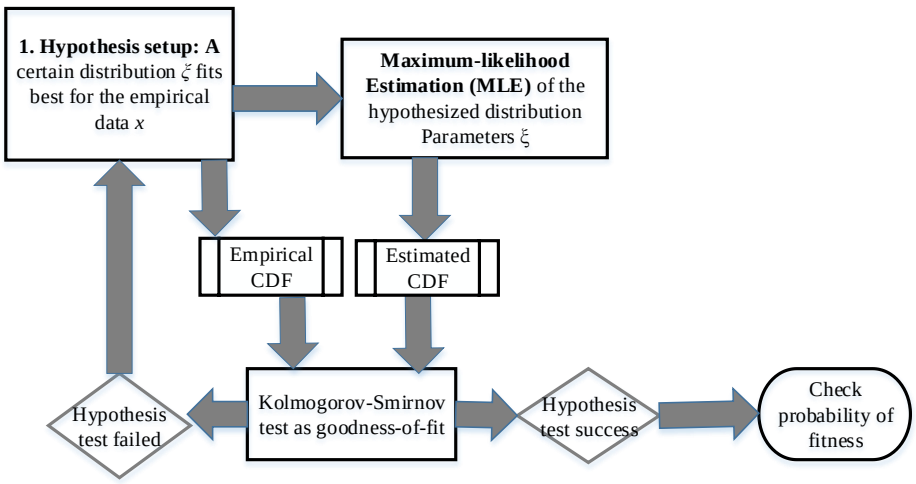

Figure 2.12. Proposed fitting algorithm for statistical study of empirical data.

MLE estimates the parameters of a statistical model (e.g., ζ) by taking the model parameters and finding particular parameter values that make the observed results (e.g., x) the most probable ones [33], i.e.,

$$L(\zeta \mid \mathrm{x}) = \frac{1}{n}\sum_{i=1}^{n} \ln\, f(xi \mid \zeta) \tag{2.5}$$

For comparison, the Probability Density Functions (PDFs) of all the attempted distributions i.e., *N*, *LG*, *R*, *W*, *G*, *E* and *NG* were constructed by using formulae (2.6)-(2.12) respectively [33] considering that the empirical random data x in each case is non-negative normalized i.e., $0 \le x \le 1$.

$$f(x \mid \mu, \sigma) = \frac{1}{\sigma\sqrt{2\pi}} e^{-\left[\frac{(x-\mu)^2}{2\sigma^2}\right]} \quad \text{(Normal)} \tag{2.6}$$

$$f(x \mid \mu, \sigma) = \frac{1}{x\sigma\sqrt{2\pi}} e^{-\left[\frac{\{\ln(x)-\mu\}^2}{2\sigma^2}\right]} \quad \text{(Lognormal)} \tag{2.7}$$

$$f(x \mid \xi) = \frac{x}{\xi^2} e^{-\left(\frac{x^2}{2\xi^2}\right)} \quad \text{(Rayleigh)} \tag{2.8}$$

$$f(x \mid \eta, \beta) = \frac{\beta x^{\beta-1}}{\eta^{\beta}} e^{-\left(\frac{x}{\eta}\right)^{\beta}} \quad \text{(Weibull)} \tag{2.9}$$

$$f(x \mid b, c) = \frac{x^{c-1} e^{-\frac{x}{b}}}{b^c \Gamma(c)} \quad \text{(Gamma)} \tag{2.10}$$

$$f(x \mid \lambda) = \frac{1}{\lambda} e^{-\frac{x}{\lambda}} \quad \text{(Exponential)} \tag{2.11}$$

$$f(x \mid m, \omega) = \frac{2m^m}{\Gamma(m)} \frac{x^{2m-1}}{\omega^m} e^{-\left(\frac{mx^2}{\omega}\right)} \quad \text{(Nakagami-}m\text{)} \tag{2.12}$$

where μ corresponds to the mean and σ is the standard deviation for both (2.6) and (2.7), and *ln*(.) is the natural logarithm in (2.7). In (2.8), ξ corresponds to the scale parameter of Rayleigh distribution, whereas for (2.9), η is the scale parameter and β corresponds to the shape parameter of Weibull distribution. In (2.10), b is the scale parameter, c is the shape parameter of Gamma distribution, and $\Gamma(.)$ is the Gamma function. In (2.11), λ corresponds to the scale parameter of Exponential distribution and last but not least, m is the shape parameter and ω is the scale parameter of Nakagami-*m* distribution in (2.12).

Likewise for K-S hypothesis testing, the CDFs of the competent distributions i.e., *N*, *LG*, *R*, *W*, *G*, *E* and *NG* were constructed using the following formulae (2.13)-(2.19) respectively [33], [34], [35] i.e.,

$$F(x\,|\,\mu,\sigma)=\frac{1}{\sigma\sqrt{2\pi}}\int_{-\infty}^{x} e^{-\left[\frac{(t-\mu)^2}{2\sigma^2}\right]}dt \qquad \text{(Normal)} \qquad (2.13)$$

$$F(x\,|\,\mu,\sigma)=\frac{1}{\sigma\sqrt{2\pi}}\int_{0}^{x} \frac{e^{-\left[\frac{\{\ln(t)-\mu\}^2}{2\sigma^2}\right]}}{t}dt \qquad \text{(Lognormal)} \qquad (2.14)$$

$$F(x\,|\,\xi)=\ 1\text{-}e^{-\left(\frac{x^2}{2\xi^2}\right)} \qquad \text{(Rayleigh)} \qquad (2.15)$$

$$F(x\,|\,\eta,\beta)=\ 1\text{-}\mathrm{e}^{-\left(\frac{x}{\eta}\right)^{\beta}} \qquad \text{(Weibull)} \qquad (2.16)$$

$$F(x\,|\,b,c)=\frac{1}{c^{b}\Gamma(b)}\int_{0}^{x} t^{b-1}e^{-\frac{t}{c}}dt \qquad \text{(Gamma)} \qquad (2.17)$$

$$F(x\,|\,\lambda)=\ 1\text{-}\mathrm{e}^{-\left(\frac{x}{\lambda}\right)} \qquad \text{(Exponential)} \qquad (2.18)$$

$$F(x\,|\,m,\omega)=\ \mathrm{P}\left(m,\frac{m}{\Omega}x^2\right) \qquad \text{(Nakagami-}m\text{)} \qquad (2.19)$$

where *P*(.) is the incomplete Gamma function in (2.19). The empirical CDF was constructed using (2.20) [36]

$$F(x)=\ \sum_{i=1}^{n}\frac{x_i\le t}{n} \qquad (2.20)$$

where x_i corresponds to the non-decreasing set of observations and *n* is the total number of observations. Once the CDFs are built using above equations, the K-S hypothesis testing is performed using empirical CDF and estimated CDFs as inputs. The K-S test statistic [37] is based on comparing the distance between the two CDFs i.e., empirical and estimated CDF given by

$$\xi=\ \max.\left\{\left|F(x)-G(x)\right|\right\} \qquad (2.21)$$

where $F(x)$ is the empirical CDF and $G(x)$ is the estimated CDF. The idea is to choose the distribution whose CDF fits closest to that of the empirical data based on the significance

level α. The K-S statistic ξ is further used to compute the p value (probability of fitness), thus creating the H matrix as described in [38] which is finally compared with the significance level α to either accept or reject the null hypothesis. α was chosen as 5 % which corresponds to a confidence level of 95 % (= (1-α) × 100). This is indicated by the output h of the algorithm. If h = 1, it implies that the test fails, hence rejecting the null hypothesis and indicating that the hypothesized distribution cannot be considered. However, when h = 0, the test fails to reject the null hypothesis, and hence the p value should be investigated. Finally, we set the criterion of choosing the distribution function with maximum score of p as the optimum fitting model for our empirical data. Such a distribution function will indeed be the one whose CDF fits closest to that of the empirical data and hence, will be the optimum choice for the model stochastically.

2.5.3. Theoretical validation and accuracy

In order to validate the algorithm and to ensure that the algorithm detects the underlying distribution of the data correctly, standard random data was generated in MATLAB for all the competent distributions using pseudorandom data generators which was further used as input to the algorithm. Moreover, in order to investigate the stochastic performance and stability of the algorithm, the random number generator was shuffled 1000 times (i.e., 1000 experiments with standard data). Also the data was normalized properly for each case before analysis.

For validation of algorithm with Normal distribution, standard Normal random generator in MATLAB (randn()) was used which actually generates random data following the standard normal distribution as given by (2.6) with μ = 0 and σ =1. The Normal distribution with mean μ and variance σ^2 was then generated by (2.22)

$$X = \mu + \sigma X' \tag{2.22}$$

where X' is the standard normal deviate i.e., $X' \sim N(0, 1)$ generated by the standard Normal random number generator and hence, $X \sim N(\mu, \sigma^2)$. A mean value (μ) of 4 and standard deviation (σ) of 1 was considered for graphical simplicity for comparison later. The random samples were accumulated in a vector which was further used as input to the algorithm. To study the convergence and stability, the process was repeated for 1000 trails. The resulting p values for 1000 sample runs of the algorithm are shown in Fig. 2.13 for only those distributions which qualified the test during each of the 1000 successive runs (i.e., h = 0). This implies that for remaining competent distributions, K-S test failed i.e., h = 1 and hence, p = 0. As evident from Fig. 2.13, the algorithm always correctly detects the default Normal distribution of the data, based on the criterion of maximum p value. The mean and standard deviation computed during first 50 runs of the algorithm (out of 1000 for brevity purpose) are also shown in Fig. 2.14. The mean and standard deviation of the data are also correctly estimated with an average value of 4.000 and 0.999 for μ and σ respectively for all the thousand trials. This demonstrates that the algorithm correctly detects the inherent distribution of the empirical data each time along

with the associated distribution parameters with minimal error in case when the underlying distribution of the empirical data is a Normal one.

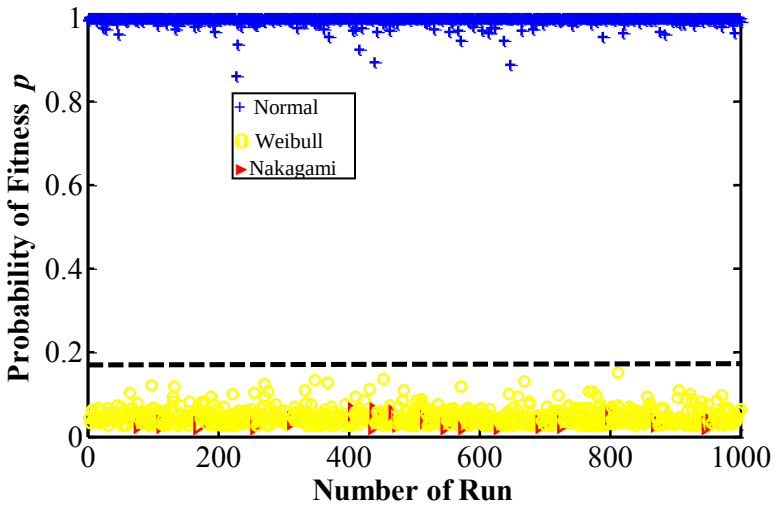

Figure 2.13. Validation of fitting-algorithm for statistical study of standard Normal random data for 1000 sample runs of algorithm shuffling random generator each time.

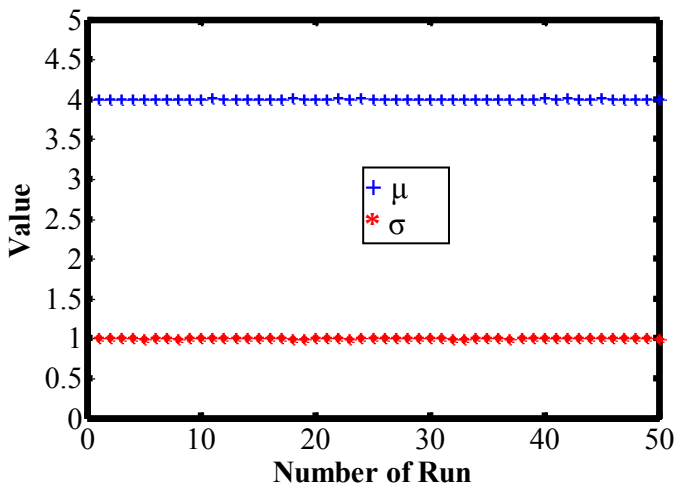

Figure 2.14. Mean (μ) and standard deviation (σ) of attempted Normal random data for first 50 sample runs of algorithm shown in Fig. 2.13

The working principle of the algorithm is explained here with the help of one sample run of the algorithm where the CDFs and PDFs corresponding to the attempted fittings are shown in Fig. 2.15. Both the axes of the data were normalized properly i.e., the amplitude (x-axis) was normalized with respect to the absolute maximum value and the data frequency (y-axis) was normalized such that the total area under the PDFs is unity. The resulting test statistics given by the algorithm are shown in Table 2.2. As evident from the CDFs, the empirical data fits closest to the Normal CDF which is correctly detected by the algorithm also resulting in a h value of 0 and a p value of 0.992 in Table 2.2. Moreover, the test disqualifies the possibility of all other distribution functions as

indicated by h =1. This validates the reliable working of the proposed algorithm for real-time measured channel data when the underlying distribution is a Normal one. Each point (abscissa and ordinate) in Fig. 2.13 and Fig. 2.14 indeed corresponds to the curve fitting as shown in Fig. 2.15 and selection of the best-fit based on the maximum p value criterion (Table 2.2).

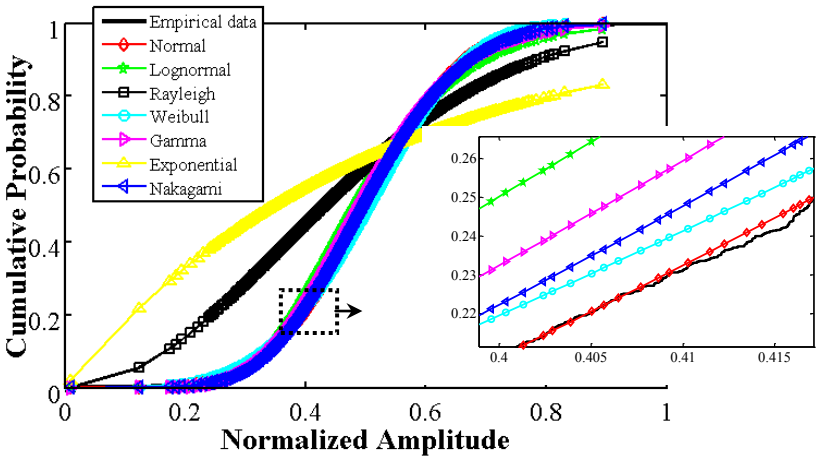

(a)

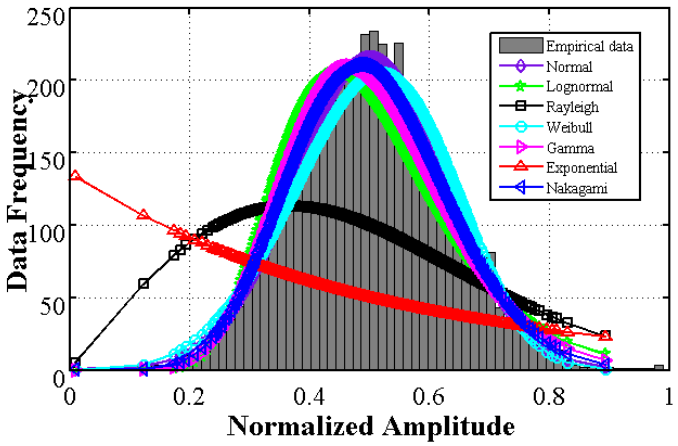

(b)

Figure 2.15. (a) CDF and (b) PDF of empirical (simulated) Normal data ~ $N(4, 1)$ against competent distributions.

TABLE 2.2. RESULTS OF CHANNEL STATISTICS FOR SIMULATED NORMAL DATA ~ $N(4, 1)$

Distribution	KS test statistic		Estimated parameters	
	h	p	μ	σ
N	0	0.992		
LG	1	0		
R	1	0		
W	1	0	4.0017	1.0055
G	1	0		
E	1	0		
NG	1	0		

Likewise, the performance of the algorithm was validated for all the competent distributions using standard random data generators in MATLAB and was found be in excellent agreement with the theory in each case. The performance of the algorithm corresponding to some of the other competent distributions can be found in Appendix A. This validates the performance of the fitting-algorithm on real-time empirical data also where the underlying experimental distribution will be unknown.

2.5.4. Fitting statistical study for off-body channels

The fitting algorithm presented in Sections 2.5.2 and 2.5.3 was further applied to real-time off-body channel measurements for statistical study. The objective was to find the best-fit model for small-scale, first-order fading for quasi-static LoS and NLoS scenarios in an off-BAN perspective. The Zyggie sensors as presented in Section 2.2 were used again here as Tx and Rx for channel measurements.

Experimental Setup

In order to investigate the off-body channel, one Zyggie sensor (Tx) was strapped to the centre of the chest of a human subject (antenna-body spacing ~ 6 *mm*) and another Zyggie sensor (Rx) was deployed on a "free space" (foam) phantom (ε_r = 1) as shown in Fig. 2.16. This free space phantom was used to model an Access Point (AP) or a Base Station (BS) in an off-BAN context and also for alignment and orientation of Rx sensor. The resulting frequency domain channel statistics were recorded using an Agilent VNA. The human subject considered for measurement was a 177.8 *cm*/163 pounds healthy male who stood static throughout the measurement sweeps apart from the involuntary breathing movements caused by the chest, hence termed as quasi-static. Measurements were carried out for both LoS and quasi-NLoS (QNLoS) scenarios.

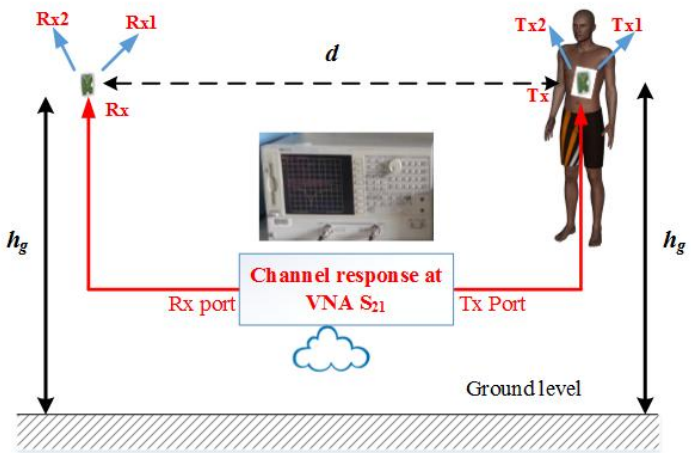

Figure 2.16. Off-body channel measurement setup (LoS).

For LoS, the subject faced in the direction of Tx, hence simulating a strong LoS component, whereas for QNLoS, the measurement subject masked the path between Tx-Rx, hence blocking the LoS propagation due to the exceptionally high attenuation caused by the human tissues at ISM frequencies [3]. Same height above the ground level h_g was maintained for both Tx and Rx sensors throughout the measurements. Equivalent measurement scenarios were also conducted by placing Tx sensor on a liquid phantom simulating human tissue properties at 2.4 GHz and having approximate dimensions comparable to that of human torso (i.e., 44×25×21 cm^3). Such phantom can be useful for a more robust statistical studies in future due to the possibility of recording arbitrarily large number of points for improved statistical accuracy. This is not possible with human subjects due to various constraints such as time and patience. The measurement setup for liquid phantom is shown in Fig. 2.17.

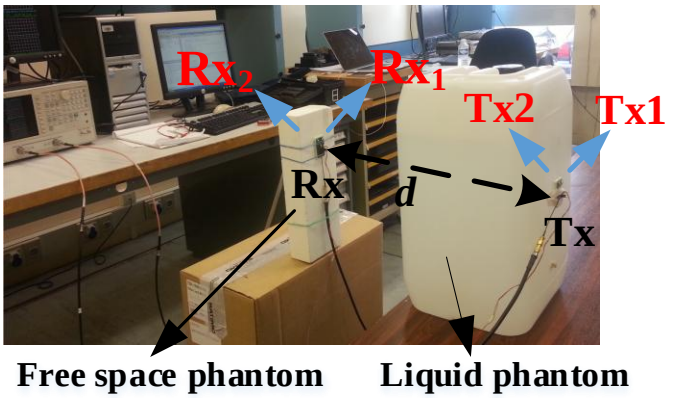

Figure 2.17. (a) Off-body channel measurement scenario (QNLoS) on a liquid phantom modeling human tissue properties at 2.4 GHz.

Low-loss 50-Ω cables (max. $|\hat{S}_{21}| < 2$ dB for 2-3 GHz) were used between the sensors front-end access ports and VNA inputs for channel measurements. In order to eliminate cable response from channel measurements, a full 2-port calibration was performed including the coaxial cables i.e., the calibration plane was considered at the interfaces of long coaxial cables instead of the direct interfaces of VNA to eliminate the cable response from measured channel transmission coefficients. The VNA was tuned in channel transfer function mode to record the complex channel transfer function at 2.40 GHz. A VNA transmit power of 0 dBm was used throughout the measurements which complies with the maximum permissible transmitted power limit for WBASN applications [17]. For statistical analysis, 1000 channel measurements were recorded for each of the scenarios corresponding to various sub-channels i.e., Tx_iRx_j, $(i, j) \in \{1, 2\}^2$ and also varying inter Tx-Rx distance to study the stability of channel model. A sweep time of 2.375 *msec* was used which was carefully chosen to be much lower than typical channel coherence time reported for off-body applications (e.g., [27] reports a typical value of 25 *msec* for off-BAN channel coherence time). The resultant data was stored for off-line processing with MATLAB™ using a GPIB™ interface. The experimental data generated by the measurement campaign was also used by BoWI project partners for numerical channel studies for the project demonstrator.

Results and Discussion

Before applying the algorithm for channel fitting studies, in order to have an idea of the noise margin, the relative strength of noise level was also measured in the laboratory environment at the time of measurement on both the human subject and liquid phantom. This was done by terminating the Tx port of VNA by 50 Ω and recording the statistics of random spare signal on the Rx which was situated either on the chest of human subject or on the liquid phantom at 2.40 GHz to gather the amplitude statistics. Same positioning of Rx sensor was used for each case as used in the channel measurement scenarios later. The normalized histogram for both the measured scenarios on human subject and liquid phantom is shown in Fig. 2.18. Data frequency corresponds to the number of occurrences for various bins of measured data. Bin size was chosen as $\sqrt{N}$ where N is the number of measurement samples. The mean (μ') and variance (σ'^2) of the noise statistics on the human subject were found to be 8.98×10^{-5} and 2.36×10^{-9} and those on liquid phantom were found to be 9.46×10^{-5} and 2.71×10^{-9} respectively. This corresponds to a noise power of -79.8 dBm on human subject and -79.3 dBm on liquid phantom which are comparable. The received signal amplitude on Rx side was observed to be higher than the reported noise level.

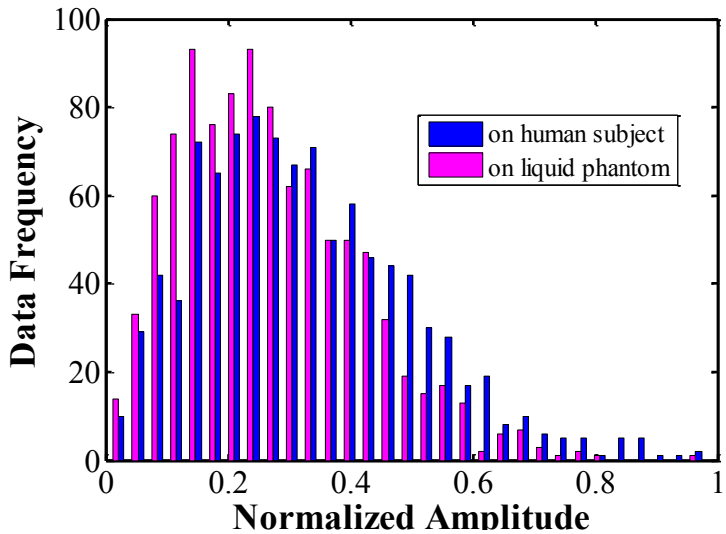

Figure 2.18. Normalized histogram of measured noise statistics (1000 recorded samples) on real human subject versus liquid tissue phantom at 2.4 GHz.

LoS scenarios

After above pre-processing, the measured data was then used for statistical study using the proposed fitting algorithm presented in Sections 2.5.2 and 2.5.3. The PDF and CDF of the empirical (measured) data for LoS off-body channel (Tx_2Rx_2) on human subject at 2.4 GHz and a Tx-Rx distance of 100 *cm* are represented in Fig. 2.19 along with those of the competent distributions. For the PDFs, both the axes of the data were normalized properly i.e., the amplitude (*x*-axis) was normalized with respect to the

absolute maximum value and the data frequency (*y*-axis) was normalized such that the total area under the PDFs is unity.

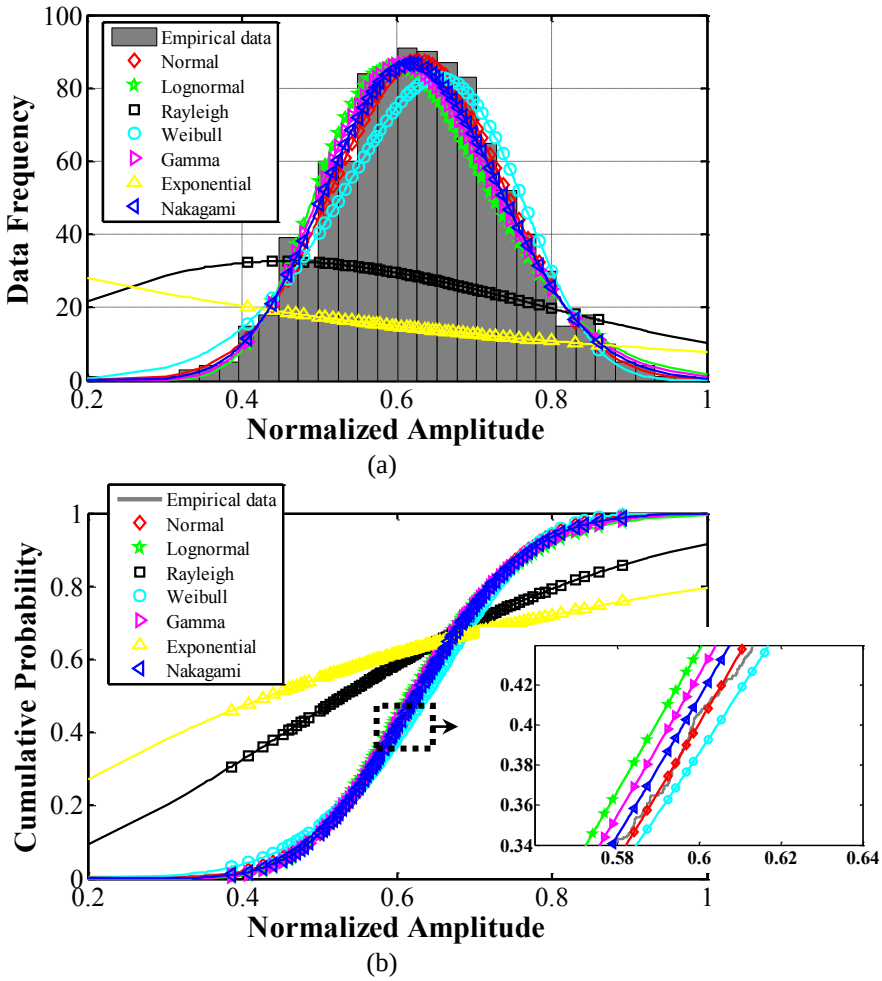

Figure 2.19. (a) PDF and (b) CDF of measured empirical data against fitted distributions for LoS off-body channel (Tx_2Rx_2) on human subject at 2.4 GHz (Tx-Rx distance of 100 *cm*).

As evident from the PDF and CDF plots (Fig. 2.19), the distribution types Normal, Lognormal, Weibull, Gamma and Nakagami-*m* fit very close to the empirical data making the selection of the best distribution a very tight constraint. However, Rayleigh and Exponential distribution clearly reject the possibility being located far away from empirical data. However, if we observe the CDF plots (Fig. 2.19 (b)), the Normal CDF seems to fit closest to the empirical CDF. The corresponding numerical data output by the fitting algorithm (along with various other measured scenarios) are provided in Table 2.3. As evident from Table 2.3 for corresponding channel dataset, the algorithm clearly rejects the possibility of Rayleigh and Exponential distributions (represented by indicator $h = 1$) and correctly detects the Normal distribution of the data as per the shortest distance K-S criterion (with maximum p value of 0.999 than all other qualified competent distributions i.e., *LG*, *W*, *G* and *NG*).

An example of fitting with statistical data from liquid phantom is discussed here. The PDF and CDF of the empirical (measured) data for LoS off-body channel (Tx_1Rx_1) on liquid tissue phantom at 2.4 GHz and a Tx-Rx distance of 100 cm are shown in Fig. 2.20 along with the corresponding PDFs and CDFs for the competent distributions estimated by the fitting algorithm. The corresponding test statistics output by the algorithm are also shown in Table 2.3. As evident from the CDFs (inset in Fig. 2.20 (b)), the empirical data fits closest to the Normal CDF (followed by Weibull CDF). This is correctly detected by the algorithm with a *p* value of 0.864 for Normal distribution (followed by 0.423 for Weibull distribution) in Table 2.3. The fitting study for LoS scenarios was verified by varying the sub-channels using the on-board antenna diversity and also inter Tx-Rx distance to study the variability of channel. All the corresponding numerical results are presented in Table 2.3.

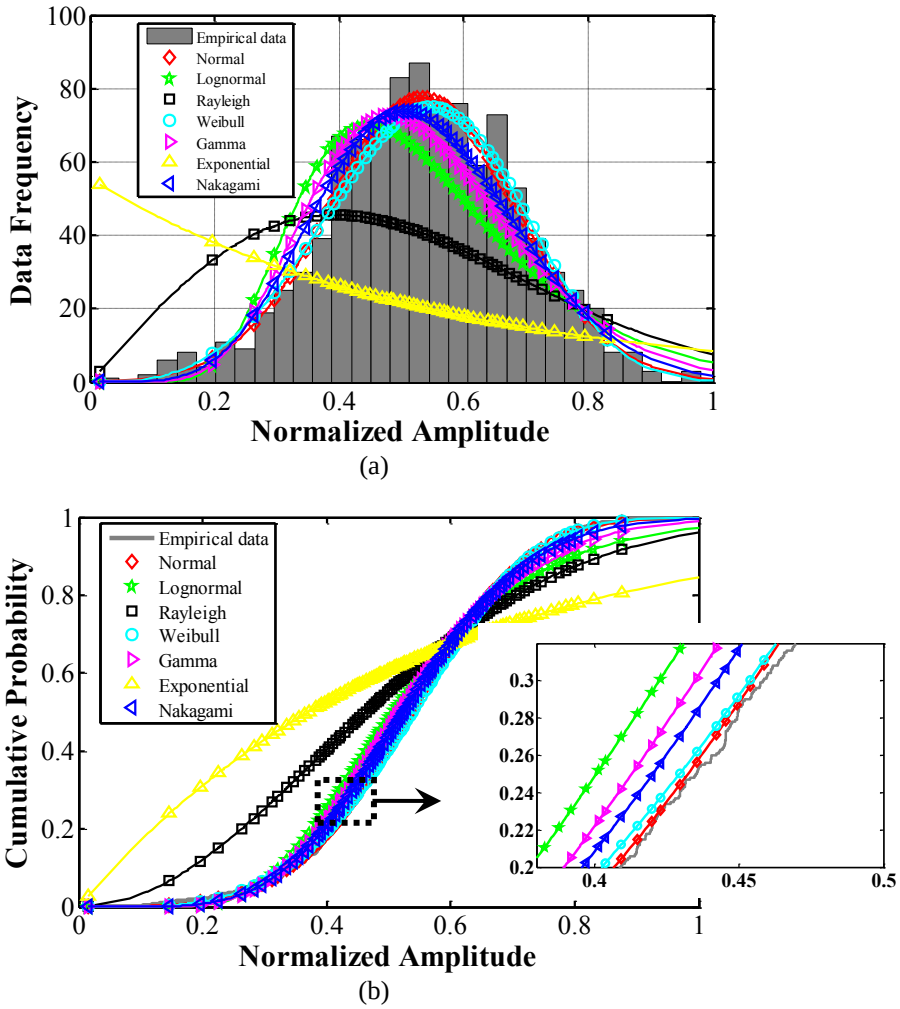

Figure 2.20. (a) PDF and (b) CDF of measured empirical data against fitted distributions for LoS off-body channel (Tx_1Rx_1) on liquid tissue phantom at 2.4 GHz and Tx-Rx distance of 100 *cm*.

QNLoS scenarios

For demonstrating fitting with QNLoS data, the off-body channel Tx_2Rx_2 is discussed here. The PDF and CDF of the empirical (measured) data for QNLoS on human subject at 2.4 GHz and a Tx-Rx distance *d* of 100 *cm* are shown in Fig. 2.21 compared to the estimated PDFs and CDFs respectively for the competent distributions using the fitting algorithm. The corresponding test statistics output by the algorithm are also shown in Table 2.3. As evident from the CDFs (inset in Fig. 2.21 (b)), the empirical CDF in this case fits closest to the Weibull CDF (followed by that of Nakagami-*m* distribution). This is correctly detected by the algorithm with a *p* value of 0.824 for Weibull distribution (followed by 0.78 for Nakagami-*m* distribution) in Table 2.3.

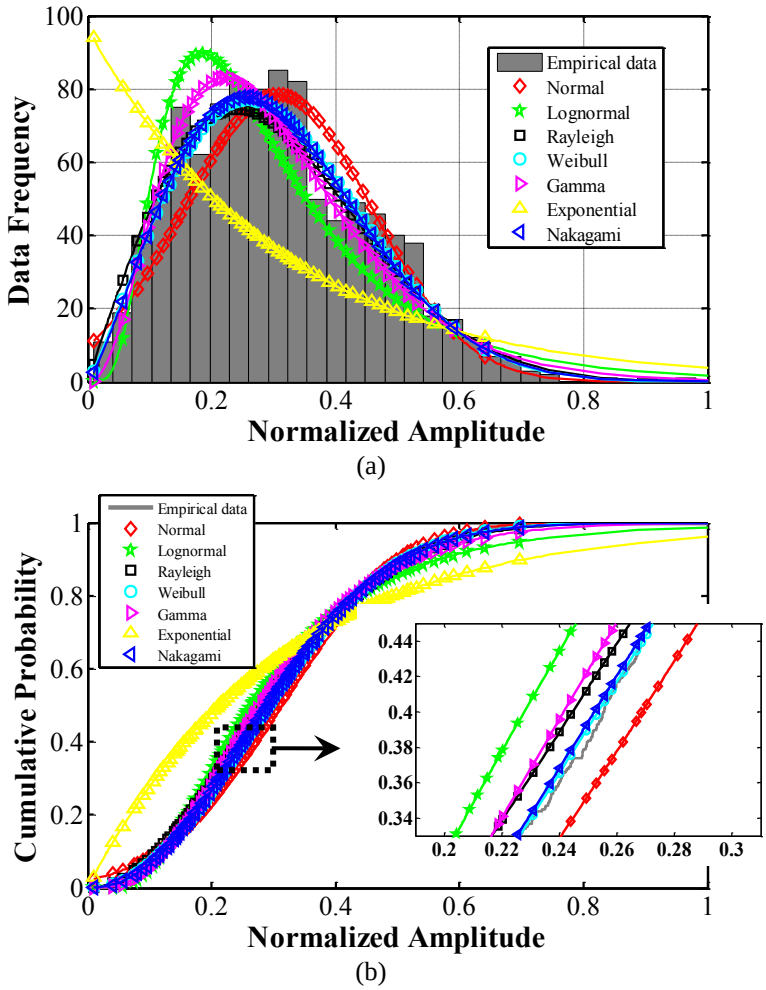

Figure 2.21. (a) PDF and (b) CDF of measured empirical data against fitted distributions for QNLoS off-body channel (Tx_2Rx_2) on human subject at 2.4 GHz and Tx-Rx distance of 100 cm.

The PDF and CDF of the empirical (measured) data for QNLoS off-body channel (Tx_1Rx_1) on liquid tissue phantom at 2.4 GHz and a Tx-Rx distance of 100 *cm* are shown in Fig. 2.22 along with the corresponding estimated PDFs and CDFs for the competent

distributions using the fitting algorithm. The corresponding test statistics output by the algorithm are also shown in Table 2.3. As evident from the CDFs (inset in Fig. 2.22 (b)), the empirical data fits closest to the Weibull CDF (followed by Nakagami-*m* and Rayleigh CDFs). This is correctly detected by the algorithm with a *p* value of 0.795 for Weibull distribution (followed by 0.711 and 0.652 for Nakagami-*m* and Rayleigh distributions respectively) in Table 2.3. The statistical study for various QNLoS scenarios was also verified by varying the sub-channels using the on-board antenna diversity along with the Tx-Rx distance. All the corresponding numerical results are presented in Table 2.3.

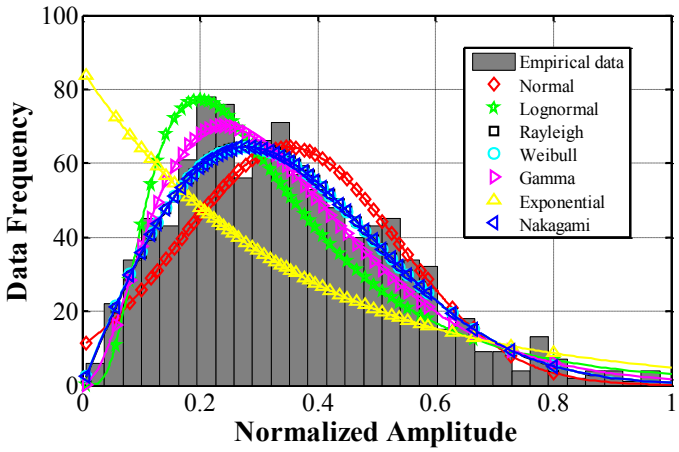

(a)

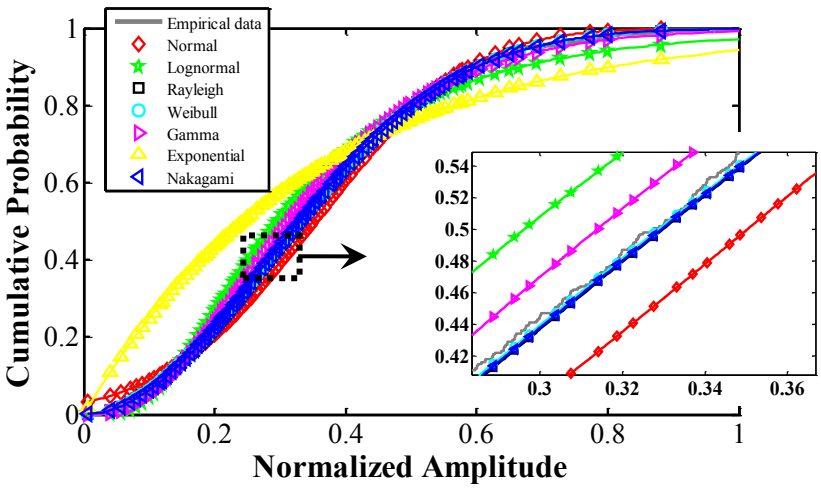

(b)

Figure 2.22. (a) PDF and (b) CDF of measured empirical data against fitted distributions for QNLoS off-body channel (Tx_1Rx_1) on liquid tissue phantom at 2.4 GHz and Tx-Rx distance of 100 *cm*.

TABLE 2.3. RESULTS OF CHANNEL STATISTICS USING THE PROPOSED FITTING ALGORITHM FOR VARIOUS MEASURED OFF-BODY CHANNEL SCENARIOS AT 2.40 GHZ

Tx location	Link	*d* (cm)	Scenario	K-S test statistics	Distribution function							Best-Fit
					N	***LG***	***R***	***W***	***G***	***E***	***NG***	
Human subject	Tx_1Rx_1	50	LoS	***h***	0	1	1	0	1	1	0	N(μ = 0.6356, σ = 0.1226)
				p	0.625	0	0	0.421	0	0	0.141	
			QNLoS	***h***	0	1	0	0	1	1	0	W(η = 0.3564, β = 2.0059)
				p	0.115	0	0.302	0.323	0	0	0.278	
	Tx_1Rx_1	100	LoS	***h***	0	0	1	1	0	1	0	N(μ = 0.6430, σ = 0.0857)
				p	0.834	0.05	0	0	0.169	0	0.431	
			QNLoS	***h***	0	1	0	0	1	1	0	W(η = 0.3542, β = 2.0265)
				p	0.076	0	0.491	0.707	0	0	0.557	
	Tx_2Rx_2	100	LoS	***h***	0	0	1	0	0	1	0	N(μ = 0.6277, σ = 0.1105)
				p	0.999	0.027	0	0.152	0.191	0	0.649	
			QNLoS	***h***	1	1	0	0	0	1	0	W(η = 0.3467, β = 2.1415)
				p	0	0	0.193	0.824	0.046	0	0.78	
Liquid phantom	Tx_1Rx_1	50	LoS	***h***	0	0	1	1	0	1	0	N(μ = 0.8129, σ = 0.0650)
				p	0.552	0.155	0	0	0.256	0	0.385	
			QNLoS	***h***	1	1	0	0	0	1	0	NG(m = 0.9878, ω =0.1775)
				p	0	0	0.926	0.944	0.04	0	0.979	
	Tx_1Rx_1	100	LoS	***h***	0	1	1	0	1	1	0	N(μ = 0.5349, σ = 0.1521)
				p	0.864	0	0	0.423	0	0	0.0257	
			QNLOS	***h***	1	1	0	0	0	1	0	W(η = 0.3954, β = 1.9845)
				p	0	0	0.652	0.795	0.25	0	0.711	
	Tx_1Rx_2	100	LoS	***h***	0	0	1	1	0	1	0	N(μ = 0.8524, σ = 0.0466)
				p	0.979	0.554	0	0	0.736	0	0.891	
			QNLOS	***h***	0	1	0	0	1	1	0	W(η = 0.4087, β = 2.2560)
				p	0.029	0	0.036	0.901	0	0	0.525	

Conclusion

Based on the statistical results presented above, it can be concluded that the off-body LoS channel can be best modeled by a Normal distribution considering the criterion of maximum probability of fitness score. This is also evident from Central Limit Theorem when applied to the multipath channel components as random variables which are being added up on the Rx side. Moreover, for QNLoS off-body channel, Weibull distribution seems to be an appropriate model based on the probability criterion, whose special case is also Rayleigh distribution ($\eta = \xi\sqrt{2}$). A Rayleigh model is known to be generally legitimate for a multipath propagation environment where there is no dominant LoS. Indeed, for the reported QNLoS scenarios, the transmission is mainly due to the multipath propagation due to the high attenuation of human tissue at microwave frequencies which blocks the direct or LoS component e.g., the attenuation constant α = 4.32 dB/cm @ 2.40 GHz for equivalent muscle tissue parameters (i.e., ε_r = 51.95, σ = 1.89 S/m) [3]. Consequently, the Weibull model comes out to be the best one out of the competent ones most of the times. Moreover, the parameters of the fitted distributions are also reported in each case, hence fully characterizing the recommended fitted distributions.

2.5.5. Fitting statistical study for on-body channels

Statistical model for on-body channels is also required for system-level modeling. Channel model for narrowband on-body communications for received signal strength versus angle around the body was proposed in [22] using FDTD method. The effect of surrounding environment was also considered in [23], hence presenting a more complete narrowband statistical model. Statistical characterization of dynamic narrowband on-body channels was presented in [29] and it was shown that Weibull, Gamma and Lognormal distributions generally provide good fitting for received signal amplitude. The stability of dynamic narrowband on-body area channel was characterized in [39] based on real-time measurements. Small scale narrowband fading for on-body channels was presented in [40] for an open office area and a Nakagami-*m* model was recommended.

Small-scale statistics for narrowband on-body channels for various mixed everyday activities were presented in [17] using a range of transceiver locations on-body and it was proposed that Gamma and Weibull distributions provide excellent fits for the agglomerated data for various on-body links. Moreover, it has also been reported that Lognormal, Weibull, and Gamma models are most often the best fits for first-order, small-scale fading for body-centric channels out of the commonly attempted distributions for fitting [17].

Here we present the small-scale statistical characterization for both static and dynamic narrowband on-body radio channels using real-time multipath measurements and channel cross-correlation as a possible metric to increase the number of points for improved statistical accuracy of channel fitting. Zyggie sensors as presented in Section 2.2 with miniaturized chip antennas were reused again in the measurement campaign. The best-fit model for first-order channel statistics is further estimated using the proposed fitting algorithm as presented in Sections 2.5.2 and 2.5.3.

Experimental Setup

Two identical Zyggie sensors as presented in Section 2.2 with miniaturized chip antennas were used as Tx and Rx for channel measurements as shown in Fig. 2.23. An antenna-body spacing of 6 *mm* was maintained between the sensor antennas (Tx/Rx) and the body using foam spacers (ε_r = 1) to avoid frequency detuning due to the high permittivity influence of the body tissue. The experiments were taken on a 177.8 *cm*/163 pounds adult male human subject in a multipath indoor laboratory environment. Three on-body channels were considered for statistical study with Tx on the centre of chest and Rx on three different positions i.e., left wrist, right hip and right thigh (Fig. 2.23). These channels were selected due to the common prospective WBASN applications [17]. The counterpart sub-channels i.e., chest to right-wrist, left-hip/thigh were not considered because of the inherent body symmetry. For each of the measured channels, further two scenarios were considered i.e., quasi-static and artificial walk. For quasi-static, the subject stood static throughout the measurements except the involuntary movements caused by breathing of chest (hence, quasi-static). For motion, the subject performed a

slow walk on spot at a nearly constant rate with arms and legs moving to and fro in a walk-like posture (hence, named as artificial walk). A similar experimental set up was used as discussed already for off-body case in Section 2.5.4. The experimental data generated by this measurement campaign was also used by BoWI project partners for numerical channel studies.

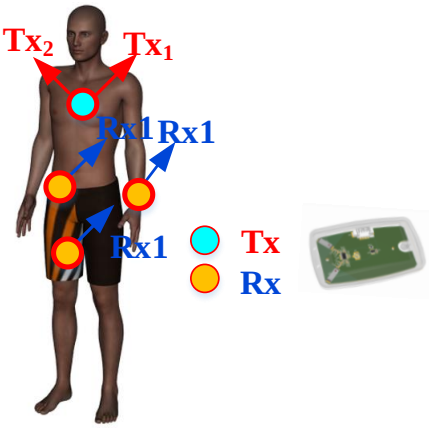

Figure 2.23. Location of Tx/Rx sensor nodes for on-body channel measurements on a human test subject.

Results and discussion

Measured data was recorded for the on-body channels at three ISM frequencies i.e., 2.40, 2.44 and 2.48 GHz for both quasi-static and artificial walk scenarios. Before the statistical analysis, the autocorrelation was computed from the discrete time series of the set of the observations to ensure that the data is uncorrelated and appropriate for statistical study. The temporal autocorrelation function (ACF) was computed by (2.23) [41] i.e.,

$$\rho_k = \frac{1}{Nc_0}\sum_{i=1}^{N-k}(y_i - \hat{y})(y_{i+k} - \hat{y}) \qquad k = 0,1,2,....K \tag{2.23}$$

where $\hat{y}$ is the sample mean of the measured data y, c_0 corresponds to the sample variance and N is the total number of measurement samples.

The autocorrelation was computed for all the measured scenarios using (2.23) for both quasi-static and dynamic scenarios. For reference, the first 50 values of ACF based on the entire series of 1000 observations are plotted in Fig. 2.24 for chest-wrist channel (Tx_1Rx_1) under quasi-static and artificial walk scenarios. As evident from Fig. 2.24, the channel for static posture is more stable, hence undergoing less temporal variations compared to the channel for artificial walk scenario which suffers deep fading. Quite low values of ACF for static posture are observed due to the fact that the link between the Tx (chest) and Rx (wrist) is obstructed by the torso of the body, hence principally causing a QNLoS propagation scenario. Whereas, the channel of artificial walk scenario suffers deep temporal fades and is characterized by correlations that alternate in sign due to the arms movement which cause the link to slowly change from LoS to QNLoS shadowed by the human torso as the arm is moved from the front to the back of the body respectively.

Also the ACF shows that one cycle of walk is completed in approximately four time lags which corresponds to a period of 520 *msec* and the ACF damps out further with increasing lag.

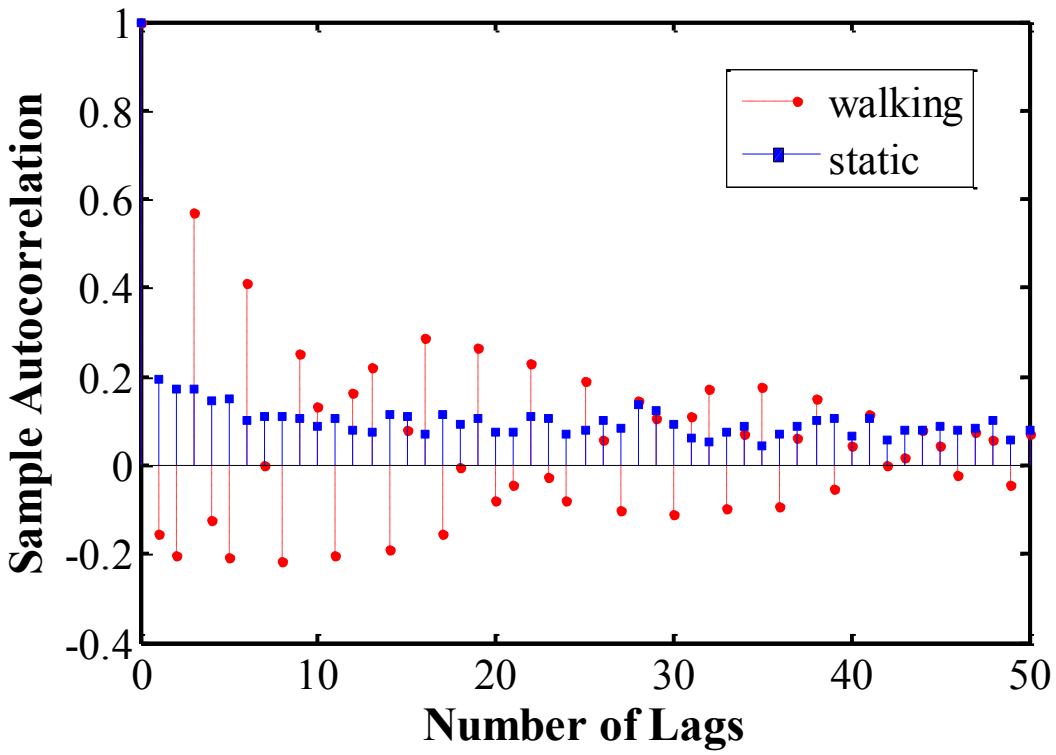

Figure 2.24. Empirical autocorrelation for chest-wrist channel (Tx_1Rx_1) at 2.40 GHz for quasi-static and artificial walk scenarios. One time lag corresponds to a period of 130 *msec*.

The temporal autocorrelation between the measured data samples was also computed for all other measured scenarios using (2.23), and was found to be much lower than the threshold of 0.7 (apart from $\rho_0 = 1$ which is obvious) where the correlation is generally considered to be significant for values of 0.7 or higher [4]. Therefore, the measured data samples can be considered as uncorrelated.

Once the autocorrelation is observed to be insignificant, the cross-correlation between the channel data is then investigated at the three ISM frequencies using (2.24) [42]

$$\rho_i^{\,j} = \frac{E\left[\left(h_i - \mu_{h_i}\right)\left(h_j - \mu_{h_j}^{\,*}\right)\right]}{\sigma_{h_i}\sigma_{h_j}} \qquad (2.24)$$

where h_i and h_j correspond to the measured channel data at frequencies i and j where (i, j) ϵ {2.40, 2.44, 2.48}^{2} (in GHz), μ_i, μ_j are the mean and σ_i, σ_j are the standard deviation of the channel data h_i and h_j respectively. Considering the correlation coefficients between the channel data at the three frequencies, the correlation matrix for each scenario was then built using (2.25)

$$R = \begin{bmatrix} 1 & \rho_1^2 & \rho_1^3 \\ \rho_2^1 & 1 & \rho_2^3 \\ \rho_3^1 & \rho_3^2 & 1 \end{bmatrix} \tag{2.25}$$

Knowing the symmetry of channel cross-correlation i.e., $\rho_i^j = \rho_j^{i*}$, only three correlation coefficients in the correlation matrix (2.25) are important to know i.e., ρ_1^2, ρ_1^3 and ρ_2^3. The correlation coefficient matrix for each on-body channel was computed at the three ISM frequencies for both quasi-static and dynamic scenarios. The magnitude of the resulting complex correlation matrices are listed in Table 2.4. As can be observed from the correlation matrices, the correlation coefficient between all the channel data at the three frequencies is always less than 0.7. Hence the sub-channel data at the three frequencies can be considered as uncorrelated knowing that the correlation is generally considered to be significant for values of 0.7 or higher [4].

Table 2.4. CROSS-CORRELATION MATRICES FOR CHANNEL DATA AT 2.40, 2.44 AND 2.48 GHZ

Scenario	**Tx_1: Chest, Rx_1: Wrist**		**Tx_2: Chest, Rx_1: Hip**		**Tx_2: Chest, Rx_1: Thigh**	
	Quasi-static	Artificial walk	Quasi-static	Artificial Walk	Quasi-static	Artificial Walk
Corr. Matrix *R*=	$\begin{bmatrix} 1 & 0.25 & 0.27 \\ 0.25 & 1 & 0.35 \\ 0.27 & 0.35 & 1 \end{bmatrix}$	$\begin{bmatrix} 1 & 0.68 & 0.61 \\ 0.68 & 1 & 0.54 \\ 0.61 & 0.54 & 1 \end{bmatrix}$	$\begin{bmatrix} 1 & 0.19 & 0.21 \\ 0.19 & 1 & 0.23 \\ 0.21 & 0.23 & 1 \end{bmatrix}$	$\begin{bmatrix} 1 & 0.64 & 0.61 \\ 0.64 & 1 & 0.65 \\ 0.61 & 0.65 & 1 \end{bmatrix}$	$\begin{bmatrix} 1 & 0.05 & 0.08 \\ 0.05 & 1 & 0.07 \\ 0.08 & 0.07 & 1 \end{bmatrix}$	$\begin{bmatrix} 1 & 0.55 & 0.57 \\ 0.55 & 1 & 0.63 \\ 0.57 & 0.63 & 1 \end{bmatrix}$

Chest-wrist channel

The measured data at the three ISM frequencies was hence, merged into common vectors having three times more points (3×1000) than the discrete sub-channel vectors. Moreover, the sub-channel data was also normalized prior to merging to ensure that the inherent channel distributions for each narrowband frequency are preserved. This cannot be ensured if the normalization is not performed a priori. The merged channel vectors were then used as input to the fitting algorithm as presented in Sections 2.5.2 and 2.5.3 for statistical study. For reference, PDF and CDF of the empirical data along with those of the fitted models for chest-wrist quasi-static channel are shown in Fig. 2.25. The resulting *h* and *p* values as output by the fitting algorithm are listed in Table 2.5 along with those for all the investigated scenarios. As evident from the inset of Fig. 2.25 (b), the fitting statistics are in good agreement with those proposed by the fitting algorithm i.e., Weibull distribution fits closest to the empirical CDF followed by Nakagami-*m* distribution. This is correctly detected by the algorithm resulting in *p* values of 0.744 and 0.1 for Weibull and Nakagami-*m* respectively as listed in Table 2.5.

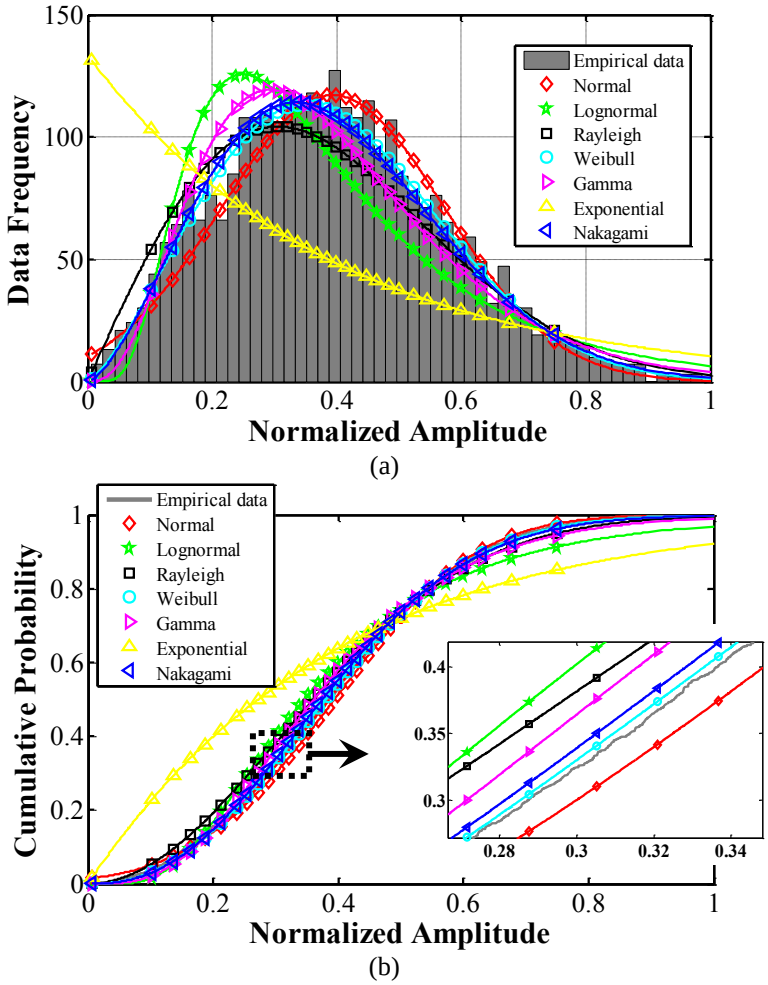

Figure 2.25. (a) PDF and (b) CDF of empirical data (measured) vs. fitted models for chest-wrist quasi-static merged channel.

Chest-hip channel

The PDF and CDF of the empirical data along with those of the fitted models for chest-hip quasi-static channel are shown in Fig. 2.26. The resulting *h* and *p* values as output by the fitting algorithm are listed in Table 2.5 along with those for all the investigated scenarios. As evident from the inset of Fig. 2.26(b), the fitting statistics are in good agreement with those proposed by the fitting algorithm i.e., Normal distribution fits closest to the empirical CDF followed by Weibull distribution. This is correctly detected by the algorithm resulting in *p* values of 0.798 and 0.44 for Normal and Weibull respectively as listed in Table 2.5.

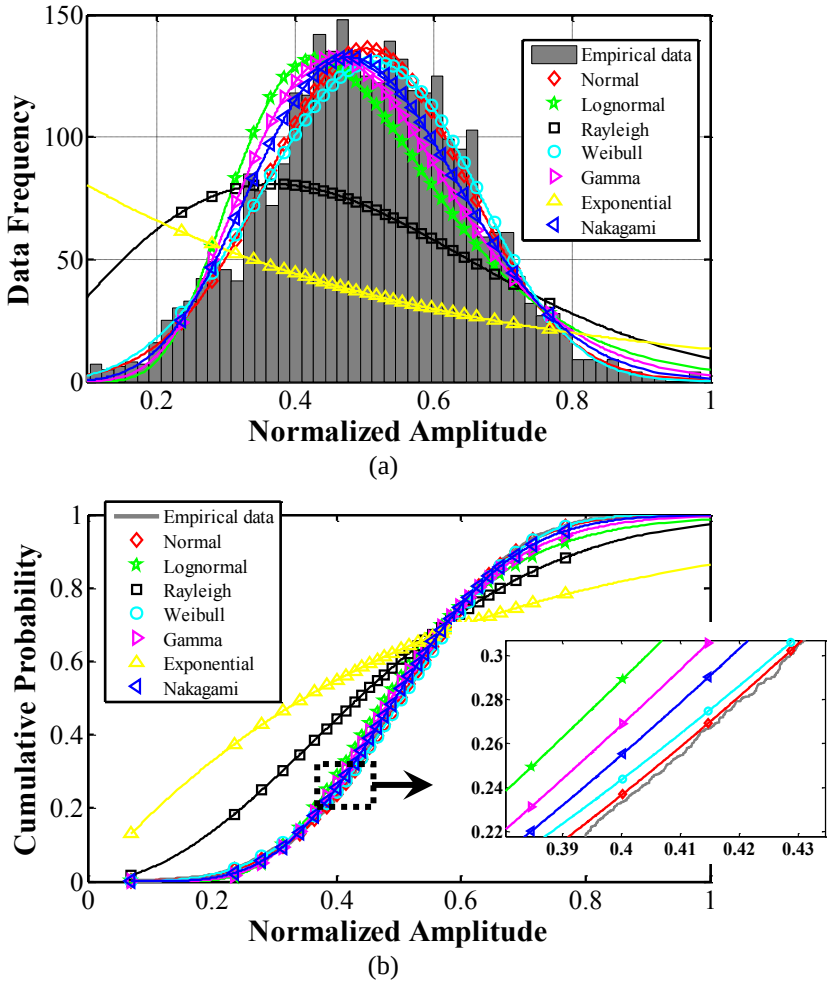

Figure 2.26. (a) PDF and (b) CDF of empirical data (measured) vs. fitted models for chest-hip quasi-static merged channel.

The PDF and CDF of the empirical data along with those of the fitted models for chest-hip channel in case of artificial walk scenario are shown in Fig. 2.27. As evident from the inset of Fig. 2.37 (b), the fitting statistics are in good agreement with those proposed by the fitting algorithm i.e., Nakagami-*m* distribution fits closest to the empirical CDF followed by Gamma distribution. This is correctly detected by the algorithm resulting in *p* values of 0.452 and 0.159 for Nakagami-*m* and Gamma distributions respectively as listed in Table 2.5.

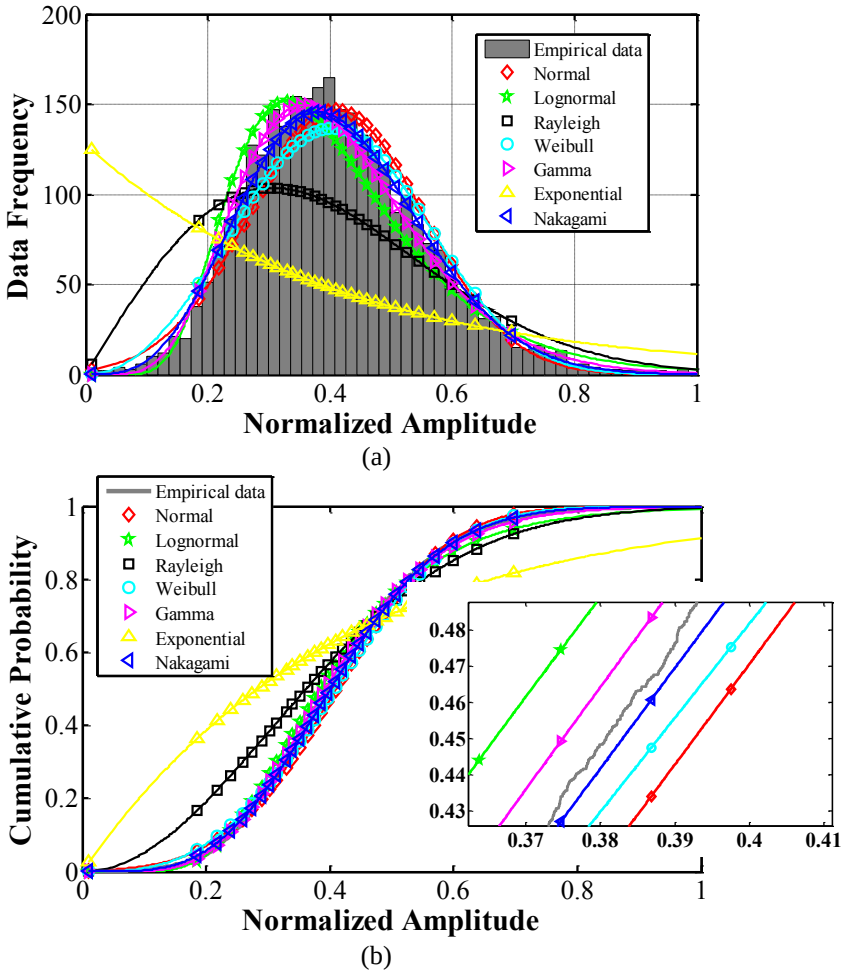

Figure 2.27. (a) PDF and (b) CDF of empirical data (measured) vs. fitted models for dynamic chest-hip merged channel.

TABLE 2.5. RESULTS OF CHANNEL STATISTICS FOR MERGED CHANNEL DATA WHERE *N* = NORMAL, *LG* = LOGNORMAL, *R* = RAYLEIGH, *W* = WEIBULL, *G* = GAMMA, *E* = EXPONENTIAL, *NG* = NAKAGAMI

Channel	Scenario	K-S test statistic	Distribution Function							Best-Fit	Estimated Parameters of Best -Fit Distribution	
			N	*LG*	*R*	*W*	*G*	*E*	*NG*			
Tx_1: Chest, Rx_1: Wrist	Quasi-static	***h***	1	1	1	0	1	1	0	*W*	η = 0.4443	β = 2.3312
		p	0	0	0	0.744	0	0	0.1			
	Artificial walk	***h***	1	1	1	0	0	1	0	*W*	η = 0.3247	β = 1.7278
		p	0	0	0	0.143	0.04	0	0.07			
Tx_2: Chest, Rx_1: Hip	Quasi-static	***h***	0	1	1	0	1	1	1	*N*	μ = 0.5035	σ = 0.1443
		p	0.798	0	0	0.44	0	0	0			
	Artificial walk	***h***	1	1	1	1	0	1	0	*NG*	*m* = 2.1766	ω = 0.1888
		p	0	0	0	0	0.159	0	0.452			
Tx_2: Chest, Rx_1: Thigh	Quasi-static	***h***	1	1	1	0	1	1	1	*W*	η = 0.4094	β = 2.2560
		p	0	0	0	0.16	0	0	0			
	Artificial walk	***h***	1	1	1	0	1	1	0	*W*	η = 0.4286	β = 2.3301
		p	0	0	0	0.681	0	0	0.09			

Conclusion

Based on the statistical study presented above, Weibull distribution is recommended as the best-fit model for first-order fading for chest-wrist and chest-thigh channels. For chest-hip quasi-static channel, Normal distribution is observed for first-order fading due to dominant LoS propagation which changes to Nakagami-*m* for dynamic walk scenario due to the shadowing caused by the body movement. The best-fit models were also reported for each scenario along with the corresponding best-fit parameters, hence fully charactering the fitted models.

2.6. Conclusions

The Zyggie prototype platform as developed by the BoWI partners was introduced demonstrating the miniaturized chip antennas exploiting pattern diversity. Characterization of commercial chip antennas on an arbitrary substrate was then presented showing proper matching of chip antennas at ISM 2.4 GHz frequency band and their radiation performance both in free space and on-body.

Off-body channel measurements were presented for both LoS and QNLoS scenarios in multipath indoor environments exploiting the chip antenna, pattern diversity configuration. Typical values of RMS delay spread were also reported to control the transmit symbol duration to avoid ISI without the use of equalization. The reported ergodic channel capacity proves that the proposed miniaturized chip antenna configuration can offer improved capacity compared to the SISO systems which also validates the usefulness of miniaturized chip antennas for smart, low power WBASNs.

A robust algorithm has been proposed for channel distribution fitting based on MLE and K-S test as a measure of goodness of fit. The algorithm was well validated using standard data for all the competent distributions and observed to perform in excellent agreement with standard analytical data. Moreover, the proposed algorithm is generic and useful in the sense that it can be applied to find the optimum channel fitting statistics for various types of empirical radio channel data i.e., both simulations and measurements. The algorithm can also be modified for radio channel statistical studies corresponding to various microwave frequency bands such as UWB, millimeter-wave band etc. The fitting was attempted against seven competent distributions here, which are generally known to hold true for wireless WBAN channels at ISM frequencies. However, the algorithm can be further modified to include more distribution functions while following the same proposed principle based on the known benchmarks for the particular channel data under study.

The fitting algorithm was then applied on real-time off-body channel measurements suggesting a Normal distribution for small-scale, first order fading for LoS scenarios and a Weibull distribution (whose special case is Rayleigh model) for that of QNLoS scenarios. Moreover, the statistical results match for the case of human body and presented liquid phantom. This also suggests the suitability of using phantoms for statistical BAN channel studies to accumulate arbitrarily large number of points for improved statistical accuracy which is not possible with real human subjects.

Being a statistical method, the accuracy of the proposed fitting algorithm is controlled by the number of samples. Therefore, to increase the number of empirical samples, correlation coefficients were investigated at three ISM frequencies for both static and dynamic on-body channels and the sub-channel data was merged to have increased statistical accuracy subject to the insignificant channel cross-correlation. Based on the statistical study, a Weibull distribution was recommended as the best-fit model for first-order fading for chest-wrist and chest-thigh channels. For chest-hip quasi-static channel, Normal distribution is recommended for first-order fading due to dominant LoS

propagation and a Nakagami-*m* distribution for dynamic walk scenario due to the shadowing caused by the body movement. Moreover, the parameters of the best-fit distributions are also estimated in each case, hence fully characterizing the fitted models. These models are also useful for deriving overall fading models for BANs while incorporating also other factors such as Doppler's effect and shadowing which is still a challenge due to the highly dynamic nature of BAN environments.

References

[1] "http://www.bowi.cominlabs.ueb.eu/," [Online].

[2] P. S. Hall and Y. Hao, Antennas and Propagation for Body-Centric Wireless Communications, Norwood, MA, USA: Artech House, Inc, 2006.

[3] I. Yamaura, "Measurements of 1.8 - 2.7-Ghz Microwave Attenuation in the Human Torso," *IEEE Transactions on Microwave Theory and Techniques,* vol. 25, no. 8, pp. 707-710, Aug. 1977.

[4] W. C. Jakes, Microwave Mobile Comms., New York: Wiley, 1974.

[5] http://johansontechnology.com/, [Online].

[6] [Online]. Available: http://www.satimo.com/.

[7] "https://www.cst.com/," [Online].

[8] Ian Oppermann, Matti Hämäläinen, Jari Iinatti, UWB: Theory and Applications, Wiley, Sep. 2004.

[9] A. Khaleghi, I. Balasingham , "On human body ultra wideband channel characterizations for different wave polarizations," in *Sarnoff Symposium*, Princeton, NJ, April, 2009.

[10] L. Akhoondzadeh-Asl, I. Khan, and P.S. Hall, "Polarisation diversity performance for on-body communication applications," *IET Microw. Antennas Propag.,* vol. 5, no. 2, p. 232–236, 2011.

[11] M. O. Munoz, R. Foster, and Y. Hao, "On-Body Channel Measurement Using Wireless Sensors," *IEEE Transactions on Antennas and Propagation,* vol. 60, no. 7, pp. 3397-3406, July 2012.

[12] I Khan, L Yu, Y I. Nechayev, and P S. Hall, "Space and pattern diversity for on-body communication channels in an indoor environment at 2.45 GHz," in *2nd European Conference on Antennas and Propagation (EuCAP)*, Edinburgh, UK , Nov 2007.

[13] I. Khan, P.S. Hall, A. A. Serra, A. R. Guraliuc, and P. Nepa, "Diversity performance analysis for on-body communication channels at 2.45 GHz," IEEE Transactions on Antennas and Propagation," vol. 57, no. 4, pp. 956-963, April 2009.

[14] S.L. Cotton and W.G. Scanlon, "Measurements, modeling and simulation of the off-body radio channel for the implementation of bodyworn antenna diversity at 868 MHz," *IEEE Transactions on Antennas and Propagation,* vol. 57, no. 12, pp. 3951-3961, Dec. 2009.

[15] A.A. Goulianos, T. Brown, and S. Stavrou, "Power delay profile modelling of the ultra wideband off-body propagation channel," *IET Microwaves, Antennas & Propagation,* vol. 4, no. 1, pp. 62-71, January 2010.

[16] Q.H. Abbasi, A. Alomainy, and Y. Hao, "Ultra wideband antenna diversity techniques for on/off-body radio channel characterisation," in *IEEE International Workshop on Antenna Technology (iWAT)*, March 2012.

[17] D. B. Smith, D. Miniutti, T.A. Lamahewa, and L.W. Hanlen, "Propagation models for body-area networks: a survey and new outlook," *IEEE Antennas and Propagation Magazine,* vol. 55, no. 5, pp. 97-117, Oct. 2013.

[18] P. Pagani, F. T. Talom, P. Pajusco, and B. Uguen, Ultra Wideband Radio Propagation Channels : A Practical Approach, Wiley, 2008.

[19] P. Pagani, F. T. Talom, P. Pajusco, and B. Uguen, Ultra Wideband Radio Propagation Channels : A Practical Approach, Wiley, 2008.

[20] I. Khan and P S. Hall, "Experimental evaluation of MIMO capacity and correlation for narrowband body-centric wireless channels," *IEEE Transactions on Antennas and Propagation*, vol. 58, no. 1, pp. 195-202, Jan. 2010.

[21] E. Biglier, R. Calderbank, A. Constantinides, A. Goldsmith, A. Paulraj, and H. V. Poor, MIMO Wireless Communications, New York: Cambridge Univ. Press, 2007.

[22] J. Ryckaert, P. De Doncker, R. Meys, A. de Le Hoye, and S. Donnay, "Channel model for wireless communication around human body," *Electron. Lett.*, vol. 40, no. 9, p. 543–544, Apr. 2004.

[23] A. Fort, C. Desset, P. Wambacq, and L. V. Biesen, "Indoor body-area channel model for narrowband communications," *IET Microw. Antennas Propag.*, vol. 1, no. 6, p. 1197–1203, 2007.

[24] Q.H. Abbasi, M. M. Khan, S. Liaqat, A. Alomainy, and Y. Hao, "Ultra wideband off-body radio channel characterization for different environments," in *7th International Conference on Electrical & Computer Engineering (ICECE)*, Dec. 2012.

[25] A. A. Goulianos, T. W. C. Brown, B. G. Evans, and S. Stavrou, "Wideband power modeling and time dispersion analysis for UWB indoor off-body communications," *IEEE Trans. Antennas and Propag.*, vol. 57, no. 7, p. 2162–2171, Jul.2009.

[26] M. M. Khan, Q. H. Abbasi, A. Alomainy, and Y. Hao, "Radio propagation channel characterisation using ultra wideband wireless tags for body-centric wireless networks in indoor environment," in *International Workshop on Antenna Technology (iWAT)*, Hong Kong, Mar. 2011.

[27] D. Smith, L. Hanlen, J. Zhang, D. Miniutti, D. Rodda, and B. Gilbert, "Characterization of the dynamic narrowband on-body to off-body area channel," in *IEEE Int. Conf. on Communications*, Jun. 2009.

[28] H. Akaike, "A new look at the statistical model identification," *IEEE Trans. Automatic Control*, vol. 19, no. 6, pp. 716-723, 1974.

[29] D. Smith, L. Hanlen, J. Zhang, D. Miniutti, D. Rodda, and B. Gilbert, "First- and second-order statistical characterizations of the dynamic body area propagation channel of various bandwidths," *Annals of Telecommunications*, vol. 66, no. 3-4, pp. 187-203, 2011.

[30] A. Fort, C. Desset, P. De Doncker, P. Wambacq, and L. Van Biesen, "An ultra-wideband body area propagation channel model – from statistics to implementation," *IEEE Trans. Microwave Theory and Tech.*, vol. 54, no. 4, pp. 1820-1826, Jun. 2006.

[31] G. Schwarz, "Estimating the dimension of a model," *Annals of Statistics, vol. 6, pp. ,*

vol. 6, pp. 461-464, 1978..

[32] M. Wax and T. Kailath, "Detection of signals by information theoretic criteria," *IEEE Trans. Acoustics, Speech and Signal Processing*, vol. 33, no. 2, pp. 387- 392, April 1985.

[33] M. Evans, N. Hastings, and B. Peacock, Statistical Distributions, 2nd edition, Wiley, 1993.

[34] M. Abramowitz and I.A. Stegun, Handbook of Mathematical Functions, New York: Dover, 1964.

[35] D. I. Laurenson, Indoor Radio Channel Propagation Modeling by Ray Tracing Techniques, PhD thesis, University of Edinburgh, 1994.

[36] A.W. van der Vaart, Asymptotic Statistics, Cambridge University Press, 2000.

[37] F. J. Massey, "The Kolmogorov-Smirnov Test for Goodness of Fit," *Journal of the American Statistical Association*, vol. 46, no. 253, pp. 68-78, 1951.

[38] G. Marsaglia, W.W. Tsang, and J. Wang, "Evaluating Kolmogorov`s distribution," *Journal of Statistical Software*, vol. 8, no. 18, pp. 1-4, 2003..

[39] J. Zhang, D.B. Smith, L.W. Hanlen, D. Miniutti, D. Rodda, and B. Gilbert, "Stability of narrowband dynamic body area channel," *IEEE Antennas and Wireless Propagation Letters*, vol. 8, pp. 53-56, 2009.

[40] W. G. Scanlon and S. L. Cotton, "Understanding on-body fading channel at 2.45 GHz using measurements based on user state and environment," in *Loughborough Antennas and Propagation Conference* , Loughborough, UK, Mar. 2008.

[41] G. E. P. Box, G. M. Jenkins, G. C. Reinsel, Time Series Analysis: Forecasting and Control, 3rd edition: Prentice Hall, 1994.

[42] R. E. Jaramillo, O. Fernandez, and R. P. Torres, "Empirical analysis of 2x2 MIMO channel in outdoor-indoor scenarios for BFWA applications," *IEEE Antennas Propag. Mag.*, vol. 48, no. 6, p. 57–69, Dec. 2006.

Chapter 3. Antenna design and interaction with human body at ISM frequencies

Contents

3.1. Introduction

Human body is a lossy medium with high tissue parameters at microwave frequencies e.g., permittivity and conductivity. Therefore, the human body can strongly affect the antenna performance as the latter operates in its near vicinity. Most significant antenna performance parameters which should be considered are its resonant frequency, impedance bandwidth, radiation pattern, gain, and radiation efficiency. Therefore, the impact of human body on antenna performance should be carefully investigated and reduced as much as possible.

At ISM frequencies, the on-body propagation component plays a significant role which involves in particular the propagation around the body surface by creeping waves [1]. Therefore, it is also necessary to use representative body models to study the antenna behavior to obtain approximate results equivalent to those in realistic environments. The principle objective to design an antenna for body-oriented applications is to achieve nearly comparable performance in proximity to body as that in free space. Moreover, due to the wearable application and mobility of BAN user, the antenna should be compact, low-profile and unobtrusive.

The optimum radiation and polarization requirements of the antenna for wearable BANs depend on the particular application scenario. For wearable applications, devices can communicate in two levels i.e., on-body and off-body. On-body communication involves transmission scenarios between two devices located on different parts of the body of a single BAN user. On the other hand, off-body applications involve transmission scenarios between a body-worn sensor and an external access point situated away from the body e.g., a smartphone, relay or base station. For the case of on-body applications, the antenna should radiate an omnidirectional beam directed along the body surface to boost the on-body links with a preferably vertical polarization [2]. Such a scenario is known to excite surface waves [3]- [4] which can be useful to improve the link efficiency. The monopole antenna is considered to be a good candidate for on-body applications since it meets both the optimum radiation and polarization requirements for such applications. However, the main difficulty is the height of the monopole which is typically quarter wavelength at the operating frequency ($\lambda_0/4$ @ f_0). This makes it obtrusive and hence, unfavorable for portable applications.

For the case of off-body links, the antenna radiation should be directed in the broadside direction or away from the body, whereas the polarization is not as critical as for the on-body case [2] due to the depolarization effect in real environments [5]. A patch antenna is an appropriate solution for off-body applications since it radiates in the broadside direction with maximum radiation directed away from the body and is a viable solution also due to its favorable mechanical properties such as compactness and unobtrusiveness.

Moreover, this implies that separate antennas are required for both on- and off-body operation for optimum BAN performance from radiation and polarization perspective. Therefore, there is also need of a single antenna which can serve for both on- and off-body applications by dynamically reconfiguring its radiation or polarization features

instead of using antenna arrays, since space and form factor are crucial for wearable applications.

This chapter is organized as follows. In Section 3.2, a printed monopole antenna is designed for ISM 2.4 GHz band (2.40-2.4835 GHz) which includes a partial ground plane to offer direct near-file interaction with the body. The impact of body proximity is then studied on antenna output parameters such as reflection coefficient, radiation pattern, efficiency, and gain etc. The influence of antenna-body spacing is also presented here. In Section 3.3, the design of an Inverted-F antenna is presented for ISM 2.4 GHz which meets both the radiation and polarization requirements for on-body applications as for a monopole antenna but meanwhile, offers a much reduced profile. The performance of the antenna in proximity to a realistic body model is studied and its SAR is also computed numerically for compliance considerations. In Section 3.4, the design of a short-circuited patch antenna is presented which can offer multiple modes for optimum radiation and polarization requirements for both on- and off-body applications. Furthermore, the performance of the antenna is evaluated in proximity to realistic human body model for both on- and off-body operational modes. The idea of exciting multiple modes at same frequency is also demonstrated here for the design of a pattern and polarization diversity antenna. Finally, conclusions are drawn in Section 3.5.

Throughout this chapter, the tissue parameters have been chosen appropriately while considering the resonant frequency of interest. Moreover, different body models have been considered based on the parameters e.g., when SAR studies are required, detailed multilayer models are considered where single layer models may be insufficient. However, for scenarios where investigation of far-field and impedance matching is required only, single layer tissue models are appropriate and have been considered using state-of-the-art [6]-[10].

3.2. Printed monopole antenna

3.2.1. Antenna design

In order to investigate impact of human body on the antenna parameters at ISM 2.4 GHz frequencies, various simulation setups were considered using CST MWS^{TM}. For preliminary studies, an antenna without a full ground plane was considered to study the impact of body proximity, since such an antenna introduces direct near-field interaction with the body and its performance should suffer prominently. Printed monopole antenna was used for the study since it does not include a complete ground plane and also offers broad impedance bandwidth.

The antenna dimensions were optimized using CST MWS employing a low-cost FR-4 substrate as dielectric (ε_r = 4.3 and h = 1.6 *mm*). A width of 3.1 *mm* for the microstrip line was chosen, which corresponds to 50 Ω for the given substrate at the ISM central frequency of 2.45 GHz. The layout of the antenna is shown in Fig. 3.1. The resonant frequency f_r of the antenna is mainly controlled by the length of printed element l_a and the width of ground plane (w_g) which also controls the impedance bandwidth. The dimensions of the antenna optimized by CST MWS for resonance inside ISM 2.4 GHz band are also shown in Fig. 3.1 along with its reflection coefficient shown in Fig. 3.2. As

evident, the optimized antenna offers broadband impedance matching with nearly 20% fractional bandwidth ($|S_{11}|$<-10dB, VSWR<1.9) covering the entire ISM 2.4 GHz bandwidth. The radiation patterns of the antenna are shown in Fig. 3.3. The antenna offers a gain of 3.0 dBi at 2.45 GHz with a radiation efficiency of 95.7 % in free space.

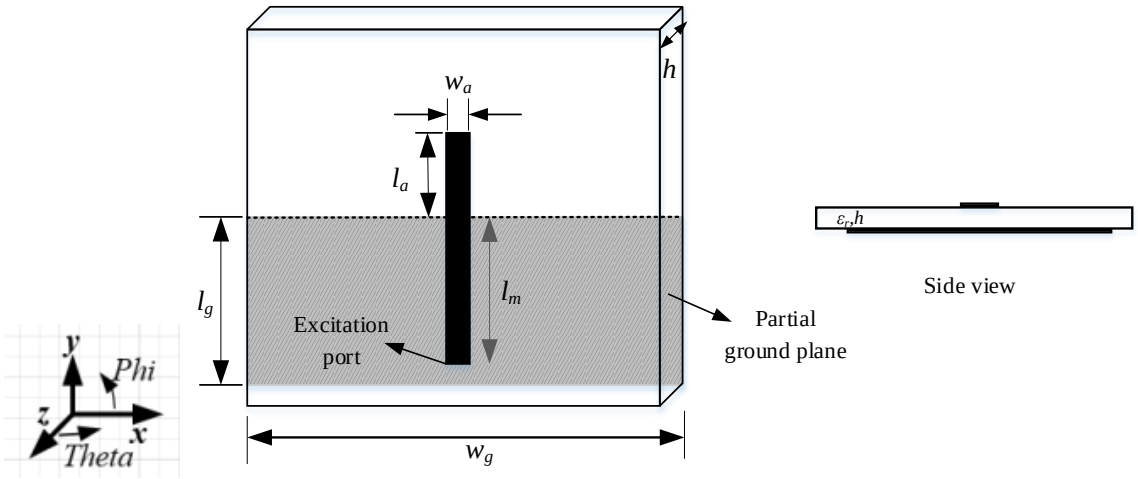

Figure 3.1. Printed monopole antenna designed in CST MWS. Optimized dimensions are (Units: *mm*) w_a = 3.1, l_g = 53.2, w_g = 80, l_m = 43.2, l_a = 20.8 (substrate FR-4; ε_r = 4.3, h = 1.6 mm).

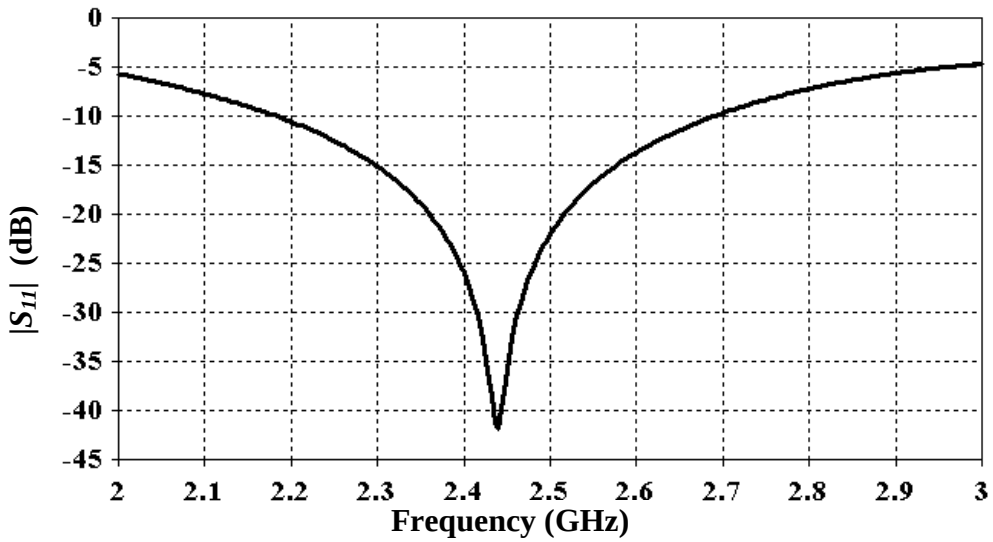

Figure 3.2. Simulated reflection coefficient of the antenna in free space.

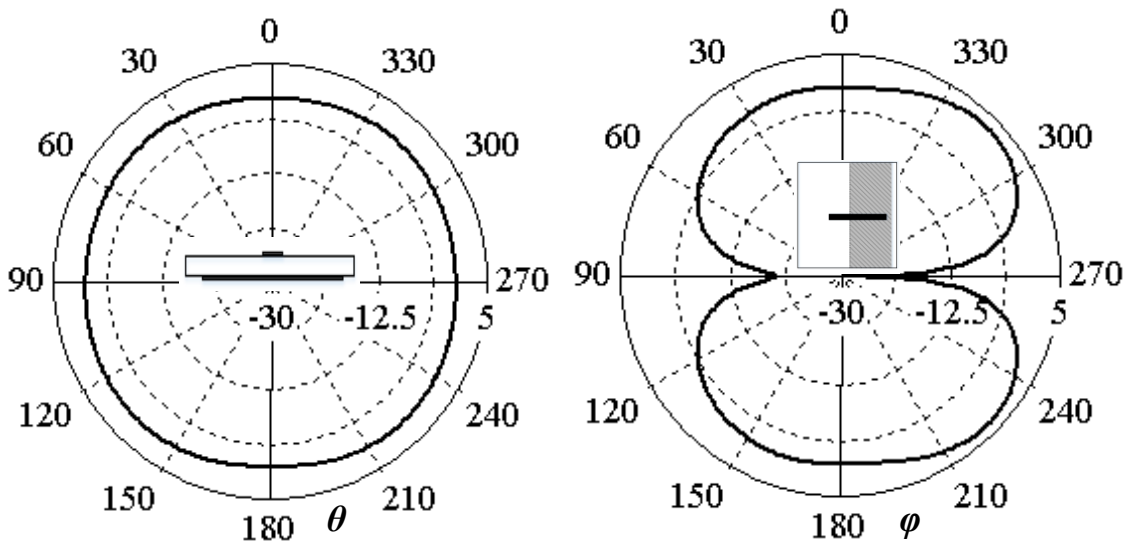

(a) (b)

Figure 3.3. Radiation patterns in (a) *xz*-plane (H-plane) and (d) *xy*-plane (E-plane) of the antenna at 2.45 GHz in free space (Reference coordinate system shown in Fig. 3.1).

3.2.2. Antenna-body Interaction

To study the antenna-body interaction, a homogeneous body model was considered for simplicity in the initial stage. Such a model is sufficient for radiation and S-parameter characterization of the antenna in proximity to human body unless accurate SAR studies are also required. To this end, the antenna was placed directly (i.e., no spacing) on a lossy homogenous body model with ε_r = 37.9, σ = 1.48 S/m which is equivalent to skin tissue [11] (since the skin depth at ISM 2.4 GHz frequencies is only few *mm*). To consider maximum body impact, infinite PML boundaries were used across the length, width and depth of the phantom to investigate impact of infinite tissue. Due to the presence of the lossy tissue, the simulation problem size is also significantly increased from 45,000 mesh cells to simulate the antenna stand-alone in free space (Section 3.2.1) to 340,000 mesh cells required for the antenna-body problem. This corresponds to a rise in simulation size of 7.5 times.

The resulting reflection coefficient and radiation patterns of the antenna in E- and H-planes are shown in Fig. 3.4 for both free space and body model. As evident from the results, the antenna parameters are highly degraded in proximity to body. The frequency detuning is due to high permittivity of body which results in an overall increased $\varepsilon_{r,eff}$ of antenna and hence, lowers the resonant frequency of antenna. The impedance bandwidth is increased due to the losses ($\sigma \neq 0$) offered by the body. The E and H-plane patterns are also highly degraded (> 20dB with respect to those in free space). The radiation efficiency of the antenna also drops significantly from 95.7% in free space to only 2.6 % in proximity to the body model. The reason for this severe degradation is due to the zero spacing (direct contact) between the antenna and the lossy body and also the lack of a full ground plane.

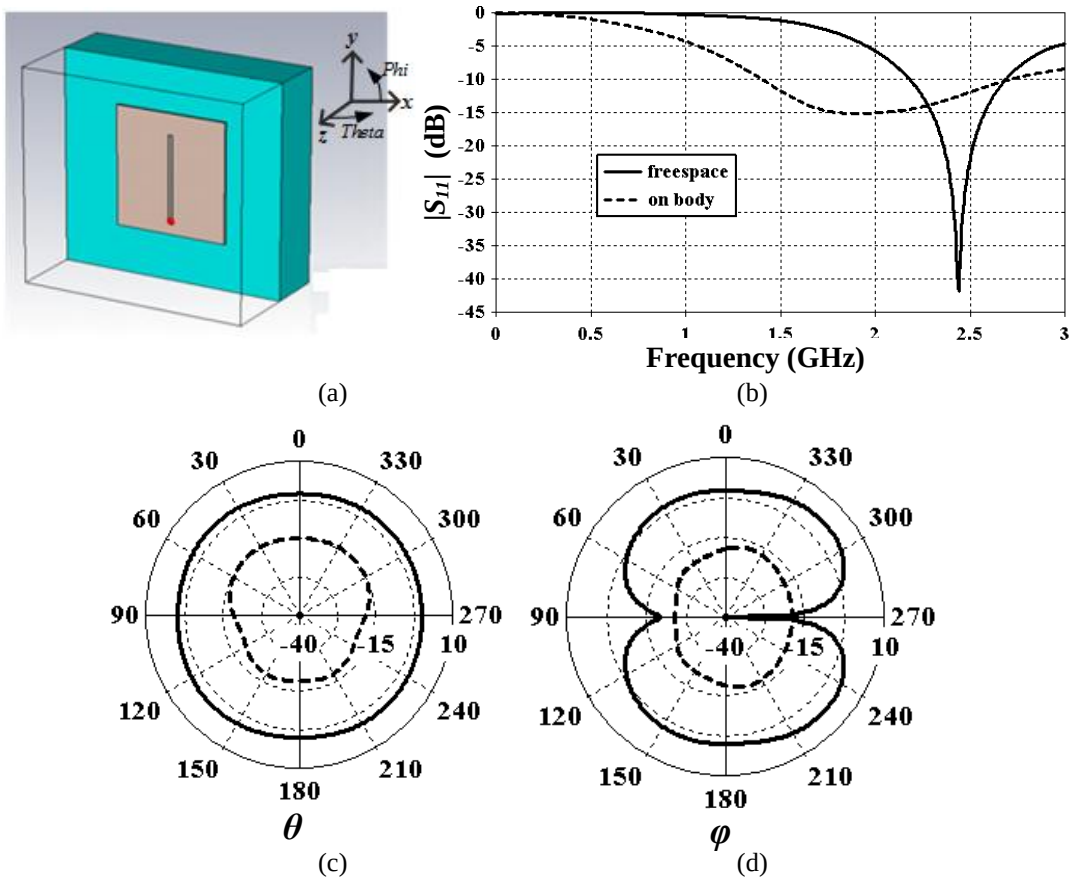

Figure 3.4. (a) Printed monopole on homogenous body model (ε_r = 37.9, σ = 1.48 S/m). (b) Simulated $|S_{11}|$ in free space compared to on body-model (c) Radiation patterns in *xz*-plane and (d) *xy*-plane at 2.45 GHz for free space (——) and body model (– – –) (reference coordinate system also shown in (a)).

Moreover, the antenna radiation is also seriously attenuated in the backward direction (Fig. 3.4 (c)). This is due to the very high attenuation of human tissue at microwave frequencies e.g., the attenuation constant α = 3.96 dB/cm @ 2.45 GHz for tissue model with ε_r = 37.9, σ = 1.48 S/m as given by (3.1) [12].

$$\alpha = \omega\sqrt{\mu\varepsilon}\sqrt{\frac{\sqrt{1+\left\{\frac{\sigma}{\omega\varepsilon}\right\}^2}-1}{2}} \text{ (Nepers/m)} \qquad (3.1)$$

which can be converted to dB/m using (3.2)

$$\alpha\ (dB/m) = \alpha\ (Np/m) \times 20/\ln 10\ dB = \alpha\ (Np/m) \times 8.686 \qquad (3.2)$$

The impact of spacing between the antenna and the body was also studied varying the inter antenna-body spacing *d* (Fig. 3.5 (a)). The variation of the reflection coefficient of the antenna as the antenna-body spacing is varied is also shown in Fig. 3.5. As evident from the results, the maximum frequency detuning is observed for minimum spacing. This is due to an overall increased $\varepsilon_{r,eff}$ due to the high tissue permittivity which lowers the resonant frequency of the antenna. However, the impact of body tissue on the resonant frequency of the antenna becomes less severe as the spacing is increased. As we approach close to the operating wavelength (λ_0=12.5 cm), the antenna reflection

coefficient also approaches that in free space and the impact of body becomes less significant as the near-field interaction of the antenna-body is reduced due to the spacing approaching the antenna far-field condition .

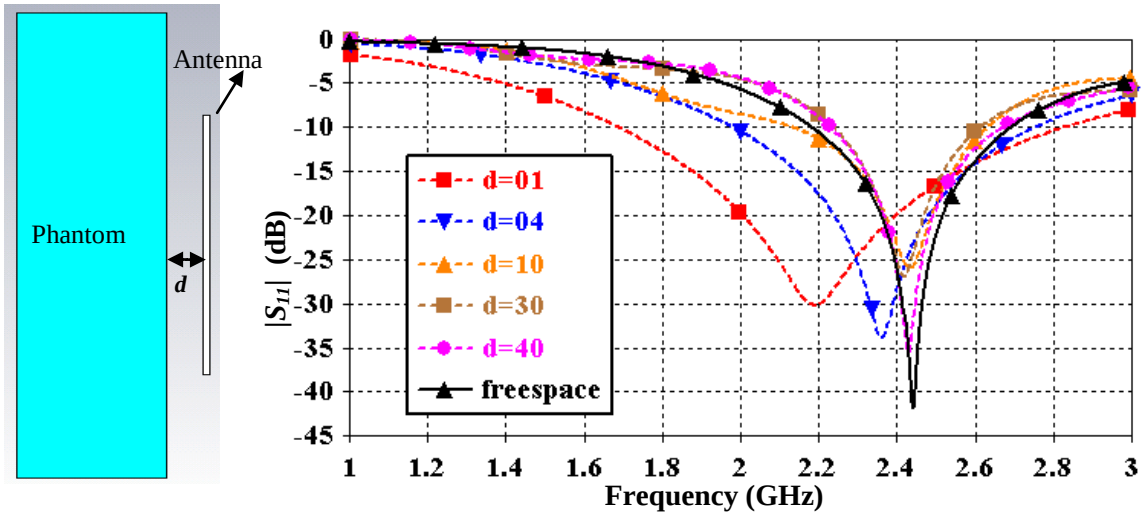

(a) (b)

Figure 3.5. (a) Printed monopole on homogenous body model (b) Reflection coefficient of the antenna when the antenna body spacing *d* (*mm*) is varied.

The impact of antenna-body spacing on the radiation patterns is also studied and the results are shown in Fig. 3.6. Again, the antenna radiation patterns are degraded, when placed with minimum spacing from the body. They improve further as the spacing is increased relative to the operating wavelength λ_0 in the broadside direction. However, there are still significant losses in the backward direction in the *xz* plane ($90° < \theta < 270°$, Fig. 3.6 (a)) even with increasing the distance *d*. This is due to the presence of body tissue in the backward direction which has high conductivity (σ = 1.48 S/m) and hence, absorbs most of the incident radiation.

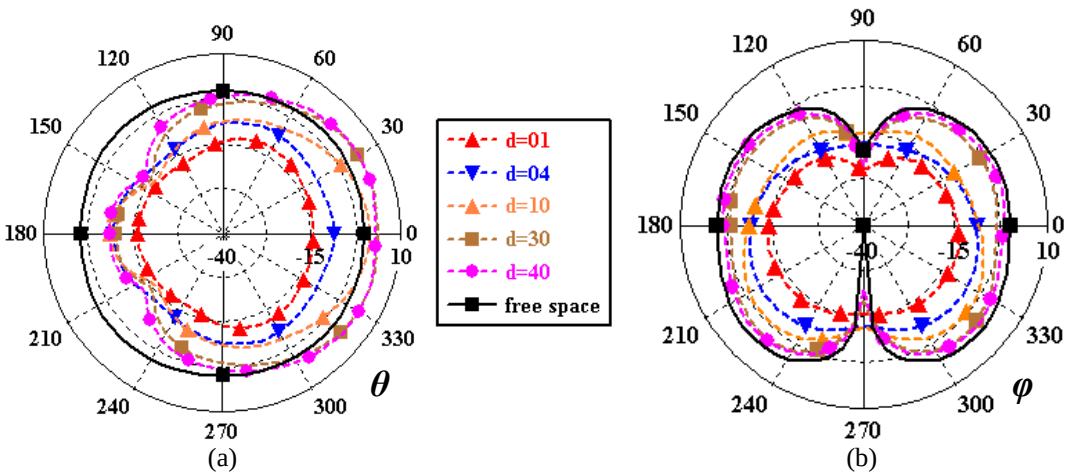

(a) (b)

Figure 3.6. Radiation patterns of printed monopole on body model when the antenna body spacing *d* (*mm*) is varied (a) in *xz*-plane and (b) *xy*-plane at 2.45 GHz for free space and body model (reference coordinate system shown in Fig. 3.4 (a)).

The simulated gain and radiation efficiency of the antenna are also provided in Table 3.1 when the spacing *d* between the antenna and body is varied compared to the reference values for free space. As evident from the numerical data, the antenna gain and radiation efficiency are seriously degraded when placed directly on the body (zero spacing) with gain and radiation efficiency of -11.4 dBi and 2.6% respectively compared to the free space values of 3.0 dBi and 95.7 % respectively. As the spacing *d* is increased relative to the operating wavelength λ_0, the antenna efficiency increases until it reaches a value close to that of free space; however the gain becomes even greater than the free space value. This is due to the high conductivity of the tissue which also causes some reflections of the radiation in the broadside direction, hence increasing the antenna gain as also evident from Fig. 3.6 (a) (e.g., for spacing of 30 and 40 *mm* compared to free space value at θ = 0°). It can also be concluded that the lossy tissue medium acts like a reflecting conducting plate [13] along with absorption of backward incident radiation.

TABLE 3.1. ANTENNA GAIN AND RADIATION EFFICIENCY VARYING ANTENNA-BODY SPACING AT 2.45 GHZ.

Spacing *d* (mm)	**Antenna gain (dBi)**	**Radiation efficiency (%)**
0	-11.4	2.6
1	-8.4	4.5
4	-3.3	10.8
10	2.9	32.2
30	6.5	84
40	6.2	92
Free space	**3.0**	**95.7**

3.3. Inverted-F antenna

An efficient antenna design for WBASN applications is a fastidious task. This is due to the close proximity of human body which has high permittivity and conductivity and causes direct interaction with the near-field of antenna. As also proved in Section 3.2, this results in distortion of the antenna radiation patterns, a shift in antenna resonant frequency along with reduction in the radiation efficiency due to absorption caused by the lossy tissue.

As already stated, for on-body applications, an omni-directional radiation along the body surface is required with a preferable polarization normal to the body surface. A monopole antenna is considered to be a good candidate for such applications however, it has a too large profile (height of $\lambda_0/4$ where λ_0=12.5 cm@ 2.40 GHz) and hence, is not a realizable solution for on-body applications which require portability and unobtrusiveness.

Therefore, at the first stage, a more appropriate solution rather than a monopole antenna for ISM 2.4 GHz on-body applications was considered. An Inverted-F antenna (IFA) was chosen since it meets the requirements of radiation pattern and polarization for on-body applications as for the case of monopole antenna. However, meanwhile it offers a much lower profile than monopole since its height is not critical parameter for controlling resonance unlike for the monopole antenna (i.e., $\lambda_0/4$). Moreover, it also includes a ground plane which can mask the near-field interaction with the body and hence can result in nearly comparable on-body performance as that of free space in the plane parallel to the body which is more crucial plane for on-body links.

The IFA can be seen as an evolution of monopole with horizontally bent arm (to reduce its height), or half-wavelength aperture or slot antenna with one end kept as open. These modifications enable IFA to preserve the good radiation efficiency of wire monopole along with low profile property of slot antenna.

3.3.1. Free space performance

The layout of the IFA is shown in Fig. 3.7. The height of the IFA (*h*) is normally small fraction of wavelength. The radiation characteristics and impedance of IFA are not strongly dependant on *h*, therefore we exploited this property to keep the height of the antenna to a minimum (i.e., $\lambda_0/12$ at 2.4 GHz instead of $\lambda_0/4$ for monopole case) and investigating the other possible degrees of freedom for required matching in ISM 2.4 GHz bandwidth (2.40-2.4835 GHz). However, the feed spacing *s* plays a central role for impedance matching and also the characteristics impedance along with the element length *l* which also controls the resonant frequency. The length of the ground plane 'h_g' should be at least $\lambda_0/4$, nevertheless lower values would result in reduction of bandwidth and efficiency of IFA. The width of ground plane 'w_g' is not so critical but should be at least equal to length '*l*' of IFA (to maintain the vertical field oriented between IFA and ground plane).

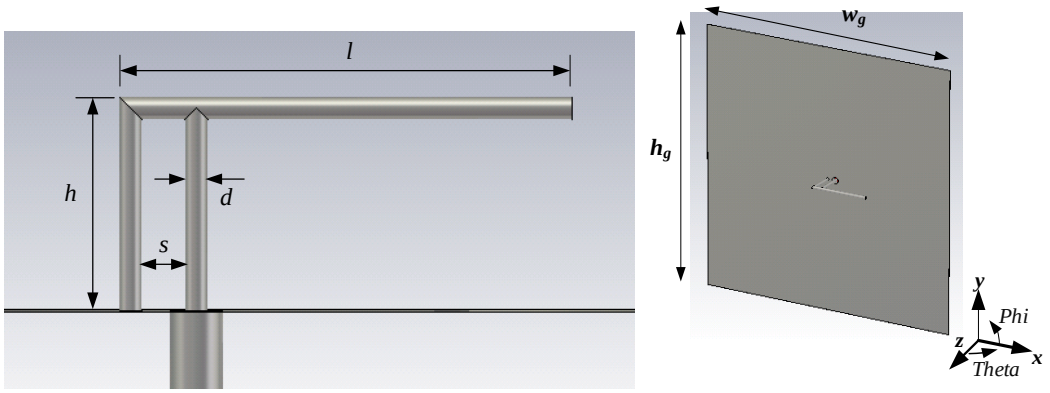

(a) (b)

Figure 3.7. Layout and important dimensions of IFA (a) Side view (b) Perspective view ($h_g = w_g = 11$ *cm*).

The dimensions of the antenna were optimized for ISM band using CST MWS. A height of $\lambda_0/12$ at 2.4 GHz was chosen instead of $\lambda_0/4$ above the ground place for the monopole case. A square ground plane of approximate dimensions of $\lambda_0 \times \lambda_0$ at 2.4 GHz was considered. Moreover, a 50-Ω coaxial feed was designed using the impedance calculator macro in CST considering standard Teflon PTFE ($\varepsilon_r = 2.1$) as the intervening dielectric medium for excitation of the antenna. This corresponds to a diameter of 1.6 *mm* for the central conductor and 5.4 *mm* for the outer conductor of coaxial feed. Also the fundamental TEM mode was excited in the coaxial feed. The reflection coefficient of the antenna is plotted in Fig. 3.8 along with the optimized dimensions for resonance inside ISM 2.4 GHz band. As evident from the reflection coefficient, the antenna offers a broad impedance bandwidth of 9% ($|S_{11}| < -10$ dB) covering the entire ISM 2.4 GHz bandwidth i.e., 2.40-2.4835 GHz. The radiation patterns of the antenna at 2.4 GHz are also shown in Fig. 3.9. They look like a monopole oriented along *z*-axis. The gain of the antenna is 5 dBi with a total efficiency of 95% (considering the mismatch loss).

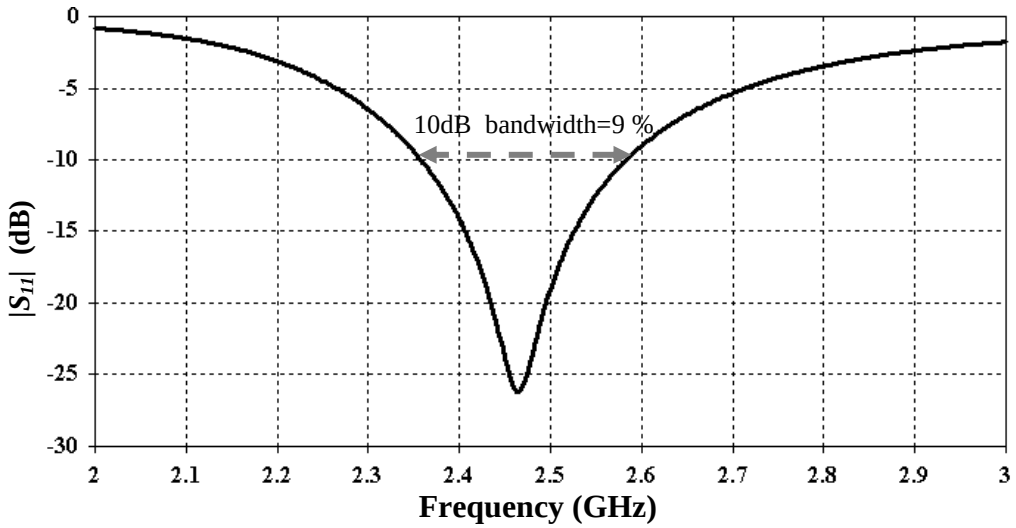

Figure 3.8. Simulated reflection coefficient of the antenna. Optimized dimensions (in *mm*) are $l = 24.1$, $h = 10.2$, $s = 2.3$, $d = 1.2$, $l_g = 110$, $w_g = 110$ in Fig. 3.7.

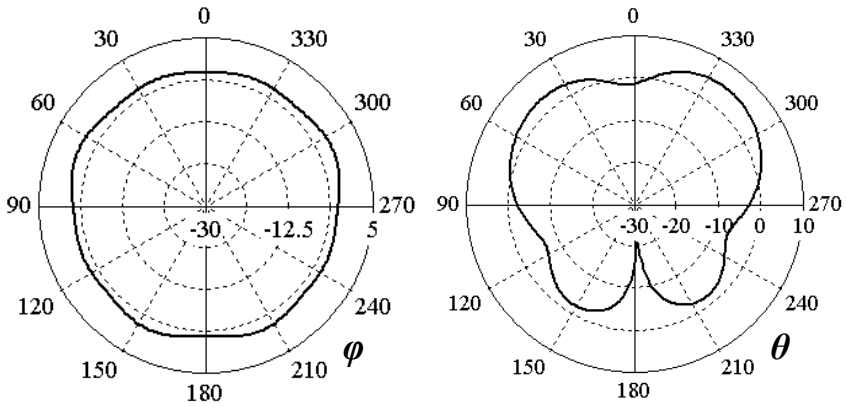

(a) (b)

Figure 3.9. Radiation patterns in (a) *xy*-plane (H-plane) and (b) *xz*-plane (E-plane) at 2.4 GHz in free space (reference coordinate system shown in Fig. 3.7 (b)).

3.3.2. On-body performance

The performance of the proposed antenna presented in Section 3.3.1 was then studied in proximity to a dispersive three-layer body model as commonly used in applications concerning BAN [14]- [15]. An infinite body model was considered (using PML absorbing boundaries) to investigate impact of body thoroughly as shown in Fig. 3.10. The tissue parameters used for body model at 2.40 GHz are listed in Table 3.2 which can be considered as nearly stable over the limited ISM 2.4 GHz bandwidth [11]. Due to the presence of the lossy media, the simulation problem size is significantly increased from 734×10^3 mesh cells for simulation problem of stand-alone antenna in free space (Section 3.3.1) to 32×10^6 mesh cells for the antenna-body problem. A spacing (d) of 2 *mm* only was retained between the antenna and body model since the antenna is fed from bottom using a coaxial feed and needs some spacing. The reflection coefficient of the antenna on the body model compared to that of free space is shown in Fig. 3.11. As evident from the results, the antenna offers stable performance in proximity to the body with acceptable resonance throughout ISM 2.4 GHz bandwidth (2.40-2.4835 GHz).

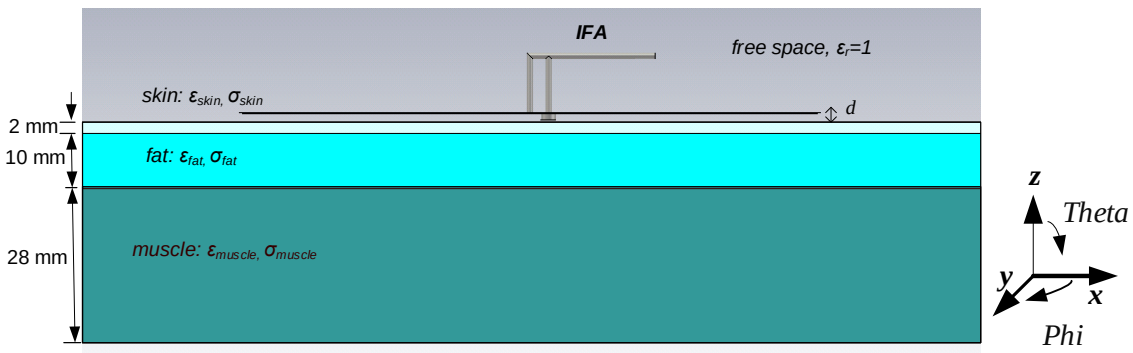

Figure 3.10. IFA placed on three layer body model, d = 2 mm (ground plane dimensions $h_g = w_g$ = 11 *cm*).

TABLE 3.2. TISSUE PARAMETERS FOR BODY MODEL AT 2.40GHz

Tissue	ε_r	σ *(S/m)*	*tan δ*
Skin	38.063	1.441	0.284
Fat	5.285	0.102	0.145
Muscle	52.791	1.705	0.242

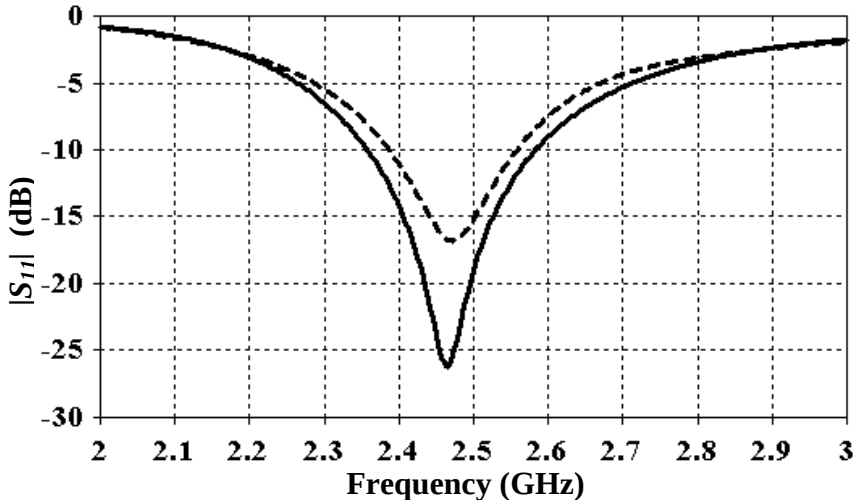

Figure 3.11. Simulated reflection coefficient of the antenna on body model (– – –) compared to that of free space (——).

The radiation patterns of the antenna in the E- and H-planes at 2.4 GHz are also shown in Fig. 3.12 on body model compared to those in free space. The gain of the antenna on the body model is 4.2 dBi with a total radiation efficiency of 77% compared to the corresponding free space values of 5 dBi and 95% respectively. Therefore, the antenna performance on the body is quite comparable to that in free space despite of a very small spacing (2 *mm*) from the body surface. This is also evident from the antenna patterns in the horizontal plane (Fig. 3.12 (a)) which is the more crucial plane for on-body links to boost them. This is due to the ground plane of the antenna which introduces a masking effect and reduces near-field interactions with the body. Moreover, the ground plane size was also varied from $0.5\lambda_0$ to $1.5\lambda_0$ (where λ_0 = 12.5 cm @ 2.4 GHz) and the far-fields were observed to be quite stable due to the masking effect of ground plane in all cases. In the elevation plane (Fig. 3.12(b)), the radiation patterns stay comparable to those in free space in the broadside direction apart from the back direction ($90° < \theta < 270°$). This is due to the body tissue which absorbs the incident radiation being dispersive with quite high conductivity and loss tangent.

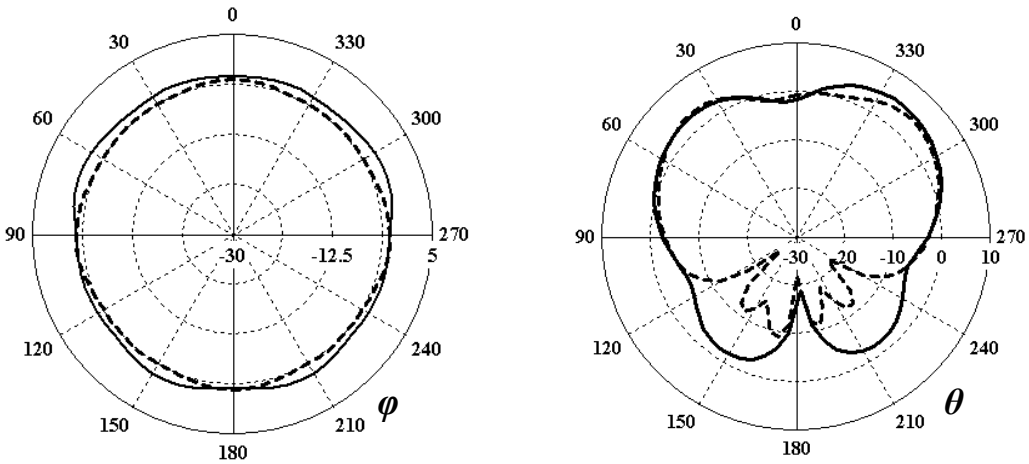

Figure 3.12. Radiation patterns of IFA in (a) *xy*-plane and (b) *xz*-plane at 2.4 GHz for free space (——) compared to on body model (– – –) (reference coordinate system for patters shown in Fig. 3.10).

3.3.3. Specific Absorption Rate Computation

For compliance constraints, the Specific Absorption Rate (SAR) was also considered for the antenna which is a measure of electromagnetic energy absorbed by biological tissue when exposed to electromagnetic radiation source (e.g. mobile phone). SAR is defined as the power absorbed per given mass of tissue contained in a given volume of a medium with density ρ and is measured in watts per kilogram (W/kg) i.e.,

$$SAR = \frac{P}{\rho} = \frac{\sigma E^2}{2\rho} \tag{3.3}$$

Typical local SAR values are averaged in tissue mass of 10*g* as specified by the Telecommunication Technology Council Agenda No. 89 and CENELEC 1995 [16]. Moreover, the maximum permissible limit is 2.0 W/kg for 10*g* SAR for European Union (EU) [17] and also for Japan and Brazil. However, for the United States (US), a maximum value of 1.6 W/kg is allowed for 1*g* mass averaged SAR as specified by the Federal Communications Commission (FCC) for the US.

The SAR was computed for the antenna on body model using CST MWS at 2.4 GHz for the same antenna-body spacing of 2 *mm* which gave nearly comparable performance on body model as that in free space (Section 3.3.2). IEEE C 95.3 standard was used for averaging using 1 W peak stimulated power. Simulated results are shown in Fig. 3.13. The maximum SAR was computed to be 0.182 W/kg which is much less than the SAR compliance standard for EU (max. SAR (10*g*) < 2W/kg).

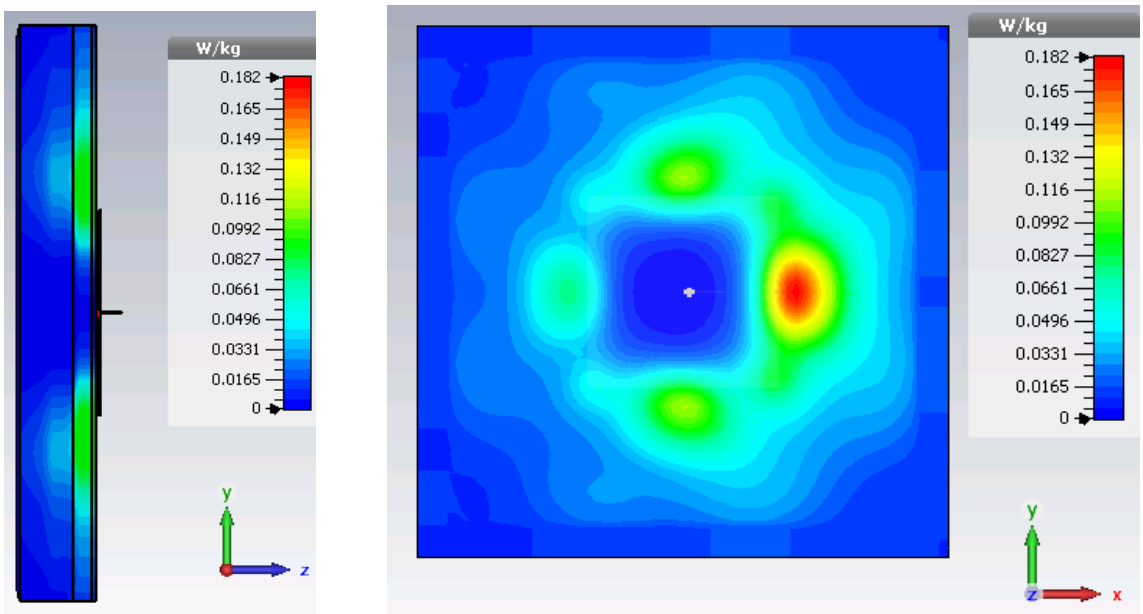

(a) (b)

Figure 3.13 10*g* SAR of IFA at 2.40 GHz (a) cross-sectional view (overall body model) (b) over the skin layer (top view).

3.4. Dual-mode Patch Antenna

As discussed in previous section, the IFA satisfies both the radiation and polarization requirements for on-body applications. However the major difficulty was the size of the ground plane which was quite large ($\lambda_0 \times \lambda_0$ @ 2.4 GHz) where $\lambda_0 = 12.5\ cm$ at 2.4 GHz. This is still quite a large size for BAN applications which require portability and unobtrusiveness. Therefore, to reduce the antenna size further, another interesting antenna was considered which is known as a Short-circuited Ring Patch Antenna (SRPA).

3.4.1. Characteristics Mode Theory

The SRPA has the beauty that it is multimode with the first two modes being TM_{01} and TM_{11} respectively. The TM_{01} mode offers an omni-azimuthal radiation pattern with a vertical polarization just like a monopole antenna (i.e., suitable for on-body links) whereas TM_{11} mode offers radiation maximum in the broadside direction similar to a rectangular patch antenna (i.e., suitable for off-body links). Moreover, the antenna offers favorable mechanical properties being low profile, unobtrusive and ergonomic which are very suitable properties for wearable applications. The analysis of the fundamental (TM_{01}) mode of this antenna has been done in [18]. In the first design stage, the characteristic mode theory of ring patch antennas was considered knowing that the radiation characteristics of such antennas can be controlled by their resonant modes [18]. The layout of the SRPA is shown in Fig. 3.14 along with its crucial dimensions.

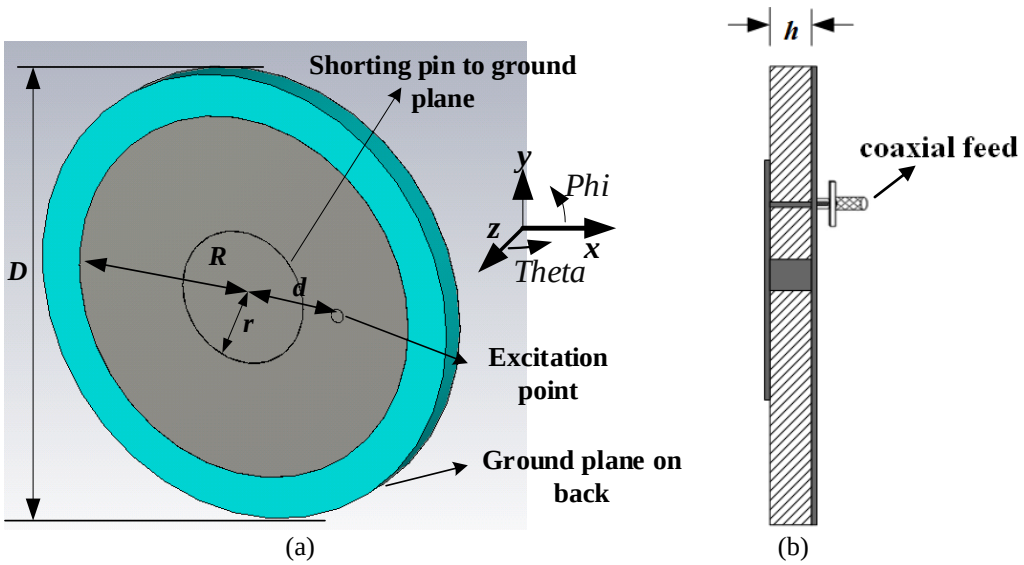

Figure 3.14. (a) Layout of shorted ring patch antenna (b) Side view.

The resonant frequencies of this antenna can be determined by (3.4) with the assumption that there are only TM modes propagating in the cavity (considering the field distribution is invariant due to the small substrate thickness i.e., $h << \lambda_0$ and that the substrate is not magnetic) [18] i.e.,

$$f_{mn} = \frac{k_{mn}.c}{2\pi R.\sqrt{\varepsilon_r}} \tag{3.4}$$

where f_{mn} corresponds to the resonant frequency of corresponding TM_{mn} mode, c is the velocity of light or electromagnetic radiation, ε_r is the permittivity of the substrate and k_{mn} correspond to the roots of the characteristic equation (3.5)

$$J_m^{'}(k_{mn})N_m(k_{mn}g) - J_m(k_{mn}g)N_m^{'}(k_{mn}) = 0 \tag{3.5}$$

which comes from the boundary conditions in a ring cavity (with electric wall for inner and magnetic wall for outer edges in the cavity model); g is the ratio r/R, $J_m(x)$ and $N_m(x)$ are the first and second kind m^{th} order Bessel functions and prime represents the first derivative [18].

The goal was to achieve both of the resonant modes at same frequency (2.4 GHz) in order to further study the interest of pattern diversity for body-centric applications. Therefore, the first design phase was to study excitation of its first two resonant modes (i.e., TM_{01} and TM_{11}) at ISM 2.45 GHz frequency.

3.4.2. TM_{01} mode

In the first design phase, the fundamental TM_{01} mode was optimized using CST MWS for first resonance at 2.45 GHz for on-body applications and second resonance at 3.1 GHz for off-body applications. A coaxial feed (50 Ω) was used to excite the antenna (Fig. 3.14) which was designed using impedance calculator macro in CST employing Teflon (ε_r = 2.1) as dielectric. The antenna was designed on substrate RT5880 with relative permittivity ε_r of 2.2 and thickness of 3.175 *mm* to achieve improved bandwidth. The overall size of the optimized antenna is 5.4 × 0.3 cm^2 (excluding the coax. feed).

3.4.2.1. Free space performance

The dimensions of the antenna were optimized using CST MWS for first resonance at 2.45 GHz and second resonance at 3.1 GHz. This idea is useful to utilize a single sensor/antenna for both on- and off-body applications where the on-body mode is operating in ISM band and the off-body mode is operating at lower edge of ultra-wide band (3.1-10.6 GHz). The simulated reflection coefficient of the antenna is shown in Fig. 3.15 showing a first resonance at 2.45 GHz for on-body mode (TM_{01}) and a second resonance at 3.1 GHz for off-body mode (TM_{11}).

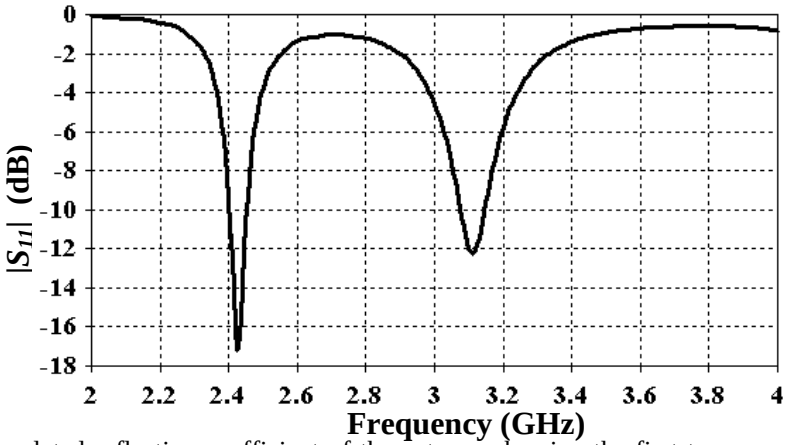

Figure 3.15. Simulated reflection coefficient of the antenna showing the first two resonances at 2.45 and 3.1 GHz respectively. Optimized dimensions in *mm*: R = 21.8, r = 8, d = 12.45, D = 53.6 in Fig. 3.14.

The surface current distribution of the antenna at 2.45 and 3.1 GHz respectively is also shown in Fig. 3.16. The current distribution of the antenna at 2.45 GHz corresponds to the TM_{01} mode and that at 3.1 GHz corresponds to the TM_{11} mode as also presented in [18]. The difference between the radiation of these two modes is also evident from the current distribution. In case of TM_{01} mode, the currents have opposite directions in the plane orthogonal to the antenna i.e. along *z*-axis, hence resulting in a null in the broadside direction, whereas for the TM_{11} mode, they have the same direction in the plane orthogonal to the antenna, hence giving maximum radiation in that direction. Consequently, the radiation of the antenna is similar in form to that of a monopole antenna at first resonant mode (TM_{01}) and that of a patch antenna at second resonant mode (TM_{11}) making it suitable for both on-body and off-body applications.

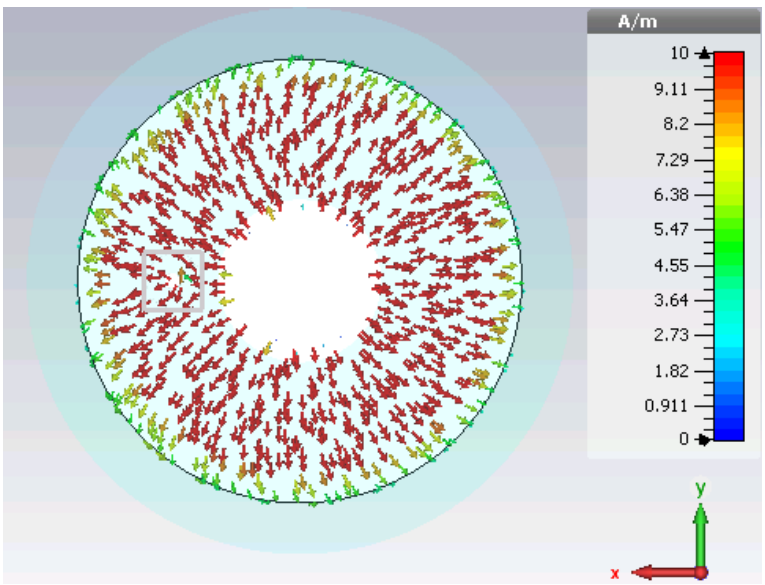

(a)

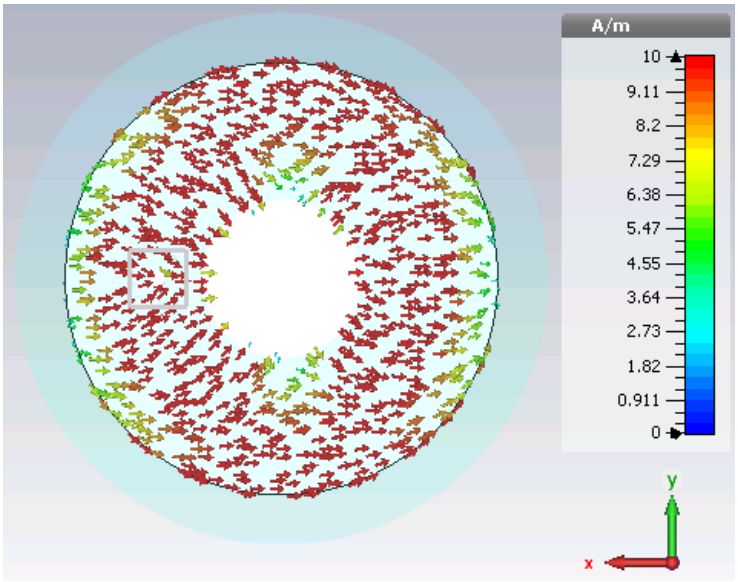

(b)

Figure 3.16. Surface current distribution (a) at 2.45 (TM_{01} mode) and (b) 3.1 GHz (TM_{11} mode).

The 3D radiation patterns of the two resonant modes (TM_{01} and TM_{11}) are also illustrated in Fig. 3.17. The antenna gain reaches 1.13 dBi at 2.45 GHz with a total efficiency of 91% for the fundamental TM_{01} mode. The gain for the TM_{11} mode is 7.75 dBi with a total efficiency of 93.5% at 3.1 GHz. The gain and efficiency at 3.1 GHz is higher than that at 2.45 GHz because the TM_{11} mode here is a directional mode. Therefore, the antenna generates a radiation with the maximum in the azimuth direction at 2.45 GHz to boost the on-body links and a maximum radiation in the broadside direction at 3.1 GHz to boost the off-body links.

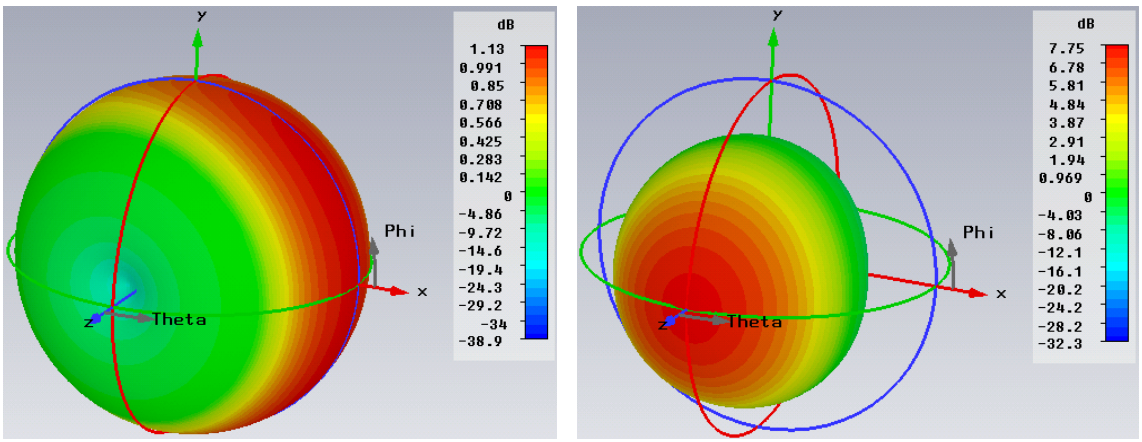

(a) (b)

Figure 3.17. 3D radiation patterns of the antenna at (a) 2.45 GHz and (a) 3.1 GHz (Coordinate system shown in Fig. 3.14).

The 2D radiation patterns of the antenna are also shown in Fig. 3.18 for the two modes. The patterns again show a maximum radiation in the azimuth direction (*xy*-plane) for the TM_{01} mode at 2.45 GHz and in the elevation direction (*xz*-plane) for the TM_{11} mode at 3.1 GHz.

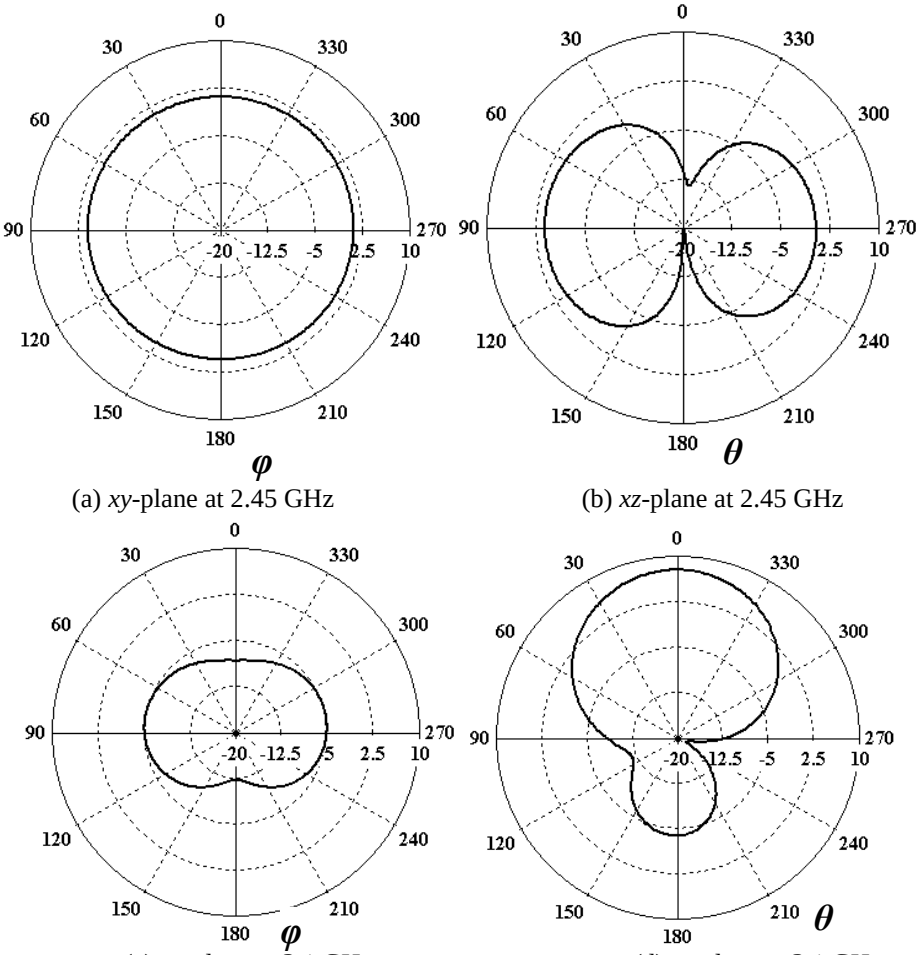

(a) *xy*-plane at 2.45 GHz (b) *xz*-plane at 2.45 GHz

(c) *xy*-plane at 3.1 GHz (d) *xz*-plane at 3.1 GHz

Figure 3.18. Radiation patterns of the two resonant modes (TM_{01} and TM_{11}) at 2.45 GHz and 3.1 GHz (coordinate system shown in Fig. 3.14).

3.4.2.2. Performance in proximity to body

To investigate antenna performance on the body, the SRPA was placed on a lossy uniform body model equivalent to muscle tissue properties [6]. In order to consider the frequency dependency, the two scenarios of on- and off-body resonant modes (i.e., TM_{01} and TM_{11} respectively) were studied separately using different equivalent tissue parameters i.e., permittivity ε_r and conductivity σ based on the operating frequency.

a. On-body resonant mode

To investigate antenna performance for on-body resonant mode i.e., TM_{01} at 2.45 GHz, the antenna was placed on a realistic full body phantom imported from a commercial CAD program POSER^{TM} [19] in CST MWS^{TM} as shown in Fig. 3.19. To consider lossy tissue impact, dielectric properties of uniform muscle tissue at 2.45 GHz i.e., ε_r=52 and σ = 1.7 S/m were allocated to the phantom [6]- [7]. These tissue parameters are appropriate for modeling a uniform body and have been widely considered in BAN literature e.g., [4], [6]-[10]. A minimal spacing (≈0.1 *mm*) was maintained between the antenna and body to consider maximum impact. However, due to

the non-conformal body shape, the spacing is non-uniform indeed. This simulation problem comprised of a mesh size of 31×10^6 cells which took a simulation time of around 188 minutes on a CST server with Intel Xeon 2.60 GHz CPU and 128 GB of RAM for full-wave simulation results.

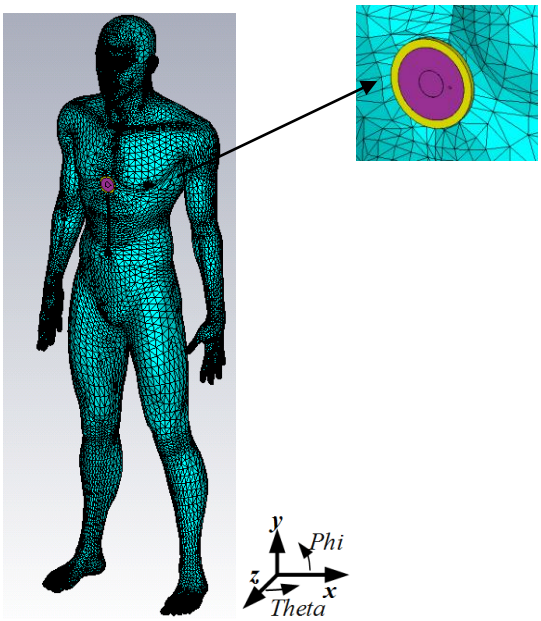

Figure 3.19. (a) Placement of the antenna on a realistic 3D ghost phantom.

The reflection coefficient of the antenna in proximity to the body model is shown in Fig. 3.20 compared to that in free space. As evident from the results, the antenna offers nearly stable performance in proximity to body. There is no noticeable frequency detuning which is indeed due to the full ground plane of the antenna which masks the near-field interaction with the body. The radiation patterns of the antenna for the fundamental resonant mode at 2.45 GHz are also shown in Fig. 3.21 for body model compared to those in free space. The gain of the antenna on the body model is 2.2 dBi compared to 1.13 dBi at 2.45 GHz in free space. This increase in gain is due to the high tissue conductivity (σ = 1.7 S/m) which causes some reflection in the broadside direction as also evident from the antenna gain in the elevation plane (i.e., *xz*- plane in Fig. 3.21 (b)). However, the total radiation efficiency of the antenna falls to 49% compared to the free space value of 91% due to the body proximity.

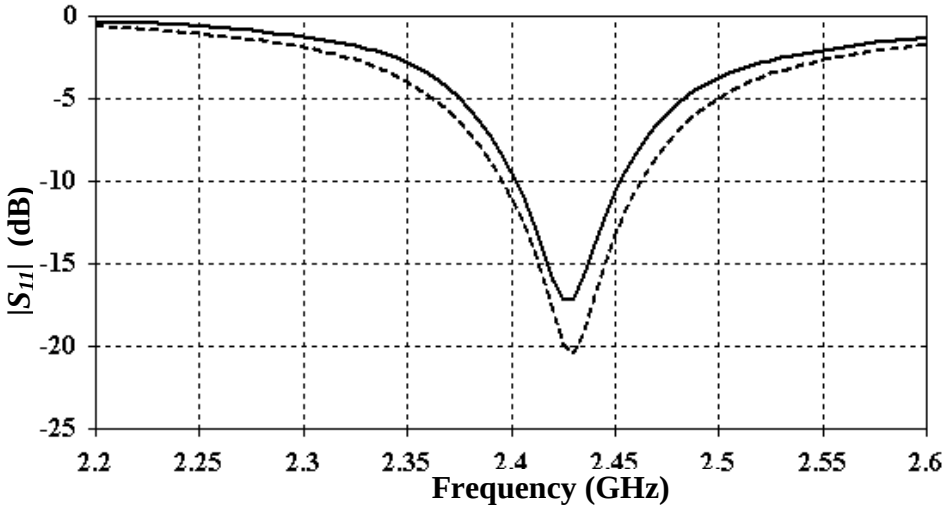

Figure 3.20. Reflection coefficient of the antenna for first resonant mode on body model (– – –) compared to that of free space (——).

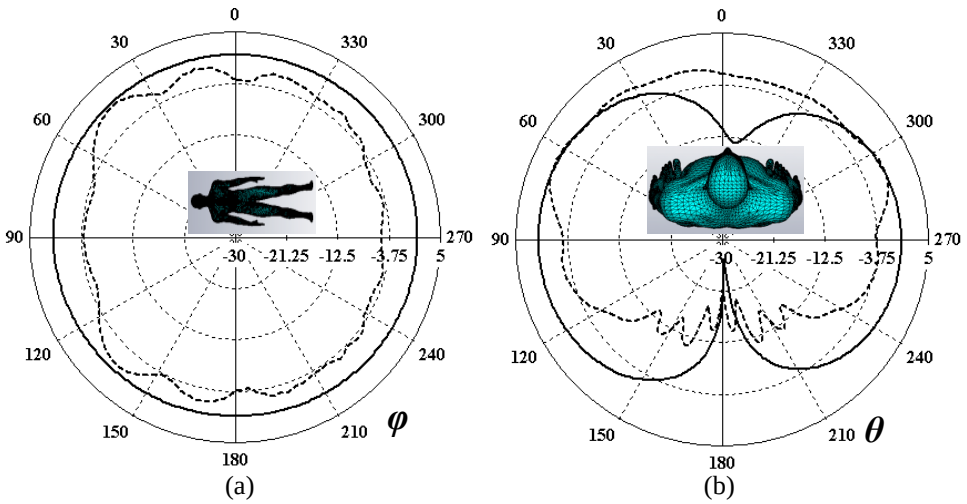

(a) (b)

Figure 3.21. Radiation patterns of the fundamental resonant mode (TM_{01}) at 2.45 GHz in (a) *xy*-plane and (b) *xz*-plane on body model (– – –) compared to those in free space (——) (coordinate system shown in Fig. 3.19).

b. Off-body resonant mode

To investigate antenna performance for off-body resonant mode i.e., TM_{11} mode at 3.1 GHz, the antenna was again placed on the same realistic ghost phantom imported from the CAD program POSER^{TM} [19] in CST MWS^{TM} as shown in Fig. 3.19. However, now the uniform muscle tissue properties at 3.1 GHz were used i.e., ε_r = 52 and σ = 2.2 S/m [9]. Again the same minimal spacing (≈ 0.1 *mm*) was maintained between the antenna and body.

The reflection coefficient of the antenna on the body model is shown in Fig. 3.22 compared to that in free space. Again, the antenna offers nearly stable performance in proximity to body with $|S_{11}|$ < -10 dB at 3.1 GHz. The radiation patterns of the antenna for the TM_{11} resonant mode at 3.1 GHz are also represented in Fig. 3.23 for body model compared to those in free space. The gain of the antenna on the body model is 7.3 dBi compared to free space value of 7.8 dBi at 3.1 GHz. The total radiation efficiency of the

antenna also falls to 78.4% compared to the free space values of 93.5% due to the body proximity which is still quite acceptable value since the antenna-body spacing was quite small (≈ 0.1 *mm*). The efficiency improves as the spacing increases (as presented in Section 3.2.2).

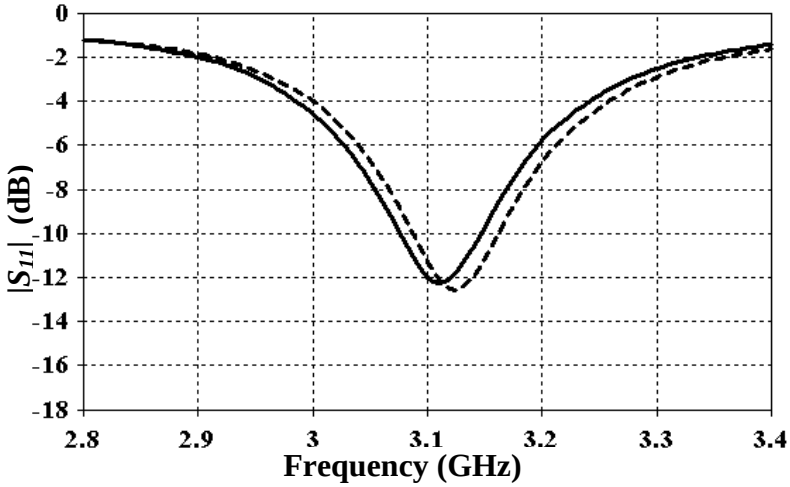

Figure 3.22. Reflection coefficient of the antenna on-body model (– – –) compared to that in free space (——).

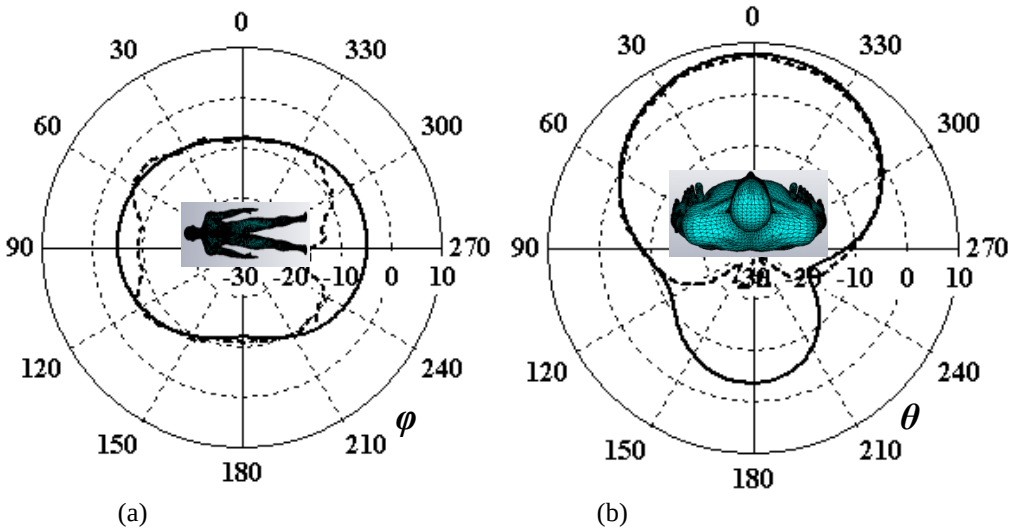

(a) (b)

Figure 3.23. Radiation patterns of the off-body resonant mode (TM_{11}) at 3.1 GHz in (a) *xy*-plane and (b) *xz*-plane on body model (– – –) compared to those in free space (——) (coordinate system shown in Fig. 3.19).

Also the radiation is significantly attenuated in the backward direction ($90° < \theta < 270°$) (Fig. 3.23 (b)) which is due to the high tissue conductivity (σ = 2.2 S/m). This causes absorption of most of the incident radiation as also evident from the *E*-field distribution in Fig. 3.24.

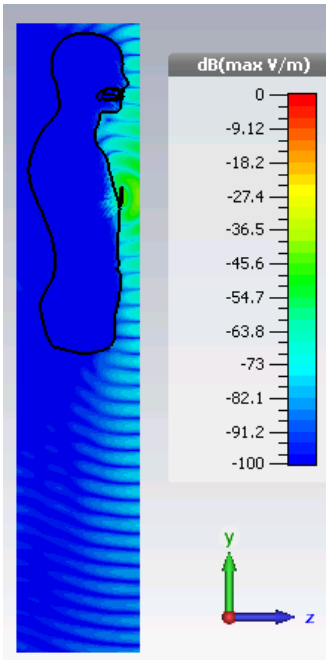

Figure 3.24 Electric field distribution at 3.1 GHz inside the body model (cutting plane through the middle section of the body model in *yz*- plane).

3.4.3. TM_{11} mode

The multiple modes of a SRPA are also an interesting application for the design of a pattern and polarization diversity antenna at same frequency e.g., ISM 2.45 GHz. In order to study the excitation of both modes at same frequency, the antenna (as shown in Fig. 3.14) was also optimized to excite the second order mode (TM_{11}) at ISM 2.45 GHz using CST MWS^{TM} after various parametric studies. The first mode in this case is detuned and at a lower frequency (1.8 GHz) which is redundant for our application. Again, the same substrate RT/duroid 5880 with relative permittivity ε_r of 2.2 and thickness of 3.175 *mm* was used. A coaxial feed (50 Ω) was designed (with diameter of 1.6 *mm* and 5.4 *mm* for the central and outer conductors respectively) to excite the antenna using impedance calculator macro in CST considering Teflon PTFE (ε_r = 2.1) as dielectric. The coaxial feeds were excited under the fundamental TEM mode. The overall size of the optimized antenna is 6.2×6.2×0.3 cm^3 (excluding the coaxial feed). The simulated reflection coefficient of the antenna is shown in Fig. 3.25 showing the second order resonance at 2.45 GHz which corresponds to the TM_{11} mode.

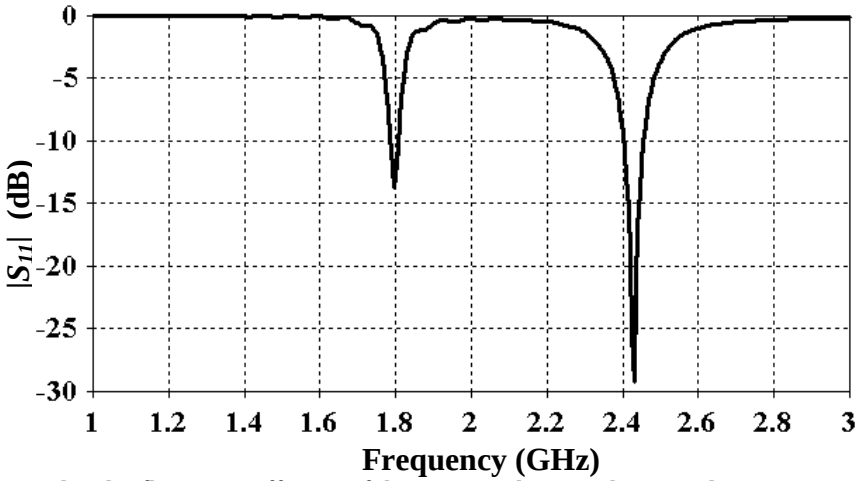

Figure 3.25. Simulated reflection coefficient of the antenna showing the second resonance at 2.45 GHz. Optimized dimensions in *mm*: R = 26, r = 7.5, d = 11.45, D = 62 in Fig. 3.14.

The surface current distribution of the antenna for the second resonant mode at 2.45 GHz is also shown in Fig. 3.26. This current distribution corresponds to the TM_{11} mode as also presented in [18]. Such a current distribution plays the key role in the radiation pattern of the antenna. Since the currents have same direction in the plane orthogonal to the antenna i.e. along *z*-axis, the antenna has maximum radiation in that direction. Consequently, the radiation of the antenna is similar in form to that of a patch antenna oriented along *xy*-plane (Fig. 3.26) at the second resonant mode (TM_{11}).

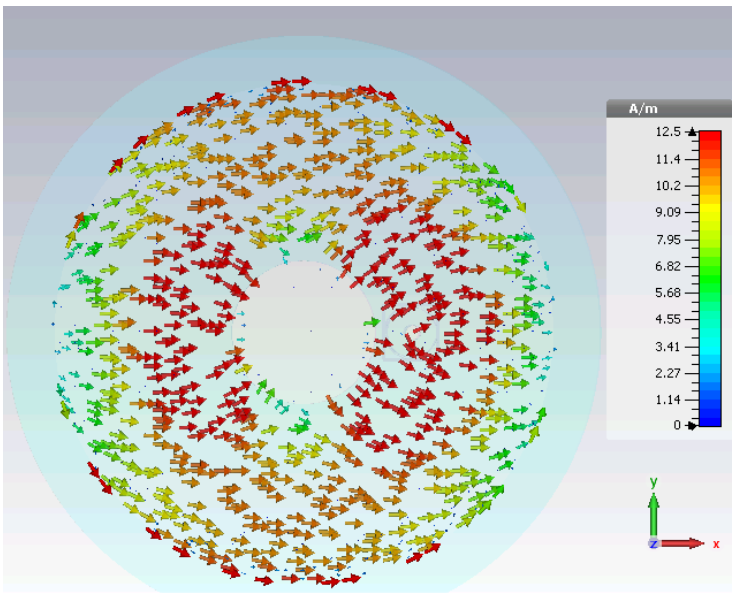

Figure 3.26. Surface current distribution of the antenna at 2.45 GHz.

The 3D radiation pattern of the antenna at 2.45 GHz is also illustrated in Fig. 3.27 along with the corresponding 2D patterns in E- and H-planes shown in Fig. 3.28. The antenna gain reaches 7.3 dBi at 2.45 GHz. Such a maximum radiation in the broadside direction at 2.45 GHz also makes this antenna suitable for off-body applications to boost the links with gateway devices which are situated away from the body.

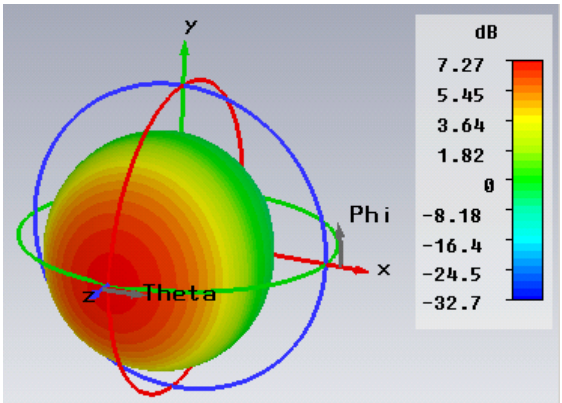

Figure 3.27.3D radiation patterns of the antenna at 2.45 GHz (coordinate system shown in Fig. 3.14).

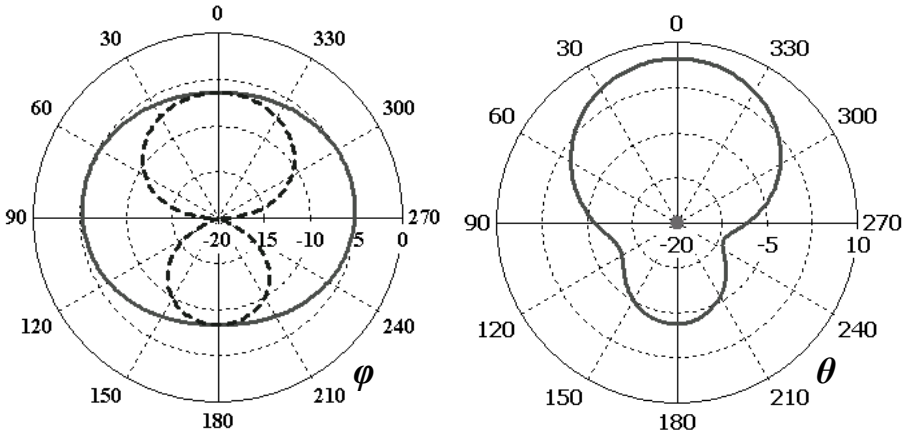

(a) (b)

Figure 3.28. Radiation patterns of the TM_{11} mode for (a) *xy*-plane (E-plane) and (a) *xz*-plane (H-plane) at 2.45 GHz showing co-polarization (——) and cross-polarization (– – –) (coordinate system shown in Fig. 3.14).

This concept of exciting multiple modes at same frequency (ISM 2.458 GHz) will be further used in Chapter 5 for the design of a single antenna offering both pattern and polarization diversities simultaneously for body-centric applications.

3.5. Conclusions

The impact of human body on the antenna performance has been studied. The body has been found to significantly distort the antenna performance due to high tissue parameters at ISM frequencies. The frequency has been found to detune and the radiation efficiency drops compared to the free space values. It has been shown that the on-body performance can be improved by increasing the antenna-body spacing. This impact is less severe for antennas with complete ground plane and they need comparatively less spacing for a stable on-body performance.

An Inverted-F antenna has been designed covering full ISM 2.4 GHz bandwidth with appropriate radiation and polarization requirements as needed for on-body applications. Meanwhile, it offers much lower profile than a monopole antenna (height of $\lambda_0/12$ @ 2.4 GHz instead of $\lambda_0/4$ for the monopole case). Its 10g SAR was also computed and found to be much lower than the international compliance standards.

Finally, a compact dual-mode patch antenna has been designed with appropriate radiation characteristics for both on- and off-body applications for ISM 2.45 GHz and UWB 3.1 GHz respectively. The performance of the antenna has been evaluated in proximity to body for both on- and off-body modes (TM_{01} and TM_{11} respectively) and has been found to be quite comparable to the free space performance. Both modes were also matched at same frequency (2.45 GHz) using all degrees of freedom. This concept will be further used in Chapter 5 to integrate two antennas excited under different modes in a single package for the design of a pattern and polarization diversity antenna.

References

[1] P. S. Hall and Y. Hao, Antennas and Propagation for Body-Centric Wireless Communications, Norwood, MA, USA: Artech House, Inc, 2006.

[2] S. Dumanli, "On-body antenna with reconfigurable radiation pattern," in *RF and Wireless Technologies for Biomedical and Healthcare Applications (IMWS-Bio)*, London (UK), Dec. 2014 .

[3] A.A. Serra, I. Khan, P. Nepa, G. Manara, P.S. Hall, "Dual-polarization and dual-pattern planar antenna for diversity in body-centric communications," in *Antennas and Propagation Society International Symposium*, 2008.

[4] T. Alves, B. Poussot, and J. M. Laheurte, "Analytical propagation modeling of BAN channels based on the creeping-wave theory," *IEEE Transactions on Antennas and Propagation*, vol. 59, no. 4, pp. 1269 - 1274, 2011.

[5] P. Kyritsi, and D. C. Cox, "Propagation characteristic of horizontally and vertically polarized electric fields in an indoor environment: simple model and results," in *IEEE vehicular Technology Conference*, 2001.

[6] L. A-Asl, P. S.Hall, Y. Nechayev, and I. Khan, "Depolarization in On-Body Communication Channels at 2.45 GHz," *IEEE Transcatiosn on Antennas and Propagation*, vol. 61, no. 2, pp. 882-889, 2013.

[7] K. LUOSTARINEN, M. A. JADOON, J. SILTANEN, and T. HÄMÄLÄINEN, "Spatial Diversity and Correlation for MIMO in BANs: Parametric Simulation Scheme," in *Proceedings of the 6th international conference on Communications and Information Technology*, , Wisconsin, USA, 2012.

[8] D.D. Cara, J. Trajkovikj, R. T. Sanchez, J. Zurcher, A.K. Skrivervik, "A low profile UWB antenna for wearable applications: The tripod kettle antenna (TKA)," in *7th European Conference on Antennas and Propagation (EuCAP)*, , Gothenburg, 8-12 April 2013.

[9] K. Fuji, M. Takahashi, K. ITO, and N. Inagaki, "Study on the electric field distributions around whole body model with a wearable device using the human body as a transmission channel," in *First European Conference on Antennas and Propagation*, , Nov. 2006.

[10] P.S. Hall, Y. Hao, Y. I. Nechayev, A. Alomainy, C. C. Constantinou, C. Parini, M. R. Kamarudin, T. Z. Salim, D. T. M. Hee, R. Dubrovka, A. S. Owadally, S. Wei, A. Serra, P. Nepa, M. Gallo, M. Bozzetti, "Antennas and propagation for on-body communication," *IEEE Antennas and Propagation Magazine*, , vol. 49, no. 3, pp. 41 - 58, June 2007.

[11] "http://niremf.ifac.cnr.it/tissprop/," [Online].

[12] I. Yamaura, "Measurements of 1.8 - 2.7-Ghz Microwave Attenuation in the Human Torso," *IEEE Transactions on Microwave Theory and Techniques*, vol. 25, no. 8, pp. 707-710, Aug. 1977.

[13] K. L. Wong and C. I. Lin, "Characteristics of a 2.4-GHz compact shorted patch antenna in close proximity to a lossy medium," *Microw. Opt. Technol. Lett.*, vol. 45, no. 6, p. 480–483, Jun. 2005.

[14] D. Ma, and W. X. Zhang., "A dual-band dual-polarized antenna for body area network," in *Proceedings of the Fourth European Conference on Antennas and Propagation (EuCAP)*, Barcelona, Spain, April 2010.

[15] Vladimír Hebelka, "Planar Antennas in Proximity of Human Body Models," *Elektrorevue*, vol. 3, no. 4, December 2012.

[16] "https://www.cst.com/," [Online].

[17] "Mobiltelefoner och Strålning," Sweden's Radiation Protection Authority, Tech. Rept., 2003.

[18] V. G. Posadas, D. S. Vargas, E. R. Iglesias, J.L. Vazquez-Roy, C. M. Pascual, "Approximate analysis of short circuited ring patch antenna working at TM01 mode," *IEEE Transactions on Antennas and Propagation*, vol. 54, no. 6, pp. 1875-1879, Jun. 2006.

[19] "http://my.smithmicro.com/poser-pro-2014.html," [Online].

[20] R. Anupam, R. Chandran, G. A. Conway and W. G. Scanlon, "Pattern switching compact patch antenna for on-body and off-body communications at 2.45 GHz," in *3rd European Conference on Antennas and Propagation*, Berlin, Germany, March 2009 .

[21] T. Alves, B. Poussot, and J. M. Laheurte, "Analytical propagation modeling of BAN channels based on the creeping-wave theory," *IEEE Transactions on Antennas and Propagation*, vol. 59, no. 4, pp. 1269 -1274, 2011.

[22] D. Ma, and W.-X. Zhang, "Coupling-fed circular-patch antenna for onbody communication system," *Microwave & Optical Tech. Lett.*, vol. 51, no. 11, pp. 2623-2627, November 2009.

[23] G. A. Conway, W. G. Scanlon, "Antennas for over-body-surface communication at 2.45 GHz," *IEEE Transactions on Antennas and Propagation*, vol. 57, no. 4, pp. 844 - 855, April 2009.

[24] "http://johansontechnology.com/," [Online].

[25] L. Vallozzi, W. Vandendriessche, L. Vallozzi, W. Vandendriessche, H. Rogier, C. Hertleer, and M. L. Scarpello, "Wearable textile GPS antenna for integration in protective garments," in *Europ. Conf. Antennas Propag., EuCAP'2010*, Barcelona, Spain, Apr. 12.

[26] M. M. Khan, A. Alomainy, and Y. Hao, "Dual band and diverse radiation pattern antenna for power efficient and reliable on-body and off-body communications for healthcare applications," in *IEEE Ant. Propag. Society Int. Symp.*, Spokane (WA), Jul. 2011.

[27] S. Blanch, J. Romeu, and I. Corbella, "Exact representation of antenna system diversity performance from input parameter description," *Electron. Lett.*, vol. 39, no. 9, p. 705–707, 2003.

[28] Bon Guo, "Antenna diversity in mobile phone," MS Thesis, Chalmers university of technology (department of signals and systems), Sweden, 2008.

[29] Kent Rosengren, P-S. Kildal, "Radiation efficiency, correlation, diversity gain and capacity of a six monopole antenna array for a MIMO system: Theory, Simulation and Measurement in Reverberation Chamber," *Proceedings IEE, Microwaves,*

Optics and Antennas, vol. 152, no. 1, pp. 7-16, Feb. 2005..

[30] G. Vaughan and J. Bach Andersen, "Antenna diversity in mobile communications," *IEEE Trans. Veh. Technol.*, vol. 36, 1987.

[31] "http://www.satimo.com/," [Online].

Chapter 4. Miniaturized chip antenna design and numerical channel simulator

Contents

4.1. Introduction

BoWI is based on a body-centric wireless network of various sensors at different on-body locations and further using a set of body postures (called alphabets) to interact with the digital world as discussed in Chapter 1. Therefore, one of the prime objectives of the radio sub-project was to develop a numerical channel simulator. Such a simulator should be able to simulate radio communication scenarios under specific BoWI posture grammar to investigate the link budget corresponding to various on-body links. Moreover, the channel simulator should have the power to simulate any arbitrary WBASN scenario with varying body posture, and sensor/antenna locations etc. under limited simulation resources to predict the real-life performance.

The realistic body morphology is a very important factor for evaluating on-body propagation which plays a significant role in body-centric transmission scenarios. The simplistic body models made up of regular geometric blocks e.g., the parallelepipedic ones [1]- [2] are useful for dosimetry studies along with antenna characterization stand-alone. However, when multiple on-body links are considered, these models are not appropriate, since the on-body propagation can vary significantly between the multiple communicating nodes due to the non-conformal body surface. Moreover, the antenna-body spacing is also non-uniform in real-life applications due to the non-planar body surface, compared to the planar surface of such standard geometrical models [1]- [3] which offer uniform spacing. However, the spacing has crucial impact on antenna performance for body-centric applications as also discussed in Chapter 3. Therefore, despite of their simplicity, such geometrical models are not suitable for numerical channel studies for reliable results.

The first task was hence, to explore a tool which can generate realistic 3D body models along with the possibility to influence the body postures as desired for the BoWI posture alphabets. Therefore, we investigated the BAN simulation application of some of such commercial tools as those used by artists/designers e.g., DAZ 3D® [4], POSER® [5]. These tools offer the possibility of exporting postured 3D ghost phantoms directly in full wave simulation tools (e.g., CST MWS) and hence can be used for body-centric simulations as well.

The second biggest challenge in simulating the full body models involves the computational complexity caused by the resulting electrically extraordinary large size of the body-centric simulation problem due to two main factors i.e., quite large height of the human body for realistic simulation results, and quite high values of human tissue parameters at ISM frequencies e.g., a human model of height 1.8 *m* corresponds to 104λ @ 2.4GHz (for a homogenous medium with ε_r = 52) resulting in an unreasonably large computation problem size (with multi-billion mesh cells). Such a simulation problem is not realizable to be stored on a computer's limited memory resources. Exhaustive steps were undertaken to realize the simulation results while well considering the convergence of simulation problem in each case, resulting in reliable and stable results. Once the various posture grammar are simulated, the results can be applied to identify the body gestures for interactive gesture recognition concept as the one of BoWI project and also for posture classification.

This chapter is organized as follows. In Section 4.2, the design and implementation of a miniaturized meander chip antenna is presented along with its characterization in both free space and on human body. In Section 4.3, the development of WBASN channel simulator is presented along with various considerations in CST MWS. The validation of the 3D body models for BAN simulation is presented here along with necessary preventive measures which should be carefully taken using such 3D, CAD based body models in full-wave simulation tools as CST MWS. The convergence and accuracy of simulation results is also presented here along with demonstration of the power of simulator with few examples from BoWI posture grammar. The application of the simulator for posture classification is also discussed. Finally, conclusions are drawn in Section 4.4.

4.2. Meander Chip Antenna

As discussed in Chapter 2, BoWI project employs specific prototype sensors with miniaturized chip antennas having overall dimensions of few *mm* only. Therefore, in order to approximate the radiation patterns of the BoWI prototype chip antennas in simulation, a miniaturized antenna model was first required to obtain reliable simulation results. As presented in Chapter 2, the radiation pattern of the chip antennas of the BoWI prototype is similar in form to that of a monopole antenna. With that reference, a miniaturized meander chip antenna (MCA) was first designed to roughly approximate the radiation characteristics of Zyggie chip antenna. .

4.2.1. Performance in free space

An electrically small chip antenna was designed inspired by the one proposed in [6] using extensive simulation studies in CST MWS to achieve a resonance inside ISM 2.4 GHz bandwidth (2.40-2.4835 GHz). The laminate RO3010 having ε_r = 10.2, and h = 0.635 *mm* was chosen for size reduction. The overall size of the designed chip is 9.5 × 4 × 0.635 mm^3 which corresponds to an approximate length of $\lambda_0/13$ only at 2.40 GHz. The layout and dimensions of the optimized MCA are shown in Fig. 4.1. For simulation, the MCA was fed by a 50-Ω microstrip line (having width of 0.59 *mm*) designed on the same laminate RO3010 (ε_r = 10.2, h = 0.635 *mm*) as MCA itself. There is no ground plane under the antenna, however the implementation includes the ground plane of the microstrip feed line. The major electric field of the antenna is along *y*-axis in Fig. 4.1 since the currents in the meander line are aligned along *y*-axis whereas along *x*-direction the currents cancel each other, being equal and opposite. Therefore, the radiation pattern of the antenna is similar in form to that of a monopole oriented along *y*-axis (Fig. 4.1). The simulated reflection coefficient of the antenna is represented in Fig. 4.2 showing that the antenna resonates in the ISM 2.4 GHz band with $|S_{11}| < -10$ dB throughout ISM 2.4 GHz bandwidth (2.40-2.4835 GHz).

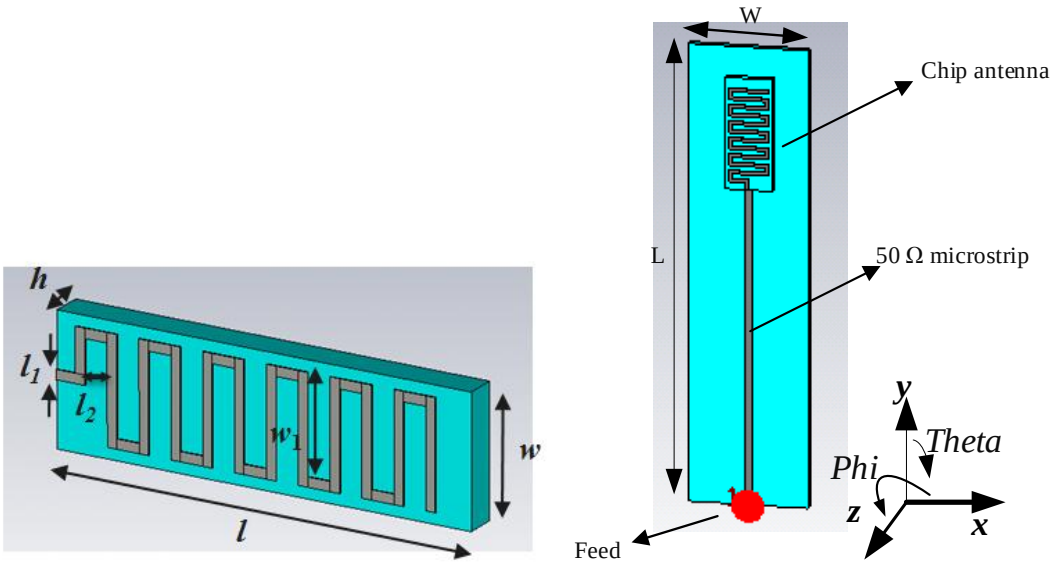

(a) (b)

Figure 4.1 (a) Layout of MCA with dimensions (mm): l = 9.5, w = 4, h = 0.635, l_1= 0.3, l_2= 0.4, w_1= 3 (b) MCA with a 50Ω microstrip matched to the antenna, dimensions (*mm*): L = 39, W = 10.

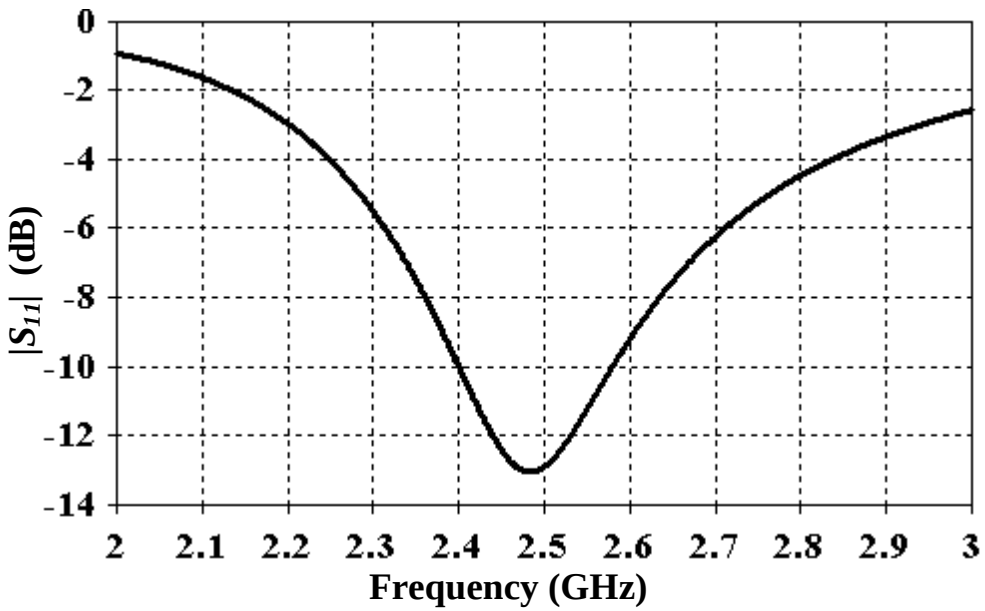

Figure 4.2. Simulated reflection coefficient of MCA in free space.

The 3D radiation pattern of the antenna at 2.45 GHz is illustrated in Fig. 4.3 which shows that the radiation pattern of the chip antenna matches in form to that of a monopole antenna oriented along *y*-axis. The radiation patterns of the chip antenna in the *E*- and *H*-planes are also plotted in Fig. 4.4 showing both the co- and cross-polarization components (E_{theta} and E_{phi} respectively). The principal polarization of the chip antenna is in the theta plane (co-polarization) which is the *xy*-plane of the coordinate system (Fig. 4.1 (b)). The antenna offers a horizontal ***E***-field polarization i.e., parallel to the principal axis of antenna.

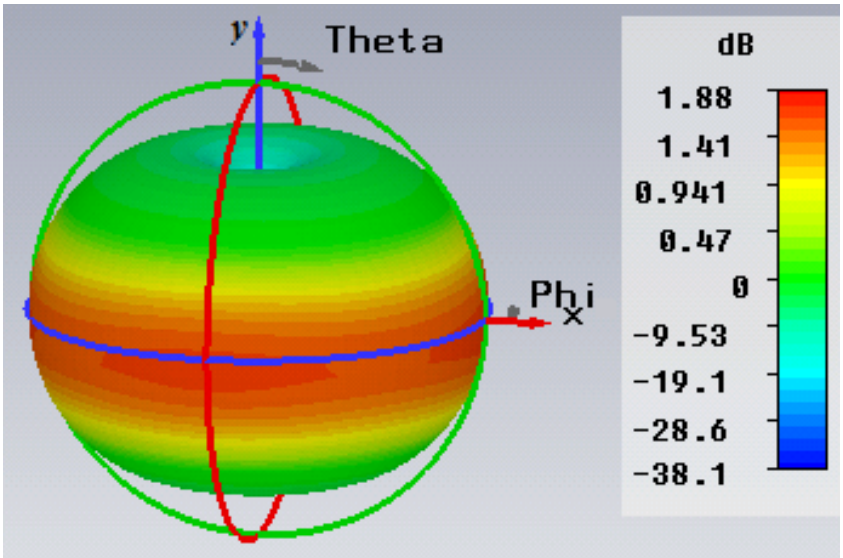

Figure 4.3. 3D Radiation pattern of the chip antenna at 2.45 GHz.

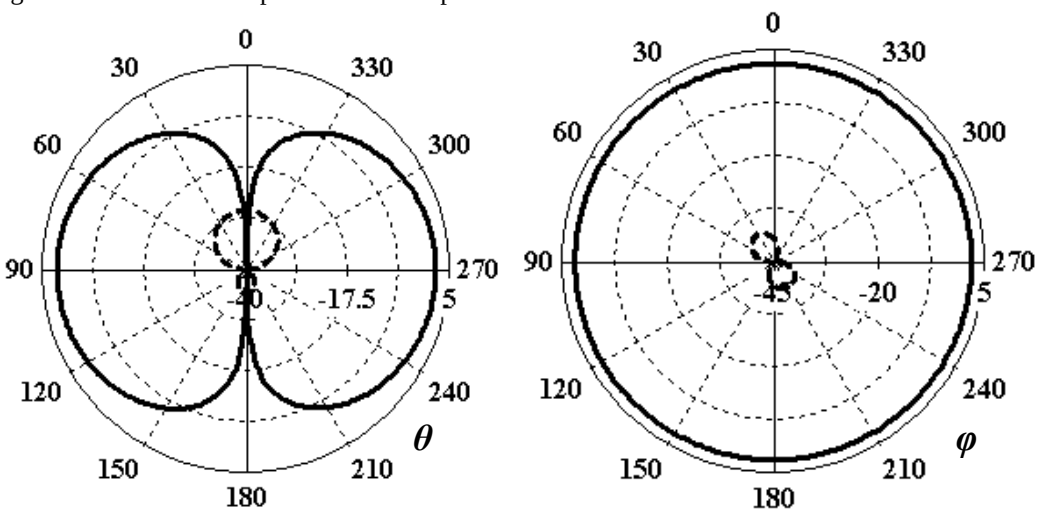

(a) (b)

Figure 4.4. (a) Radiation patterns of the chip antenna in (a) *xy*-plane (E-plane) and (b) *xz*-plane (H-plane) at 2.45 GHz. ——— E_θ (co-polarization) and – – – E_φ (cross-polarization) (coordinate system shown in Fig. 4.1).

4.2.2. Performance in proximity to body

To investigate MCA interaction with the body, the antenna was placed on a lossy body model having parameters of uniform body i.e., $\varepsilon_r = 52$, $\sigma = 1.7$ S/m at 2.45 GHz [7]-[8] in CST MWS as shown in Fig. 4.5. The reflection coefficient of the antenna in proximity to body model is shown in Fig. 4.6 compared to that in free space. A spacing of 1.8 *cm* was chosen to avoid the frequency detuning impact due to the high tissue parameters as discussed in Chapter 3. This spacing was chosen as the minimum to cause 10-dB impedance bandwidth ($|S_{11}|$ < -10 dB) within ISM 2.4 GHz band (2.40-2.4835 GHz) as will also be discussed further in Section 4.3.4. Quite large spacings have been reported in BAN literature to counter the frequency detuning impact caused by the lossy tissue e.g., an antenna-body spacing of 30 *mm* was used in [9] for on-body channel

measurements to maintain the on-body resonance ($|S_{11}|$ < -10 dB) within ISM 2.4 GHz bandwidth. A spacing of 7–10 *mm* (including the clothing) was reported in [10] which resulted in an $|S_{11}|$ of -7 dB for on-body channel measurements at 2.45 GHz.

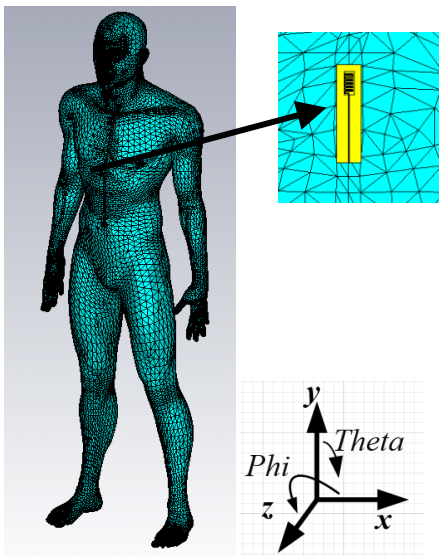

Figure 4.5. MCA placed on a realistic body model.

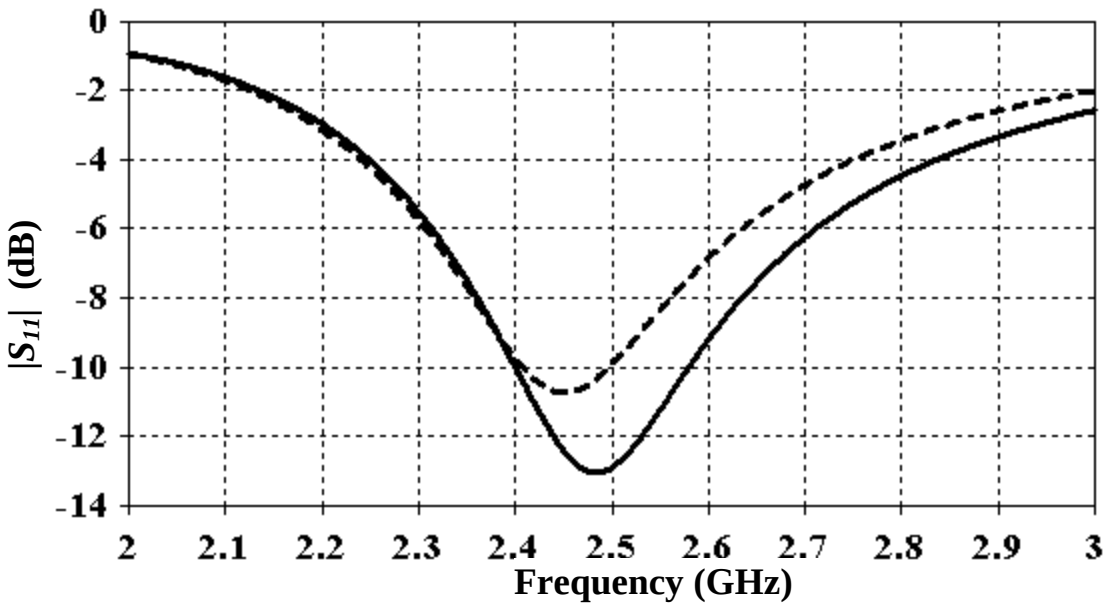

Figure 4.6. Simulated reflection coefficient of MCA on body model (– – –)compared to that in free space (——).

The radiation patterns of the chip antenna in proximity to body model are also shown in Fig. 4.7 compared to those in free space for the same spacing of 1.8 *cm* which resulted in 10-dB resonance bandwidth within ISM 2.4 GHz frequencies. The radiation patterns are not seriously degraded in the *xy*-plane which is the more crucial for on-body links. However, the antenna patterns are more seriously degraded in the *xz*-plane in the backward direction ($0°<\varphi<180°$) which indeed corresponds to the back of the body in

Fig. 4.5. This is due to the high attenuation caused by the lossy tissue as described in Chapter 3.

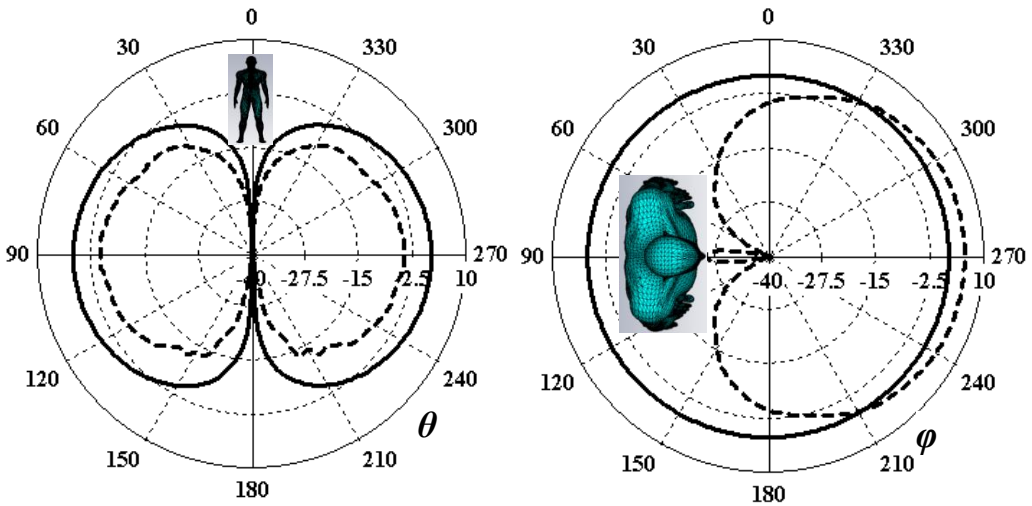

(a) (b)

Figure 4.7. Radiation patterns of the chip antenna at 2.45 GHz in (a) *xy*-plane and (b) *xz*-plane on body model (– – –) compared to those in free space (——) (coordinate system shown in Fig. 4.5 along with the avatar).

4.2.3. Prototype measurement

A prototype of the chip antenna was fabricated to verify the simulated results. The photograph of the measured prototype is shown in Fig. 4.8 along with the measured reflection coefficient shown in Fig. 4.9. The antenna resonates in ISM 2.4 GHz bandwidth with $|S_{11}| < -10$ dB throughout ISM 2.4 GHz bandwidth ($2.4 < f$ (GHz) < 2.5).

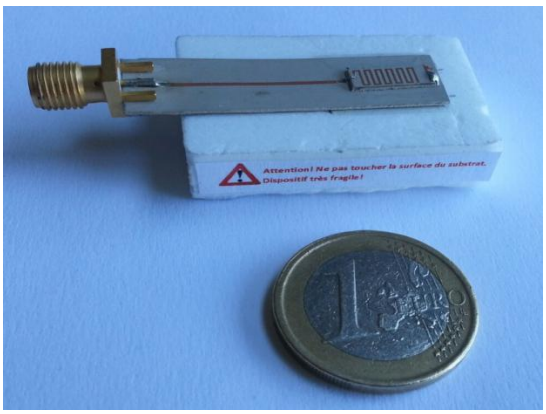

Figure 4.8. Photograph of the fabricated prototype of chip antenna.

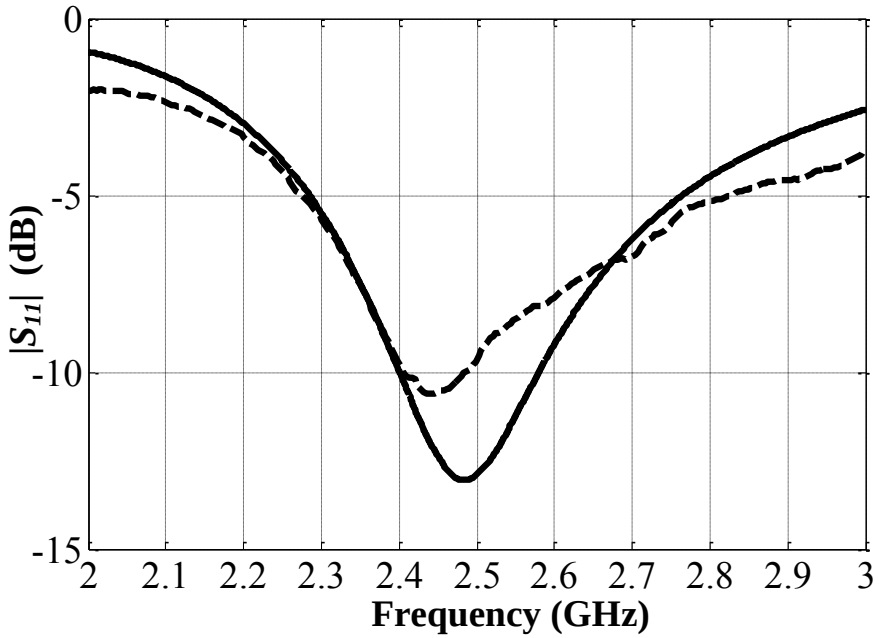

Figure 4.9. Reflection coefficient of the chip antenna in free space. Simulation (——) and measurement (– – –).

The refection coefficient of the antenna was measured in proximity to human body by placing the antenna on the arm of a human subject. In order to avoid dynamics caused by the slight body movements, the antenna was also measured on a static liquid phantom simulating human tissue properties at ISM 2.4 GHz (i.e., ε_r = 51.9, σ = 1.8 *S/m*). The corresponding results are shown in Fig. 4.10 compared to those in free space. The antenna still resonates inside ISM 2.4 GHz bandwidth with an with $|S_{11}|$ either less than -10 dB or a worst case $|S_{11}|$ of less than -8 dB at 2.48 GHz for liquid tissue.

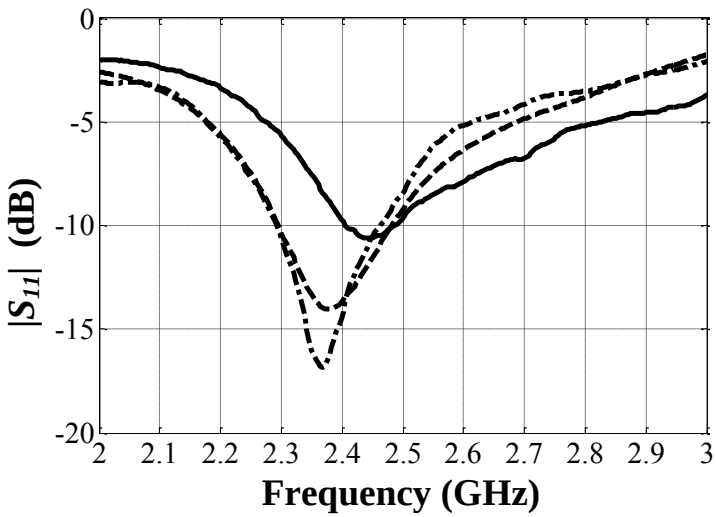

Figure 4.10. Measured reflection coefficient of the chip antenna in free space (——), on human arm (– – –), and liquid tissue (– · – ·).

4.3. Numerical channel simulator

4.3.1. Introduction

BoWI is based on a body-centric wireless network of various sensors at different on-body locations and considering a set of various body postures (called alphabets) to interact with the digital world. Some of such postural alphabets are shown in Fig. 4.11. Hence, one of the prime objectives was to perform radio simulations for BoWI posture grammar to investigate the strength of various on-body links when one of the nodes communicates with another one during a specific postural alphabet transmission scenario. The first task was to use a tool which can generate realistic 3D body models along with the possibility to influence the body postures as desired for the BoWI posture alphabets. We investigated the BAN simulation application of some of such commercial tools as those used by artists/designers e.g., DAZ 3D® [4], POSER® [5]. These tools offer the possibility of exporting postured 3D ghost phantoms directly in full wave simulation tools as CST MWS which can then be used for full-wave simulations. To illustrate the concept, the postural alphabets produced by one of such commercial tool (POSER® [5]) are shown in Fig. 4.12 corresponding to the posture alphabets shown in Fig. 4.11. Once imported in CST MWS, these models can be assigned desired tissue properties (e.g., ε_r, σ) at ISM frequencies by material assignment feature of CST MWS. This results in a uniform body with fixed material properties throughout the periphery of the models.

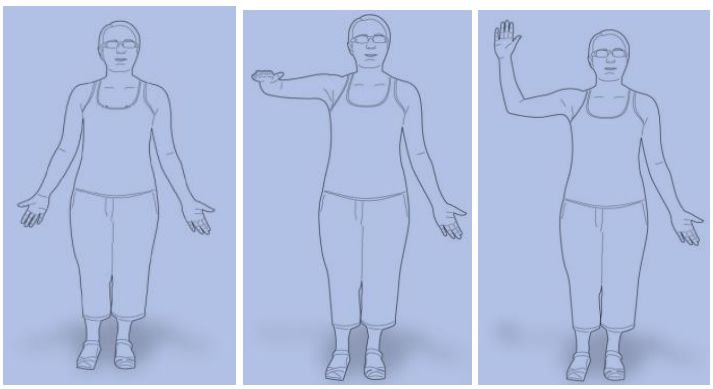

(a) (b) (c)

Figure 4.11. (a)-(c) Some of the sample BoWI postural alphabets.

(a) (b) (c)

Figure 4.12. (a)-(c) 3D ghost phantoms generated by POSER® [5] (corresponding to postures in Fig. 4.11 (a)-(c) respectively) .

4.3.2. Validation of body models

Once the preliminary tools were selected, the next task was to validate the appropriateness of the body models for body-centric numerical channel studies. For example, the Poser® [5] objects library offers a number of human body models which have different morphology and also different intrinsic geometrical constructions. The first objective was hence, to choose a body model which can be used in the simulation studies for body-centric applications. We considered firstly body model from the tool DAZ 3D® [4] and further various models from Poser® [5]. These different body models were imported into CST MWS for geometric studies as well as the study of their internal medium.

For numerical studies using different body models, the miniaturized chip antenna as described in Section 4.2 was reused. After a number of extensive simulation studies using the chip antennas under specific test scenarios on a number of such CAD based body models in CST MWS, we discovered that the choice of such models for body-centric simulations is a rigorous and cautious task. Our extensive study led to the discovery of the fact that many of such CAD-based body models apparently may appear solid but indeed are empty from their internal volume. This can lead to erroneous or misleading results from radio perspective.

As an example, one of the test scenarios is shown in Fig. 4.13 which was simulated using three different CAD based body models named as Model-1 [4], Model-2 [5], and Model-3 [5]. Model-1 comes from the software DAZ 3D® [4] whereas each of Model-2 and Model-3 come from the software POSER® [5]. For validation of these body models, we used exactly similar quasi-NLoS (QNLoS) scenario for all cases where one of the chip antennas (as described in Section 4.2) was placed on the chest and the other chip antenna was placed on the back of these models. Homogeneous muscle tissue (ε_r = 52, σ = 1.7 Sm^{-1}) was further used to model uniform human body at ISM 2.4 GHz for all the three cases [7]- [8].

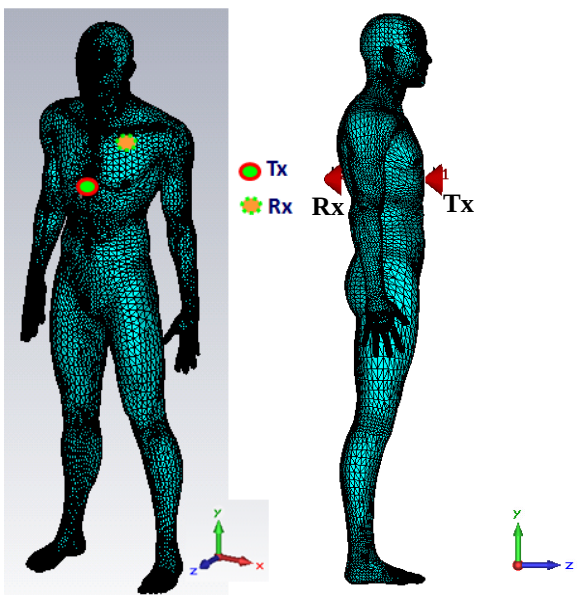

Figure 4.13. QNLoS transmission scenario on CAD based body model.

The resulting ***E***-field distribution around and inside the body model in the *yz*-plane due to the Tx antenna is shown in Fig. 4.14 for all the three models. It can be seen that despite of large value of tissue parameters (ε_r and σ), the ***E***-field can propagate inside the Model-1 [4] and Model-2 [5] indicating that both of these models are indeed empty from internal volume (though apparently they look solid in CST MWS). However for the case of Model-3 [5], we can see that the field attenuation inside the body is enormous as expected due to the large value of tissue parameters (apart from a few *mm* from the body surface due to skin depth). It proves that selection of the CAD based body models for BAN simulations is a cautious task and special care must be taken when using such CAD based body models in full wave simulation tools. Moreover, this study was also verified by various geometric dissection capabilities in CST MWS to fragment the 3D CAD models into their constituent components. It was observed that each of the CAD based models have specific morphology and are made up of sub-geometries which vary haphazardly and should be carefully investigated in each case.

The validated model (like the one in Fig. 4.14 (c)) was considered for all the subsequent simulation studies in this chapter. The height of this model is 180 *cm* (or 5 feet, 9 inches) which corresponds to the average height of adult males. The body model can approximately represent a real-human subject with a realistic shape for considering on-body propagation which is not the case for regular geometric phantoms e.g., [1]- [3].

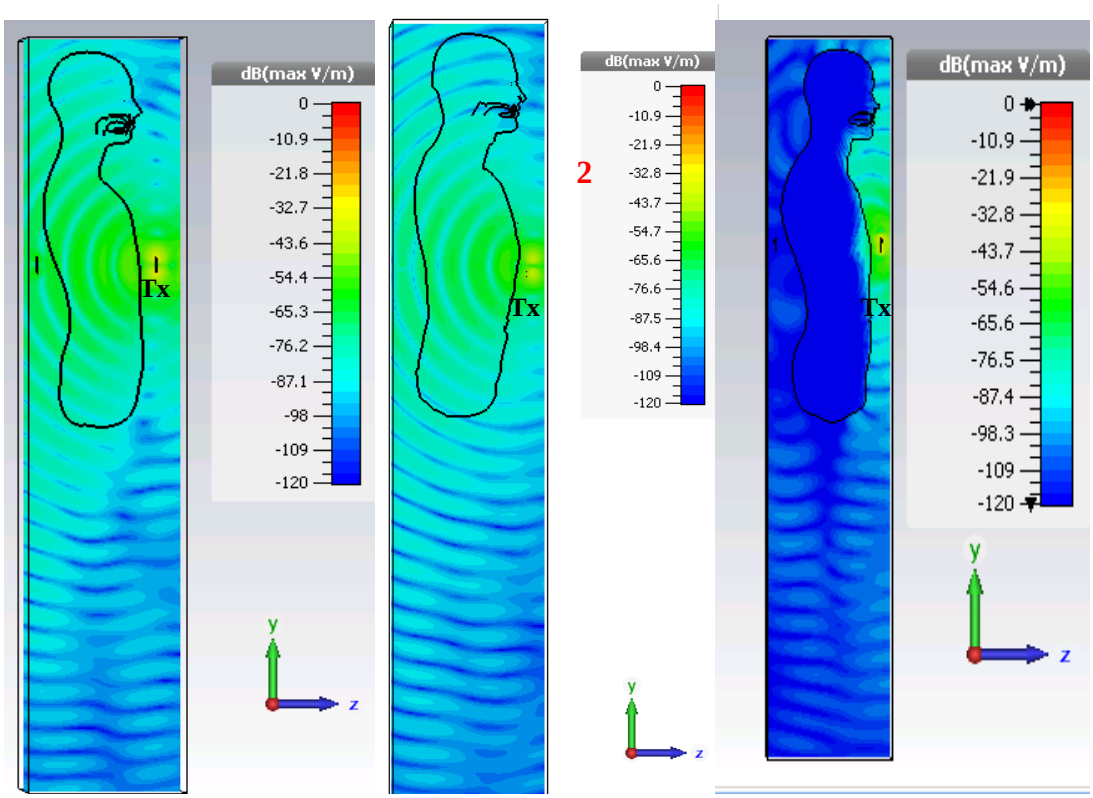

(a) (b) (c)

Figure 4.14 (a) ***E***-field distribution due to Tx around and inside the body (*yz*-cut plane) for (a) Model-1 [4] (b) Model-2 [5] and (c) Model-3 [5].

In order to consider also the validity of S-parameters on the realistic 3D body model (Fig. 4.14 (c)), an equivalent QNLoS scenario was also simulated in CST MWS on a 3D rectangular phantom as shown in Fig. 4.15. Approximate dimensions equivalent to the torso of the realistic 3D body model (Fig. 4.13) were used for the rectangular phantom. Similar homogeneous muscle tissue properties (ε_r = 52, σ = 1.7 Sm^{-1}) were used to model the human body at ISM 2.4 GHz as for the case of 3D body model [7]- [8]. The corresponding full-wave S-parameters are shown in Fig. 4.16 with those for the equivalent QNLoS scenario on the realistic 3D body model (Fig. 4.14 (c)) shown in Fig. 4.17. The S-parameters for the two scenarios are comparable with values of transmission coefficient (S_{21}) of -90 and -95 dB respectively at 2.45 GHz for the 3D body model (POSER®) and the rectangular phantom from CST MWS respectively. This small difference (ΔS_{21}= 5 dB) can be attributed to various factors such as the non-uniform body spacing in case of 3D body model due to its non-planar shape and also due to different overall morphology of the two simulation problems. Small difference between S_{21} and S_{12} in Fig. 4.17 e.g., at 2.9 GHz is due to the simulation inaccuracies which can be neglected since it lies out of the band of interest (ISM 2.4 GHz).

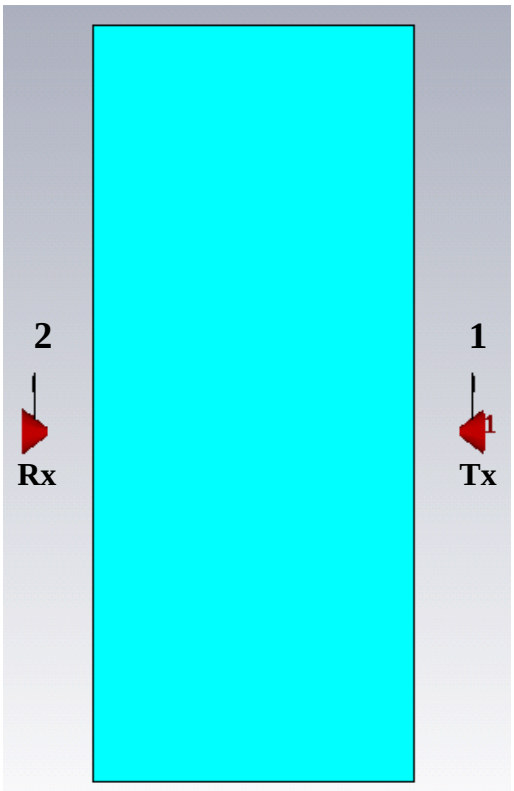

Figure 4.15. QNLoS transmission scenario on a 3D rectangular phantom created in CST MWS.

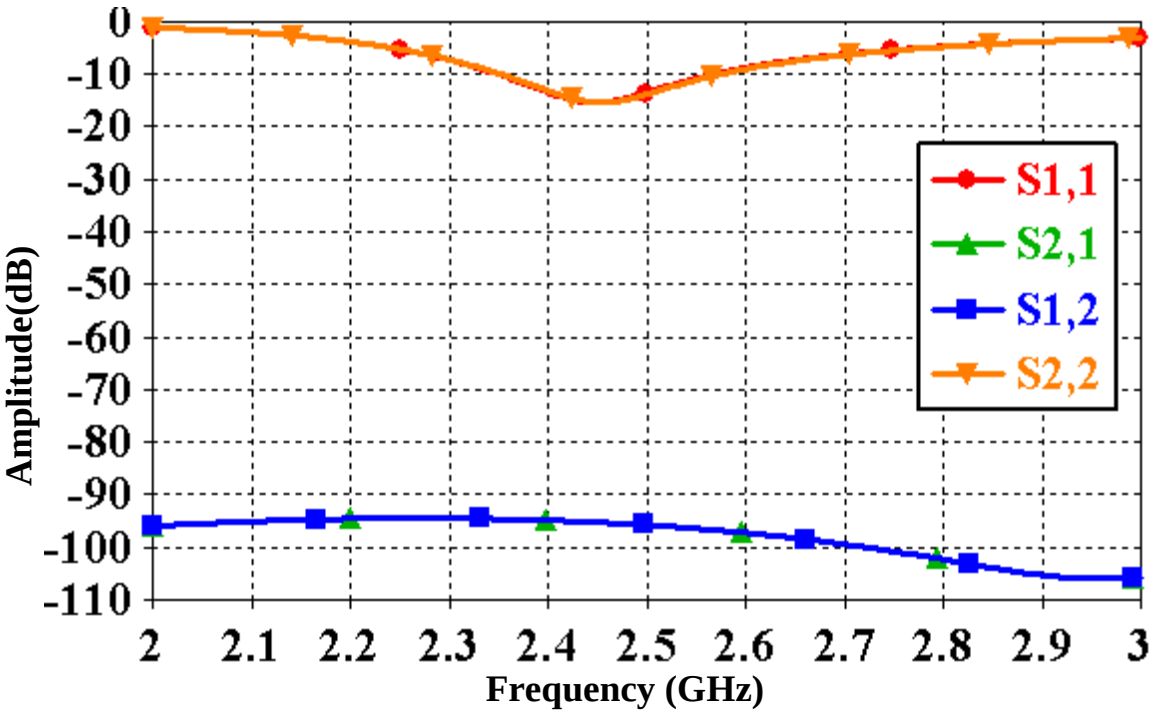

Figure 4.16. Full-wave simulated S-parameters on 3D rectangular phantom.

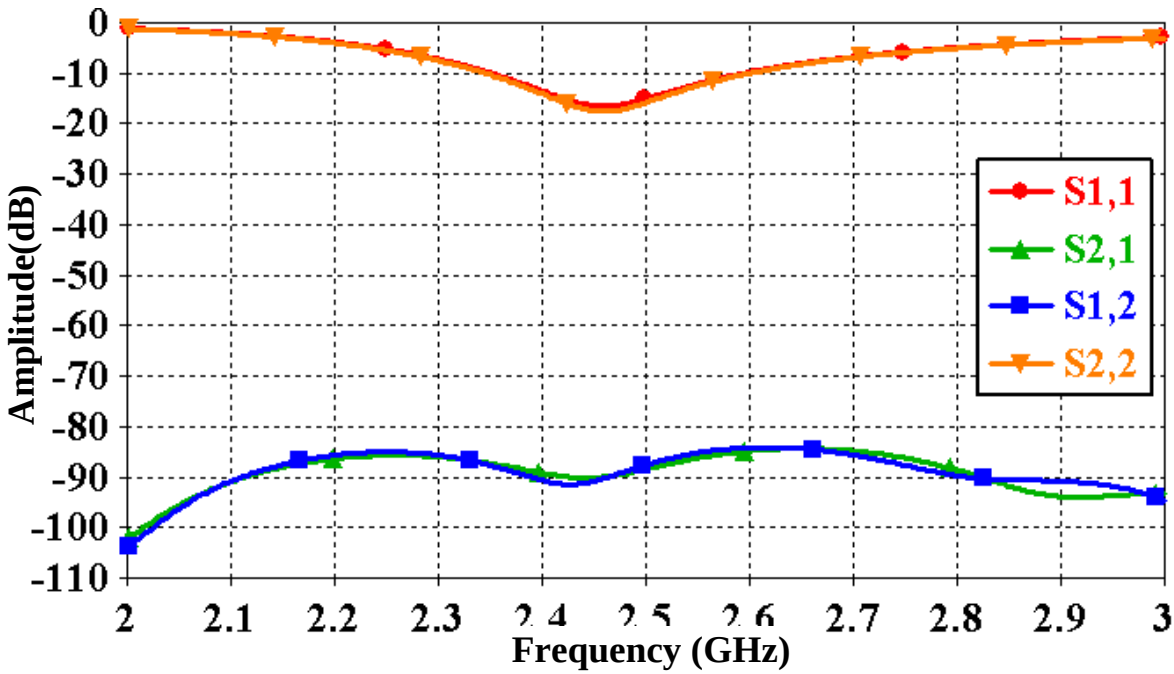

Figure 4.17. Full-wave simulated S-parameters for the realistic 3D body model from Poser®.

The ***E***-field distribution across the cross-section of rectangular phantom is shown in Fig. 4.18. The field distribution is comparable to the case of realistic 3D body model around the thoracic region (Fig. 4.14 (c)). This proves the suitability of the realistic 3D body model for numerical channel studies along with the on-body propagation subject to

the appropriate computation of ***E***-field as well as scattering parameters as compared to the canonical rectangular phantom from CST MWS.

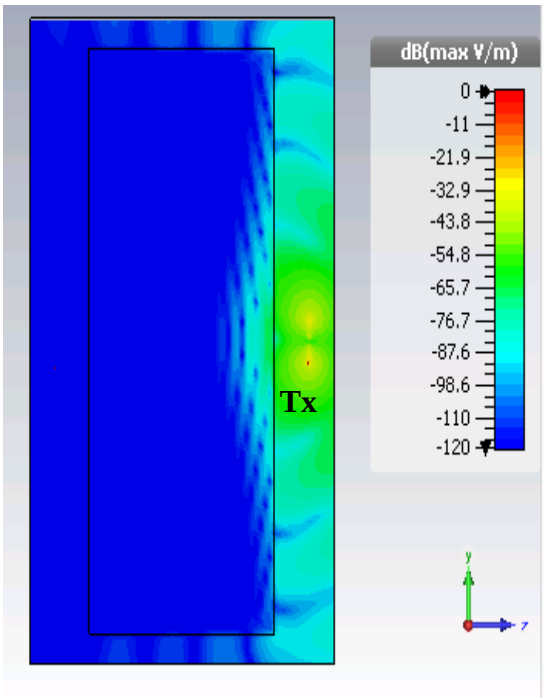

Figure 4.18. Electric-field distribution due to Tx antenna for 3D rectangular phantom (Fig. 4.15).

4.3.3. Mesh convergence and accuracy

The major challenge in the development of numerical channel simulator was the computational overhead (i.e., simulation time and memory) which is caused by the electrically large size of the problem. e.g., the human model of height 1.8 *m* corresponds to 104λ @ 2.4GHz (for a homogenous medium with ε_r = 52). This results in an unreasonably large computation problem size (with multi-billion mesh cells) when the chip antennas of Section 4.2 were used for simulations in proximity to such a model. Meanwhile, it was imperative to achieve accurate and convergent results. Therefore, exhaustive steps were undertaken to realize the simulation results while well considering the convergence of simulation problem to have reliable results.

The accuracy of the simulation studies was verified in CST MWS using an energy based mesh refinement technique. This technique repeatedly runs the simulation while locally refining the mesh in regions with high field concentration or gradients. The mesh adaptation terminates as the deviation of the results falls below a certain threshold of error (named as delta) which was defined as 2%. This means that adding extra mesh cells in critical gradient regions of overall simulation domain should not result in more than 2% deviation from originally computed results, hence implying accurate and reliable simulation results.

Convergence was also studied for QNLoS scenario as shown in Fig. 4.13 while locally refining the mesh in critical areas e.g., inside the antenna or across the meander lines of antenna, meanwhile using a less dense mesh inside the body model, as also

shown in Fig. 4.19. The body mainly attenuates the signal here, in contrast to the antennas which control the overall resonance and hence, antennas are given more priority in mesh refinement than the body model itself. This approach also helped us to end up to a realistic mesh size and hence, realizable simulation problem with limited time and memory resources.

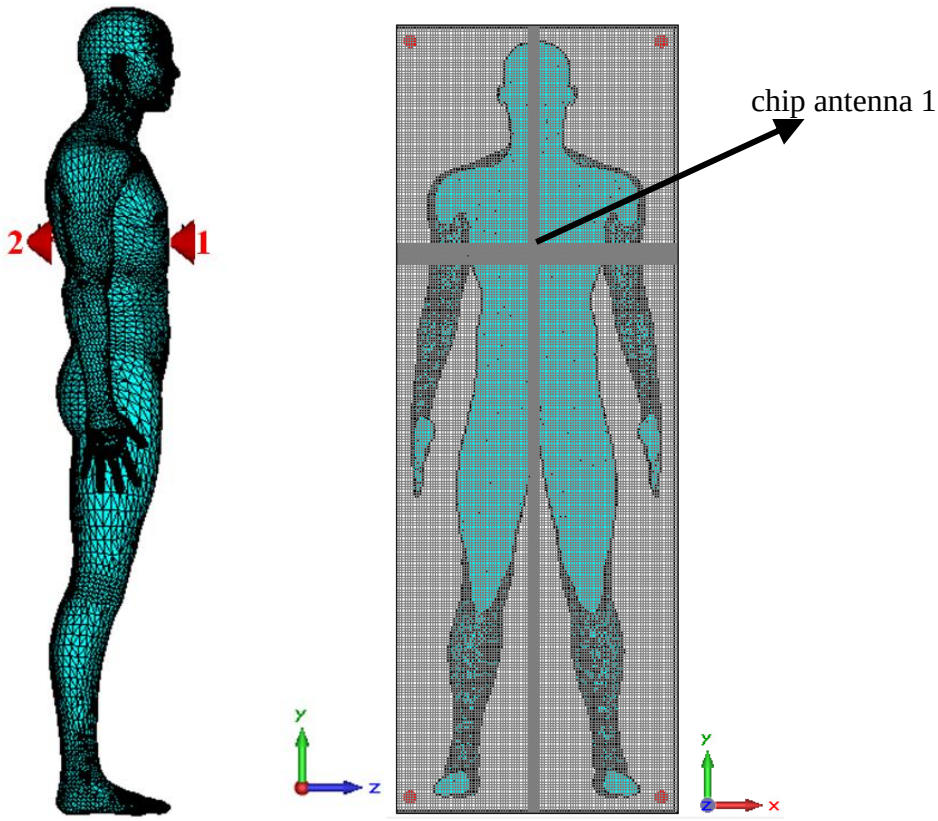

(a) (b)

Figure 4.19. (a) QNLoS transmission scenario for convergence study (b) Mesh view of the antenna on 3D body model in *xy*-plane.

All full-wave simulation results for S-parameters as computed by CST MWS for multiple passes of the energy based mesh refinement system are shown in Fig. 4.20. All the S-parameters converge nicely with an error (Δ) of 1.28 % using 12 million cells. Moreover, The two mesh refinement passes correspond to an increase in cells from 7 million to 12 million which causes a rise in the simulation time from 225 minutes to 488 minutes. Corresponding solver results can be seen in the Appendix B at the end of this thesis. Since the same antennas and body model were used throughout the gesture-based studies, the same mesh settings were conserved for all the subsequent simulation studies.

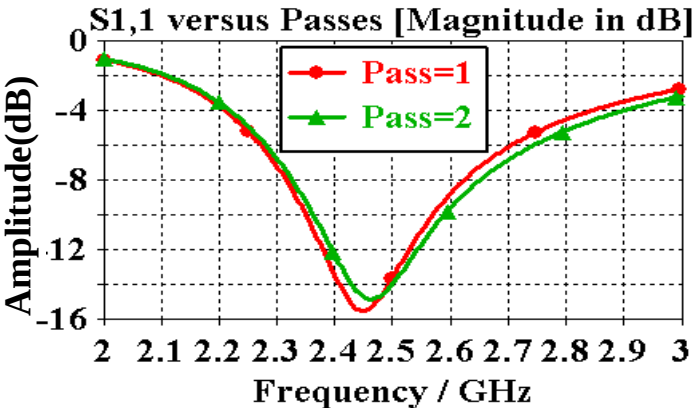

(a) S_{11}

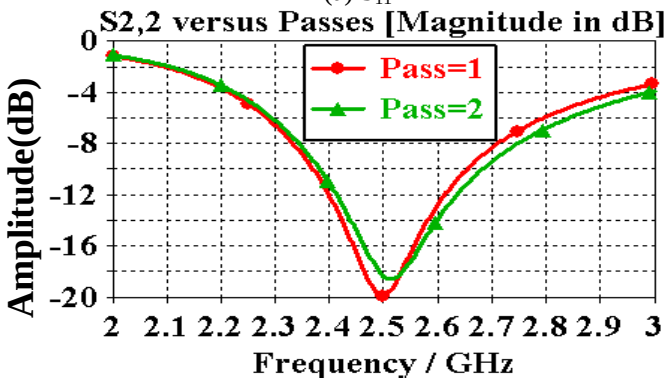

(b) S_{22}

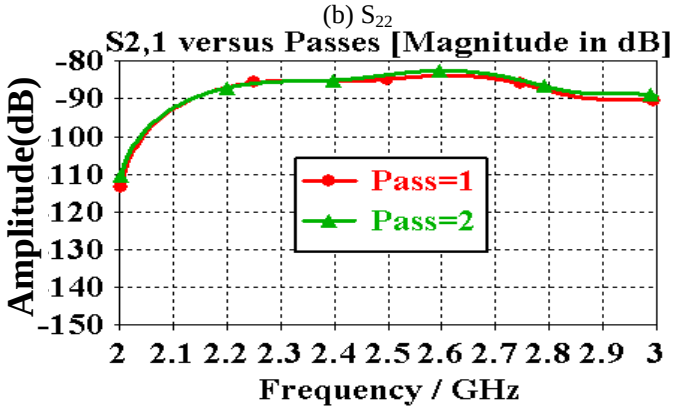

(c) S_{21}

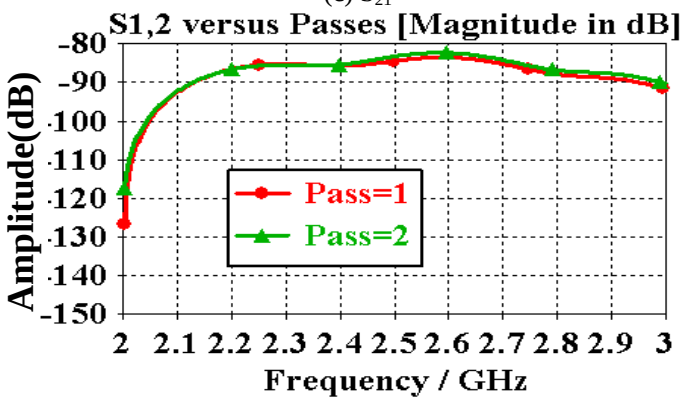

(d) S_{12}

Figure 4.20. All simulated S-parameters on 3D body model for energy-based mesh refinement scheme.

4.3.4. Significance of antenna-body spacing

In order to initiate the gesture-based numerical channel studies, the next major task was to choose an appropriate antenna-body spacing for resonance inside ISM 2.4 GHz bandwidth to ensure that the antennas are resonating properly. The impact of spacing was studied using the same 3D realistic body model with a spacing *d* as shown in Fig. 4.21. The chip antenna was placed on the centre of chest to have maximum body impact and the antenna body spacing *d* was varied. Moreover, since the body surface is not planar, the spacing was chosen as the one corresponding to the minimum along the curved surface. Simulated results for S_{11} are shown in Fig. 4.22 for various antenna-body spacing *d* along with the corresponding radiation patterns at 2.45 GHz shown in Fig. 4.23. As evident for a minimum spacing of 18 *mm*, the antenna resonates inside ISM 2.4 GHz band with $|S_{11}| < 10$ dB throughout ISM 2.4 GHz bandwidth ($2.4 < f$ (GHz) < 2.5) and a gain of 5dBi at 2.45 GHz. A minimum spacing *d* of 18 *mm* was hence, chosen for subsequent numerical channel studies.

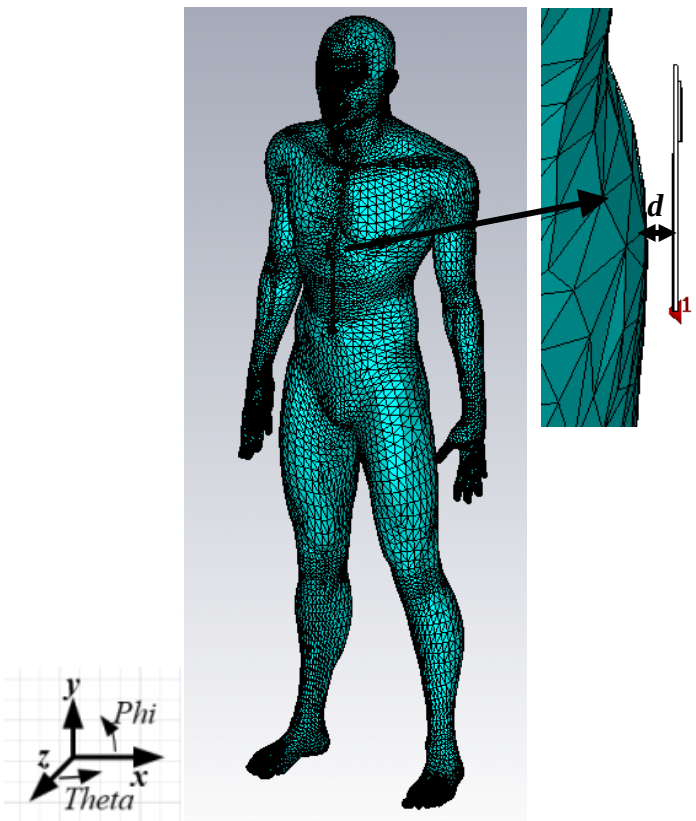

Figure 4.21. Chip antenna placed on realistic 3D body model with spacing *d*.

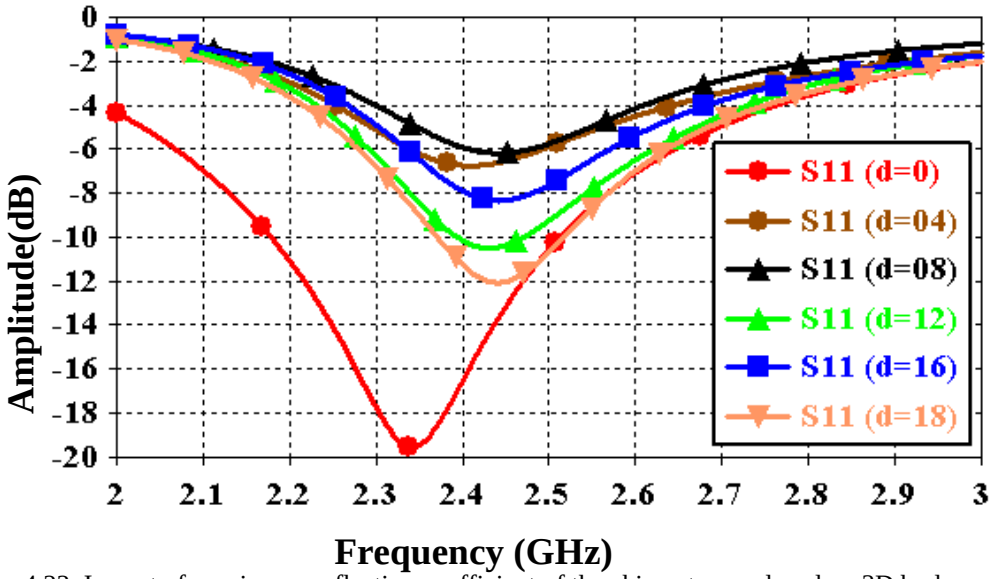

Figure 4.22. Impact of spacing on reflection coefficient of the chip antenna placed on 3D body model.

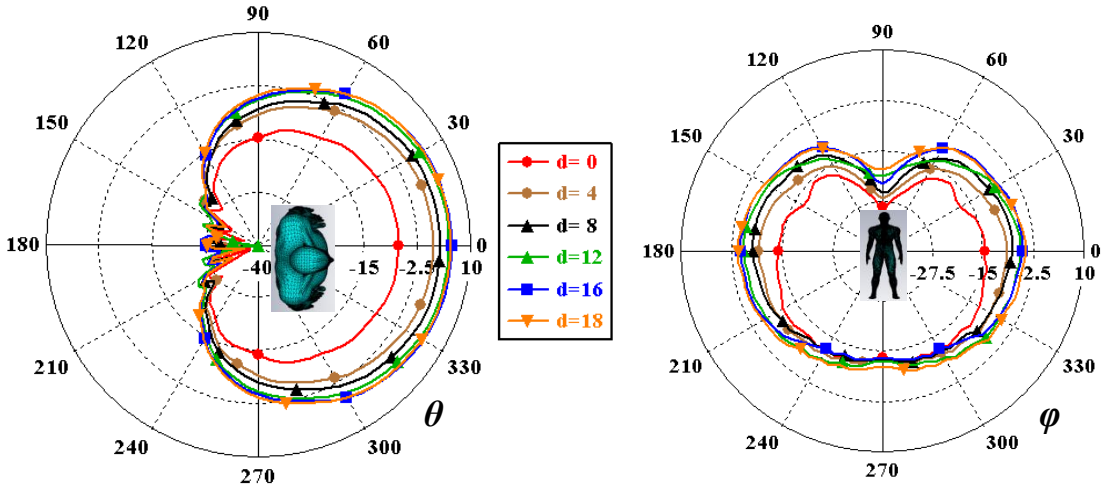

(a) (b)

Figure 4.23. Impact of spacing on radiation patterns of the chip antenna at 2.45 GHz in (a) *xz*-plane and (b) *xy*-plane on body model (coordinate system shown in Fig. 4.21 along with the avatar).

4.3.5. Demonstration with few examples

Basic Posture 1

After verifying the various pre-requisites as described previously, the numerical channel simulator was then used to simulate few posture grammar for BoWI project. The basic posture alphabet 1 is shown in Fig. 4.24. It comprises five nodes on the body model using the miniature chip antennas as described in Section 4.2. Homogeneous muscle tissue (ε_r = 52, σ = 1.7 Sm^{-1}) was used to model the human body at ISM 2.4 GHz [7]- [8]. A minimum antenna-body spacing of 18 *mm* was maintained for all the five antennas to avoid frequency detuning impact of the body as discussed already (Section 4.3.4). Moreover, all the antennas face the head of the model in Fig. 4.24 and are aligned parallel to the corresponding body segment (e.g., arm, shoulder or chest).

In fact, this scenario can also study the equivalent transmission scheme for nine antennas using symmetry, when the other four antennas could be located on the left arm, while maintaining a perfect symmetry with their right-hand counterparts. Even with five nodes, such a simulation scenario is computationally quite complex due to the electrically large size of the problem as discussed previously. This simulation problem resulted in a mesh size of 137 million approximately which took a simulation time of around 33 hours on a CST server with Intel Xeon 2.60 GHz CPU and 128 GB of RAM for full-wave simulation results for each of the five antennas. The simulated results for S-parameters are shown in Fig. 4.25. As expected all the S-parameters are symmetric due to the reciprocity of antennas.

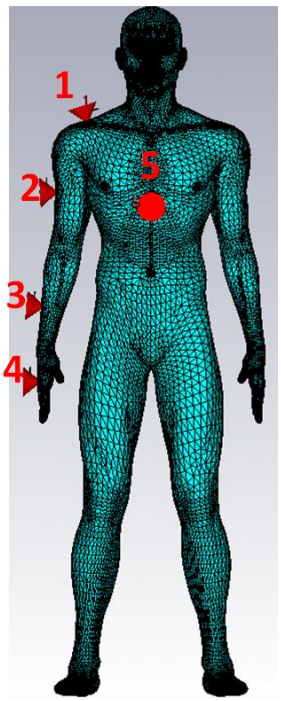

Figure 4.24. Node placement for basic posture alphabet 1.

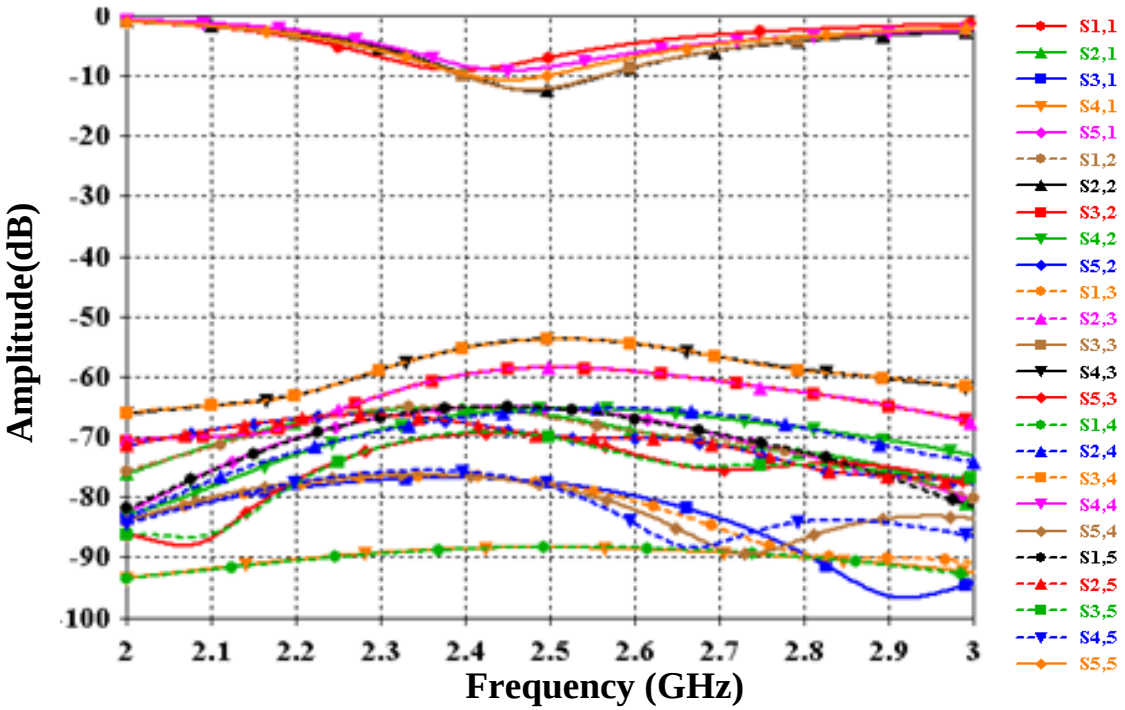

Figure 4.25. Full-wave simulated S-parameters for basic posture 1.

The channel results presented in Fig. 4.25 include both the free space propagation component which is mainly linked to the S-parameters and antenna radiation patterns and also the on-body propagation component for each link. This is also evident from the ***E***-field distribution as shown in Fig. 4.26 for the central antenna 5 (situated on chest). Moreover, it is also evident that the radiation is significantly attenuated inside the body cross-section which is due to the high tissue conductivity (σ = 1.7 S/m) which attenuates most of the incident radiation in the backward direction.

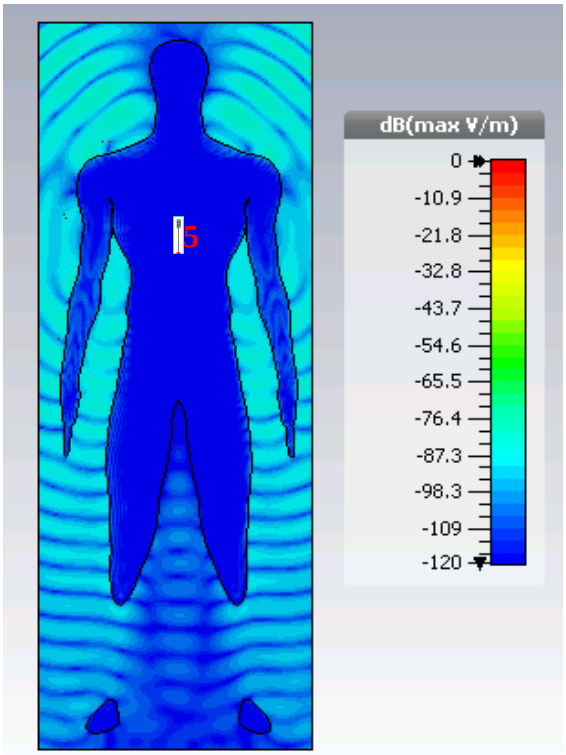

Figure 4.26. Electric field due to antenna 5 showing on-body propagation for basic posture 1.

Posture 2

The simulation challenges for another BoWI postural alphabet (named as posture 2) are discussed here. This posture alphabet is shown in Fig. 4.27 (a). This problem posed even a much higher complexity in terms of computational size having 332 million mesh cells with five nodes compared to 137 million mesh cells for the scenario of basic posture 1 (Fig. 4.24). This corresponds to an increase in simulation problem complexity by a factor of 2.4. The cause of this enormous rise in computational volume is indeed the arm which lies in front of the model for this posture, hence resulting in additional mesh cells needed to fill up the volume in front of the body.

Therefore, in order to reduce the problem complexity, the body model was reduced (or cut) at a distance of approximately 34 *cm* which corresponds to $3\lambda_0$ at 2.4 GHz from the nearest antenna (antenna 5 in Fig. 4.27(b)). Such a reduction of the body model does not cause noticeable influence on channel results for the reduced body being located in the far-field of antennas 1-5. The resulting reduced problem offered much lower mesh cells of 244 million compared to 332 million without simplification.

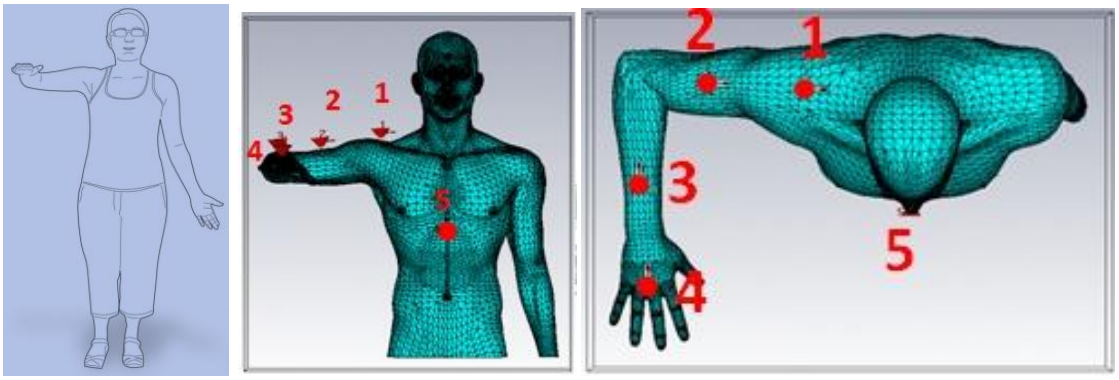

(a) (b) (c)

Figure 4.27. (a) Posture alphabet 2 (b), (c) Node placement for posture alphabet 2 (b) front and (c) top views.

Full-wave simulations were then undertaken for the posture 2 using CST MWS. The problem took a simulation time of 56 hours approximately on a CST server with Intel Xeon 2.60 GHz CPU and 128 GB of RAM for computing 25 S-parameters in total along with the overall ***E***-field for each of the five antennas. The complete simulated S-parameters are shown in Fig. 4.28. The results for the case when there are also four more antennas on the left arm for this posture (i.e., nine antennas in total) will be analogous to those of the basic posture alphabet 1, when a perfect symmetry is maintained with the placement of the four antennas on the left arm of this posture with their right-hand counterparts of the basic posture 1.

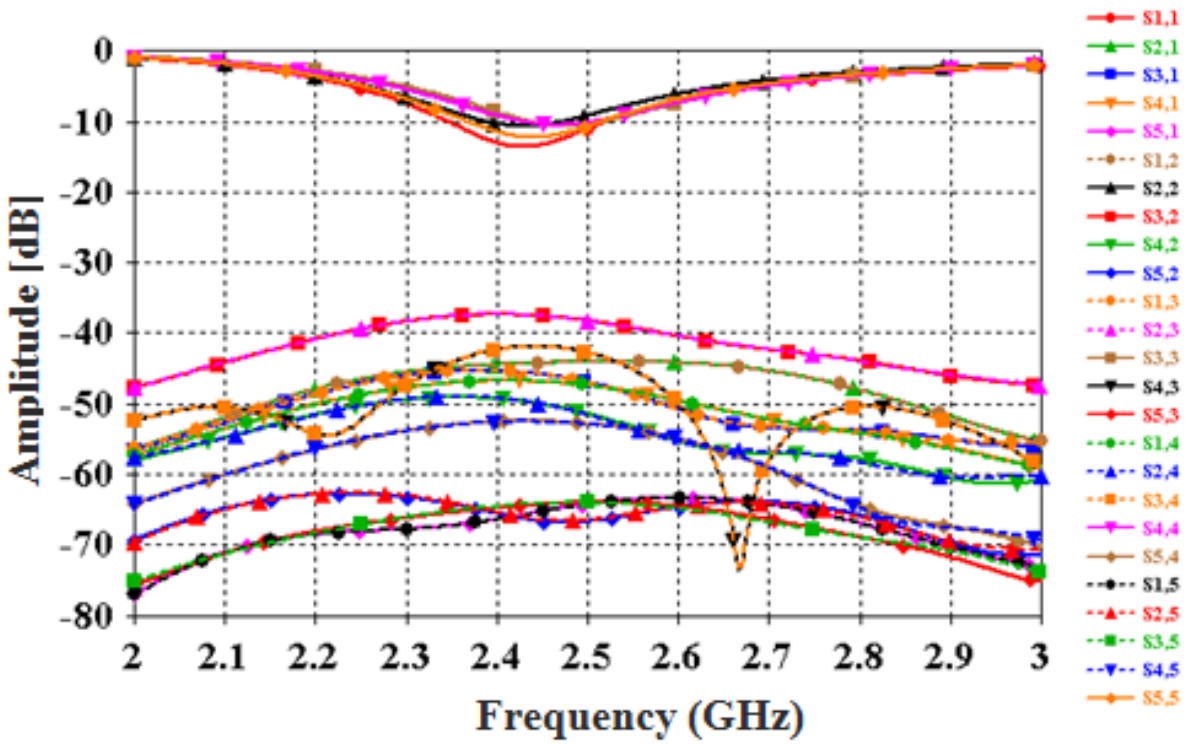

Figure 4.28. Full-wave simulated S-parameters for posture alphabet 2.

Some other posture alphabets were also simulated for analysis of results with varying body postures. The posture alphabets 3, 4 and 5 along with the corresponding full-wave simulation results using CST MWS are shown in Fig. 4.29, 4.30 and 4.31 respectively.

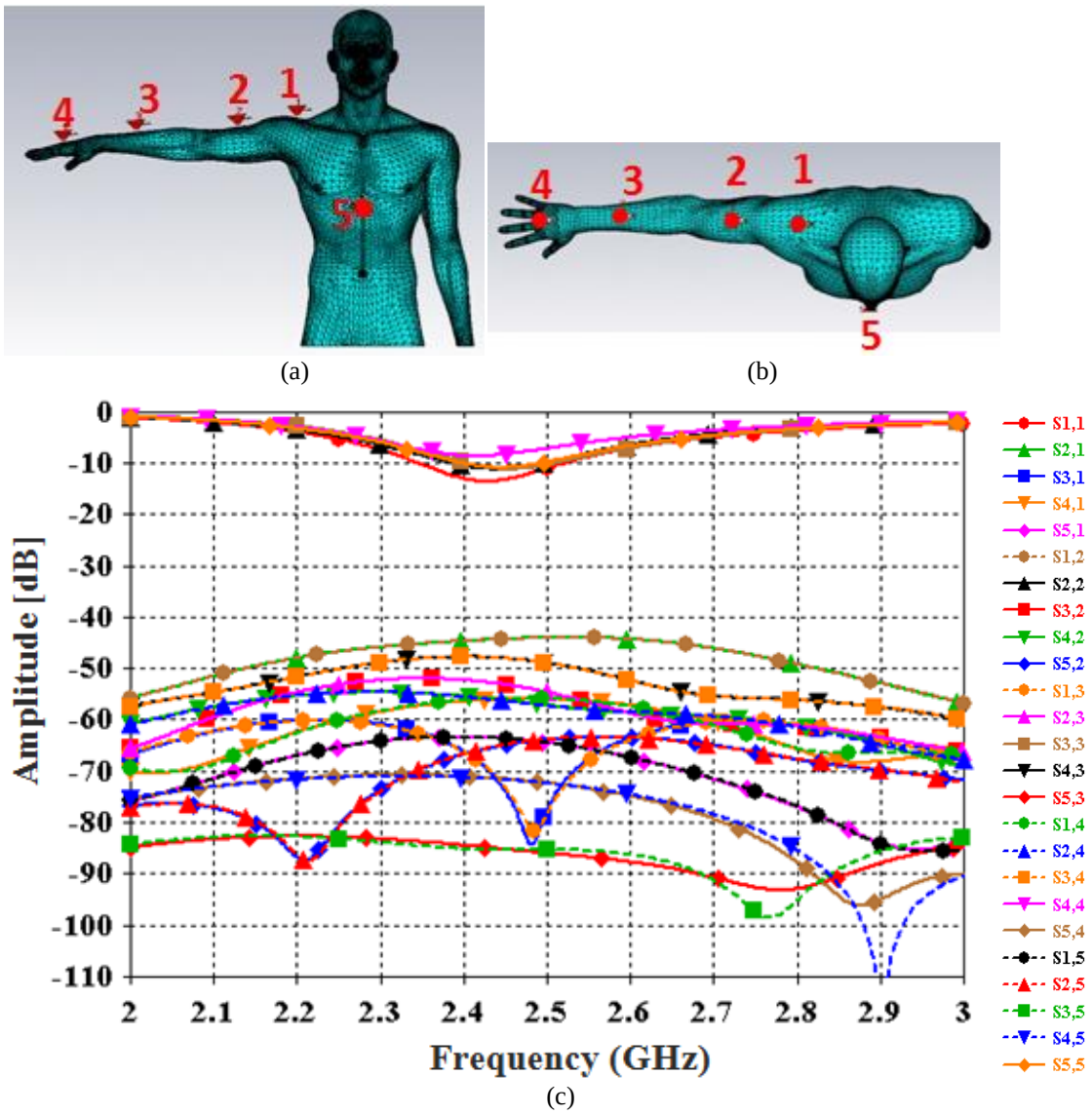

Figure 4.29. Posture alphabet 3 (a) front view, (b) top view (c) Full-wave simulated S-parameters.

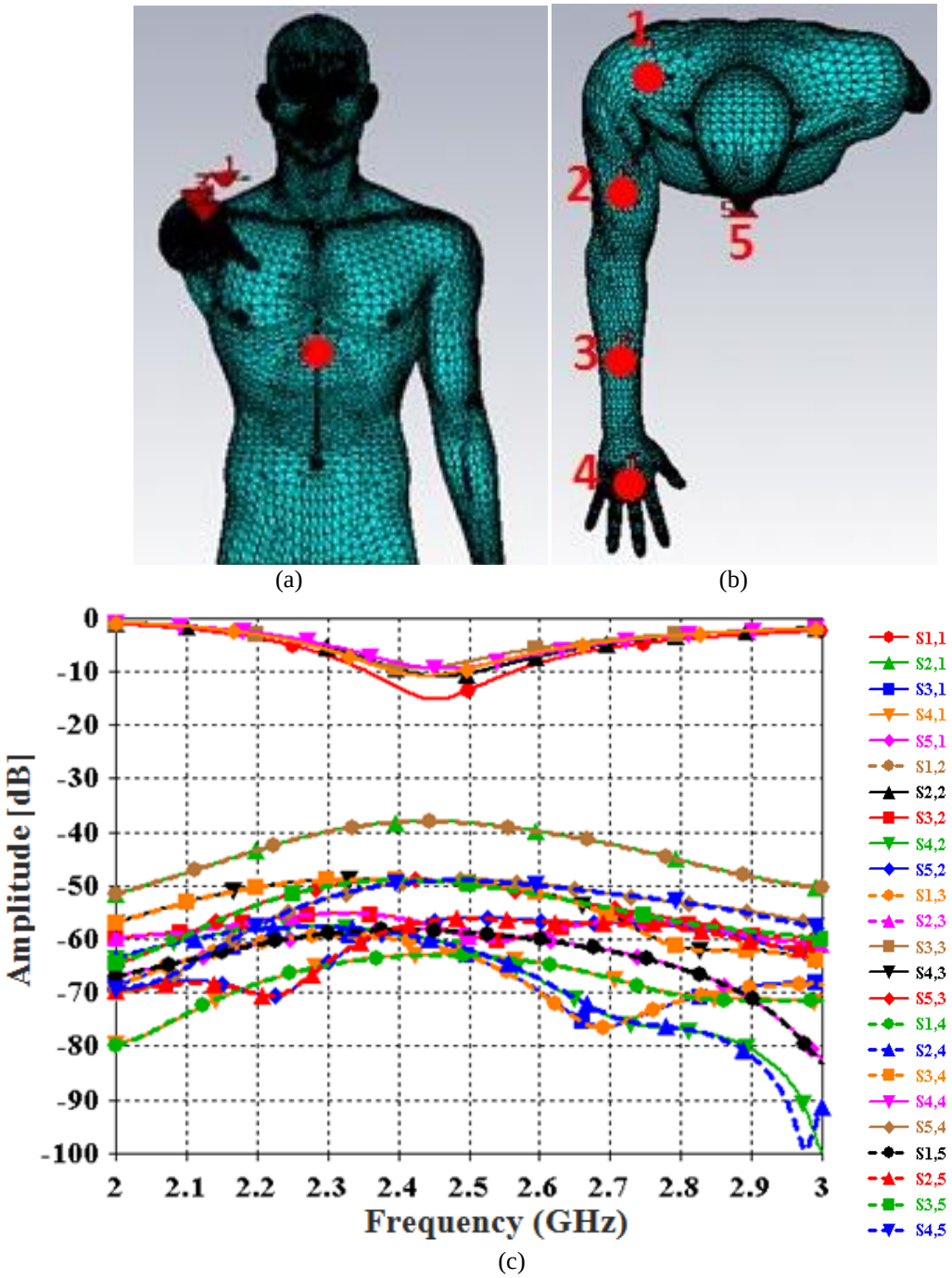

Figure 4.30. Posture alphabet 4 (a) front view, (b) top view (c) Full-wave simulated S-parameters.

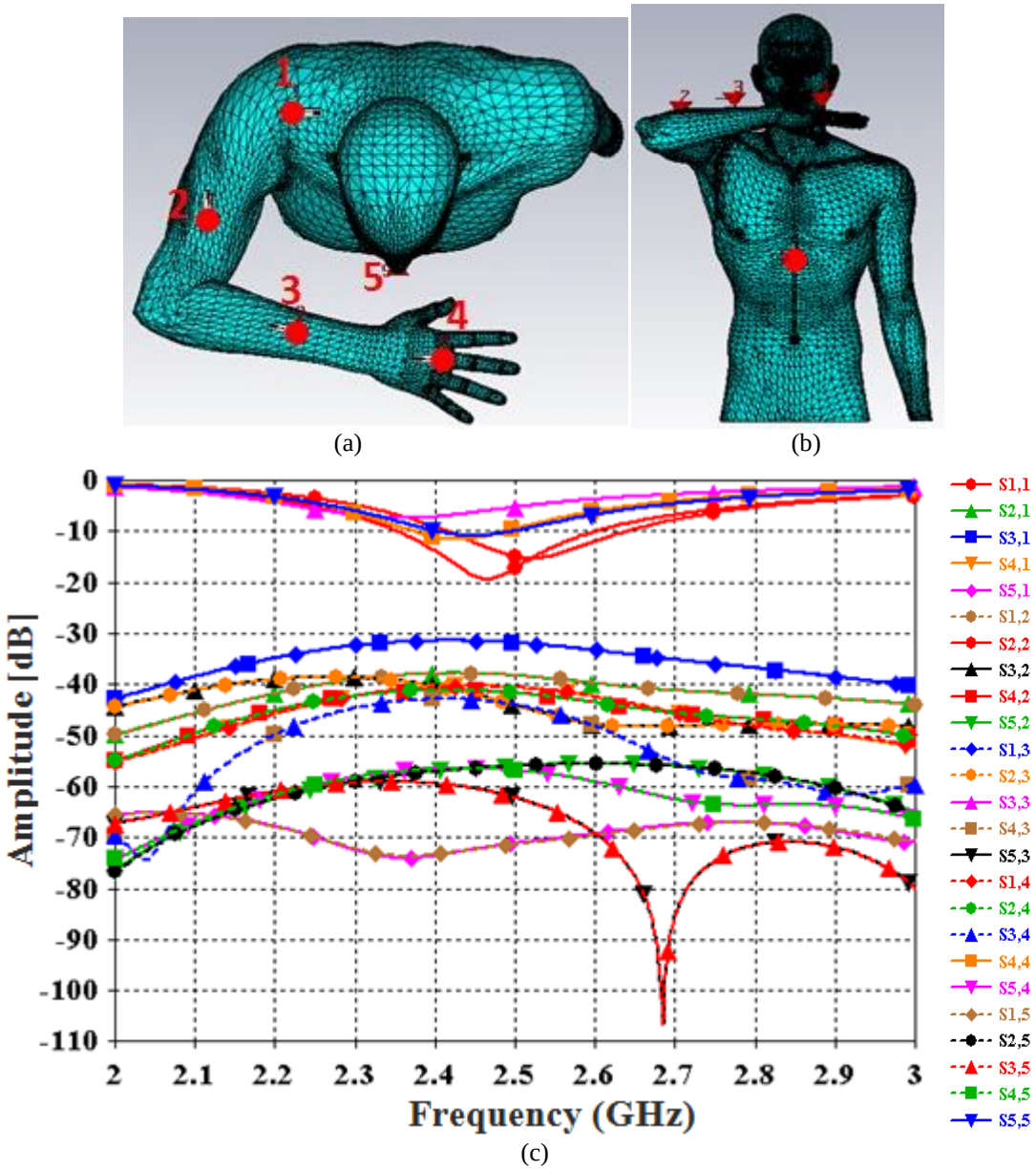

Figure 4.31. Posture alphabet 5 (a) front view, (b) top view (c) Full-wave simulated S-parameters.

The variation of link budget between antennas 4 and 5 (situated on right hand and chest respectively) is presented in Table 4.1 for all the simulated postures shown again in Figure 4.32. The levels of link budget are listed in ascending order. For link between antennas 4 and 5, posture 4 has the strongest level followed by postures 2, 5, 3 and 1 respectively. This is due to the dominant LoS path in posture 4 for link (4, 5) as the arm is extended fully in front of chest. Posture 2 also contains a QLoS path for the link (4, 5) with relatively weaker link budget (-53 dB) compared to posture 4 (-49 dB) due to the interaction of head which is more close to Tx antenna (4) in this case compared to that in posture 4. Posture 5 corresponds to the shortest distance for link (4, 5) compared to all other postures and has a level of -56 dB for link budget due to the strong interaction of head also with Tx (4). Posture 3 corresponds to the longest distance for link (4, 5),

therefore has a link budget of -72 dB only. Posture 1 has the minimum link budget of -77 dB only since it simulates a QNLoS scenario due to the torso blocking the Tx-Rx link (4, 5). This information is useful for posture classification as will be discussed in the following section using overall simulation results.

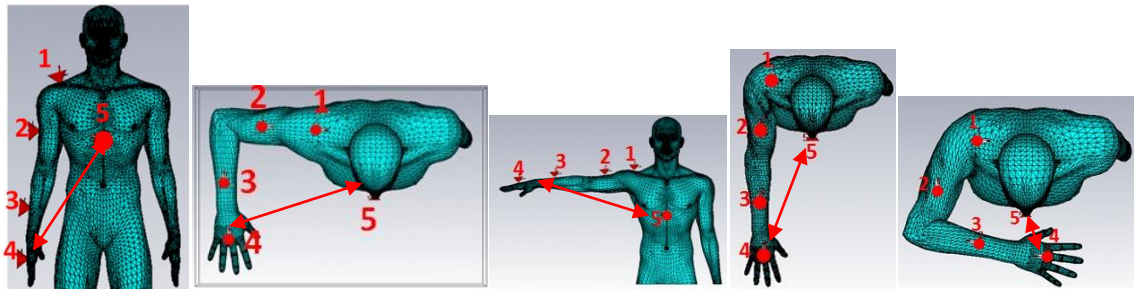

(a) (b) (c) (d) (e)

Figure 4.32. (a) Posture 1 (b) Posture 2 (c) Posture 3 (d) Posture 4 (e) Posture 5.

TABLE 4.1. LINK BUDGET FOR TX= 4 AND RX=5 FOR VARIOUS POSTURES AT 2.45 GHZ

Tx-Rx Link	**Posture**	S_{ij} **(dB)**
(4, 5)	4	-49
	2	-53
	5	-56
	3	-72
	1	-77

4.3.6. Application for posture classification

The channel simulator as presented in Section 4.3 can be useful for posture classification for interactive gesture-based projects as BoWI. The objective of posture discrimination using radio involves rigorous scientific challenges which are discussed in this section.

If the antennas are properly matched with respect to impedance and polarization at operating frequency and with the assumption that they are located in the far-field along with the multipath effects being negligible, Friis formula can be expressed as (4.1) [11]

$$\frac{P_r}{P_e} = G_t.G_r.\left(\frac{\lambda}{4\pi D}\right)^N \tag{4.1}$$

where P_e is the average input power to Tx antenna, P_r is the average output power from Rx antenna, G_t is the peak gain of transmitting antenna and G_r is the peak gain of receiving antenna [11]. λ is the operating wavelength, d is the inter Tx-Rx distance and N is the path loss exponent which indicates the rate at which the path loss increases with distance (considered as 2 for free space).

In case of body-centric scenarios, the propagation is much more complex than the free space propagation as represented by (4.1). Each pair of on-body nodes provides independent radio links for communication [12]- [13]. Each link provides different channel characteristics due to the different properties of unique areas of the body [9]. External perturbations such as user mobility and operation in diverse environments create a complex communication scenario from radio perspective between sensors for wearable applications [14]- [15]. The transmission also involves diffused free space and on-body propagation in the form of creeping waves along the body surface [8], [16]- [17].

The path loss cannot be generalized by the Friis formula for free space as given by (4.1) due to the significant influence of various factors such as antenna positioning on body, spacing from the body and most of all the body orientation and gestures. These effects are not taken into account by (4.1). For on-body propagation, we modify (4.1) to consider two additional coefficients β and γ to take into account the antenna gain and on-body propagation also. (4.1) can be rewritten as (4.2)

$$Pr = \frac{1}{D^2} \times \beta \times \gamma \times \left(Pe\left(\frac{\lambda}{4\pi}\right)^2\right) \tag{4.2}$$

where β mainly accounts for the gain of the antennas which is a function of the body posture (for fixed antenna-body spacing) and γ considers the on-body propagation component. Furthermore, the received power in a body-centric propagation scenario can be considered as a function of various factors e.g., the human subject H_k (since the coefficients can vary based on the body morphology of human subject), the body posture P which can further be split into the posture on the right arm (d) and left arm (g), and the gain of antennas comprising the link i.e., Tx antenna Ce_i and Rx antenna Cr_j, and the distance D which for on-body case, is the distance between the Tx (Ce_i) and Rx (Cr_j)

antennas for a specific posture *P*. Therefore, using these functions, (4.2) can be rewritten as (4.3)

$$Pr_{(H_k,P_{(g,d)},Ce_i,Cr_j)} = \frac{1}{D^2_{(P_{(g,d)},Ce_i,Cr_j)}} \times \beta_{(P_{(g,d)},C_e,C_r)} \times \gamma_{(H_k,P_{(g,d)},Ce_i,Cr_j)} \times \left(Pe\left(\frac{\lambda}{4\pi}\right)^2\right) \quad (4.3)$$

where the multipath effect is neglected subject to ideal boundary conditions in CST. If the coefficients β and γ are known, the distance between the critical nodes can be identified considering the other factors which are known in (4.3). This implies that based on the distance estimation, the postures can be identified since the distances can be calculated easily for each posture a priori based on the body morphology.

Starting from the basic posture 1, it was observed that the gain of all the antennas can be considered as constant for fixed antenna-body spacing for each posture (which is approximately 5 dBi, see Appendix B). Therefore, β can be considered as constant for each posture and γ can be evaluated from (4.3) for different antennas comprising Tx-Rx link (See Appendix B for conversions)

$$\gamma_{(H_k,P_{(g,d)},Ce_i,Cr_j)}[dB] = S_{ij}[dB] - \beta_{(P_{(g,d)},C_e,C_r)}[dB] - 20log10\left(\frac{\lambda}{4\pi d}\right) \quad (4.4)$$

where S_{ij} corresponds to the link budget corresponding to antennas Ce_i and Cr_j. With the assumption of fixed antenna-body spacing, β can be written as

$$\beta_{(P_{(g,d)},C_{ei},C_{rj})} = G_t + G_r \quad (4.5)$$

Therefore, once the coefficient γ is known, the distances between the antennas can be evaluated using (4.4) which can be rewritten as (4.6)

$$d = \frac{\lambda}{4\pi[10^{\frac{S21-\beta-\gamma}{20}}]} \quad \text{[meters]} \quad (4.6)$$

where λ is in meters and each of S_{21}, β and Υ are in dB. Once the distances are known, the posture can be identified subject to the fact that the distance between the antennas for each posture is known a priori and the channel link budget (S_{ij}) is known.

The numerical values of link budget for all the five simulated postures (Section 4.3.5) is listed in Table 4.2 for all the Tx, Rx antennas (with the most critical values shown in shaded). It can be inferred from the values of the link budget that it is not necessary to use information of all the Tx (Ce_i) and Rx (Cr_j) antennas. e.g., Antennas 3 and 4 mostly stay in the LoS condition even with changing posture from 1-5, therefore the link budget does not change significantly for them giving a value of -54 dB, -42 dB, -48 dB, -49 dB and -43 dB respectively for postures 1-5 respectively. Likewise, between antennas 1 (Ce_i) and 5 (Cr_j) which remain under comparable transmission conditions for all the postures 1-5, the link budget remains quite stable with values of -65 dB, -65 dB, -64 dB, -58 dB and -72 dB respectively for postures 1-5 respectively. On the other hand, for antennas 1 and 4, the link budget vary significantly with changing postures from 1-5 resulting in values of -88 dB, -47 dB, -56 dB, -63 dB and -40 dB respectively. Likewise, the link budget between antennas 1, 3 and also the link budget corresponding to antennas 4, 5 vary significantly which can also be useful for posture classification.

Therefore, such critical node can be useful for classification of postures based on large variations in the link budget. Meanwhile, this information can be helpful to eliminate redundant nodes for simplicity of distance estimations model.

TABLE 4.2. LINK BUDGET FOR VARIOUS POSTURES AT 2.45 GHZ

Posture	Ce_i	Cr_j	S_{ij} (dB)
1	1	2	-66
	1	3	-77
	2	3	-59
	1	4	-88
	2	4	-66
	3	4	-54
	1	5	-65
	2	5	-69
	3	5	-69
	4	5	-77
2	1	2	-44
	1	3	-46
	2	3	-37
	1	4	-47
	2	4	-50
	3	4	-42
	1	5	-65
	2	5	-66
	3	5	-64
	4	5	-53
3	1	2	-44
	1	3	-74
	2	3	-53
	1	4	-56
	2	4	-56
	3	4	-48
	1	5	-64
	2	5	-65
	3	5	-85
	4	5	-72
4	1	2	-38
	1	3	-61
	2	3	-57
	1	4	-63
	2	4	-60
	3	4	-49
	1	5	-58
	2	5	-56
	3	5	-49
	4	5	-49
5	1	2	-38
	1	3	-31
	2	3	-42
	1	4	-40
	2	4	-41
	3	4	-43
	1	5	-72
	2	5	-56
	3	5	-60
	4	5	-56

Based on the link budget corresponding to the most critical antennas Ce_i and Cr_j, the coefficient Υ can be estimated e.g., the coefficient Υ corresponding to various postures between antennas Ce_i = 1 and Cr_j = 4 is listen in Table 4.3 as computed by (4.4). Once the coefficients are known, the distances can be estimated between antennas (1,4) using (4.6), hence resulting in identification of corresponding posture.

TABLE 4.3. COEFFICIENT Γ FOR $(C_{E_i}, C_{R_j})= (1, 4)$

Posture	***d*** **(cm)**	$\mathbf{S_{ij}(Ce_i, Cr_j)}$ **[dB]**	**γ**
1	72	-88	-60.6
2	42	-47	-24.3
3	63	-56	-29.7
4	62	-63	-37
5	36	-40	-18.6

4.4. Conclusions

The design of an electrically small chip antenna is presented covering full ISM 2.4 GHz bandwidth and having radiation characteristics identical in form to that of a monopole antenna. The on-body performance of the antenna has also been evaluated and found to be quite comparable to the free space performance in the azimuth plane which is more crucial for on-body links considered in this chapter.

A robust numerical channel simulator is developed with the power to simulate any arbitrary WBASN scenario with customized parameters such as antennas and their locations etc. for predicting real-life performance under limited simulation resources despite of electrically extraordinarily large simulation problem size. This also helps to avoid costly redundant measurements and save time along with financial resources. The simulator has the power to extract full wave S-parameters (complex values) for a standard WBASN scenario in frequency domain. These S-parameters can also be exported in other tools e.g., MATLAB for temporal analyses using Inverse Fourier transform on the imported data.

It was also shown that the results of the channel simulator can be useful for posture classification while dropping the information of redundant nodes for simplicity of coefficients estimation models. Once the coefficients are estimated, the distances can be calculated and hence, the postures can be identified since the distance between the antennas for each posture is known a priori. However, the coefficients are subject to vary in real-life applications e.g., as the antenna gains will vary due to changes in antenna-body spacing due to textiles etc. There is still a need to explore the area for finding universal coefficients dropping out the redundant information to introduce simplicity in the posture classification models.

References

[1] K. Fuji, M. Takahashi, K. ITO, and N. Inagaki, "Study on the electric field distributions around whole body model with a wearable device using the human body as a transmission channel," in *First European Conference on Antennas and Propagation, ,* Nov. 2006.

[2] Report of national institute of bioscience and human-technology, "Human body dimensions data for ergonomic design," vol.2, no.1, 1994.

[3] Y. Uno, K. Saito, M. Takahashi, and K. Ito, , "Characteristics of Loop Antennas Closely-Placed to Different Arm Models," *IEICE Tech. Rep., AP2010-13,* vol. 110, no. 23, pp. 7-10, May 2010.

[4] "www.daz3d.com," [Online].

[5] "http://my.smithmicro.com/poser-pro-2014.html," [Online].

[6] W. Choi, S. Kwon, B. Lee, "Ceramic chip antenna using meander conductor lines," *Electronics Letters,* vol. 37, no. 15, pp. 933-934, 2001.

[7] L. A-Asl, P. S.Hall, Y. Nechayev, and I. Khan, "Depolarization in On-Body Communication Channels at 2.45 GHz," *IEEE Transcatiosn on Antennas and Propagation,* vol. 61, no. 2, pp. 882-889, 2013.

[8] T. Alves, B. Poussot, and J. M. Laheurte, "Analytical propagation modeling of BAN channels based on the creeping-wave theory," *IEEE Trans. Antennas Propag.,* vol. 59, no. 4, p. 1269–1274, 2011.

[9] M. O. Munoz, R. Foster, and Y. Hao, "On-Body Channel Measurement Using Wireless Sensors," *IEEE Transactions on Antennas and Propagation,* vol. 60, no. 7, pp. 3397-3406, July 2012.

[10] L. Akhoondzadeh-Asl, I. Khan, and P.S. Hall, "Polarisation diversity performance for on-body communication applications," *IET Microw. Antennas Propag.,* vol. 5, no. 2, p. 232–236, 2011.

[11] Mohammad Monirujjaman Khan, "Antenna and Radio Channel Characterisation for Low-Power Personal and Body Area Networks," PhD thesis, Queen Mary, University of London,, Feb. 2012.

[12] Y. Hao and R. Foster, "Wireless body sensor networks for health-monitoring applications (invited)," *Physiol. Meas.,* vol. 29, p. R27–R56.

[13] P. S. Hall and Y. Hao, Antennas and Propagation for Body-Centric Wireless Communications, Norwood, MA: Artech House, 2006.

[14] M. Gallo, P. S. Hall, and M. Bozzetti, "Simulation and measurement of body dymamics for on-body channel characteirisation," in *Proc. Antennas and Propagation for Body-Centric Wireless Communications, IET Seminar,* 2007 .

[15] Z. H. Hu, M. Gallo, Q. Bai, Y. I. Nechayev, P. S. Hall, and M. Bozzettit, "Measurements and simulations for on-body antenna design and propagation studies," in *EuCAP,* 2007.

[16] S. Dumanli, "On-body antenna with reconfigurable radiation pattern," in *RF and Wireless Technologies for Biomedical and Healthcare Applications (IMWS-Bio),* London (UK), Dec. 2014.

[17] D. Ma and W.-X. Zhang, "Coupling-fed circular-patch antenna for onbody communication system," *Microwave and Optical Tech. Lett.*, vol. 51, no. 11, p. 2623–2627, 2009.

[18] "https://www.cst.com/," [Online].

[19] "http://niremf.ifac.cnr.it/tissprop/," [Online].

[20] P. S. Hall and Y. Hao, Antennas and Propagation for Body-Centric Wireless Communications, Norwood, MA, USA: Artech House, Inc, 2006.

[21] I. Yamaura, "Measurements of 1.8 - 2.7-Ghz Microwave Attenuation in the Human Torso," *IEEE Transactions on Microwave Theory and Techniques*, vol. 25, no. 8, pp. 707-710, Aug. 1977.

[22] V. G. Posadas, D. S. Vargas, E. R. Iglesias, J.L. Vazquez-Roy, C. M. Pascual, "Approximate analysis of short circuited ring patch antenna working at TM01 mode," *IEEE Transactions on Antennas and Propagation*, vol. 54, no. 6, pp. 1875-1879, Jun. 2006.

[23] S. Dumanli, "On-body antenna with reconfigurable radiation pattern," in *RF and Wireless Technologies for Biomedical and Healthcare Applications (IMWS-Bio)*, London (UK), Dec. 2014 .

[24] G. A. Conway, W. G. Scanlon, "Antennas for over-body-surface communication at 2.45 GHz," *IEEE Transactions on Antennas and Propagation*, vol. 57, no. 4, pp. 844 - 855, April 2009.

[25] P.S. Hall, Y. Hao, Y. I. Nechayev, A. Alomainy, C. C. Constantinou, C. Parini, M. R. Kamarudin, T. Z. Salim, D. T. M. Hee, R. Dubrovka, A. S. Owadally, S. Wei, A. Serra, P. Nepa, M. Gallo, M. Bozzetti, "Antennas and propagation for on-body communication," *IEEE Antennas and Propagation Magazine, ,* vol. 49, no. 3, pp. 41 - 58, June 2007.

[26] D. Ma, and W. X. Zhang., "A dual-band dual-polarized antenna for body area network," in *Proceedings of the Fourth European Conference on Antennas and Propagation (EuCAP)*, Barcelona, Spain, April 2010.

[27] Vladimír Hebelka, "Planar Antennas in Proximity of Human Body Models," *Elektrorevue*, vol. 3, no. 4, December 2012.

[28] "Mobiltelefoner och Strålning," Sweden's Radiation Protection Authority, Tech. Rept., 2003.

[29] K. L. Wong and C. I. Lin, "Characteristics of a 2.4-GHz compact shorted patch antenna in close proximity to a lossy medium," *Microw. Opt. Technol. Lett.*, vol. 45, no. 6, p. 480–483, Jun. 2005.

[30] A.A. Serra, I. Khan, P. Nepa, G. Manara, P.S. Hall, "Dual-polarization and dual-pattern planar antenna for diversity in body-centric communications," in *Antennas and Propagation Society International Symposium*, 2008.

[31] D. Ma, and W.-X. Zhang, "Coupling-fed circular-patch antenna for onbody communication system," *Microwave & Optical Tech. Lett.*, vol. 51, no. 11, pp. 2623-2627, November 2009.

[32] P. Kyritsi, and D. C. Cox, "Propagation characteristic of horizontally and vertically polarized electric fields in an indoor environment: simple model and results," in

IEEE vehicular Technology Conference, 2001.

Chapter 5. Pattern and polarization diversity antennas

Contents

5.1. Introduction

As explained in Chapter 3, when an antenna operating at microwave frequencies is brought in close proximity to human body its performance deteriorates due to the degradations caused by the lossy human tissue and its high dielectric constant. Consequently, the antenna suffers from frequency detuning due to changes in its input impedance. Moreover, the antenna gain and radiation efficiency are reduced along with distortion of the radiation patterns [1]-[5]. Therefore, the first objective is to design the antenna which can offer nearly stable performance in proximity to human body along with being compact, low-profile, ergonomic and unobtrusive for dynamic wearable applications.

For wearable BANs, devices can communicate at two hierarchical levels from communication perspective. i.e., on-body and off-body. As stated in Chapter 3, for on-body applications, the antenna radiation should be directed along the body to radiate omni-azimuthal pattern along the body surface with a preferably vertical polarization [6]. For the case of off-body links, the antenna radiation should be directed away from the body (broadside direction), whereas the polarization is not as critical as for the on-body case [6]. The monopole antenna is considered to be a good candidate for on-body applications since it generates maximum radiation along the body surface with a vertically polarized electric field normal to the body surface which can excite surface waves [7]- [8]. However, the main difficulty is the size of the monopole antenna (i.e., $\lambda_0/4$ @ f_0) which is quite large at ISM 2.4 GHz frequencies and also its obtrusiveness which are not favorable for portable applications. A patch antenna can suit the off-body applications due to its maximum radiation in the orthogonal plane or in the direction away from the body.

This implies that separate antennas are required for both on- and off-body operations for optimum BAN performance from radiation and polarization perspectives. For on-body applications, the transceiver locations change significantly due to the user mobility which causes significant changes in the link due to the change in direction of arrival. Radiation pattern and polarization diversity can also be exploited for improving the link efficiency for on-body applications based on the propagation scenario and also on the particular transceiver nodes. The conventional solution of using antenna arrays for beam-forming is not a suitable solution for BANs since space and form-factor are crucial. The optimum situation is hence, to achieve diversity using a single antenna where the optimum operational mode for radiation pattern and polarization can be selected iteratively or dynamically instead of using multiple antenna prototypes.

From the various antenna topologies, patch antennas are appropriate solutions for wearable applications due to the ease of their construction, low-profile, and planar geometry. Therefore, we considered here the characteristic mode theory of patch antennas to exploit the multiple modes for generating pattern and polarization diversity simultaneously for WBAN applications. The objective is to design a multimode, dual-polarized, dual-pattern antenna which can be used universally for both on- and off-body application modes. Moreover, such antenna should also be capable of adapting the radiation pattern/polarization requirements for various on-body nodes based on the inherently dynamic body postures of a mobile BAN user.

This chapter is organized as follows. In Section 5.2, the design of a pattern diversity antenna is presented in the ISM 2.4 GHz band using short-circuited ring patch antennas. However, the antenna offers quite poor coupling between the multiple modes. Therefore, another dual-mode, dual-pattern polarization diversity antenna is presented in Section 5.3 with improved cross-modal coupling and broader impedance bandwidth. Its on-body performance is evaluated along with the diversity performance parameters such as envelope correlation coefficient and diversity gain. In Section 5.4, the interest of using radiation pattern and polarization diversities simultaneously is presented for on-body applications using both simulations and measurements. Finally, conclusions are drawn in Section 5.5.

5.2. Shorted ring patches based pattern diversity antenna

In the first design stage, the characteristic mode theory of short-circuited ring patch antennas was considered in Chapter 3 (Section 3.4) where two different prototypes of a shorted ring patch antenna were designed with excitation under two different modes namely TM_{01} and TM_{11} at the same ISM 2.4 GHz frequency. It was also demonstrated that the two modes meet also the appropriate radiation and polarization requirements for both on-and off-body applications. Once the two modes are optimized at 2.4 GHz, the next objective was to perform a co-integration of these two antennas which are excited under two different modes for the design of pattern diversity antenna at single frequency (2.4 GHz). The co-integration was attempted using two prototypes stacked on each other with the first prototype excited under TM_{01} mode at the bottom and the second prototype excited under TM_{11} mode at the top (Fig. 5.1). The motivation behind this choice was the radius of the shorting post b_1 (=6 *mm*) in Fig. 5.1 was less than the radius b (=8 *mm*) for the prototypes excited under TM_{11} and TM_{01} modes respectively. The prototype with TM_{01} mode was kept at the bottom to make enough room for the short circuit of the top prototype to penetrate through the periphery of TM_{01} mode short circuit (which was kept as hollow from inside). The layout of the proposed diversity antenna is shown in Fig. 5.1. 50-Ω coaxial feeds were designed for excitation ports 1 and 2. The overall size of the antenna is 6 × 0.64 cm^2.

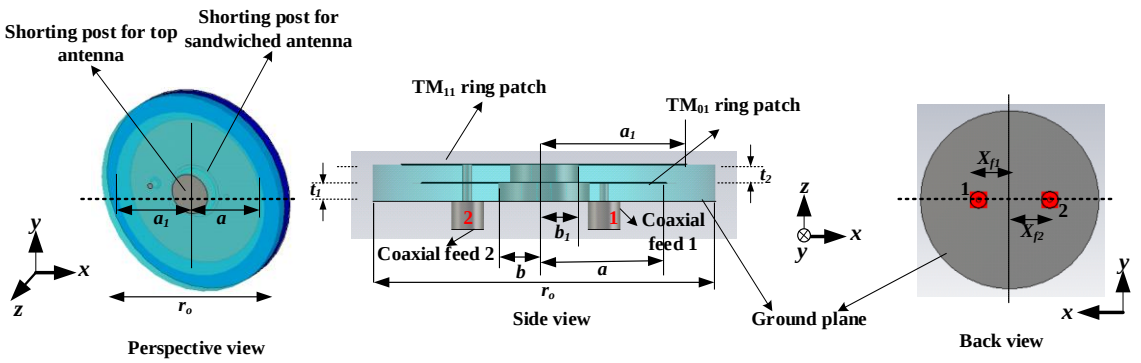

(a) (b) (c)

Figure 5.1. Layout of the dual-mode diversity antenna (substrate RT5880, ε_r = 2.2) (a) Perspective view (b) Side view (c) Bottom view. Optimized dimensions (in *mm*): a = 21.5, b = 8, a_1 = 25, b_1 = 6, r_o = 60, X_{f1} = 10.4, X_{f2} =14.3, t_1 = t_2 =3.175 *mm*.

The dimensions of the antenna were optimized using a number of parametric analyses using CST MWS^{TM} for generating the two resonant modes simultaneously at 2.4 GHz. The reflection coefficient of the bottom antenna (port 1 in Fig. 5.1) is represented by S_{11} and that of the top antenna (port 2 in Fig. 5.1) is represented by S_{22}. The coupling between the two ports is represented by S_{21}. The resonant frequency for S_{11} is mainly controlled by parameters *a* and *b* and that for S_{22} is controlled by parameters a_1 and b_1; a_1 and *a* correspond to the radii of the top and bottom ring resonators respectively (Fig. 5.1 (b)), b_1 and *b* correspond to radii of the top and bottom shorting elements respectively (Fig. 5.1 (b)). The impact of the dimensions a_1 and b_1 on the resonance of the top antenna (S_{22}) is shown in Fig. 5.2 where all other dimensions are kept constant. The resonant frequency for S_{22} drops with increasing the radius of ring element a_1 or decreasing the radius of short-circuit b_1. Similar analyses apply also for S_{11} of the bottom antenna for equivalent dimensions *a* and *b* (Fig. 5.1 (b)).

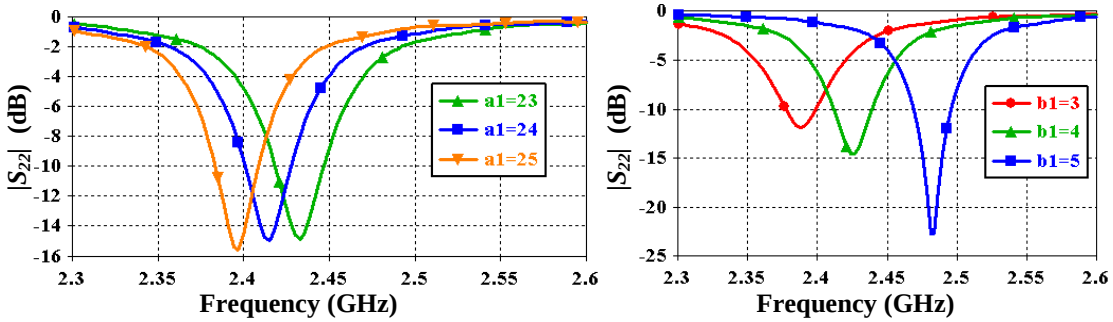

(a) (b)

Figure 5.2. Impact of dimensions (a) a_1 (*mm*) and (b) b_1 (*mm*) on the resonance of top antenna (Fig. 5.1).

The feed positioning mainly controls the matching of the two modes (S_{11} and S_{22}) along with the coupling (S_{21}) between them. The impact of feed positioning X_f on all the S-parameters of the antenna is shown in Fig. 5.3 when both ports of the antenna are moved in opposite direction along *x*-axis by factor X_f (*mm*) i.e., $X_f = -X_{f1} = X_{f2}$ in Fig. 5.1 (c). As evident, the magnitude of both S_{11} and S_{22} changes along with the coupling between the two modes due to changes in impedance matching.

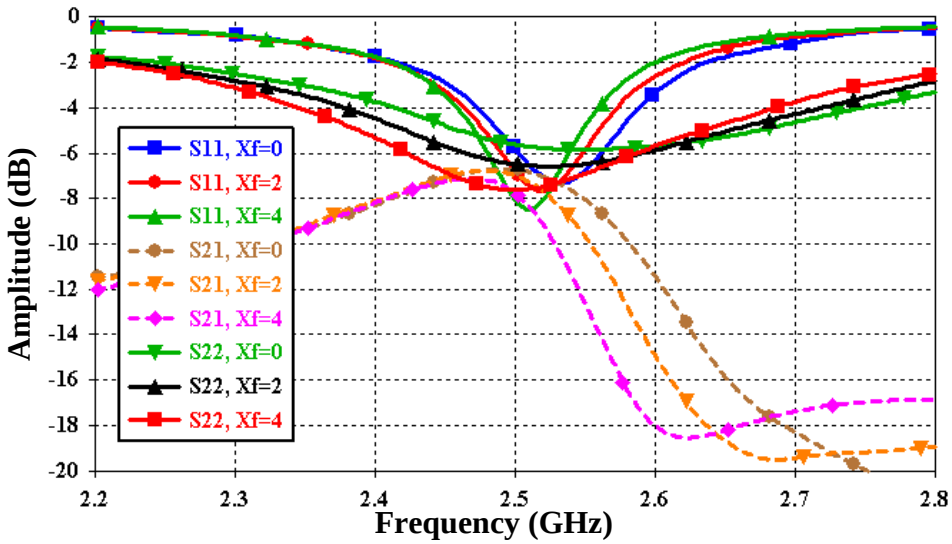

Figure 5.3. Impact of feed positioning X_f (*mm*) when both feeds are displaced in opposite directions along *x*-axis by factor X_f.

The overall dimensions of the antenna were hence, optimized using all the possible degrees of freedom for exciting the two resonant modes simultaneously at 2.4 GHz while keeping also a minimum possible coupling between them. The overall S-parameters of the optimized antenna are shown in Fig. 5.4 showing the proper matching of the two modes with both S_{11} and S_{22} less than -10 dB at 2.4 GHz. It will be proved further that these resonances indeed correspond to the TM_{01} and TM_{11} modes for port 1 and 2 respectively. The coupling is observed to be quite high being greater than -10 dB. This will also be analyzed in the following sections.

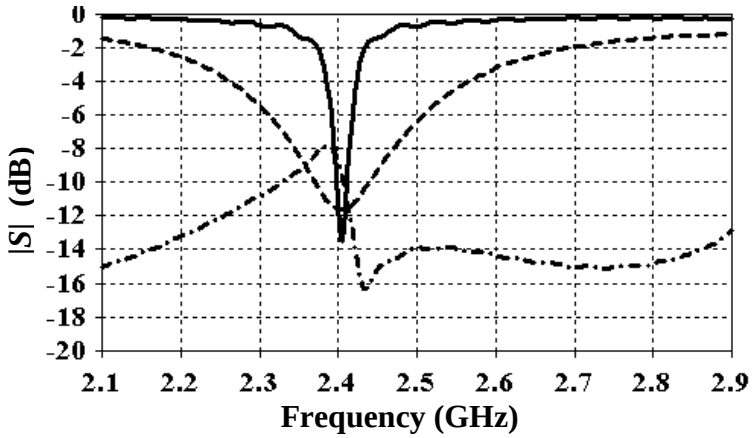

Figure 5.4. Simulated S-parameters of the diversity antenna S_{11} (———), S_{22}(– – –), S_{21}(– · – ·).

The current distribution excited by the two ports at 2.4 GHz is also shown in Fig. 5.5. Such distribution corresponds to the TM_{01} mode for lower antenna (port 1 in Fig. 5.1) and TM_{11} mode for antenna 2 (port 2 in Fig. 5.1) as presented in [9] also. The asymmetry in surface current distribution of the patch elements (Fig. 5.5) is caused by the feed probes which pierce the substrate, hence making contact with the patches.

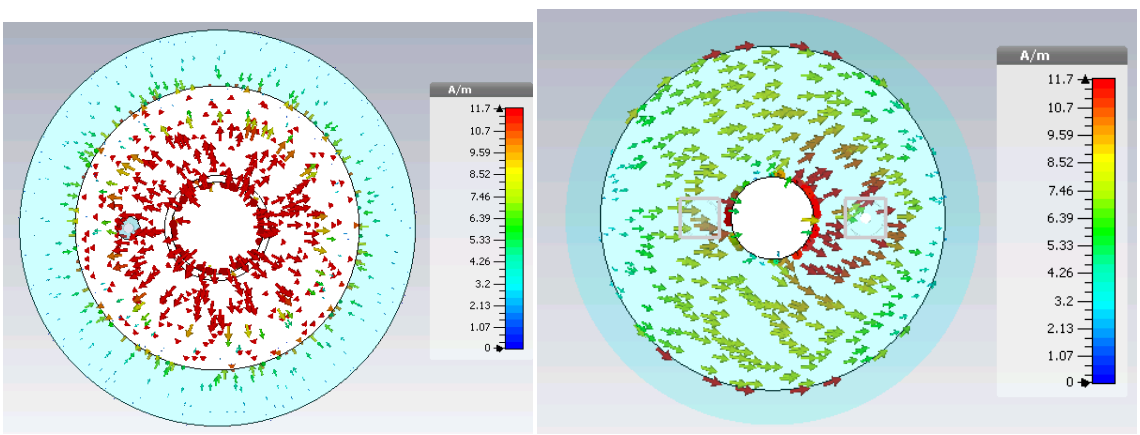

(a) (b)

Figure 5.5. Surface current distribution at 2.4 GHz for (a) port 1 (TM_{01} mode) and (a) port 2 (TM_{11} mode).

The 3D radiation patterns of the two resonant modes (TM_{01} and TM_{11}) are also illustrated in Fig. 5.6 along with the corresponding 2D patterns in E- and H planes plotted in Fig. 5.7. The antenna gain reaches 1.4 dBi for the fundamental TM_{01} mode and 7.3 dBi for the TM_{11} mode at 2.4 GHz. Moreover, the total radiation efficiency is 76% for

the TM_{01} mode compared to 82% for the TM_{11} mode at 2.4 GHz. The gain and radiation efficiency of the TM_{11} mode are greater than those for TM_{01} mode because the former is a directional mode compared to the latter which is omnidirectional. As evident from Fig. 5.6 and Fig. 5.7, the antenna can generate radiation with the maximum in the azimuth direction at port 1 for the on-body operation, meanwhile a maximum radiation in the broadside direction at port 2 for off-body operation. Therefore, the antenna successfully achieves the radiation pattern diversity for both on- and off-body applications.

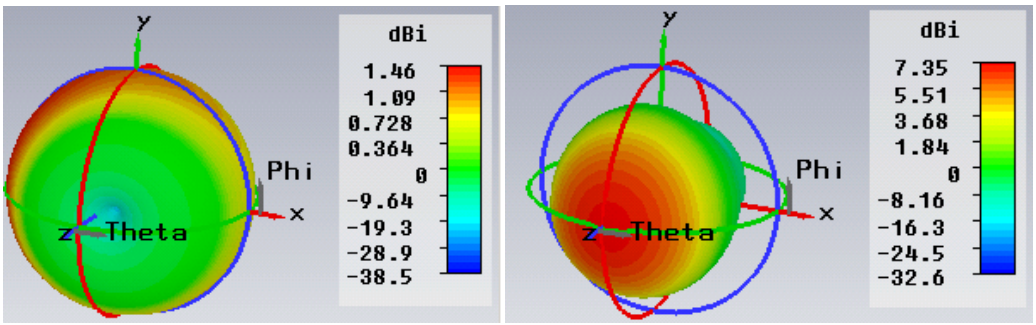

(a) (b)

Figure 5.6. 3D radiation patterns of the pattern diversity antenna at 2.4 GHz for (a) TM_{01} mode (port 1) and (a) TM_{11} mode (port 2).

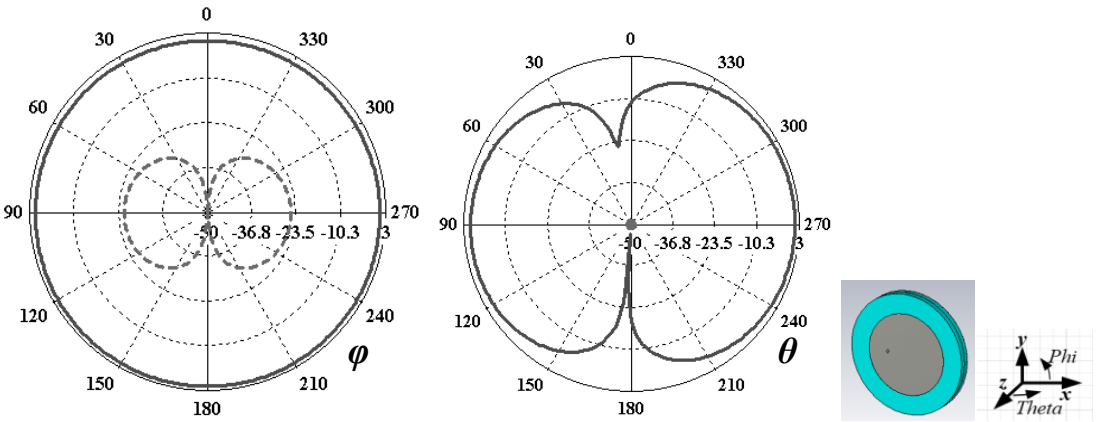

(a) *xy*-plane (TM_{01} mode) (b) *xz*-plane (TM_{01} mode)

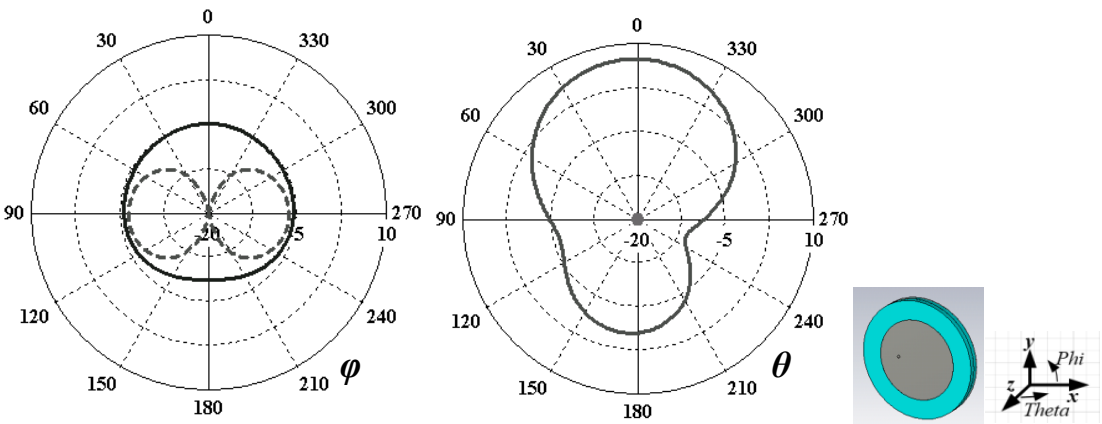

(c) *xy*-plane (TM_{11} mode) (d) *xz*-plane (TM_{11} mode)

Figure 5.7. Radiation patterns of the pattern diversity antenna at 2.4 GHz showing both co-polarization (——) and cross-polarization (– – –) (dot at centre shows value less than the minimum scale).

As evident from Fig. 5.4, the coupling between the two modes of the pattern diversity antenna was observed to be quite high in this case, being greater than -10 dB i.e., ≈ -8 dB at 2.4 GHz. This is due to the high coupling between the two short circuits which connect the two antenna layers to the same ground plane. The distribution of ***E***-field for the sandwiched antenna at 2.4 GHz is also illustrated in Fig. 5.8. As evident, the field on the central shorting post has quite high strength which results in strong coupling with the central short circuit of top antenna which is connected to the same ground plane. This can also adversely affect the diversity performance of the antenna since the cross-coupling has direct influence on envelope correlation coefficient which controls the diversity gain in real-time diversity systems e.g., in MIMO systems as will be discussed in coming sections.

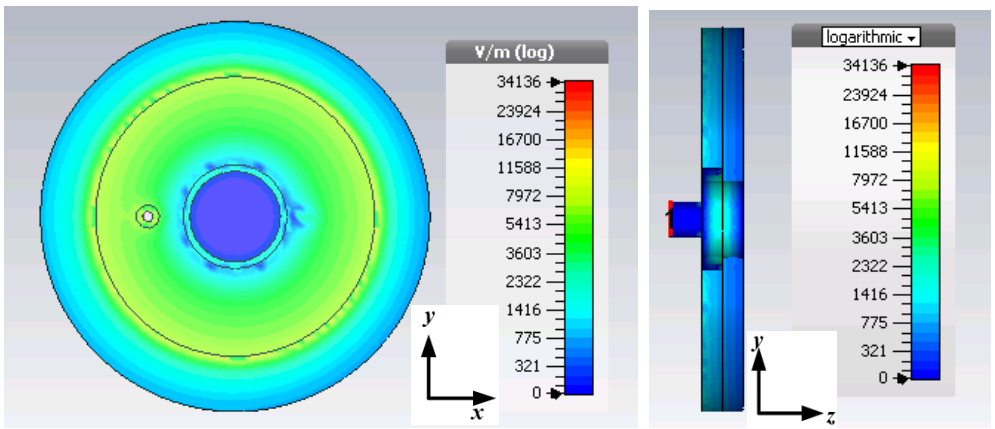

(a) (b)

Figure 5.8. Electric field distribution at 2.4 GHz for the sandwiched antenna layer (a) Front view (b) cross-sectional view.

5.3. Dual-mode diversity antenna with improved cross-coupling

As presented in Section 5.2, the pattern diversity antenna inspired by the shorted ring patch antennas meets successfully the radiation pattern requirements for both on- and off-body applications at 2.4 GHz. However, the coupling between the two modes was observed to be quite poor i.e., ≈ -8 dB @ 2.4 GHz. This implies that approximately 15 % of the power transmitted via the port 1 will be coupled passively to the port 2, hence causing unwanted spurious radiation. The coupling is also important to avoid spurious radiation to ensure that only one of the two resonant modes is active at a given instant of broadcast. Poor coupling can result in passive radiation from the inactive antenna which can result in cross-talk in real-time communication systems. Also, the bandwidth of the antenna presented in Section 5.2 is observed to be quite narrow which is insufficient for ISM 2.4 GHz application bandwidth (2.40-2.4835 GHz).

In this section, a novel pattern- and polarization diversity antenna with improved bandwidth and reduced cross-coupling is presented. The motivation behind the improved design lies on the principle that the TM_{11} radiation mode can also be generated by using an open circular patch antenna which offers TM_{11} mode as its dominant mode (i.e., at its

fundamental resonant frequency) [9]. The resonant frequencies of the TM_{mn} modes in an open patch antenna can be controlled using the cavity model with two PECs at the top and bottom to represent the conducting element and ground plane respectively, and a cylindrical PMC around the circular cavity which results in (5.1) [10]

$$f_{mn} = \frac{\chi'_{mn}}{2\pi R\sqrt{\mu\varepsilon_r}} \tag{5.1}$$

where χ_{mn} represents the zeroes of the derivative of the Bessel function $J_m(x)$ and R is the radius of the radiating element.

Moreover, the TM_{11} mode is the dominant mode (with lowest cut-off) in case of open patch which offers the same broadside radiation pattern e.g.., similar to the TM_{11} mode in shorted ring patches or the TM_{10} mode for rectangular patches [9]. The resonant frequency of TM_{11} mode for open circular patch is given by (5.2) [10] (neglecting the fringing fields)

$$f_{11} = \frac{1.8412c}{2\pi R\sqrt{\varepsilon_r}} \tag{5.2}$$

In order to avoid the double short-circuit to the same ground plane, an open circular patch antenna was considered for generating the TM_{11} mode while still considering the shorted ring patch for TM_{01} mode excitation (Section 5.2). Therefore, the top antenna of Section 5.2 was now replaced by a circular patch antenna, whereas the bottom antenna still employs a shorted ring patch (TM_{01} mode).

This idea could also result in number of other advantages such as ease of fabrication since now only one short circuit is needed to be implemented. It also results in reduction in size for fixed frequency (i.e., 2.4 GHz). since open circular patch offers TM_{11} at its first or fundamental mode. This mode on the other hand, is a second order mode in case of a shorted ring patch antenna which implies increase of size to tune its second resonant mode to a fixed frequency (i.e., 2.4 GHz).

5.3.1. Antenna design

The idea was to excite the two different modes i.e., TM_{11} and TM_{01} using open and short-circuited patch antenna topologies respectively in a co-integrated, single package for the same ISM 2.4 GHz frequency. The co-integration was performed with the two prototypes stacked on each other. The first prototype namely the shorted ring patch antenna at bottom was excited under its fundamental TM_{01} mode. The second prototype at the top namely open circular patch was excited under its fundamental TM_{11} mode. The same substrate was considered for both antenna layers i.e., Rogers RT/duroid 5880 (ε_r = 2.2, t = 3.175 mm) with 50-Ω coaxial feeds for the two excitation ports. The coaxial feeds comprise diameters of 1.6 *mm* and 5.4 *mm* respectively for the central and outer conductors respectively. The layout of the proposed diversity antenna is shown in Fig. 5.9 along with the optimized dimensions for operation within ISM 2.4 GHz band. The overall size of the antenna is 6.8×0.64 cm^2.

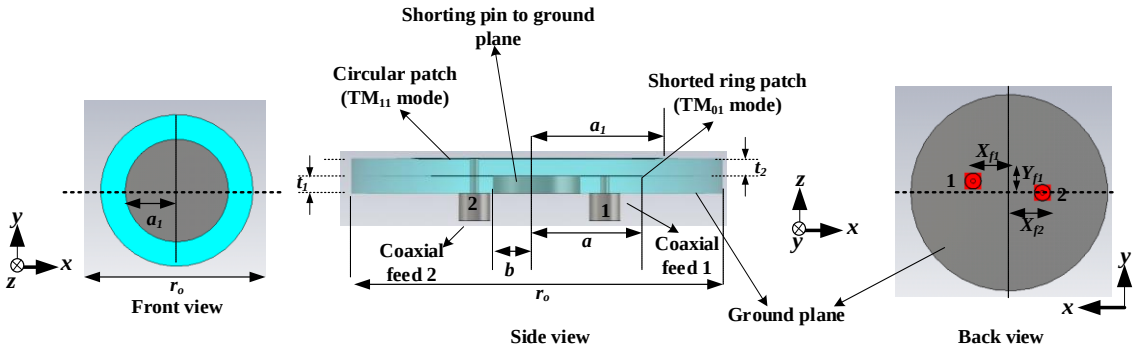

Figure 5.9. Layout of dual-mode diversity antenna with improved cross-modal coupling (substrate RT5880, ε_r = 2.2, $t_1 = t_2$ = 3.175 *mm*) (a) Front view (b) Side view (c) Back view. Optimized dimensions (in *mm*): a = 19.35, b = 8, a_1 = 23, r_o = 68, X_{f1} = 12.5, Y_{f1} = 4, X_{f2} = 11.4.

The dimensions of the antenna were optimized using a number of parametric analyses in CST MWS^{TM} for generating the two resonant modes simultaneously in ISM 2.4 GHz bandwidth (2.40-2.4835 GHz). The reflection coefficient of the shorted ring patch (bottom antenna with port 1 in Fig. 5.9) is represented by S_{11} and that of the open circular patch (top antenna with port 2 in Fig. 5.9) is represented by S_{22}. The coupling between the two antenna ports is represented by S_{21}. The resonant frequency for S_{11} is mainly controlled by parameters a and b as already demonstrated in Section 5.2 for the shorted ring patches based diversity antenna (Fig 5.2). The resonant frequency for S_{22} is controlled by the radius of the element a_1 as shown in Fig. 5.10. The resonant frequency for S_{22} rises with decreasing the radius of ring element a_1.

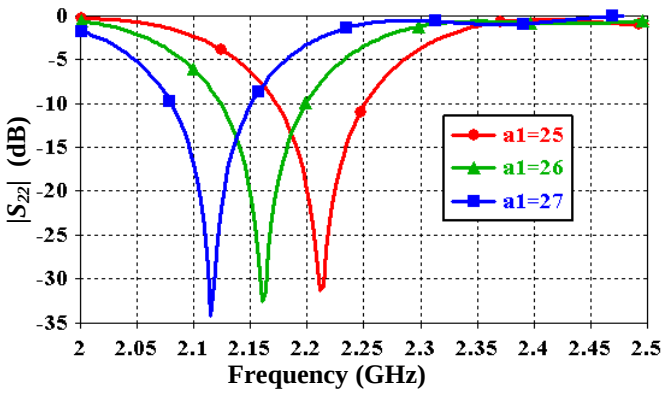

Figure 5.10. Impact of dimension a_1 (*mm*) on the resonance of open circular patch antenna (Fig. 5.9).

The feed positioning mainly controls the matching of the two modes (S_{11} and S_{22}) along with the cross-coupling (S_{21}) between them. The impact of dimension X_{f2} (Fig. 5.9) on all the S-parameters of the antenna is shown in Fig. 5.11. As evident, the magnitude of S_{22} changes along with the coupling between the two modes due to changes in impedance matching. S_{11} is not influenced here since its matching is mainly controlled by positioning of port 1 as presented in Section 5.2 (Fig. 5.3).

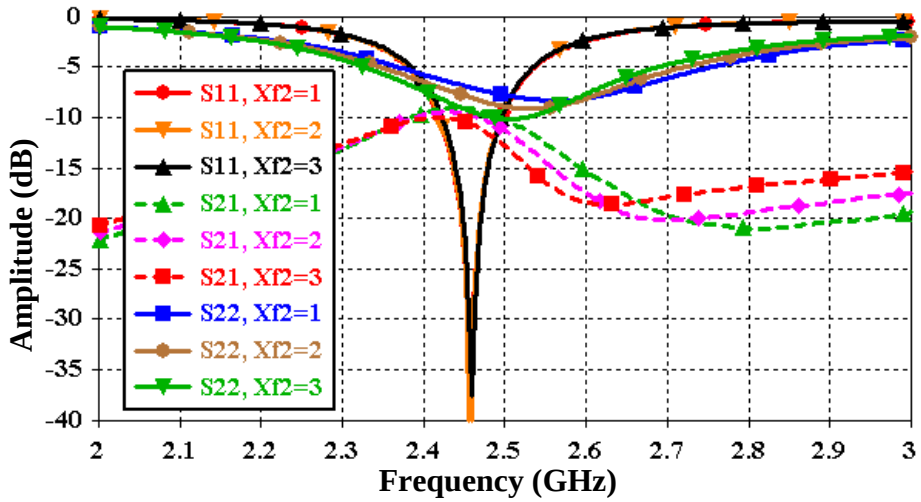

Figure 5.11. Impact of feed positioning X_{f2} (*mm*) on overall S-parameters of the antenna.

The dimensions of the two antennas were hence tuned after a number of intensive and careful optimizations in CST MWS for exciting the two resonant modes for ISM 2.4 GHz bandwidth while keeping also the minimum possible coupling between them. The simulated S-parameters of the optimized antenna are shown in Fig. 5.12 showing proper matching of the two modes throughout the ISM 2.4 GHz bandwidth with $|S_{ij}| < 10$ dB where $(i, j) \in \{1,2\}^2$; S_{11} and S_{22} here correspond to the TM_{01} and TM_{11} modes respectively. The coupling between the two modes (S_{21}) is now observed to be better with a value less than 10 dB throughout the ISM 2.4 GHz bandwidth.

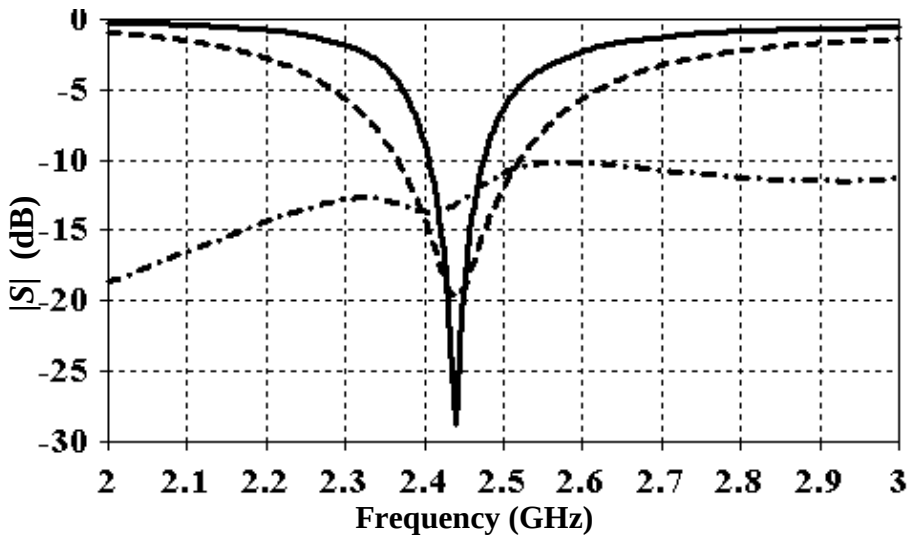

Figure 5.12. Simulated S-parameters of the diversity antenna S_{11}(———),S_{22}(– – –),S_{21} (– · – ·).

The current distribution for the two excitation ports at 2.45 GHz is also shown in Fig. 5.13. As evident, the current distribution for port 1 corresponds to the TM_{01} mode which is indeed the excitation port for lower antenna (Fig. 5.9) and that for port 2 corresponds to the TM_{11} mode [9] which is the excitation port for upper antenna (Fig. 5.9).

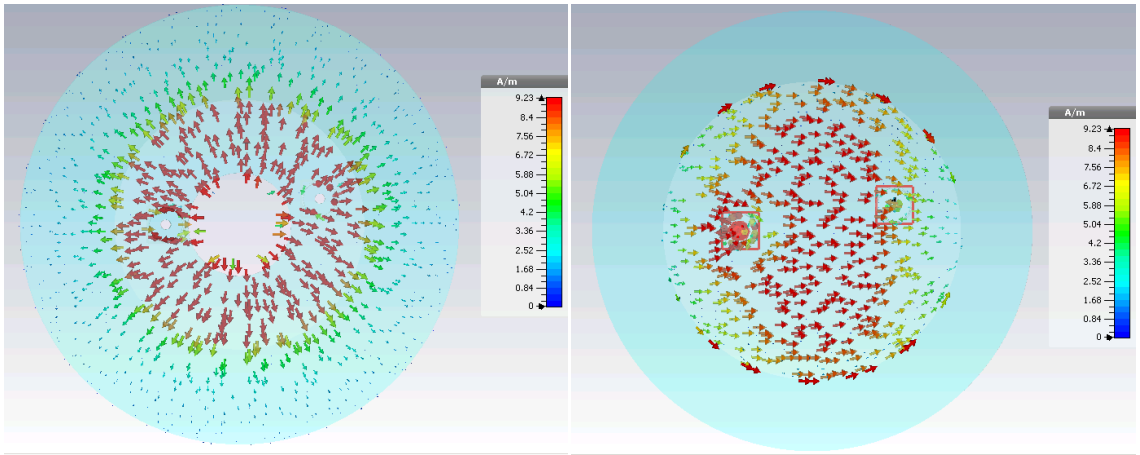

(a) (b)

Figure 5.13. Surface current distribution at 2.45 GHz for (a) TM_{01} mode and (b) TM_{11} mode.

The 3D radiation patterns of the two resonant modes (TM_{01} and TM_{11}) at 2.45 GHz are also illustrated in Fig. 5.14. As evident from the current distributions in Fig. 5.13, in case of TM_{01} mode (port 1), the currents have opposite directions in the orthogonal plane i.e., along *z*-axis, hence the antenna far-field has a null in the broadside direction resulting in an overall monopolar radiation pattern in Fig. 5.14 (a). For the TM_{11} mode, the currents are oriented in the same direction in the plane orthogonal to the antenna (Fig. 5.13 (b)). Consequently, the antenna has a maximum radiation in the broadside direction for this mode. The antenna can successfully generate the two types of radiation patterns as deemed suitable for both on- and off-body operations. The antenna gain reaches 1.11 dBi for the fundamental TM_{01} mode with a total efficiency of 92% at 2.45 GHz. The gain of TM_{11} mode is 7.12 dBi with a total efficiency of 93% at 2.45 GHz.

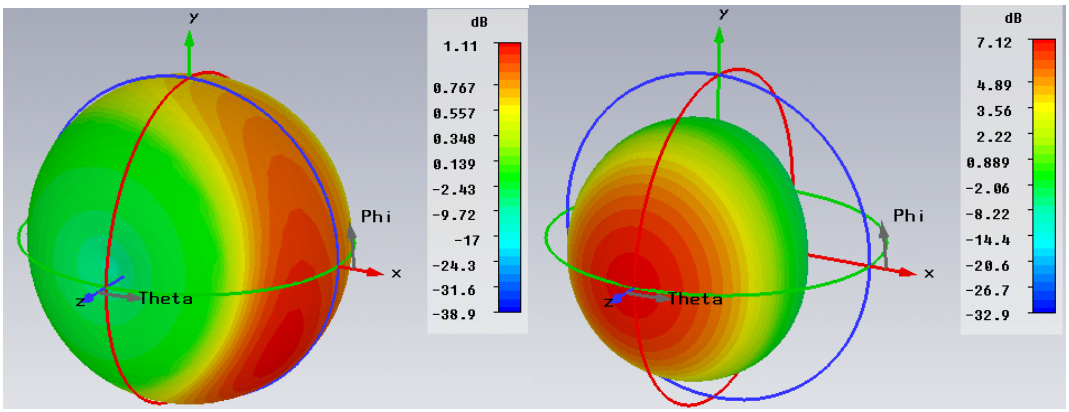

(a) (b)

Figure 5.14. 3D radiation patterns of the diversity antenna at 2.45 GHz for (a) port 1 (TM_{01} mode) and (b) port 2 (TM_{11} mode) (coordinate system shown in Fig. 5.9).

The E and H plane patterns of the antenna for both modes at various frequencies inside ISM 2.4 GHz bandwidth are plotted in Fig. 5.15 showing both the co- and cross-polarization components. For both modes, E_θ corresponds to the co-polarization and E_φ is the cross-polarization with the indicated coordinate system. It is evident that the principal polarization of the antenna for TM_{01} mode is in the *xz*-plane which is the plane orthogonal to the antenna. Whereas for TM_{11} mode, the co-polarization corresponds to

the *xy*-plane which is the plane parallel to the antenna. The antenna offers a vertical ***E***-field polarization for TM_{01} mode and a horizontal ***E***-field polarization for TM_{11} mode.

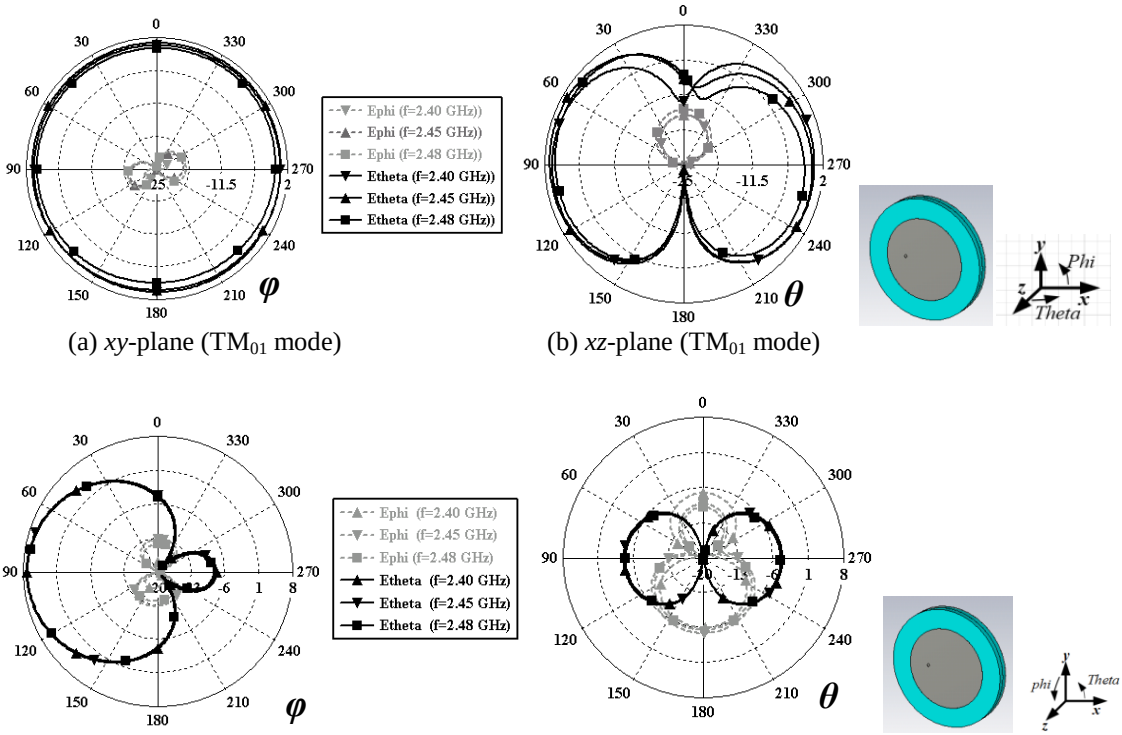

(a) *xy*-plane (TM_{01} mode) (b) *xz*-plane (TM_{01} mode)

(c) *yz*-plane (TM_{11} mode) (d) *xy*-plane (TM_{11} mode)

Figure. 5.15. Radiation patterns of the antenna at 2.45 GHz (reference coordinate system also shown on right for both modes).

The polarization was verified by electric field distribution for the two modes at 2.45 GHz which was computed by CST MWS^{TM} and shown in Fig. 5.16. As evident from the results, the TM_{01} mode has a vertical polarization of ***E***-field i.e., in the plane orthogonal to the antenna or *xz*-plane. This also confirms with [11] which states that TM_{01} mode offers a polarization of electrical field orthogonal to the patch plane. The TM_{11} mode has a horizontal polarization of ***E***-field i.e., parallel to the patch plane or in *xy*-plane. The antenna will offer a polarization orthogonal to the body for TM_{01} mode and a polarization parallel to the body for TM_{11} mode.

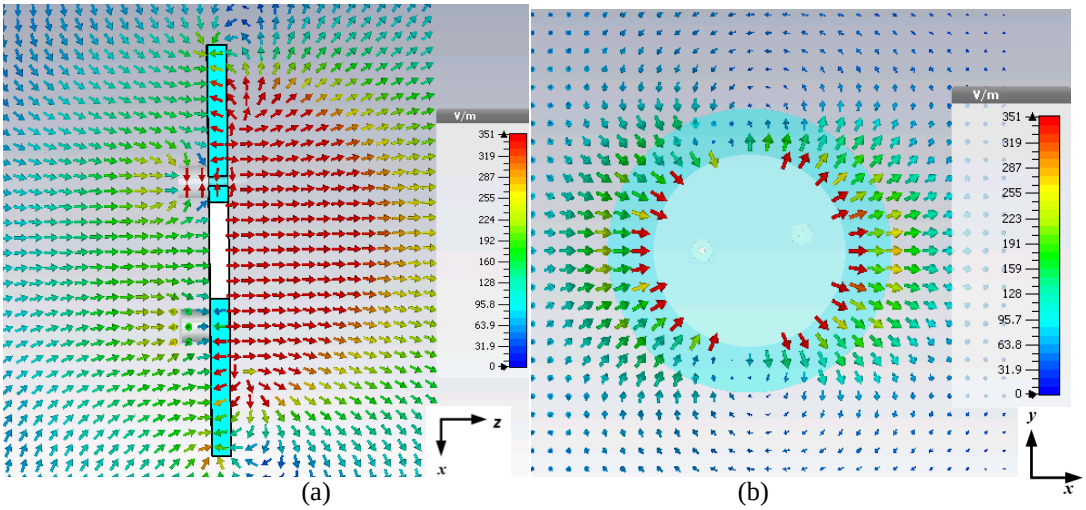

(a) (b)

Figure 5.16. Electric field distribution at 2.45 GHz for (a) TM_{01} mode (port 1) and (b) TM_{11} mode (port 2).

The antenna radiation patterns were verified throughout the ISM 2.4 GHz bandwidth and it was observed that the omni-azimuthal and broadside radiation pattern symmetry is maintained throughout the ISM 2.4 GHz bandwidth. This is logical also due to the nice matching of both resonant modes throughout ISM 2.4 GHz bandwidth i.e., $|S_{ij}| < 10$ dB where $(i, j) \epsilon \{1,2\}^2$ for $2.4< f\,(\text{GHz}) <2.5$). The variation of antenna gain throughout the ISM 2.4 GHz bandwidth is also shown in Fig. 5.17 for the two resonant modes where it can be seen that the antenna gain is also quite stable throughout the ISM 2.4 GHz bandwidth. The gain for the TM_{11} mode is higher compared to that for TM_{01} mode, since the former is a directional mode compared to the latter which is omnidirectional.

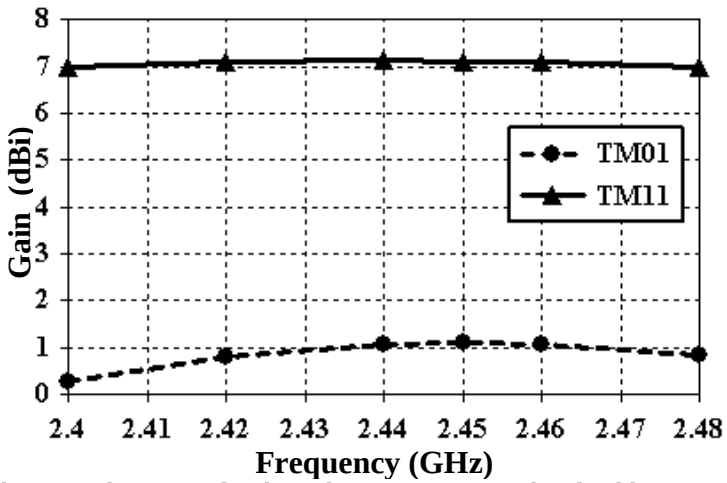

Figure 5.17. Gain of the two radiation modes throughout ISM 2.4 GHz bandwidth.

5.3.2. On-body performance

To investigate antenna performance on the body, the antenna was placed on a realistic full-body phantom imported from the commercial CAD program POSER™ [12] in CST MWS™ as shown in Fig. 5.18. To consider lossy tissue impact, dielectric properties of muscle tissue at 2.45 GHz i.e., $\varepsilon_r = 52$ and $\sigma = 1.7$ S/m were allocated to the homogenous

phantom [13]- [14]. A minimum spacing of 1 *mm* was maintained between the body and antenna to study significant body impact.

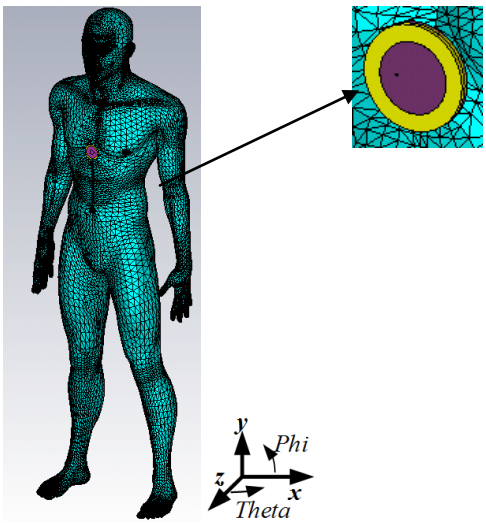

Figure 5.18. Placement of the diversity antenna on a realistic 3D ghost phantom (Antenna ground plane size is 68 *mm*).

The S-parameters of the antenna in proximity to body model are shown in Fig. 5.19 compared to those in free space. As evident from the results, the antenna offers nearly stable performance in proximity to body despite of very small antenna-body spacing (≈1 *mm*). There is no noticeable frequency detuning for both TM_{01} and TM_{11} modes and also the antenna coupling is not influenced by the body proximity which still stays below -10 dB throughout the ISM bandwidth. The antenna offers nearly stable performance in proximity to human body in terms of impedance matching.

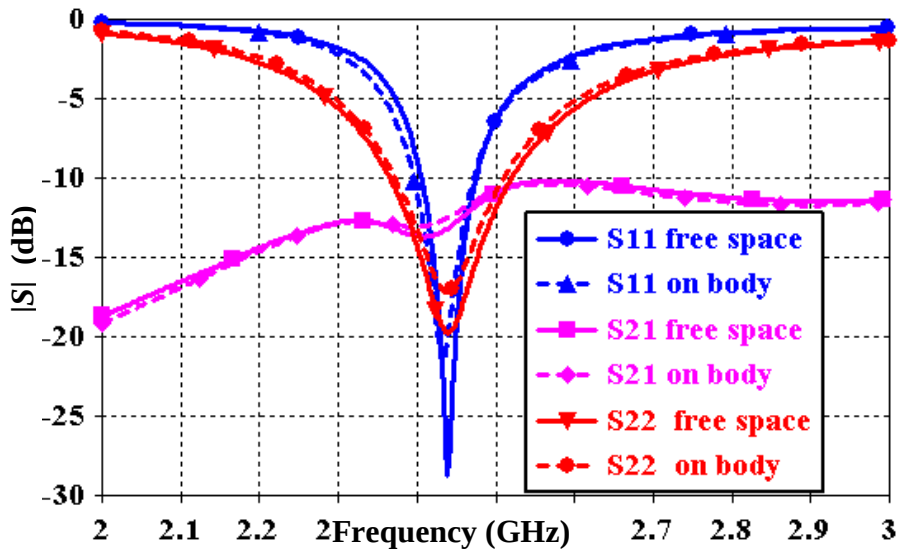

Figure 5.19. S-parameters of the antenna on-body model compared to those in free space for both modes.

The radiation patterns of the antenna for the TM_{01} and TM_{11} modes at 2.45 GHz are plotted in Fig. 5.20 and 5.21 respectively for body compared to those in free space. The antenna patterns remain quite comparable to those in free space despite a very small

antenna-body spacing (1 *mm*). The antenna radiation is significantly attenuated in the back direction (Fig. 5.20 (b), Fig. 5.21 (b)). This is due to the high attenuation caused by the human tissue at microwave frequencies e.g., the attenuation constant α = 3.9 dB/cm @ 2.45 GHz for tissue model with ε_r = 52, σ = 1.7 S/m [15]. Moreover, the total efficiency of the antenna falls to 54% for TM_{01} mode at 2.45 GHz compared to free space value of 92%. For TM_{11} mode, the total efficiency falls to 80% at 2.45 GHz compared to the free space value of 93%. These efficiencies are still quite acceptable due to the very small antenna-body separation and will improve further with spacing (e.g., as introduced by textiles) as also presented in Chapter 3.

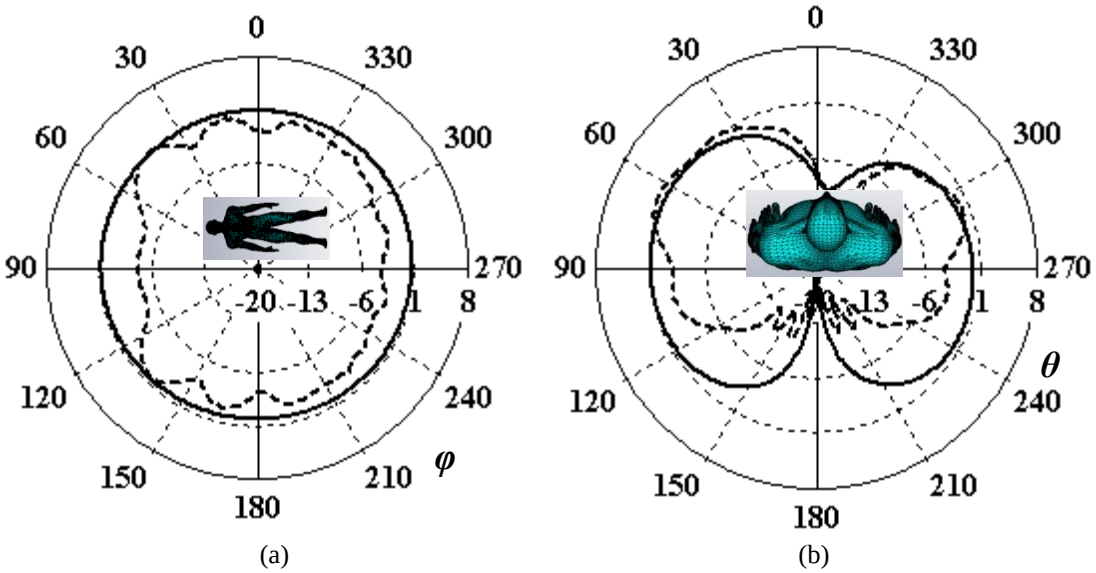

(a) (b)

Fig. 5.20. Radiation patterns of TM_{01} mode at 2.45 GHz for (a) *xy*-plane and (b) *xz*-plane on body model (– – –) compared to those in free space (——) (coordinate system shown in Fig. 5.18).

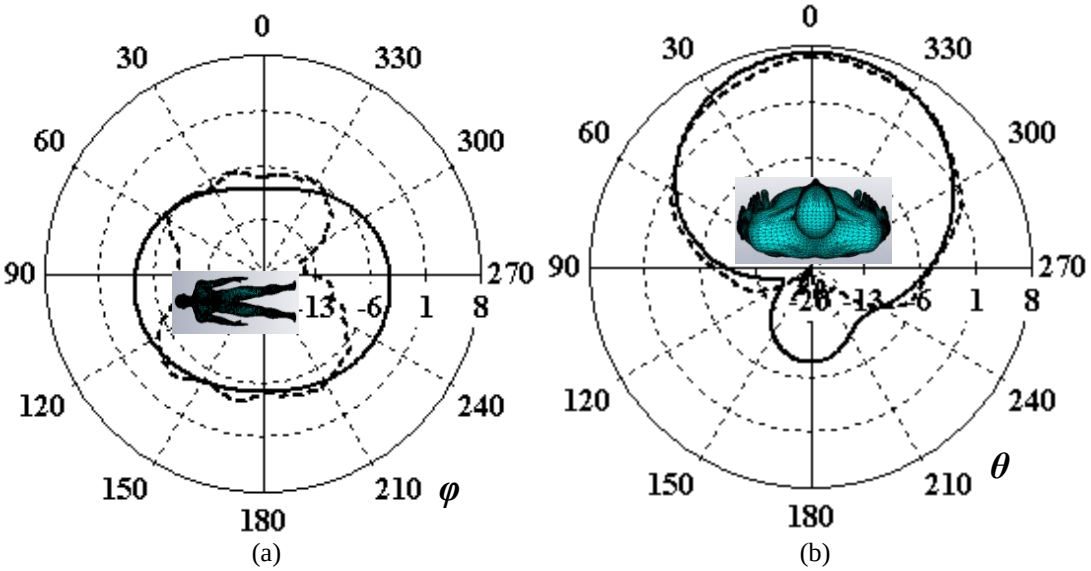

(a) (b)

Fig. 5.21. Radiation patterns of TM_{11} mode at 2.45 GHz for (a) *xy*-plane and (b) *xz*-plane on body model (– – –) compared to those in free space (——) (coordinate system shown in Fig. 5.18).

Specific Absorption Rate Computation

For compliance constraints along with safety and health considerations for RF exposure, the SAR of the antenna must lie within acceptable bounds. The approximate SAR was computed for the antenna using the 10*g* standard as specified by the Telecommunication Technology Council Agenda No. 89 and CENELEC 1995 [16]. The SAR was computed for the antenna on body model using CST MWS [16] for both resonant modes at 2.45 GHz for the same antenna-body spacing of 1 *mm* which gave satisfactory results for on-body antenna performance (Section 5.3.2). IEEE C 95.3 standard was used for averaging using 1 W peak stimulated power.

Simulated results are shown in Fig. 5.22 for both resonant modes. The maximum SAR was computed to be 1.22 W/kg for TM_{01} mode and 0.52 W/kg for TM_{11} mode which is less than the maximum 10*g* SAR permissible limit (2.0 W/kg) for European Union (EU) [17]. In all cases, 1W peak stimulated power was injected. The SAR for TM_{11} mode is lower since it radiates in the broadside direction away from the body compared to the TM_{01} mode which has omnidirectional radiation parallel to the body. SAR will improve further by increasing antenna-body spacing. e.g., 10g SAR for antenna-body spacing of 1 *cm* was computed to be 0.681 W/kg for TM_{01} mode and 0.206 for TM_{11} mode which are roughly half of the 10*g* SAR values for the case of 1 *mm* spacing. The overall variation of SAR with varying spacing *d* from the body is summarized in Table 5.1 for both modes. In all cases, SAR stays below the maximum limit of 2.0 W/kg for EU. Therefore, the antenna SAR lies within acceptable bounds and the antenna is compliant for health and safety considerations for body-centric applications.

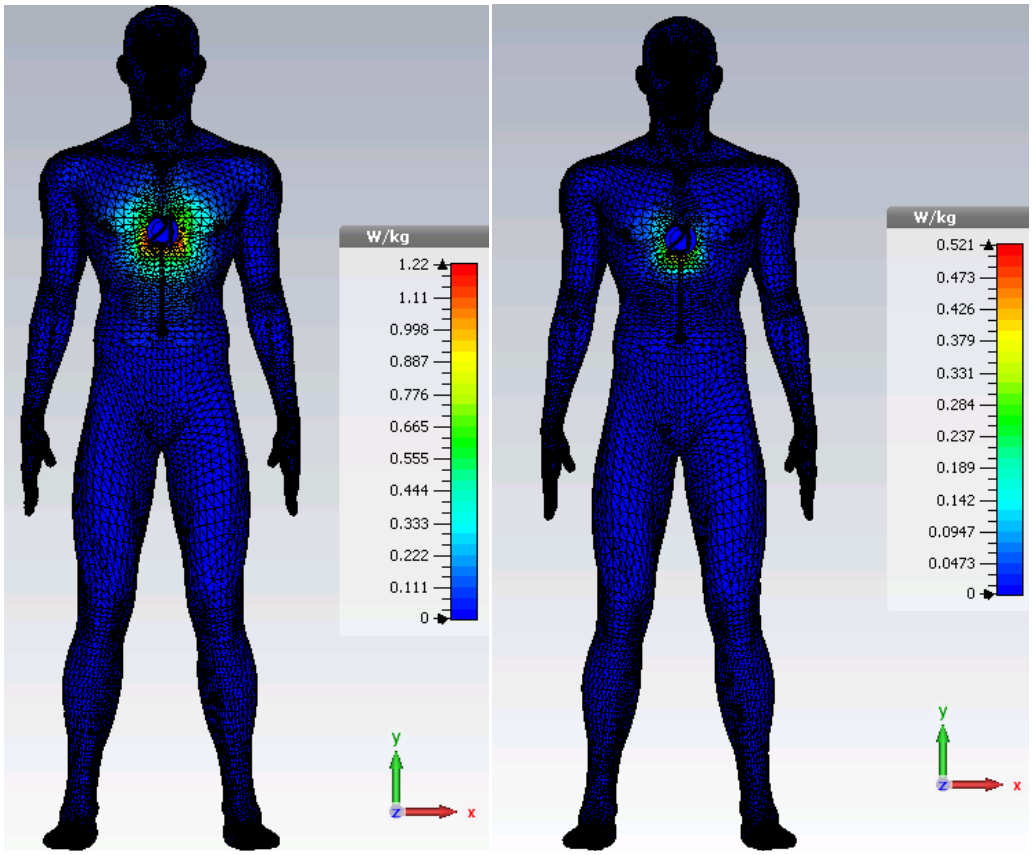

(a) (b)

Figure 5.22 10*g* SAR of the antenna at 2.45 GHz for (a) TM_{01} mode and (b) TM_{11} mode.

TABLE 5.1. SAR at 2.45 GHz with varying antenna-body spacing *d*

Spacing *d* (*mm*)	10*g* SAR(W/kg)	
	TM_{01} mode	TM_{11} mode
1	1.22	0.52
10	0.681	0.206

5.3.3. Experimental Characterization

A prototype of the antenna was also fabricated to verify the simulated results. Substrate with thickness t = 1.56 *mm* was used along with very thin Arlon bonding films CuClad 6250 (t = 38.1 microns) which were used to join the two substrates to consolidate single substrate (t = 3.12 mm) for each mode as in the simulation. The overall design is accomplished in a four layer implementation for the two modes as shown in Fig. 5.23 along with photos of the measured prototype shown in Fig. 5.24. For accurate implementation, precise marking of holes was done using computerized milling machine which was also used for the realization of short circuit for the implementation of shorted ring patch (TM_{01} mode or bottom patch).

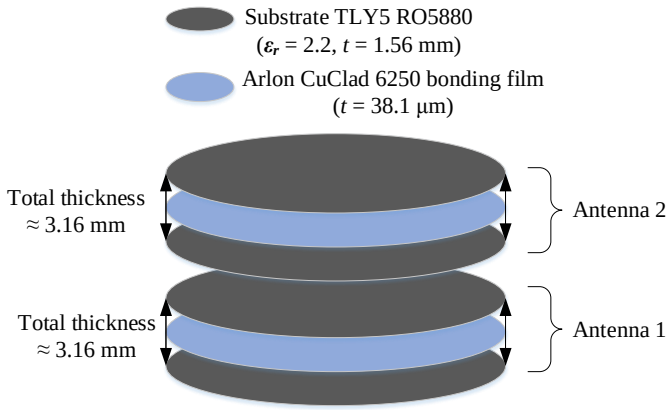

Figure 5.23. Layout of the different layers merged to realize the prototype for measurement.

(a) (b) (c)

Figure 5.24. Photograph of the manufactured prototype (a) Overall Top view (b) Top view of the sandwiched layer (c) Overall bottom view.

The measured S-parameters of the manufactured prototype are shown in Fig. 5.25 compared to the simulated S-parameters as presented in Section 5.3.1. The value of $|S_{ij}|$ for both modes is much less than -10 dB despite of the fact that the implementation of the antenna involved various approximations compared to the simulations. At 2.45 GHz, the measured $|S_{11}|$ and $|S_{22}|$ are both less than 10 dB. Moreover, the measured $|S_{21}|$ = -18 dB at 2.45 GHz which means that the coupling between the two modes can be neglected.

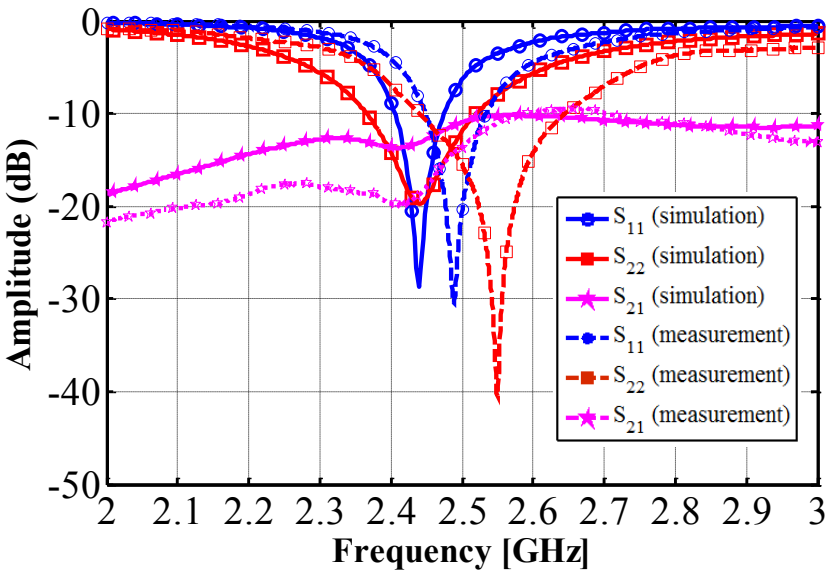

Figure 5.25. Measured S-parameters of the diversity antenna compared to the simulated ones for free space.

As evident from Fig. 5.25, the frequency is slightly detuned for both the resonant modes due to various factors. Some of such factors include the error of the substrate ε_r = 2.2 ± 0.02 and also the presence of CuClad bonding films which do not exist in the simulation. The dominant factor behind this detuning effect was observed to be the air spacing between the two antennas which is introduced by the soldering of short circuit for the shorted ring patch element (Fig. 5.24 (b)) and was not present in the simulation.

To study its impact, a spacing *d* of 0.5 *mm* (quite close to that in measured prototype) was introduced in simulation between the two antennas (Antenna 1 and 2 in Fig. 5.23). The resulting S-parameters are shown in Fig. 5.26. As evident, the frequency detuning impact is comparable to that observed in the measurements (Fig. 5.25). Such a spacing could not be avoided in real-life implementation since the soldering on the sandwiched layer has a non-zero thickness (Fig. 5.24 (b)). Consequently, resonant frequency of top antenna (S_{22}) is more detuned compared to that of first antenna (S_{11}), since the air layer will cause an overall increase in the dielectric thickness and will also change the effective dielectric constant of the overall substrate for TM_{11} mode. To reduce the spacing between the two layers of the measured prototype, its response was also measured using plastic clamps which offer significant pressing force on the antenna layers. Consequently, measurement results quite close to the simulated ones are achieved throughout the ISM 2.4 GHz bandwidth i.e., $|S_{ij}| < 10$ dB where $(i, j) \in \{1,2\}^2$ for $2.4 < f\,(\text{GHz}) < 2.5$.

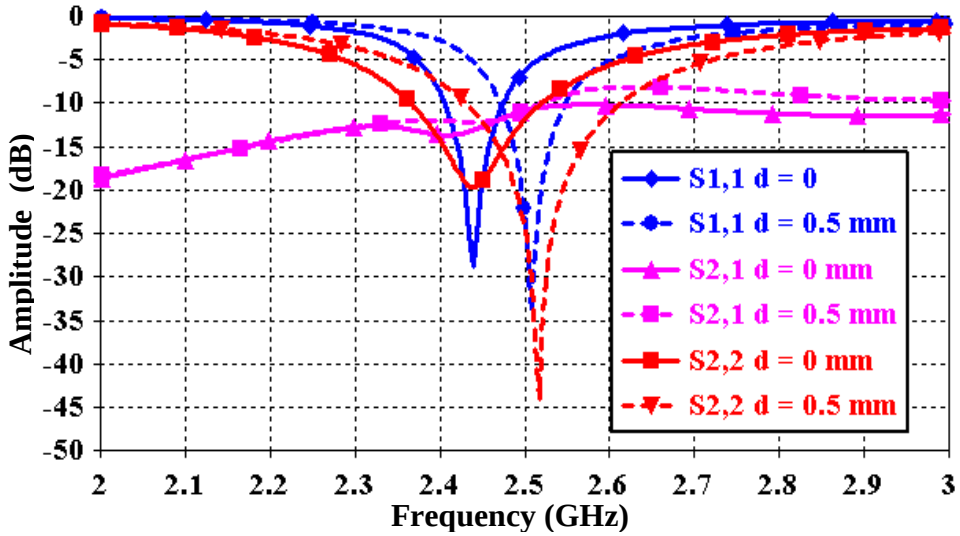

Figure 5.26. Simulated S-parameters of the diversity antenna when a spacing *d* is introduced between Antenna 1 and 2 in Fig. 5.23.

The S-parameters of the antenna were also measured in proximity to human body by placing the antenna on the chest of a human subject. The corresponding results are shown in Fig. 5.27 compared to those in free space. The antenna offers nearly stable performance in proximity to body with no noticeable frequency detuning for both TM_{01} and TM_{11} modes. Moreover, the antenna coupling is not influenced by the body proximity which is still -17 dB approximately at 2.45 GHz.

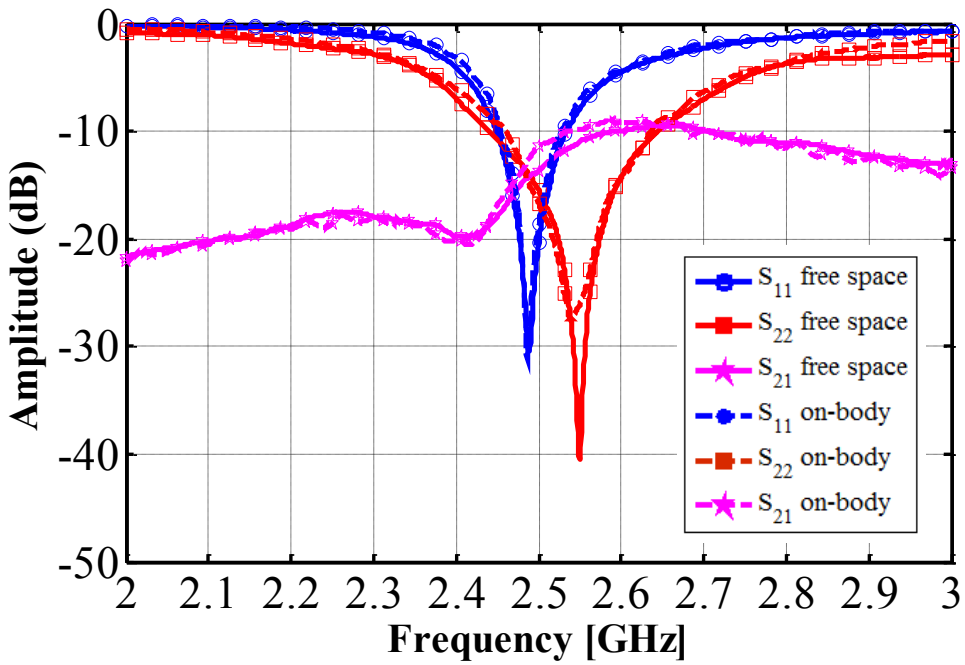

Figure 5.27. Measured S-parameters of the diversity antenna on human subject compared to those in free space.

5.3.4. Envelope correlation coefficient and diversity gain

The antenna provides both radiation pattern and polarization diversities in a single package and is also a suitable candidate for MIMO systems employing antenna diversity. Antenna diversity is a well-known technique to increase spectrum efficiency in communication systems. Diversity systems combine together the received signals at multiple antenna ports to improve the output SNR. Therefore, mutual coupling between the antennas comprising a diversity system is an important parameter to control performance. Poor coupling between the antennas degrades the overall system performance [18]. The objective of the diversity system is hence, to minimize the cross-coupling between the multiple antenna ports while also meeting the required input matching [18].

Based on the radiation and polarization diversities offered by the diversity antenna, it can be a suitable candidate for diversity applications. An important parameter for performance of antenna diversity system is the two-port envelope correlation coefficient (ECC) which can be calculated from S-parameters by using 5.3 [18]

$$ECC = \frac{\left|S_{11}^{*}S_{12} + S_{21}^{*}S_{22}\right|^{2}}{\left(1-\left(\left|S_{11}\right|^{2}+\left|S_{21}\right|^{2}\right)\right)\left(1-\left(\left|S_{22}\right|^{2}+\left|S_{12}\right|^{2}\right)\right)} \tag{5.3}$$

The envelope correlation coefficient was hence, calculated for both simulation and measurement using (5.3). The simulated and measured ECC were calculated by using the simulated and measured S-parameters of the antenna respectively (as shown in Fig. 5.25) in Eq. (5.3). The corresponding results are shown in Fig. 5.28. Results show that the ECC is very low i.e., both the simulated and measured values are below 0.01 throughout the ISM 2.45 GHz bandwidth. This means that the antenna is a very suitable for diversity applications where the combined signal from the two ports can be considered as uncorrelated.

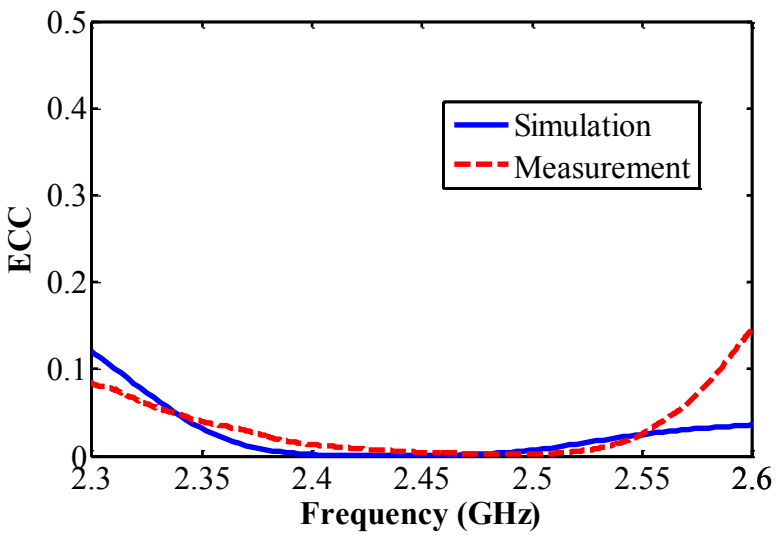

Figure 5.28. Envelope correlation coefficient for the diversity antenna.

The diversity gain is also an important metric to evaluate the performance of a diversity system. The diversity gain can be defined as the difference between the combined CDF and reference CDF at a certain level which is normally chosen to be 1% [19]. Diversity gain can be calculated from the correlation coefficient using (5.4) [20] i.e.,

$$DG = 10\sqrt{1-|\rho|^2} \tag{5.4}$$

where ρ is the complex cross-correlation coefficient which can be expressed in terms of ECC for narrowband signals as given by (5.5) [19], [21].

$$|\rho|^2 \approx \mathrm{ECC} \tag{5.5}$$

The diversity gain was hence, calculated for both simulation and measurement using (5.4) and (5.5). Corresponding results are shown in Fig. 5.29. Results show that both the simulated and measured values are greater than 9.9 dB throughout the ISM 2.45 GHz bandwidth. This shows that the diversity gain is very close to 10 dB which is its theoretical maximum value for two uncorrelated antennas for an accepted bit-rate error of 1%. This also proves that the antenna is a very suitable candidate for diversity systems while providing both radiation pattern and polarization diversities in a single package.

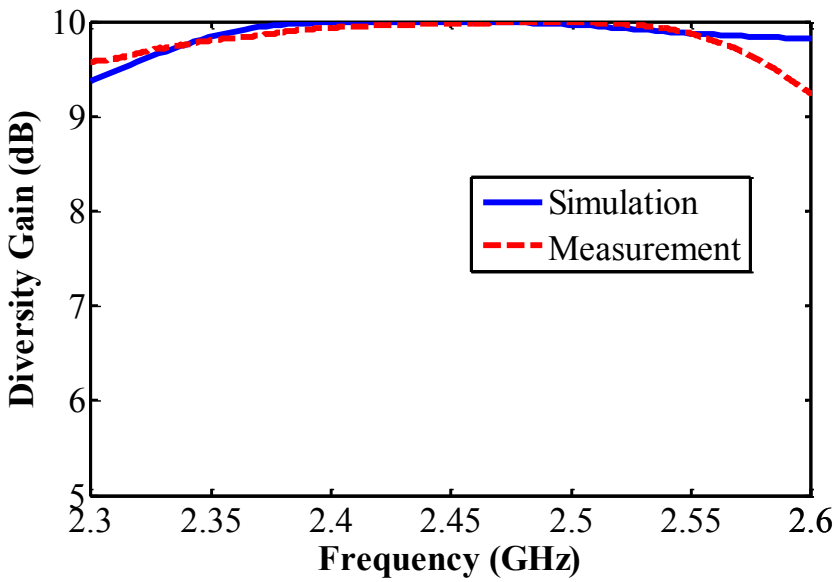

Figure 5.29. Diversity gain of the antenna.

5.4. Pattern and polarization diversity for on-body applications

Once the radiation pattern and polarization diversities are achieved using the proposed antenna, we also studied their interest for on-body applications at 2.45 GHz. For this purpose, the diversity antenna presented in Section 5.3 has been used as transmitter (Tx) and receiver (Rx) on a sample body posture simulating a link involving diffused free space and on-body propagation, as illustrated in Fig. 5.30. For simulation studies, a realistic full body model was generated using the commercial software POSER® [12] which was imported in CST MWS for full wave simulations. Muscle tissue properties at 2.45 GHz (i.e., ε_r = 52, σ = 1.7 Sm^{-1}) were used to model homogenous body [14].

The TM_{01} mode will offer a monopolar radiation parallel to the body along with a polarization orthogonal to the body surface (referred to as H in Fig. 5.30). On the other hand, the TM_{11} mode offers a broadside radiation orthogonal to the body surface along with a polarization parallel to the body surface (referred to as V in Fig. 5.30). The link budget was simulated by considering the overall four different pattern and polarization diversity scenarios, namely H-H, H-V, V-H and V-V switching the antenna modes alternately for both Tx and Rx. The corresponding full-wave simulation results are represented in Fig. 5.31. All antennas are well matched on-body at 2.45 GHz, and the mutual coupling coefficients (S_{12}, S_{34}) remain lower than -10 dB; this shows that only concerned resonant modes are radiating with negligible influence on the other mode.

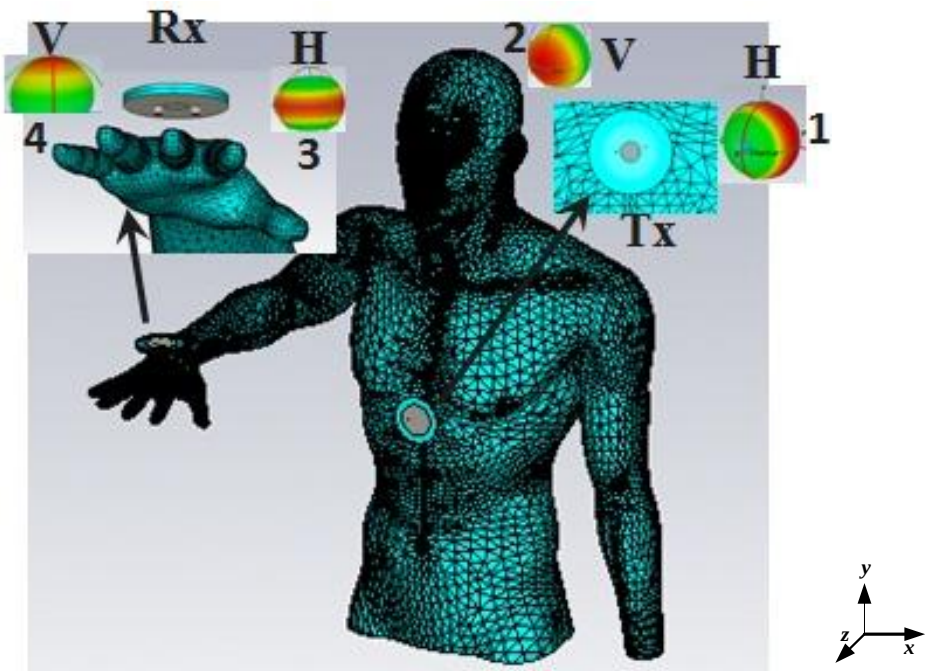

Figure 5.30. Location of antennas on the body to study diversity scenarios on a full-body ghost phantom (3D patterns are only for illustration).

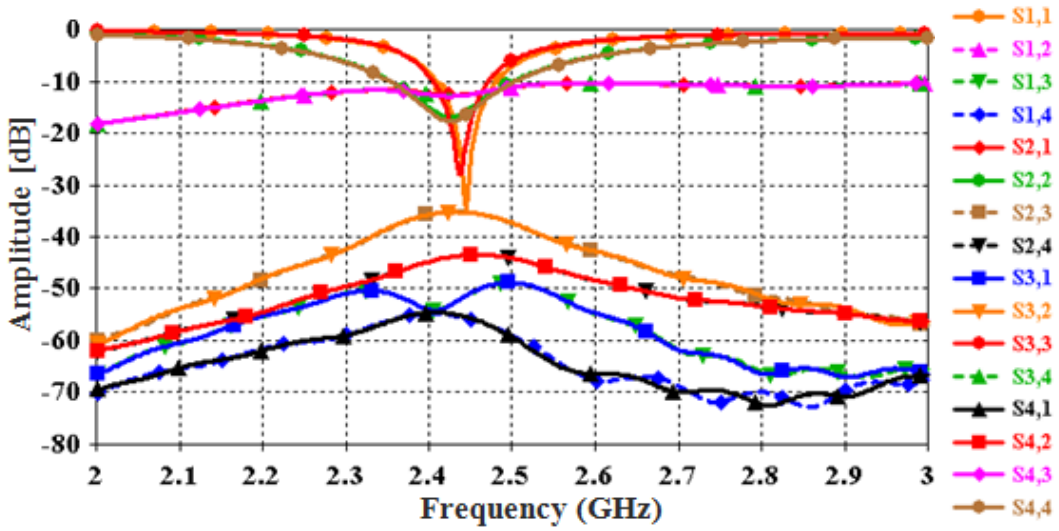

Figure 5.31. Full-wave S-parameters for the diversity scenarios.

The link budget corresponding to the four different diversity scenarios at 2.45 GHz is plotted in Fig. 5.32. The standard scenario known for optimum BAN performance was considered as reference for comparison i.e., H-H. As evident from Fig. 5.32, there is up to 15 dB improvement in link budget by just switching the pattern/polarization diversity from H to V on the Tx side (on chest), when the Rx (on arm) is radiating under reference scenario H.

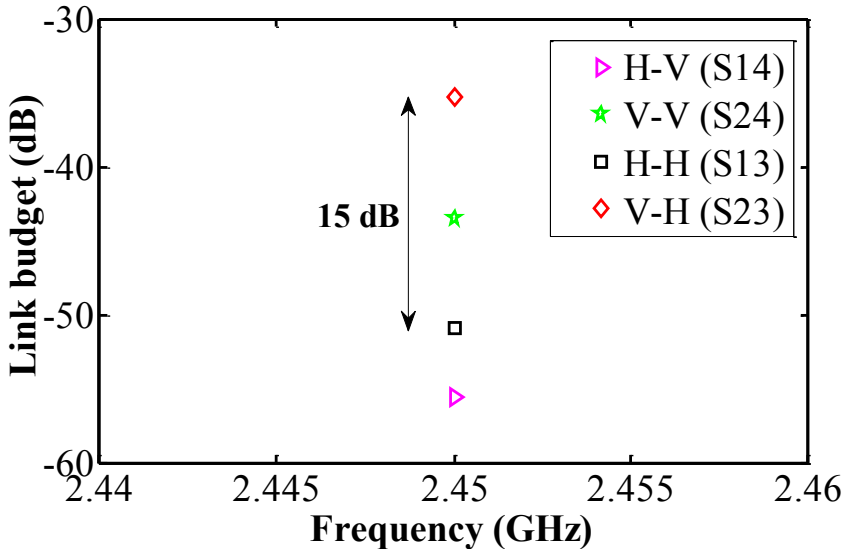

Figure 5.32. Link budget for various diversity scenarios.

To validate the simulation, the different diversity combinations have been measured using a diversity antenna prototype (as presented in Section 5.3) as Tx and the monopole chip antenna presented in Chapter 2 (from Johanson® Tech. [22]) matched at 2.45 GHz as Rx. The chip antenna and its radiation patterns are shown in Fig. 5.33 which were measured in SATIMO Stargate® system [23]. The chip antenna offers a monopole-like omni-azimuthal radiation pattern. Moreover, the antenna offers a horizontal polarization

of ***E***-field in *xy*-plane (known from manufacturer's datasheet [22]). It was verified from both simulation and measurement that when placed parallel to body (scenario V), most of the antenna radiation is reflected in the broadside direction along with absorption caused by the lossy tissue in backward direction. On the other hand, the azimuthal radiation symmetry is maintained by placing the antenna orthogonal to the body (scenario H). The antenna can hence, generate the two radiation and polarization diversity scenarios on the Rx side and can be used for comparison studies with pattern and polarization diversity antenna (Tx).

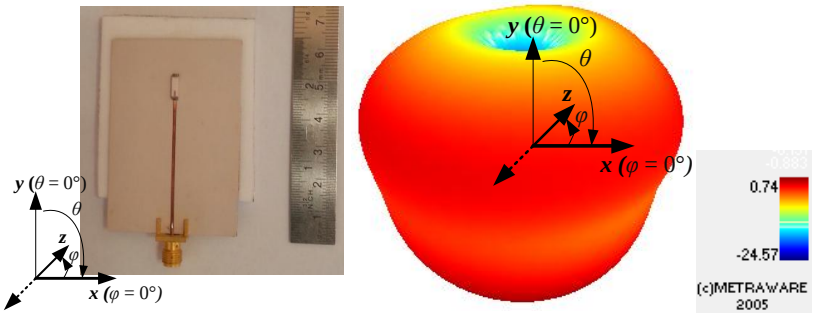

(a) (b)

Figure 5.33. (a) Monopole chip antenna used as Rx (b) Measured 3D radiation pattern at 2.45 GHz.

The two pattern and polarization diversity scenarios were generated by switching the chip antenna orientation on Rx side as shown in Fig. 5.34. The same body posture was then measured (as the one of simulation) using the diversity antenna as Tx and the monopole chip antenna as Rx on a 154 pounds/171 *cm* human subject using a VNA as illustrated in Fig. 5.34. Moreover, full 2-port calibration of VNA was performed prior to measurements to eliminate cable response from measured channel coefficients. The measured on-body return loss for all antennas were observed to be either close to or less than -10 dB at 2.45 GHz.

The results corresponding to the four different measured diversity scenarios are shown in Fig. 5.35. There is a significant improvement in link budget (up to 9 dB) by switching pattern and polarization diversity from H to V on the Tx side when the Rx is operating under reference scenario H known for optimum on-body performance (i.e., scenario V-H and H-H in Fig. 5.35 respectively).

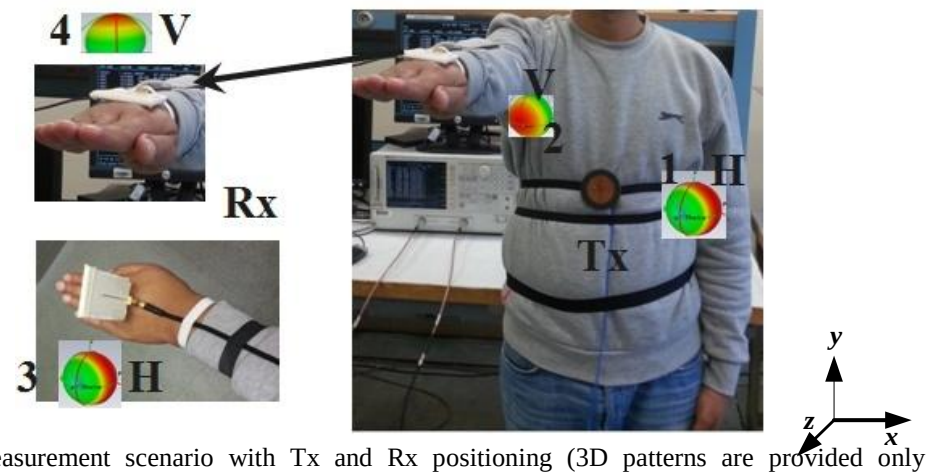

Figure 5.34. Measurement scenario with Tx and Rx positioning (3D patterns are provided only for illustration purpose).

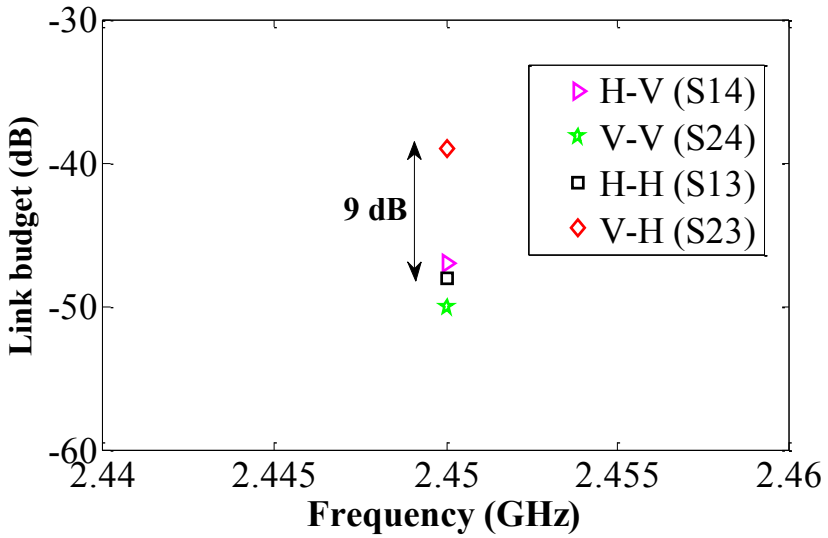

Figure 5.35. Measured link budget for various diversity scenarios.

Conclusion

Significant improvement in link budget of up to 15 dB is reported for full-wave simulations and up to 9 dB for realistic measurements by exploiting the radiation pattern and polarization diversities simultaneously. The difference in simulated and measured link budgets can be explained by the use of different Rx antenna in measurement which offers different gain compared to the diversity antenna used as Rx in simulations. The optimum link is obtained when the maximum Tx radiation is oriented towards the Rx (V-H) and the polarization of both antennas is matched also (i.e., in the *xy*-plane) where it is known that the proximity of body does not change the orientation of polarization for static scenario.

5.5. Conclusions

A dual-mode dual-pattern antenna is successfully designed at 2.4 GHz with appropriate radiation pattern requirements for both on- and off-BAN applications. However, the cross-coupling performance of the antenna was observed to be quite poor due to the high coupling between the two short circuits which lie along the same plane.

Therefore, another dual-mode, dual-pattern polarization diversity antenna has been successfully designed at 2.45 GHz with improved cross-modal coupling. The performance of the antenna has been evaluated in proximity to body and has been found to be quite stable compared to the free space performance due to the masking effect of its full ground plane. Also for diversity applications, the ECC and diversity gain of the antenna have been evaluated. The ECC has been observed to be close to zero which is the ideal correlation required for fading signals incoming to the diversity system to be independent of each other [24]. The corresponding achieved diversity gain is close to 10 dB at 2.45 GHz which is its theoretical maximum value for two uncorrelated antennas for an accepted bit-rate error of 1% [19]. This suggests the suitability of the proposed antenna for diversity systems.

Finally, the performance of pattern and polarization diversity has been demonstrated for body-centric applications at 2.45 GHz exploiting the radiation pattern and polarization diversities simultaneously. Significant improvement in link budget has been achieved for both full-wave simulations and measurements. However, this study should involve more rigorous scenarios with various body postures and antenna locations in future to investigate performance from a global perspective.

References

[1] P.S. Hall, Y. Hao, Y. I. Nechayev, A. Alomainy, C. C. Constantinou, C. Parini, M. R. Kamarudin, T. Z. Salim, D. T. M. Hee, R. Dubrovka, A. S. Owadally, S. Wei, A. Serra, P. Nepa, M. Gallo, M. Bozzetti, "Antennas and propagation for on-body communication," *IEEE Antennas and Propagation Magazine,* , vol. 49, no. 3, pp. 41 - 58, June 2007.

[2] G. A. Conway, W. G. Scanlon, "Antennas for over-body-surface communication at 2.45 GHz," *IEEE Transactions on Antennas and Propagation,* vol. 57, no. 4, pp. 844 - 855, April 2009.

[3] L. Vallozzi, W. Vandendriessche, L. Vallozzi, W. Vandendriessche, H. Rogier, C. Hertleer, and M. L. Scarpello, "Wearable textile GPS antenna for integration in protective garments," in *Europ. Conf. Antennas Propag., EuCAP'2010*, Barcelona, Spain, Apr. 12.

[4] M. M. Khan, A. Alomainy, and Y. Hao, "Dual band and diverse radiation pattern antenna for power efficient and reliable on-body and off-body communications for healthcare applications," in *IEEE Ant. Propag. Society Int. Symp.,* Spokane (WA), Jul. 2011.

[5] K. L. Wong and C. I. Lin, "Characteristics of a 2.4-GHz compact shorted patch antenna in close proximity to a lossy medium," *Microw. Opt. Technol. Lett.,* vol. 45, no. 6, p. 480–483, Jun. 2005.

[6] S. Dumanli, "On-body antenna with reconfigurable radiation pattern," in *RF and Wireless Technologies for Biomedical and Healthcare Applications (IMWS-Bio)*, London (UK), Dec. 2014 .

[7] A.A. Serra, I. Khan, P. Nepa, G. Manara, P.S. Hall, "Dual-polarization and dual-pattern planar antenna for diversity in body-centric communications," in *Antennas and Propagation Society International Symposium*, 2008.

[8] T. Alves, B. Poussot, and J. M. Laheurte, "Analytical propagation modeling of BAN channels based on the creeping-wave theory," *IEEE Transactions on Antennas and Propagation,* vol. 59, no. 4, pp. 1269 - 1274, 2011.

[9] V. G. Posadas, D. S. Vargas, E. R. Iglesias, J.L. Vazquez-Roy, C. M. Pascual, "Approximate analysis of short circuited ring patch antenna working at TM01 mode," *IEEE Transactions on Antennas and Propagation,* vol. 54, no. 6, pp. 1875-1879, Jun. 2006.

[10] C. A. Balanis , Antenna Theory: Analysis and Design, 3rd Edition, John Wiley & Sons, Inc.

[11] D. Ma, and W.-X. Zhang, "Coupling-fed circular-patch antenna for onbody communication system," *Microwave & Optical Tech. Lett.,* vol. 51, no. 11, pp. 2623-2627, November 2009.

[12] "http://my.smithmicro.com/poser-pro-2014.html," [Online].

[13] "http://niremf.ifac.cnr.it/tissprop/," [Online].

[14] L. A-Asl, P. S.Hall, Y. Nechayev, and I. Khan, "Depolarization in On-Body Communication Channels at 2.45 GHz," *IEEE Transcatiosn on Antennas and Propagation,* vol. 61, no. 2, pp. 882-889, 2013.

[15] I. Yamaura, "Measurements of 1.8 - 2.7-Ghz Microwave Attenuation in the Human Torso," *IEEE Transactions on Microwave Theory and Techniques,* vol. 25, no. 8, pp. 707-710, Aug. 1977.

[16] "https://www.cst.com/," [Online].

[17] "Mobiltelefoner och Strålning," Sweden's Radiation Protection Authority, Tech. Rept., 2003.

[18] S. Blanch, J. Romeu, and I. Corbella, "Exact representation of antenna system diversity performance from input parameter description," *Electron. Lett.*, vol. 39, no. 9, p. 705–707, 2003.

[19] Bon Guo, "Antenna diversity in mobile phone," MS Thesis, Chalmers university of technology (department of signals and systems), Sweden, 2008.

[20] Kent Rosengren, P-S. Kildal, "Radiation efficiency, correlation, diversity gain and capacity of a six monopole antenna array for a MIMO system: Theory, Simulation and Measurement in Reverberation Chamber," *Proceedings IEE, Microwaves, Optics and Antennas,* vol. 152, no. 1, pp. 7-16, Feb. 2005..

[21] G. Vaughan and J. Bach Andersen, "Antenna diversity in mobile communications," *IEEE Trans. Veh. Technol.,* vol. 36, 1987.

[22] "http://johansontechnology.com/," [Online].

[23] "http://www.satimo.com/," [Online].

[24] V. Plicanic, "Antenna Diversity Studies and Evaluation," Master of Science Thesis (in cooperation with Ericsson Mobile Communications), , Lund university, Sweden, May 2004.

Thesis Conclusions

Firstly of all, a comprehensive state-of-the-art was presented regarding the on- and off-body channel modeling from contemporary literature along with electromagnetic characterization and modeling of human body. The various existing topologies of antennas were also presented for body-centric applications.

Channel characterization using miniaturized chip antennas

The Zyggie prototype platform as developed by the BoWI partners was presented demonstrating the pattern diversity configuration offered by its miniaturized chip antennas. Off-body channel measurements were reported for both LoS and QNLoS scenarios in multipath environments exploiting the pattern diversity offered by on-board chip antennas. Typical values of delay spread have been reported to avoid ISI without the use of an equalizer. The ergodic channel capacity was also computed building 2×2 MIMO configurations and significant improvement has been observed compared to SISO systems. A robust algorithm based on MLE and K-S test as goodness of fit has also been proposed for statistical fitting of real-time channel data. Channel fading for both off- and on-body scenarios has been studied using the proposed fitting algorithm on real-time channel measurements. For off-BAN scenarios, a Normal distribution is recommended for small-scale, first order fading for LoS scenarios and a Weibull distribution for that of QNLoS scenarios. To improve the statistical accuracy, channel fading studies were also presented for on-body channels for quasi-static and dynamic scenarios. Cross-correlation between sub-channels at multiple frequencies was investigated to triple the empirical data points (3×1000) subject to the proper pre-normalization. A Weibull distribution is recommended as the best-fit fading model for chest-wrist and chest-thigh channels. For chest-hip channel, Normal distribution is recommended for quasi-static scenarios and a Nakagami-*m* distribution for dynamic scenarios.

Antenna design and interaction with body at ISM band

The impact of human body on the antenna performance has been studied thoroughly. The body has been found to significantly distort the antenna performance parameters due to high tissue properties. The frequency has been found to detune and the radiation efficiency drops compared to the free space counterparts. It has been shown that the on-body performance is very sensitive to the antenna-body spacing and performance can be improved by increasing the latter. A ground plane masks the near-field interactions resulting in less spacing for stable on-body performance compared to antennas having partial ground planes. An Inverted-F antenna incorporating a ground plane has been designed covering full ISM 2.4 GHz bandwidth with appropriate radiation and polarization requirements for on-body applications along with a much smarter profile than its competitor, monopole antenna. Its 10*g* SAR was also computed and found to be much lower than the international compliance standards. Finally, a compact dual-mode patch antenna was designed with appropriate radiation characteristics for both on- and off-body applications at ISM 2.45 GHz and UWB 3.1 GHz respectively. The antenna has been found to offer stable performance in proximity to human body as that in free space.

Both the characteristic modes of the antenna were also excited at single frequency (2.45 GHz) to illustrate the concept of exciting multiple modes at same frequency for a co-integrated antenna design offering pattern and polarization diversity.

Numerical channel simulator

The design of an electrically small chip antenna has been presented covering full ISM 2.4 GHz bandwidth and offering stable on-body performance. A robust numerical channel simulator was developed using the miniature chip antennas and realistic body morphologies with the power to simulate any arbitrary WBASN scenario with customized parameters (e.g., body posture, antenna type/location etc.). The scope of the channel simulator was also demonstrated for some sample body postures along with full-wave S-parameters characterization in each case. The application of the algorithm was also presented for posture classification. It was shown that critical nodes can be found as the body postures are varied by dropping redundant nodes which offer quite stable links even by movement. Such critical nodes were used for estimating coefficients to calculate distance between the nodes for posture identification.

Pattern and polarization diversity

A dual-mode, dual-pattern antenna was designed at ISM 2.4 GHz with appropriate radiation pattern requirements for both on- and off-BAN applications but the cross-coupling was observed to be poor. Hence, another improved dual-mode, dual-pattern polarization diversity antenna was designed with improved cross-modal coupling. The performance of the antenna was also evaluated in proximity to body and was found to be stable due to the masking effect of its full ground plane. For diversity applications, the ECC and diversity gain of the antenna have also been evaluated. The ECC has been reported to be close to zero (i.e., ideal correlation for independent fading signals) with a corresponding diversity gain close to 10 dB (i.e., theoretical maximum for an accepted bit-rate error of 1%). The antenna is hence, also a useful candidate for diversity and MIMO systems while offering both pattern and polarization diversities in a single package. The performance of pattern and polarization diversities simultaneously has also been demonstrated for body-centric applications at 2.45 GHz. Remarkable improvement in link budget has been reported using both full-wave simulations and real-time measurements.

Future perspectives

The work presented in this thesis also opens new vistas in various directions for future body-centric communications. The fitting algorithm presented in Chapter II is generic and can be applied to find the optimum channel statistical studies for body-centric channel corresponding to other microwave spectrum as well e.g., UWB, *mm*-wave band etc. The algorithm can be modified to include more distribution functions (apart from the seven distribution functions done in this work) based on the known benchmarks for the particular body-centric channel data under study e.g., UWB, *mm*-wave band. The algorithms also offers the possibility to study all types of empirical radio channel data i.e., both simulations and measurements.

The suitability of tissue phantoms have also been demonstrated for statistical study of body-centric channels. Phantoms offer the possibility to accumulate arbitrarily large number of points and should be used for improved statistical accuracy using measurements in controlled conditions.

The numerical Channel simulator (Chapter 4) can be used in conjunction with the channel fitting algorithm (Chapter 2) for channel study of pseudo-dynamic scenarios for BAN. This may involve exporting full-wave S-parameters data as generated by the numerical channel simulator from CST MWS^{TM} to MATLAB^{TM} and further post-processing it using the fitting algorithm in MATLAB^{TM}. The pseudo dynamic scenarios can also be investigated mathematically to incorporate other factors such as Doppler's effect and shadowing caused by the dynamic nature of BAN environments. This study can also be useful to find overall channel models for BAN which is still a challenge.

The posture classification scheme can be investigated further to explore universal coefficients which can be applied on human subjects with varying body-morphology or antenna configurations etc. The dual-mode, pattern and polarization diversity antenna presented in Chapter 5 can also be applied for this study. The antenna can be used on fixed body locations and all the diversity scenarios (e.g., H-H, H-V, V-H, V-V) can be investigated for various postures. The maximum link budget under such scenarios is expected to vary based on the specific posture and antenna locations. Diversity combining scheme such as Selection Combining can be used to scan the diversity branches and choose the maximum link. Subject to the maximum link for the specific antenna locations, specific body postures can be identified resulting in further simplification. This approach will not suffer from issues as faced by distance estimation scheme for posture classification. e.g., highly sensitive coefficients based on antennas and subject.

The multimode antenna concept was demonstrated in Chapter 5 at single frequency for both on- and off-body applications. This concept can be extended further to design multimode antennas operating in different frequency bands while simultaneously supporting both on- and off-body modes at each of the operating bands e.g., A four layer implementation can be used where two layers correspond to the on- and off-body excitation modes for one frequency band (e.g., ISM) and the other two layers are excited for both radiation modes at another frequency band (e.g., WLAN). This can be very

useful to add extra functionalities in BAN applications which offer stringent conditions of space and form factor.

Finally, the performance of pattern and polarization diversity for body-centric applications can also be studied using the diversity antenna for various scenarios and investigating the gain offered by different forms of diversity combining schemes e.g., Selection Combining, Switched Combining, Equal Gain Combining, and Maximal Ratio Combining. This can lead to interesting findings for application of both pattern and polarization diversities for MIMO applications.

Appendix A
Validation of fitting algorithm

Lognormal distribution

For validation of fitting algorithm for Lognormal distribution in Section 2.5.3, lognormal random generator in MATLAB was used which actually generates random data following the Lognormal distribution as given by Eq. (2.7). Resulting fitting statistics for 1000 runs of the algorithm are shown in Fig. a.1 which shows the correct detection of Lognormal distribution in each case with maximum probability of fitness *p* where all the other competent distributions fail the qualifying criterion (based on confidence level (1 - α) of 95%).

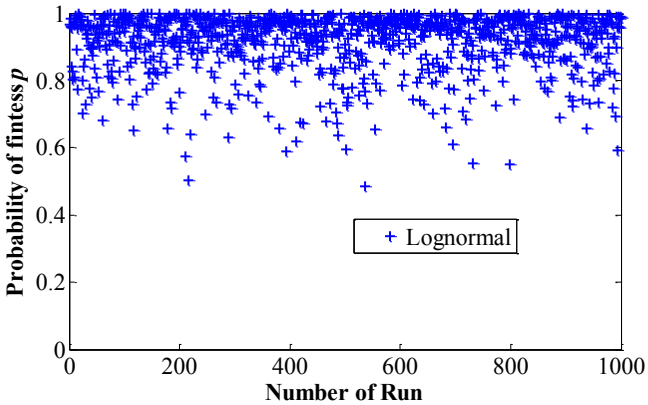

Figure a.1. Validation of fitting-algorithm for Lognormal random data shuffling random generator each time.

Weibull distribution

For validation of algorithm for Weibull distribution, weibull random generator in MATLAB was used which actually generates random data following the weibull distribution as given by Eq. (2.9). Resulting statistics for 1000 runs of the algorithm are shown in Fig. a.2 which shows the correct detection of Weibull distribution in each case with maximum probability of fitness *p* compared to other qualifying competent distributions.

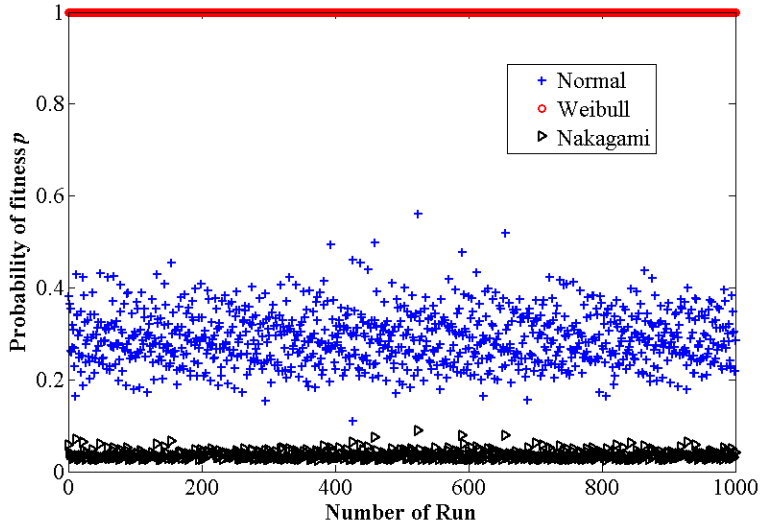

Figure a.2. Validation of fitting-algorithm for Weibull random data shuffling random generator each time.

Gamma distribution

For validation of algorithm for Gamma distribution, gamma random generator in MATLAB was used which actually generates random data following the Gamma distribution as given by (2.10). Resulting statistics for 1000 runs of the algorithm are shown in Fig. a.3 which shows the correct detection of Gamma distribution in each case with maximum probability of fitness p compared to other qualifying competent distributions.

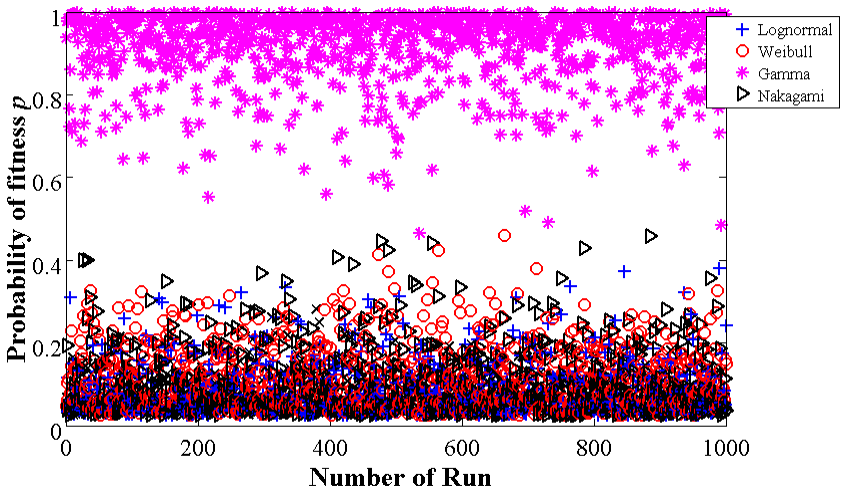

Figure a.3. Validation of fitting-algorithm for Gamma random data shuffling random generator each time.

Nakagami-*m* distribution

For validation of algorithm for Nakagami-*m* distribution, gamma random generator was used in MATLAB to generate Nakagami-*m* distribution of Eq. (2.12) using Eq. (a.1).

$$F(x \mid m, \omega) = \sqrt{\mathrm{X}\left(m, \frac{\omega}{m}\right)} \tag{a.1}$$

where X is the Gamma random variable. Resulting statistics for 1000 runs of the algorithm are shown in Fig. a.4 which shows the correct detection of Nakagami-*m* distribution in each case with maximum probability of fitness *p* compared to other qualifying competent distributions.

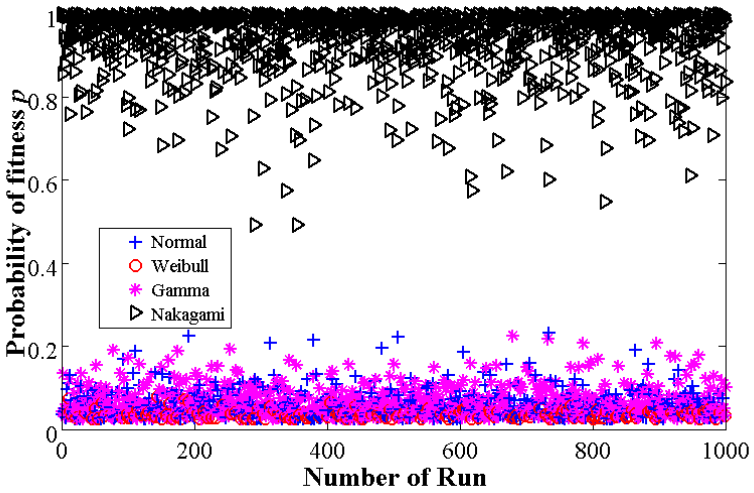

Figure a.4. Validation of fitting-algorithm for Nakagami-*m* random data shuffling random generator each time.

Appendix B

Mesh convergence and accuracy in Section 4.3.3

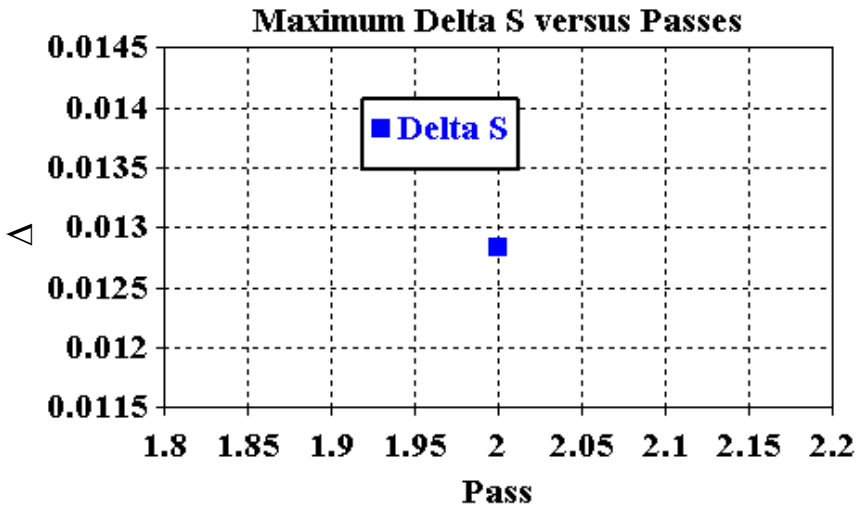

Figure b.1. Maximum error for the energy based mesh refinement in Fig. 4.20.

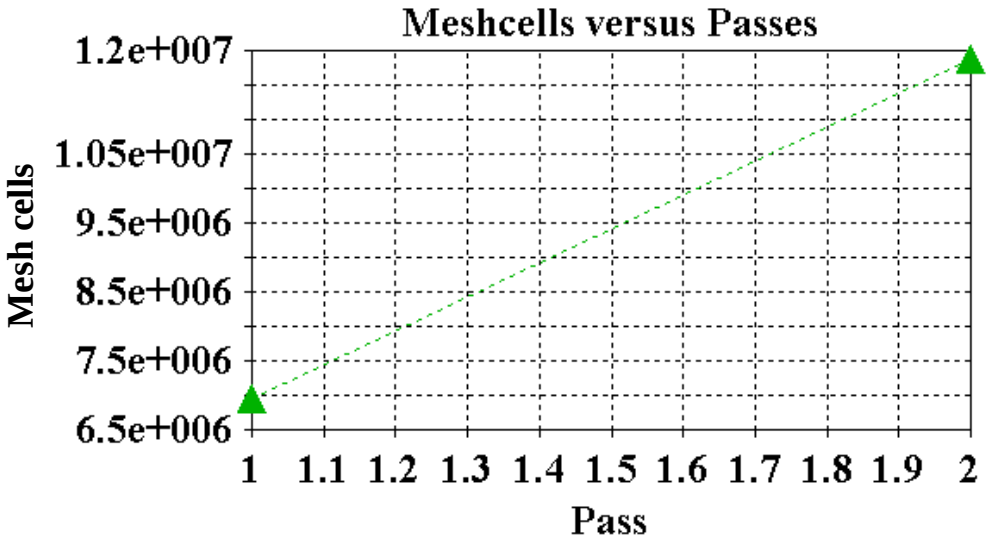

Figure b.2. Mesh cells with energy based mesh refinement in Fig. 4.20.

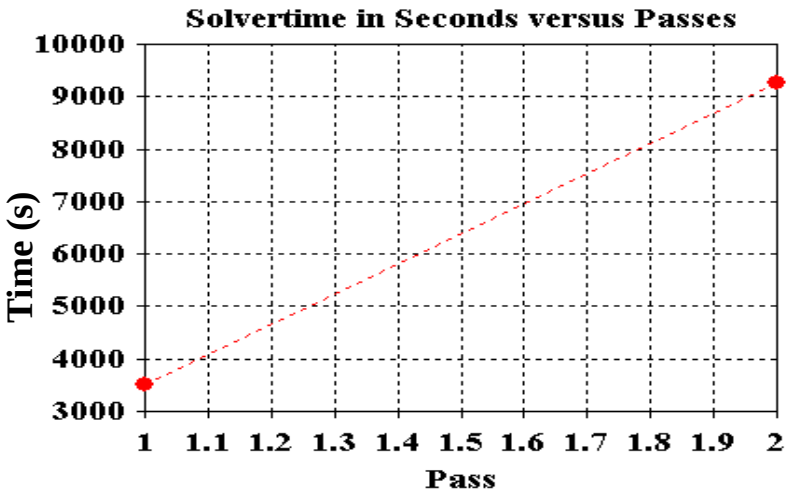

Figure b.3. Solver time versus passes with energy based mesh refinement in Fig. 4.20.

3D Far-fields for basic posture 1 at 2.45 GHz in Section 4.3.5

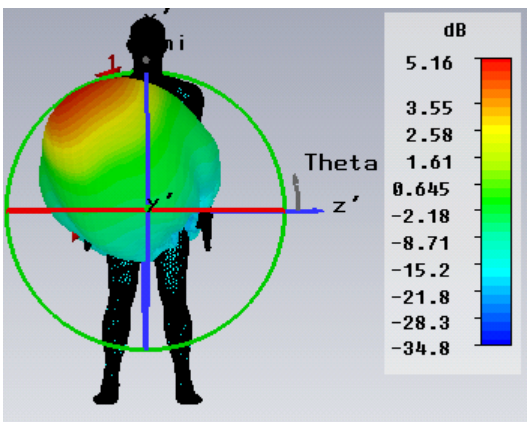

Figure b.4. 3D radiation patterns of Antenna 1 in Fig. 4.24.

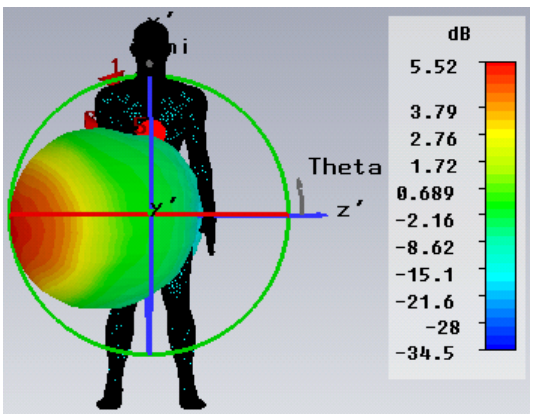

Figure b.5. 3D radiation patterns of Antenna 2 in Fig. 4.24.

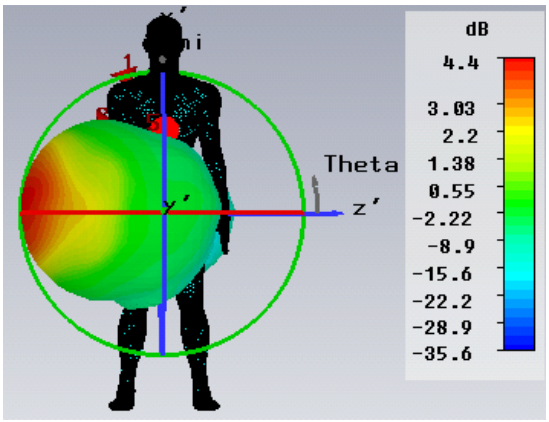

Figure b.6. 3D radiation patterns of Antenna 3 in Fig. 4.24.

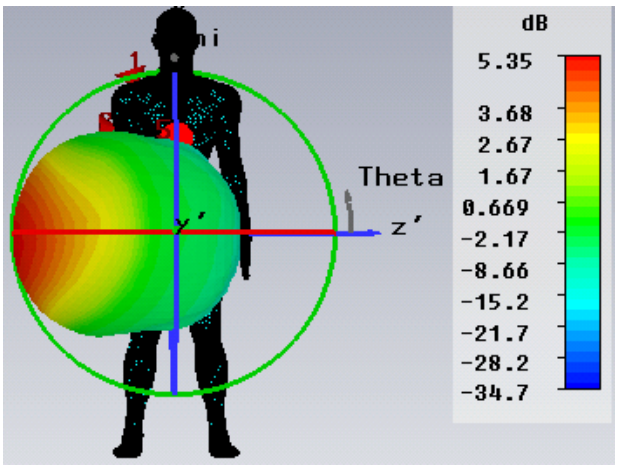

Figure b.7. 3D radiation patterns of Antenna 4 in Fig. 4.24.

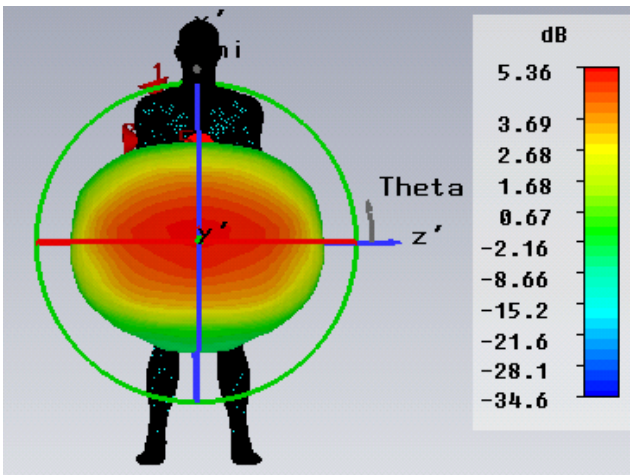

Figure b.8. 3D radiation patterns of Antenna 5 in Fig. 4.24.

Decibel conversions in Section 4.3.6

Friis formula for free space is given by (4.1) as

$$\frac{\mathrm{P_r}}{P_e} = G_t.G_r.\left(\frac{\lambda}{4\pi D}\right)^N \tag{b.1}$$

Likewise, Friis formula for on-body applications was given by (4.3) as

$$Pr_{(H_k,P_{(g,d)},Ce_i,Cr_j)} = \frac{1}{D^2_{(P_{(g,d)},Ce_i,Cr_j)}} \times \beta_{(P_{(g,d)},C_{ei},C_{rj})} \times \gamma_{(H_k,P_{(g,d)},Ce_i,Cr_j)} \times \left(Pe\left(\frac{\lambda}{4\pi}\right)^2\right) \tag{b.2}$$

where β is the coefficient which accounts for the gain of the antennas, γ is the coefficient to consider the on-body propagation component, P is the body posture which can further be split into the posture on the right arm (d) and left arm (g), H_k is the human subject, Ce_i and Cr_j correspond to the Tx and Rx antennas respectively and D is the distance between the Tx and Rx antennas (i.e., Ce_i and Cr_j respectively) for a specific posture P.

Therefore, in terms of coefficients (b.2) can be rewritten as (b.3)

$$\beta_{(P_{(g,d)},C_{ei},C_{rj})} \times \gamma_{(H_k,P_{(g,d)},Ce_i,Cr_j)} = D^2_{(P_{(g,d)},Ce_i,Cr_j)} \times \frac{Pr_{(H_k,P_{(g,d)},Ce_i,Cr_j)}}{Pe\times\left(\frac{\lambda}{4\pi}\right)^2} \tag{b.3}$$

$$\frac{Pr_{(H_k,P_{(g,d)},Ce_i,Cr_j)}}{Pe} = \beta_{(P_{(g,d)},C_{ei},C_{rj})} \times \gamma_{(H_k,P_{(g,d)},Ce_i,Cr_j)} \times \left(\frac{\lambda}{4\pi D}\right)^2 \tag{b.4}$$

which can be written in dB as (b.5) and hence (b.5)

$$\frac{Pr_{(H_k,P_{(g,d)},Ce_i,Cr_j)}}{Pe} = S_{ij} = 10log10[\beta_{(P_{(g,d)},C_e,C_r)} \times \gamma_{(H_k,P_{(g,d)},Ce_i,Cr_j)}] + 10log10\left(\frac{\lambda}{4\pi d}\right)^2 \tag{b.5}$$

$$S_{ij}[dB] = \beta_{(P_{(g,d)},C_e,C_r)}[dB] + \gamma_{(H_k,P_{(g,d)},Ce_i,Cr_j)[}[dB] + 20log10\left(\frac{\lambda}{4\pi d}\right) \tag{b.6}$$

Publications

1. R. Masood, R. Burghelea, A. Carer, M. Le Gentil, O. Sentieys, P. Pajusco, C. Person, and R. Sauleau, "Indoor off-Body channel measurements using miniaturized chip antennas with pattern diversity," in *European Microwave Conference (EuMC)*, Rome (Italy), Oct. 2014.

2. R. Masood, C. Person, and R. Sauleau, "Distribution fitting for real-time off-Body channel measurements," in *IEEE International Microwave Workshop Series on RF and Wireless Technologies for Biomedical and Healthcare Applications*, London (UK), Dec. 2014.

3. R. Masood, C. Person, R. Sauleau, and P. Pajusco, "Ajustements statistiques pour l'étude du canal off-body en configuration NLoS à 2,4 GHz," in *XIXèmes Journées Nationales Microondes*, Bordeaux (France), Jun. 2015.

4. R. Masood, C. Person, and R. Sauleau, "Performance of Radiation Pattern and Polarization diversity for Body-Centric Applications at 2.45 GHz," *submitted, European Microwave Conference (EuMC)*, London (UK), Oct. 2016.

5. R. Masood, C. Person, and R. Sauleau, " A Compact Dual-mode, Dual-pattern Polarization Diversity Antenna for 2.45 GHz Body-Centric Communications," *submitted, IEEE Antennas and Wireless Propagation Letters*.

Seminars

1. "Channel Fitting in BAN context", *Capteurs - Homme instrumenté (journée scientifique du pôle MOM)*, Telecom Bretagne, Brest, 11 July 2014.

2. "Distribution Fitting for BAN Channel Measurements", *4eme journée des doctorants SICMA*, ENSTA Bretagne, Brest, 25 Sep. 2014.

3. "Mesure et modélisation du canal en contexte BAN," *Séminaire propagation*, Telecom Bretagne, Brest, 08 Oct. 2015.

Résumé

Cette thèse trouve sa place dans le cadre du projet BoWI qui signifie l'interaction entre le monde et le corps et qui présent une nouvelle et innovante inspiration des réseaux corporal sans fil (WBANs). Les principales contributions scientifiques de cette thèse se concentrent sur deux thèmes principaux pour des applications WBAN: (i) caractérisation du canal radio et (ii) la conception de l'antenne avec des performances stables à proximité du corps humain tout en offrant des caractéristiques réglables tel que le diagramme de rayonnement et de polarisation.

Pour le premier projet, les capteurs intelligents ont été utilisés incorporant des antennes puce ultra-miniaturisées sous la configuration de la diversité de rayonnement. Le canal off-body a été étudié à fond en tenant compte de divers paramètres radio tel que l'étalement du temps de propagation et la capacité du canal en utilisant des mesures du canal multi-trajets en temps réel. Une amélioration significative de la capacité du canal a été rapportée en exploitant les configurations MIMO 2×2 par rapport aux systèmes SISO en particulier pour un RSB élevé. L'évanouissement du canal à petite échelle a également été étudié pour les deux canaux off- et on-body à l'aide des données de mesure en temps réel. Un algorithme robuste d'ajustement a été développé à cet effet, et les modèles optimaux du premier ordre d'évanouissement ont été rapportés pour les deux types de canaux on- et off-body. Pour les études de canaux numériques, un simulateur du canal robuste a également été développé en utilisant une antenne puce électriquement petite sur des morphologies réelles en 3D avec des gestes réglables en tenant compte diverses améliorations telles que les techniques de raffinement et de réduction de maillage local, offrant ainsi le pouvoir de simuler des scénarios de WBASN arbitraires sous des ressources limitées. La portée du simulateur du canal a également été démontrée pour plusieurs postures du corps montrant son intérêt pour la classification de posture tel qu'il est utilisé dans le projet BoWI pour la reconnaissance gestuelle interactive.

Pour le deuxième sous-projet, diverses études de simulation ont d'abord été entreprises pour examiner l'impact critique du corps humain sur les performances de l'antenne. Les topologies d'antennes avec des performances stables sur le corps et les diagrammes de rayonnement appropriés ont été conçues pour des applications on- et off-body telles que l'antenne Inverted-F et l'antenne patch anneau court-circuité. Sur la base de la théorie de mode caractéristique d'antennes patch, une antenne bi-mode a été conçue fournissant la diversité de rayonnement et de polarisation. L'antenne offre des caractéristiques de rayonnement appropriées à la fois pour des applications on- et off-body à fréquence unique, tout en présentant un couplage croisé négligeable entre les deux modes et une performance stable sur le corps. L'antenne est également un candidat approprié pour des applications de la diversité et des applications MIMO tout en offrant un gain de diversité raisonnable (~10 dB). Enfin, les performances de la diversité de rayonnement et de polarisation ont été démontrées pour des applications portables. Des améliorations significatives dans le budget de liaison ont été rapportées et renforcées par des simulations et des mesures.

Mots-clés : Antennes, Réseaux de communication corporels, BAN, Modèle de canal, Interactions ondes personnes

Abstract

This thesis finds its place in the framework of BoWI project which stands for Body-World Interaction and is a novel and innovative inspiration of Wireless Body Area Networks (WBANs). The major scientific contributions of this thesis are focused around two main topics for WBAN applications: (i) Radio channel characterization and (ii) antenna design with stable performance in proximity to human body while offering tunable features e.g., radiation pattern and polarization.

For the first project, smart sensors were used incorporating ultra-miniaturized chip antennas under pattern diversity configuration. The off-body radio channel has been studied thoroughly considering various parameters such as delay spread and channel capacity using real-time multipath channel measurements. Significant improvement in channel capacity has been reported exploiting the 2×2 MIMO configurations compared to SISO systems especially at high SNRs. Small-scale channel fading has also been investigated for both off- and on-body channels using real-time measurement data. A robust fitting algorithm has been developed for this purpose and optimum first-order fading models have been reported for both off- and on-body channels. For numerical channel studies, a robust channel simulator was also developed using an electrically small chip antenna on realistic 3D body morphologies with tunable gestures and numerous enhancements such as local mesh refinement and reduction techniques, hence offering the power to simulate arbitrary WBASN scenarios under limited simulation resources. The scope of the channel simulator has also been demonstrated for sample body postures showing its interest for posture classification in interactive gesture recognition concept as used in BoWI project.

For the second sub-project, various simulation studies were first undertaken to consider the critical impact of human body on antenna performance. Antenna topologies with stable on-body performance and appropriate radiation patterns were designed for both on-and off-body applications e.g., Inverted-F antenna and short-circuited ring path antenna. Based on the characteristic mode theory of patch antennas, a dual-mode dual-pattern polarization diversity antenna has been designed. The antenna offers appropriate radiation characteristics for both on- and off-body applications at single frequency, meanwhile offering a negligible cross-coupling between the two modes and a stable on-body performance. It provides two different forms of diversities (radiation and polarization) in a single package, hence circumventing the use of antenna arrays since space and form factor are crucial for wearable applications. The antenna is also a suitable candidate for diversity and MIMO applications while providing reasonable diversity gain (close to 10 dB). Finally, the performance of radiation pattern and polarization diversities simultaneously has been demonstrated for body-centric applications. Significant improvements in link budget have been reported which are corroborated by both full-wave simulations and real-time measurements.

Keywords : Antennas, Wireless Body Area Networks, WBAN, Channel modeling, Antenna-body interaction.

TELECOM Bretagne

n° d'ordre : 2016telb0396

Télécom Bretagne

Technopôle Brest-Iroise - CS 83818 - 29238 Brest Cedex 3

Tél : + 33(0) 29 00 11 11 - Fax : + 33(0) 29 00 10 00